EPFL

Thèse n° 8201

Mapping of Chemical Heterogeneity at Surfaces with High-Throughput Wide-Field Second Harmonic Microscopy

Présentée le 1 septembre 2020

à la Faculté des sciences et techniques de l'ingénieur
Chaire Julia Jacobi de photomédecine - Laboratoire de biophotonique fondamentale
Programme doctoral en photonique

pour l'obtention du grade de Docteur ès Sciences

par

Igor NAHÁLKA

Acceptée sur proposition du jury

Prof. J.-E. Moser, président du jury
Prof. S. Roke, Dr A. Marchioro, directrices de thèse
Dr K. Domke, rapporteuse
Prof. E. Vauthey, rapporteur
Prof. A. Radenovic, rapporteuse

École polytechnique fédérale de Lausanne

2020

Your time is limited, so don't waste it living someone else's life. Don't be trapped by dogma - which is living with the results of other people's thinking. Don't let the noise of others' opinions drown out your own inner voice. And most important, have the courage to follow your heart and intuition.
— Steve Jobs

The only impossible journey is the one you never begin.
— Tony Robbins

To my parents, my brother, and my fiancée,
I couldn't do this without you. . .

Acknowledgements

First and foremost, I would like to express my sincere gratitude to my supervisor, Professor Sylvie Roke, for giving me the opportunity to do my Ph.D. at one of the leading technical universities in the world, EPFL. Furthermore, Sylvie gave me the opportunity to join the crème de la crème of European state-of-the-art research in the Marie Skłodowska-Curie Action project focused on Multimodal Functional BioPhotonic Imaging (FBI). During my Ph.D., I frequently traveled to different European cities for FBI meetings. Most of the time, I had top-class workshops there that built up my career and broadened my perspective. For the last four years, Sylvie supported me in my Ph.D., providing scientific guidance and sharing her life's philosophy. What I learned here will stay with me for the rest of my life, and for that I will say thank you again, Sylvie.

Second, I would like to deeply thank my co-supervisor, Dr. Arianna Marchioro, for all her guidance and support over the last two years. It often seemed that Arianna's day would have to be 72 hours to finish all the work she had on her plate, yet she always found time for me. I am grateful for all the writing tips and corrections she gave me during writing my manuscripts and thesis and for her patience and persistence. I have always been an optimist, but if I learned one thing from Arianna, its "Yes, I can!".

During the last two years, I was closely collaborating with Professor Kramer R. Campen and the Ph.D. student Gregor Zwaschka from his team. Our common efforts resulted in a paper and a manuscript, and I couldn't ask for a better teamwork experience. I want to thank Kramer for his critical scientific observations and his support. I would like to also thank Gregor for frequent, outstanding, several-hour long scientific discussions that shaped our research. In Gregor, I found a real friend, and I am grateful for that.

At the beginning of my Ph.D. studies, I was starting fresh in our Laboratory for fundamental BioPhotonics (LBP), and I was ready to step up the game, giving my 105%. It was Dr. Carlos Macias Romero, who introduced me to the nonlinear microscopy performed in the lab, and who guided me at the beginning. I always have had a direct conversation with Carlos, and for all this, I would like to thank him.

I want to express my gratitude to everyone in the mentioned FBI project. For the last three years, we became close to each other, like a scientific family. I would like to especially thank my fellow Ph.D. students in the FBI for sharing their insight about life, supporting each other, and, last but not least, for great parties.

I would like to thank Rebecca Veselinov and Cathy Buchs for their ever-present help with administrative processes and documents whenever I quickly needed help. This allowed me to

fully focus on my research.

Furthermore, I would like to thank my previous collaborators, Professor Aleksandra Radenovic, Professor Guillermo Villanueva, and Professor Eric Tyrode, for their support, for the provided experimental samples and programming codes.

Now comes the time to thank all the previous members of our LBP lab that composed the group spirit in my first half of Ph.D. studies. My thanks go to Dr. Cornelis U. Lütgebaucks, Dr. Nikolay Smolentsev, Dr. Yixing Chen, Dr. Evangelia Zdrali, and Filip Kovacik. Despite of busy Ph.D. life, we share snippets of memories that we won't forget, such as corridor fights with capoeira master Evi. My special thanks go to Professor Halil I. Okur, who guided me on the first paper I was participating at LBP. We spent many months living inside Illustrator software, modifying article figures on a daily basis, as well as discussing the data processing.

I want to express my gratitude to the current members of the LBP lab that started their Ph.D. studies after me: Nathan Dupertuis, Marie Bischoff, Maksim Eremchev, Sergey Kulik, Tereza Schönfeldova, Seonwoo Lee, and Saranya Pullanchery. You guys brought fresh energy into the LBP lab! I am thankful for all the scientific discussions, your support, and the fun we had together. I am grateful to know each one of you, and my only regrets are that I didn't dedicate more off-work time to spend with you. With Nathan and Sergey, we played more than one role-play games pretending to be someone we are not, and having lots of fun and uncontrollable laughing during that. I won't forget how we all shared the Christmas hot wine in Marie's place. With Maksim, we were traveling buddies, as we both were in the same FBI project. We had many in-depth discussions about technology, but also about life in general. Tereza and I were frequently complaining one to another about the things that bothered us, and I am thankful for her caring, listening ear. Seonwoo is another special person with whom I shared the details of my life. We listened to each other and gave a lot of advice to each other, which I will remember. Saranya came to the lab at the end of my Ph.D., nevertheless, we already had more than one good discussion and laugh together.

My special thanks go to my previous/current office mates that were standing next to me every day: Marie E. P. Didier, Claire Teulon, and David Roesel. We had a lot of fun with Marie, and we were supporting each other in times of need. She enriched my scientific life in Lausanne with her spontaneity and fondness for art. With Claire, we spent a lot of time doing experiments on the microscope, sharing experimental and theoretical knowledge. David joined the LBP lab approximately in half of my Ph.D., and since he came, the microscopy division of our lab experienced an awakening. I find him the center pillar for bringing Maksim, Seonwoo, and me together as a team, and have frequent discussions, drawing on the board. David also enriched me with his programming experienced, computer hardware knowledge, and few board game evenings.

I want to thank my previous LBP colleague and friend Jan Dedič, for helping me at the beginning of my Ph.D. to settle in Lausanne, and for offering his gained insights about Swiss life.

At this point, I would like to thank all my friends, both from Switzerland and Slovakia. I want to thank my EPFL friends Sanjin Marion, and Michal D. Macha for their support, travels done together, and roleplay games played together during my Ph.D.. I would like to thank

Arielle L. Planchette, Charles Gousset, Soham Basu, and Aparajita Singha for the nice dinners and board games we shared together. I further thank Martina Lihter for showing me that a person can be truly selfless, and for all the deep conversations we had about life. I also want to express my gratitude to my friends in the Archery Club of Lausanne, who showed me a part of the life outside academia.

My thanks further go to Jan & Hana Křížek, whom I know all the way from Prague. We have made it to Switzerland together, and I am grateful to call them friends. They definitely breathed an air of art over my life, and my only regrets are that I didn't spend more time with them.

My special thanks go to my "Swiss family": Séverine Coquoz and Orly Tarun. We shared together countless dinners, and birthday celebrations, supporting each other, and discussing our issues. This enriched my life in Lausanne and provided me with an anchor, being far from home.

Last but not least, in the category of friends, I want to thank my Slovak friends Adam, Zuzka, Mário, and Gabika. They were my true friends for more than a decade, and we encountered together all kinds of situations, laughing till we couldn't breathe, crying, and also feeling proud every time one of us achieved something. Although you were far, you still supported me in my Ph.D. studies.

My special thanks go to the family of my fiancée, Anjali Tarun, with whom I spent a lot of time despite the distance that separates us. I want to name Mama, Papa, Al, Cynthia, Millet, Ado, Balds, Wilbert, Emong, Roxinne, and all your families. You took me in as one of your own, and I cannot be more grateful for gaining such an amazing immersive new family.

My sincere gratitude goes to my wider family, both from father's and mother's side. These are the people that shaped me during my upbringing, and their influence will always reside in me. I would like to specifically thank my grandmother "Nagy" from the mother's side for giving me strength when she had none.

My family, my central pillars: Mother, Father, and my Brother. I cannot possibly express our connection and cohesiveness. We are a team that will always catch each other if we fall. It is exactly this sense of anchor that binds me to Slovakia and gives me the strength to conquer challenges in my life. My parents are the symbol of perfectness, and my aspiration is to be like them one day. All the virtues and values I stand for, start with them. My brother Dominik, although seven years younger, is more mature in many aspects of life than me, and conversations with him often gives me a new perspective. He can make me laugh under any circumstances, and I am ever grateful to call him my brother. I love you guys.

Last, but not least, I would like to thank my fiancée, Anjali Tarun. She is my personal sunshine no matter the weather, and she complements me in all my flaws. In the last three-and-a-half years, she showed me how to appreciate the small things in life. She also helped me grow as a person, and I can't be possibly luckier to have her. I love you, Anjali.

Lausanne, 25th May 2020 Igor Nahalka

Abstract

Many industrial processes are based on electrochemical reactions using engineered electrocatalysts. However, the current lack of theoretical knowledge hinders efforts to maximize catalysts efficiency, and the optimization process is mostly empirical. To fully understand the structure/chemical function relationship on complex surfaces, new experimental tools are needed that can evaluate electrochemical processes on nm to tens of µm length scales. These tools have to be surface-specific and ideally label-free in order not to influence the reactions. In this thesis, we apply high-throughput wide-field second harmonic (SH) microscopy together with in-situ electrochemical techniques to i) study the extent of surface heterogeneity, ii) surface changes during electrochemical cycling, and iii) to identify and characterize surface active sites.

We first investigated surface heterogeneity at the glass/electrolyte interface with the novel SH microscope developed in our laboratory, as this interface has been widely discussed in the literature with inconsistent results. The spatial resolution of our SH microscope, ~400 nm, together with the temporal resolution of 250 ms, allowed us to spatially resolve the surface $pK_{a,s}$ for the silica deprotonation reaction with values ranging from 2.3 to 10.7. The average value, 6.7, coincides well with the reported values from experimental studies lacking spatial resolution. Furthermore, we demonstrated the ability of SH microscopy to image the orientation of bulk water molecules under an externally-applied electric field in a confined 1 µm-sized glass pore.

We further applied SH imaging coupled in-situ with cyclic voltammetry to characterize the surface of gold electrodes during electrochemical cycling. Analyzing the voltage dependence of the SH signal and utilizing a novel correlation coefficient procedure for wide-field SH imaging, we have identified two types of surface areas on the polycrystalline gold. The first type remains stable during electrochemical cycling, while the second type undergoes surface reconstruction. We assign the second type of gold surface areas to domains of higher roughness, where anion adsorption occurs at lower potentials than expected.

Lastly, we focused on studying the oxygen evolution reaction (OER) on polycrystalline gold working electrodes by coupling SH imaging with electrochemical methods. We observe a large spatial heterogeneity of the OER, and we quantify that only < 1 % of the electrode surface is responsible for oxygen production. We further identify two types of active sites. The first type is observed at potentials > 2 V vs. the reverse hydrogen electrode (RHE), which is the onset of the OER. This type is stable under potential cycling, presumably extending multiple layers deep into the gold electrode. The second, anomalous type, is observed at potentials < 2

V vs. RHE. This type is removed by potential cycling, suggesting it involves a structural motif only 1-2 gold layers deep.

The findings in this thesis highlight the importance of surface heterogeneity on a sub-µm level, showing that the surface structure influences the chemical properties and reactivity. This heterogeneity needs to be considered and utilized in the industrial context to establish more efficient electrochemical processes with lower energy requirements.

Keywords: water, wide-field second harmonic microscopy, electrochemical cycling, glass-electrolyte interface, gold-electrolyte interface, surface heterogeneity, acid dissociation constant, surface reconstruction, oxygen evolution reaction, active sites

Résumé

De nombreux procédés industriels sont basés sur des réactions électrochimiques utilisant des électrocatalyseurs spécialement développés. Cependant, le manque de compréhension théorique du fonctionnement de ces catalyseurs empêche de maximiser leur efficacité. Afin de comprendre pleinement la relation entre la structure et la fonction chimique de ces surfaces complexes, il est nécessaire de disposer de nouveaux outils expérimentaux pour évaluer les processus électrochimiques sur des échelles allant du nm aux dizaines de µm. Ces outils doivent être spécifiques aux surfaces et idéalement ne doivent pas utiliser de labels afin de ne pas influencer les réactions. Dans cette thèse, nous utilisons la microscopie de seconde harmonique (SH) à champ large, couplée avec des techniques électrochimiques in-situ dans le but de i) étudier l'étendue de l'hétérogénéité de la surface, ii) les changements de la surface lors de l'application d'un potentiel, et iii) pour identifier et caractériser les sites actifs de la surface.

Nous avons tout d'abord investigué l'hétérogénéité de l'interface verre/électrolyte avec le nouveau microscope de SH développé dans notre laboratoire, car cette interface a été largement étudiée et de nombreux résultats contradictoires ont été présentés dans la littérature. La résolution spatiale de notre microscope, ~400 nm, ainsi que la résolution temporelle de 250 ms, nous ont permis de résoudre spatialement le pKa pour la réaction de déprotonation de la silice, avec des valeurs allant de 2.3 à 10.7. La valeur moyenne, 6.7, correspond à la valeur souvent reportée dans des études n'ayant pas la résolution spatiale. De plus, nous avons démontré la capabilité du microscope de SH d'imager l'orientation des molécules d'eau confinées dans le volume d'un pore en verre de 1 µm sous l'effet d'un champ électrique externe.

Nous avons ensuite utilisé l'imagerie de SH couplée in-situ avec la voltammétrie cyclique afin de caractériser la surface d'électrodes d'or lors de balayages en potentiel. En analysant la dépendance au voltage du signal de SH et en utilisant une nouvelle procédure de corrélation de coefficient pour l'imagerie de SH à champ large, nous avons identifié deux types de zones à la surface des électrodes d'or polycristallin. Le premier reste stable lors des balayages en potentiel, alors que le deuxième est sujet à une reconstruction de la surface. Nous attribuons ce deuxième type de zone à des domaines à haute rugosité, où l'adsorption d'anions intervient à des potentiels plus bas qu'initialement attendu.

Dernièrement, nous avons étudié la réaction d'évolution de l'oxygène (OER) à la surface d'électrodes d'or polycristallin, en couplant l'imagerie de SH avec des méthodes électrochimiques. Nous observons une importante hétérogénéité spatiale de l'OER, et nous quantifions

que seul < 1% de la surface de l'électrode est responsable de la production d'oxygène. Nous identifions également deux types de sites actifs. Le premier type est observé à des potentiels > 2 V dans l'échelle de l'électrode réversible à hydrogène (RHE), ce qui correspond au potentiel de début de l'OER. Ce type est stable lors des balayages en potentiel, et nous présumons qu'il s'étend sur plusieurs couches à l'intérieur de l'électrode. Le deuxième type est anormal, et n'est observé que à des potentiels < 2 V dans l'échelle RHE. Ce type est supprimé par balayage de potentiel, ce qui suggère qu'il s'agit d'un motif peu profond, de seulement 1-2 couches d'or.

Les résultats de cette thèse révèlent l'importance de l'hétérogénéité de surface sur une échelle inférieure au µm, et montrent également que la structure de la surface influence les propriétés chimiques et la réactivité. Cette hétérogénéité doit être prise en compte et exploitée dans un contexte industriel afin d'établir des processus électrochimiques à faible demande énergétique.

Mots-clés : eau, microscopie de seconde harmonique à champ large, balayage de potentiel, interface verre-électrolyte, interface or-électrolyte, hétérogénéité de surface, constante de dissociation acide, reconstruction de surface, réaction d'évolution de l'oxygène, sites actifs

Contents

List of Figures

List of Tables

1 Introduction

In the world of solid/liquid interfaces, the local surface structure dictates the (electro)chemical function and efficiency of related (electro)chemical processes [1–3]. Determining the link between the underlying structure and the desired functionality is nowadays attempted by many different imaging techniques offering complementary insights. One of these techniques is second harmonic microscopy (SHM). SHM is the central technique used in this thesis for studying the surface chemistry and dynamics at the silica glass/electrolyte interface and the gold/electrolyte interface.

In this chapter, we discuss the importance of linking surface structure/morphology and electronic structure to chemical function, together with current experimental techniques capable of studying this complex subject. Afterwards, the theory of second harmonic generation is presented, along with SH studies applied to silica/ and gold/electrolyte interfaces illustrating how to convert the SH signal into surface-property quantities. At the end of this chapter, we summarize the content of this thesis.

1.1 Importance of structural and chemical heterogeneity at solid/-electrolyte interfaces

The current lifestyle and the increase of population on Earth are causing a growth in energy consumption. While this was not a world-class issue a century ago, the present deterioration of the environmental balance is casting significant concerns about our energy consumption in the future [4–6]. The worldwide priority is now to research new fuels and new pathways of acquiring our everyday products from chemicals that are fossil-free and sustainable [7]. To achieve this, it is essential to advance (electro)chemical conversion processes converting molecules (for example, CO_2 or H_2O) into higher-value products (for instance, H_2, NH_3, metanol or hydrocarbons) by using energy from renewable sources [8]. Such conversion processes depend heavily on the used (electro)catalysts, as they dictate the efficiency of a process together with the selectivity towards a certain reaction product [9]. Knowledge of the mechanistic steps of chemical transformations is crucial for optimizing efficiency, and

lately, there have been significant progresses in understanding pivotal (electro)chemical transformations as for example, water splitting in H_2 and O_2 [10, 11]. This understanding is the foundation of catalysts design; however, despite recent advancements, there is still much room for improvement.

Finding an optimum design for an (electro)catalyst is very profoundly linked to the knowledge of the material's active site. The active site is dependent on the exact material composition, as well as the surface structure and the morphology of the catalyst. For instance, different crystalline surface facets tend to contain catalytically active sites that promote different reactions [3]. Additionally, material defects that extend to the surface also impact the design of (electro)catalysts, altering (electro)chemical reactivity. Material surface defects typically range from nm to µm length scales, and frequently span between the surface into the bulk [12, 13]. Hence, it is often difficult to properly characterize such defects, as it would require techniques that can probe the bulk material, while still being surface-sensitive. Many current experimental techniques cannot differentiate well enough between different local surface structures. As a consequence, different surface structures or defects could potentially show similar activity but have very different electronic and structural properties, therefore hindering our understanding [14]. On the atomic length scale, the relationship of surface structure versus chemical properties is largely related to the underlying local electronic structure, which has indeed been correlated to catalytic activity [15–17]. The local electronic structure influences processes such as the binding of reaction intermediates [18]. For instance, it has been recently shown that low-coordinated surface atoms (such as atoms on a step-edge site) have a decreased reaction barrier due to the modified local electronic structure [19–21].

Therefore, revealing structure-function relationship holds great promise for designing more effective material structures for (electro)catalysis, energy conversion/storage, or biosensing [21–23]. This concept is utilized in chemical and energy industries, where manufacturing (electro)catalysts that contain large amounts of Å- to nm-sized surface structures with the appropriate electronic properties and structure/morphology can maximize the catalytic efficiency [24]. However, understanding the structure-function relationship is problematic at the experimental level. Mapping the full electronic structure with Å-resolution at solid/liquid interfaces and at the same time on large sample areas brings up practical challenges. Therefore, this approach is not experimentally used for understanding the local surface chemical properties, and it is more common to map the surface properties that are influenced by the electronic structure, such as adsorption of ions, oxidation state, reactivity, surface potential, etc. [18, 25–27]. While there have been some studies characterizing the electronic structure (or chosen related-properties) of specific material structures over the last few decades, these reports usually study well-defined model systems in controlled environment, often in vacuum [28–30]. Such results cannot be used for straightforward extrapolation to real complex reaction conditions in liquids, which include interaction with solvent molecules, the presence of an electrostatic field, and fluctuations of pressure and temperature [31, 32]. To circumvent this issue, in the last two decades, there has been flourishing development of microscopy techniques tailored for solid/liquid interfaces, allowing for direct or indirect imaging of to-

pography and related chemical information. The next Section 1.2 gives a detailed overview of current imaging techniques that are being used for studying heterogeneous solid/liquid interfaces, and describes their characteristic features and specifications.

However, most of the current imaging techniques rely on a rastering scheme. While this scheme can easily provide nm resolution, it also implies a time delay in collecting the signal from different areas, therefore precluding the possibility to monitor large-scale changes in real time (with µs to ms resolution). Additionally, the rastering scheme is time-consuming if applied to large surface areas (100 μm^2 range). This can become a drawback in an application-oriented context, where large-scale screening of samples is needed. As all practical catalysts are very heterogeneous, the ability of large-scale screening of the surface is desirable to localize the presence of "hot spots" of increased reactivity. One of the imaging techniques suitable for studying solid/liquid interfaces on areas of 100 μm^2 and with millisecond time resolution is second harmonic microscopy (SHM). In this thesis, we utilize SHM to indirectly image surface properties, such as surface potential, or surface charge density, in order to characterize and understand the surface chemistry at the silica/electrolyte interface. We further use SHM to identify and distinguish between different local active surface sites responsible for oxygen evolution reaction at the gold/electrolyte interface. We also demonstrate how to identify surface areas that undergo surface restructuring during electrochemical cycling at the gold/electrolyte interface. In all three projects, we observe that heterogeneity in surface structure causes heterogeneity in surface chemistry, a result that is consistent with the literature presented above.

1.2 State of the art imaging of surface and surface properties

In this section, I introduce the main imaging techniques for studying solid/liquid interfaces. They are classified into five categories based on the approach used to acquire the signal, or on the type of information their signal provides. For quick orientation, I briefly summarize below the major features of each category.

The first two categories are scanning probe microscopies and electron-beam based microscopies. These techniques are capable of measuring both topographic and chemical information with (sub)-nm resolution. The chemical information includes, for instance, local redox properties of surfaces and adsorbates or identifications of active surface sites. On the other hand, the common downside of these techniques is that the imaging area is conventionally on the orders of μm^2, which limits their applicability in the industrial context. The third category consist of optical microscopies utilizing ultraviolet to mid-infrared wavelengths. Most of these techniques take advantage of spectroscopic analysis to identify chemical groups/molecules in the sample, which is especially suitable for studying biological solid/liquid interfaces. The spatial resolution here is on the order of hundreds of nm with imaging areas ~100x100 μm^2. The fourth category of X-ray based microscopy techniques is suited mainly for studying inorganic solid/liquid interfaces. These techniques have with the ability to deter-

mine the elemental composition of the sample, and can reach μm resolution with an imaging area of several cm^2. In the last category, I present chosen microscopy techniques that are a combination of previously described techniques.

1.2.1 Scanning probe microscopy techniques

Scanning ElectroChemical Microscopy (SECM)

SECM uses an electrode shaped into a sharp tip that is scanned above the solid/liquid surface. The electrode is insulated everywhere except at the tip apex, which indirectly interacts with the scanned surface [33]. Measurements are usually performed in an electrochemical cell with four-electrodes: a scanning probe, an imaged surface, a reference electrode, and a counter electrode. There are four main SECM modes of operation, i.e., a feedback mode, a generation/collection mode, a shielding mode, and a potentiometric mode [34]. The most common mode is the feedback mode, where the measured quantity is the tip current. In the proximity of the electrochemically inactive surface, the tip current is altered by a blockage of the diffusion of solution species, giving negative feedback (decrease in current). On the other hand, the current is increased by an electrochemically active surface due to the regeneration of redox mediator at the surface, which can then diffuse back to the tip, giving a positive feedback [35]. This configuration allows for imaging reactions that take place both at electrically insulating and at conducting surfaces.

Since the 1990s, the SECM technique has much improved its spatial imaging resolution from the mm to the nm length scale due to the development of modern SECM tips [35]. Achieving such fine resolution with a reasonable signal to noise ratio, however, comes with few experimental challenges [36]. First, exact positioning and stability are required at the nm scale as the tip is not allowed to contact the surface physically. Second, nm resolution requires nm-sized tips that are fragile, can be damaged by electrostatic effects and vibrations and can be easily contaminated. Third, using nm-sized tips means detecting currents on the order of pA or less, resulting in decreased signal-to-noise ratio. Fourth, the temperature of the SECM system has to be well stabilized to reduce the noise during the imaging. Mastering these experimental challenges gives SECM access both to the chemical and to the topographic information of the scanned surface with a nanoscale resolution. Therefore, SECM is suitable for: i) studying redox properties of surfaces and adsorbates [37], ii) monitoring highly localized chemical reactions [37], iii) studying electrocatalytic activities of single nanoparticles [38], or iv) electrochemical imaging of biological cells [39].

ElectroChemical Scanning Tunneling Microscopy (EC-STM)

The core of the EC-STM technique originates from the scanning tunneling microscopy (STM). In STM, a sharp scanning metallic tip is put to the proximity of the imaged surface while a small bias is applied between the tip and the imaged surface. Thus, only conductor or

semiconductor surfaces can be imaged, traditionally in vacuum [40]. The current that flows between electrodes has to breach an electrically insulating gap. This is called a tunneling effect inherent to quantum mechanics. The current decreases exponentially with the distance between the tip and the surface. There are two basic modes of operation in STM: i) maintaining a constant current during the imaging by finding a corresponding tip distance from the surface; or ii) keeping a constant distance between the tip and the surface, and measuring the changes in the current. The latter is used mainly on atomically flat surfaces [41].

Being able to measure electrode/electrolyte interfaces requires two major changes to the STM setup, which is then referred to as an EC-STM setup [42]. The first change is that the measurements are performed in a three-electrode electrochemical cell. The second change is that EC-STM uses a scanning tip, which is not an active electrode and only images the surface morphology. Nevertheless, the tip might still be under the potential control for applying a voltage drop in order to drive the tunneling current. This means that EC-STM can map the local reactivity on the surface only if it is associated with a change in the surface topography [43]. The described approach of EC-STM may seem similar to the SECM technique. The main difference is that the EC-STM tip measures the tunneling current in the closest vicinity of the surface, while the SECM tip measures the faradaic current from an electron transfer reaction at a further distance from the surface. The nanoscale resolution of EC-STM comes from the shorter distance between the tip and the surface, which contains the electron transfer to a confined area below the tip [43]. The nano-spatial resolution makes EC-STM a suitable candidate for studying deposition, adsorption, or dissolution reactions locally [25] and for identifying catalytically active surface sites in electrochemical reactions [18].

ElectroChemical Atomic Force Microscopy (EC-AFM)

EC-AFM is a combination of electrochemical measurements and atomic force microscopy (AFM). The AFM contains a cantilever with an atomically sharp tip oscillating in the proximity of the surface. The cantilever is illuminated by a laser beam and reflects the beam on a photodetector. The position of the beam on the photodetector is used for mapping the tip-sample interaction, creating a feedback loop. One of the important factors in AFM is the stiffness of the cantilever, which determines the speed of oscillation and the expected magnitude of tip-sample interaction. In comparison with STM, AFM has the advantage of being able to measure almost any type of surfaces, including biological samples, ceramics, or glass, while maintaining the Å resolution [44]. AFM can be tuned to measure various local forces between the tip and the imaged surface stemming from electrical, magnetic, friction, adhesion, or Van der Waals interactions [45]. The AFM system can be expanded to EC-AFM by using a three-electrode electrochemical cell, where the scanned surface represents the working electrode.

The most used configuration of EC-AFM is the passive probe configuration, where the evolution of surface morphology is monitored in-situ without additional information on the electrochemical reactivity. The studied surface acts as the working electrode; therefore, it

must be conductive. However, the EC-AFM tip is unbiased. Electrochemical measurements, such as cyclic voltammetry or pulse voltammetry, are performed in the electrochemical cell during the AFM scanning. As the potential on the surface is swept, the resulting current flow alters the morphology on the surface through electrochemical reactions [46]. This induces morphological changes that are being continuously monitored by the EC-AFM tip. The presented approach can be applied for studying ions adsorption, electrodeposition, corrosion, or volume changes in electroactive polymers [47–49].

1.2.2 Electron-beam based microscopy techniques

Liquid-Phase Transmission Electron Microscopy (LP-TEM)

The origin of this technique lies in the transmission electron microscopy (TEM). In TEM, a beam of electrons emitted from an electron gun is transmitted through the sample. The transmitted scattered/diffracted electrons are then focused on an imaging device, which can be, for instance, a fluorescent screen followed by a charge-coupled device. Instead of using glass lenses to direct and image the electrons, TEM utilizes magnetic fields. Imaging the electrons with a sufficient signal to noise ratio comes with two requirements [50]. First, the imaging has to take place in a vacuum to avoid additional scattering. Second, the sample has to be less than 100 nm thick. The contrast of images produced in TEM can arise from multiple mechanisms, and each mechanism reveals different information about the sample. For instance, the contrast can arise from differences in the atomic number (Z-contrast), from differences in the thickness/density (mass-thickness contrast), from differences in the crystal structure (diffraction contrast), etc. [51].

Utilizing TEM for imaging in liquids can be achieved by employing an ultra-thin (10-100 nm) cell separating the liquids from the vacuum. Such an extension is abbreviated as LP-TEM. The most common cell type is a flow cell allowing for a continuous fresh inflow of different reagents important for synthesis processes [52]. The resolution of LP-TEM is influenced by the liquid flow speed, thickness of the cell, viscosity of the solution, ionization damage, etc.. Despite these factors, an optimized LP-TEM system can reach a nanoscale spatial resolution, and acquisition times allowing for real-time imaging [53]. The crucial factor in LP-TEM is to understand the interaction of the electron beam with the solution as the electron beam can alter the chemistry during the imaging, such as decomposing solvent molecules into radicals, and can cause either an oxidation or a reduction of the reagents [54]. LP-TEM can be applied for studying nucleation, growth, coarsening, or self-assembly controlled by reagent mixing [54, 55].

1.2.3 Ultraviolet to Mid-infrared light microscopy techniques

Raman Microscopy

Raman microscopy is a broad term for optical techniques based on the Raman scattering effect, where a monochromatic laser light interacts inelastically with the imaged sample, probing the molecular vibrational modes. The frequency of scattered photons after such interaction can either be downshifted (lower energy) or upshifted (higher energy). This is referred to as the Stokes (see Fig. 1.1A) or the Anti-Stokes shift, respectively. The energy difference of the shift gives information on the molecular structure [56]. In Raman scattering, the signal stems from spontaneous transitions where every individual molecule contributes with an incoherent addition to the total signal, emitted in all directions. However, these transitions occur with a low probability (approximately one in every 10^8 photons); thus, the signal from Raman scattering is very weak [57]. For this reason, it is more common for a Raman microscope to be based on the coherent anti-Stokes Raman scattering (CARS) process or on the stimulated Raman scattering (SRS) process.

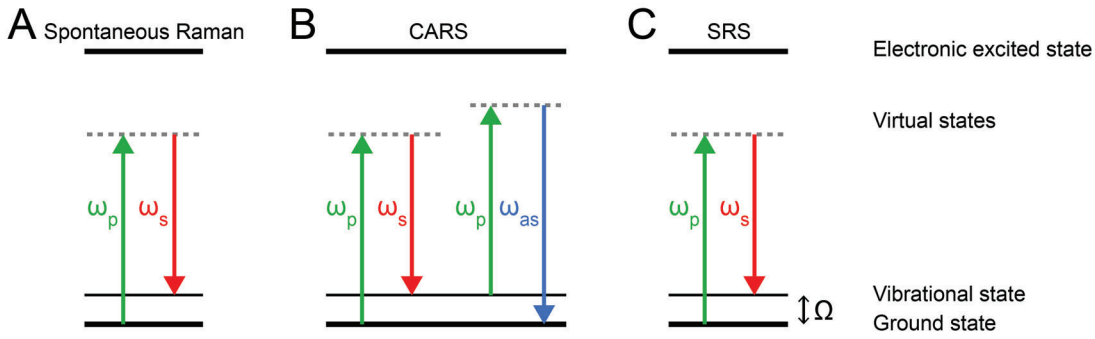

Figure 1.1 – Energy level diagrams for Raman processes. (A) Spontaneous Raman scattering. The pump photons with angular frequency of ω_p (green color) are inelastically scattered by the sample, resulting in spontaneously scattered red-shifted Stokes photons ω_s (red color) that are incoherent. (B) Coherent anti-Stokes Raman scattering (CARS). Three photons (ω_p, ω_s, ω_p) illuminate the sample and create the anti-Stokes photon (ω_{as}) labeled in blue. (C) Stimulated Raman scattering (SRS). Two photons (ω_p, ω_s) illuminate the sample, and their energy difference is matching the energy of a molecular vibration (Ω) to generate stimulated Stokes photons.

CARS is a third-order nonlinear optical process, where the sample is illuminated with a pump beam, a Stokes beam, and a probe beam. However, in practice, the probe beam can be the same as the pump beam, see Fig. 1.1B. The Anti-stokes photons are then generated from the sample as a nonlinear combination of the three beams. This process is resonantly enhanced when the frequency difference between the pump beam and the Stokes beam matches the frequency of a Raman-active vibration of the molecule [58]. Here, the signal stems from a coherently driven transition, where individual molecules add up their signal coherently in case the phase-matching condition is fulfilled. A typical spectral imaging acquisition time of collecting Anti-stokes photons from all the pixels for a few different vibration frequencies is on the order of seconds [59]. CARS is commonly applied for label-free non-invasive chemical

imaging and quantitative analysis of lipids or for temperature-dependent measurements [60, 61]. As an optical technique, the spatial resolution of CARS is typically on the order of hundreds of nm.

In SRS, only the pump beam and the Stokes beam are used for sample illumination, see Fig. 1.1C. The basic principle of this approach is that the energy difference between the pump and Stokes photons have to match the energy of a vibrational state. In contrast to CARS, SRS is an inelastic process as the energy from the pump beam is transferred to the Stokes beam [62]. The main advantages of SRS are being free from the fluorescent and the non-resonant background, and being free from considerations of phase-matching conditions. Due to SRS linear signal scaling, it can give quantitative information about chemical constituents of the sample [63, 64]. Application and the resolution of the SRS technique are similar to CARS.

Sum Frequency Microscopy (SFM)

SFM is an optical technique based on sum-frequency generation (SFG), which is a coherent second-order nonlinear process. In SFG, two laser beams illuminate the sample, most commonly a visible beam and an infrared beam. The role of the infrared beam is to generate a coherent state between the ground state and a vibrationally excited state of the sample. The role of the visible beam is to convert the vibrationally excited state into a virtual electronic state [65]. Upon relaxation back to the ground state, a sum frequency photon is emitted from the sample. This process is feasible only in the presence of spatial non-centrosymmetry at the sample, as the SFG is a second-order nonlinear process [66]. Non-centrosymmetry is automatically satisfied at the interfaces of two different media. Therefore, SFG is inherently surface-specific with sub-monolayer sensitivity. The intensity of SFG is crucially affected by satisfying the momentum (or phase-matching) conservation law, which has to be considered when designing the geometry of the experiment. Collecting sum frequency photons in a direction without taking into account the conservation law could result in no signal. The advantages of this spectroscopic technique are being label-free, non-invasive, and offering vibrational contrast.

SFM applies the presented principles of SFG in a microscopy configuration. Here, a broadband spectrum is recorded for every pixel with ~1 s acquisition time. The overall time for obtaining a hyperspectral image is, therefore, on the order of hours [67, 68]. While this is not practical, a new approach has recently emerged utilizing a compressive sensing, improving the acquisition time by one order of magnitude [69]. Common to all optical techniques, the spatial resolution is on the order of hundreds of nm. SFM has been increasingly used for studying metal surfaces, biomaterial systems, or nonlinear materials [67, 70].

Second Harmonic Microscopy (SHM)

SHM is a special case of SFM, where the two laser beams illuminating the sample have identical (fundamental) wavelengths. Therefore, the generated second harmonic (SH) photons possess exactly double the energy. In comparison with the SFM, SHM does not provide vibrational fingerprints [66]. The requirement for spatial non-centrosymmetry is still valid here, making SHM inherently sensitive to interfaces. It also maintains the advantage of being label-free and non-invasive. Because the intensity of the SH signal is tied to the degree of centrosymmetry breaking, SHM can be used for indirect dynamic monitoring of surface properties, such as surface potential, or surface charge density [71,72]; but also for indirect monitoring of dynamic changes in surface chemistry, such as anion adsorption on metals [73]. However, the main requirement in these types of experiments is that one can ensure experimental conditions where only a specific known surface reaction takes place so that the SH intensity can be uniquely assigned to the underlying physical process [74]. With the recent development of powerful femtosecond lasers and gated electron-multiplying cameras, SHM has demonstrated acquisition speed on a μs time scale, allowing dynamic surface measurements [27].

Ultraviolet Localized Mid-infrared PhotoAcoustic Microscopy (ULM-PAM)

This novel technique has been established just recently in 2019, first reported by Shi et al. [75]. Here, a pulsed mid-infrared laser illuminates the sample placed in its focal spot, resulting in thermal excitation. Consequently, a confocal pulsed ultraviolet laser photoacoustically probes the rise in the transient temperature. This step is used as an indicator for estimating the magnitude of the mid-infrared absorption by the sample. The described detection scheme is possible due to the Grüneisen relaxation effect stating that the temperature rise in the sample enhances photoacoustic signals [76]. The interesting feature of ULM-PAM is that it provides mid-infrared absorption contrast with a spatial resolution given by the ultraviolet light. ULM-PAM is designed to be biocompatible. This is due to using an ultraviolet light in the range of 200-230 nm, where this wavelength is highly absorbed by the majority of biomolecules. At the same time, this wavelength is transmissive in water, which suppresses the water background otherwise present in mid-infrared techniques. In summary, ULM-PAM can directly image various vibrational bonds, even those that are not Raman-active in the wide mid-infrared range. This technique is targeted for imaging mainly biological samples, such as lipids, and proteins, revealing structural and chemical information [75].

1.2.4 X-ray based microscopy techniques

X-ray Absorption Microscopy (XAM)

XAM originates from X-ray absorption spectroscopy (XAS). XAS can provide information about the local electronic structure of the sample by using intense and tunable X-ray beams, most commonly generated by synchrotrons. The X-ray beam with energy below 100 keV illuminates

the sample and promotes a deep-core electron to an unoccupied energy state above the Fermi energy [77]. This leaves the system with a core-hole, which is subsequently filled with an electron relaxing from a higher-level energy state. The electron decay emits an X-ray photon with characteristic energy, which is different than the illuminating X-ray photons. The spectrum is thus obtained by comparing the intensity of the illuminating X-ray beam before and after the interaction with the sample, for different X-ray wavelengths. There are two main common modes of XAS [26]: X-ray absorption near edge structure (XANES) and extended X-ray absorption fine structure (EXAFS). XANES gives information about electron transitions from occupied to unoccupied states by tuning the X-ray energy within ±1% of the absorption edge. The edge position serves as an indicator of the element's oxidation state due to its correlation to the effective nuclear charge [78]. On the other hand, the signal in EXAFS stems from the interference between ejected and backscattered photoelectrons, which can be used to obtain the local structural information. These different modes of operation are applicable for XAM, which can study catalysis with additional information about elements, their orientation, or their oxidation state [26]. Nowadays, XAM offers imaging with μm resolution covering an area of several cm^2 [79].

X-ray Photoelectron Microscopy (XPM)

XPM originates from X-ray photoelectron spectroscopy (XPS), where the sample is illuminated with an intense X-ray beam that has enough energy to eject an electron from the sample. The electron is ejected into a continuum, and it is referred to as a photoelectron. In XPS, photoelectrons from the sample's surface are ejected only from an effective depth of few nm. The number and the energy of photoelectrons provide information about the elemental composition, and about the electronic and the chemical state of the material [80]. The imaged surface must be maintained clean, which requires an ultra-high vacuum. Therefore, initially, the XPM imaging of solid/liquid interface was performed separately after the electrocatalysis by transferring the sample under vacuum [26]. Recently, a new XPM approach emerged, called the X-ray operando photoemission electron microscopy (XPEEM). In XPEEM, a flow cell is used for separating the sample and the solution from the ultra-high vacuum. The cell is sealed by a graphene membrane that is photoelectron-transparent [81]. This approach allows XPM to reach a nanoscale spatial resolution covering areas on the order of tens x tens of μm^2, suitable for studying the electrochemical reactions at electrode/electrolyte interfaces [82].

1.2.5 Combined microscopy techniques

Scanning electrochemical atomic force microscopy (SECM-AFM)

The combination of SECM and AFM techniques is accomplished by using a special scanning tip on a cantilever, which incorporates an electrode at the tip (~100 nm) serving as a probe for electrochemical imaging, while an additional protrusion of the tip below the electrode serves as a probe for topographical AFM imaging [83]. During the imaging, SECM-AFM first uses the

AFM contact mode to scan the topography of the surface. The scanning tip is then retracted to a specific distance from the surface based on the measured topographic data. The surface is then scanned by SECM modality keeping the distance from the surface constant, i.e., following the contours of the surface [84]. The advantages of SECM-AFM are that SECM modality now has the knowledge of the exact distance from the surface, and the resolution of SECM-AFM is approaching that of an AFM. The disadvantage of this technique is that performing a single scan line takes a few seconds; therefore, obtaining a whole image is a lengthy process [85]. SECM-AFM technique is suitable for studying complex heterogeneous solid/liquid interfaces, investigating the structure-activity relation [86].

Electrochemical Tip-Enhanced Raman Microscopy EC-TERM

EC-TERM originates from a combination of electrochemical scanning tunneling microscopy (EC-STM) and the tip-enhanced Raman spectroscopy (TERS). The EC-STM metallic tip acts as a local field enhancer of the laser light for the Raman processes. In this manner, the probed volume below the tip is reduced yielding a significant improvement in the Raman sensitivity of ~ 3-6 orders of magnite [87], while the spatial chemical resolution can reach ~10 nm [31]. The EC-TERM is, therefore, especially suitable for imaging the chemistry of potential-controlled active sites [88]. The two modalities of EC-TERM are used as follows. The EC-STM modality identifies the nanoscale active surface sites by comparing the local current fluctuations of the tunneling barrier above reactive vs. non-reactive nanoscale surface sites during the surface scanning. The TERS modality records the Raman spectra of local sites as a function of applied potential, which gives the chemical contrast between the reacting species. Similar to the AFM technique, the acquisition of a single line scan is on the order of seconds, making the imaging rather slow [31]. The EC-TERM technique can be applied for studying electrochemical processes at metal/electrolyte interfaces, such as the corrosion or heterogeneous catalysis-related reactions [31, 89].

Another possible combination of techniques is the atomic force microscopy and the tip-enhanced Raman spectroscopy (AFM-TERS) [90]. AFM-TERS offers similar advantages/disadvantages over the EC-TERM, as we discussed earlier for EC-AFM/EC-STM techniques. AFM-TERS is capable of nanoscale chemical mapping for nonconducting sample surfaces. Therefore, this technique is suitable for studying biological systems, or nanomaterials [91].

1.2.6 Comparison of presented imaging techniques

Previous sections (from 1.2.1 to 1.2.5) introduced essential techniques for studying surfaces and surface properties in liquids. For better visual comparison, all the presented imaging techniques are summarized in Tab. 1.1. Unfortunately, every technique from this table has multiple variations adopted by different research groups, or companies around the world, resulting in different specifications of given devices. Specifications of a given device can focus on the temporal resolution, the spatial resolution, the imaging field of view, the spectroscopic

resolution, and many others. Therefore, summarizing specifications for all imaging techniques here is a rather ambitious task. Thus, the values given in Tab. 1.1 are given as guidelines only.

Table 1.1 – Comparison of microscopy techniques.

	Information type	Resolution on the order of	Length/width of imaging area	Imaging speed per image	References
Scanning electrochemical microscopy (SECM)	Chemical Topographic	few nm	few µm	1x1 µm few minutes	[35, 38]
Electrochemical scanning tunneling microscopy (EC-STM)	Topographic	few nm	hundreds of nm	1x1 µm few minutes	[18, 92]
Electrochemical atomic force microscopy (EC-AFM)	Topographic	few nm	tens of µm	10x10 µm few minutes	[47, 93]
Liquid-phase transmission electron microscopy (LP-TEM)	Topographic	few nm	hundreds of nm	1x1 µm few seconds	[54, 94]
Raman Microscopies (CARS & SRS)	Chemical	hundreds of nm	hundreds of µm	100x100 µm sub-minute	[95, 96]
Sum frequency microscopy (SFM)	Chemical	few µm	hundreds of µm	100x100 µm few minutes	[67, 68]
Second harmonic microscopy (SHM)	Structural	hundreds of nm	hundreds of µm	100x100 µm few milliseconds	[27, 74]
UV localized MIR photoacoustic microscopy (ULM-PAM)	Chemical in 3D	hundreds of nm	hundreds of µm	100x100 µm few minutes	[75]
X-ray absorption microcopy (XANES)	Chemical Elemental composition	few µm	few centimeters	100x100 µm few seconds	[79, 97]
X-ray photoelectron microscopy (XPEEM)	Chemical Elemental composition	hundred nm	tens of µm	10x10 µm sub-hour	[82, 98]
Scanning electrochemical atomic force microscopy (SECM-AFM)	Chemical Topographic	few nm	few µm	10x10 µm few hours	[85, 99]
Electrochemical Tip-Enhanced Raman Microscopy (EC-TERM)	Chemical Topographic	few nm	hundreds of nm	1x1 µm few hours	[31, 100]

Looking at Tab. 1.1, no single technique seems to be universal for different types of applications. For instance, while SECM's nm-resolution can offer valuable information about local nanoscale surface sites, it goes hand in hand with a small field of view; therefore, enormous imaging times are necessary for sub-millimeter areas. Inspecting further Tab. 1.1, the SHM stands out by the information type it provides. Although SHM does not directly measure the topography of the surface or its chemistry, the SH signal nevertheless, carries information about the structural geometry at the interfaces and present spatial symmetries. Under certain circumstances, as will be discussed in the rest of this chapter, the SH signal can be translated to specific surface properties, allowing for indirect study of surface chemistry. Due to indirect imaging of surface chemistry, SHM is probably the fastest technique on this list, especially in a wide-field configuration presented in this thesis. Millisecond acquisition times allow for capturing the dynamics of surface chemistry with an optical resolution commonly ~ 300 nm. Furthermore, in the wide-field SHM configuration the imaging field of view can be easily up-scaled by a more intense laser source and a camera with better resolution, allowing for real-time imaging of sub-millimeter x sub-millimeter sized areas.

In this thesis, a wide-field concept of SHM was utilized for mapping the chemical heterogeneity and its dynamics at solid/liquid interfaces. Next section will give the basic theory of

SH generation.

1.3 Second harmonic generation (SHG) theory

In the previous section, we introduced the central imaging technique used in this thesis: second harmonic microscopy (SHM). SHM is a fast and versatile optical technique that can indirectly monitor the dynamic changes of surface properties and surface chemistry under specific conditions. To understand the indirect conversion of SH intensity into meaningful surface-related quantities, we introduce in this section the basic SHG theory for bulk materials and for interfaces.

1.3.1 SHG in non-centrosymmetric structures

Nonlinear optics is concerned with alterations in the optical properties of the examined material by a presence of light, most commonly, by the presence of intense laser light. One of the major milestones were reached in 1961 when Franken et al. discovered the process of second harmonic generation (SHG) [101]. Before this discovery, the optical response of the material in terms of induced polarization $\boldsymbol{P}$ was given by conventional linear optics as

$$\boldsymbol{P} = \epsilon_0 \boldsymbol{\chi}^{(1)} \boldsymbol{E}, \tag{1.1}$$

where $\boldsymbol{\chi}^{(1)}$ is the linear susceptibility of the material, and $\boldsymbol{E}$ is the incident electric field. As can be seen, $\boldsymbol{P}$ increases linearly with $\boldsymbol{E}$. After the discovery of nonlinear optical processes, such as SHG, this equation was extended to include higher-order terms. Thus, in general, $\boldsymbol{P}$ is given as the following Taylor expansion:

$$\boldsymbol{P} = \epsilon_0 \left[\boldsymbol{\chi}^{(1)} \boldsymbol{E} + \boldsymbol{\chi}^{(2)} \boldsymbol{E}\boldsymbol{E} + \boldsymbol{\chi}^{(3)} \boldsymbol{E}\boldsymbol{E}\boldsymbol{E} + ... \right], \tag{1.2}$$

where $\boldsymbol{\chi}^{(n)}$ is the n-order nonlinear susceptibility tensor [66]. Equation 1.2 is the macroscopic manifestation of the material's response. On a microscopic level, the incident electric field that interacts with a molecule (or electrons in a crystal lattice) can induce a molecular dipole $\boldsymbol{p}$. Summing then all the induced molecular dipoles considering their direction of oscillation, we can write the polarization as:

$$\boldsymbol{P} = N \langle \boldsymbol{p} \rangle, \tag{1.3}$$

where N is the number of all the induced dipoles and $\langle \boldsymbol{p} \rangle$ is the average induced molecular dipole. Similar to Eq. 1.2, also here we can express $\langle \boldsymbol{p} \rangle$ by separating the term into individual orders:

$$\begin{aligned} \langle \boldsymbol{p} \rangle &= \langle \boldsymbol{p}^{(1)} \rangle + \langle \boldsymbol{p}^{(2)} \rangle + \langle \boldsymbol{p}^{(3)} \rangle + ... \\ \langle \boldsymbol{p}^{(1)} \rangle &= \boldsymbol{\alpha}^{(1)} \boldsymbol{E} \\ \langle \boldsymbol{p}^{(2)} \rangle &= \frac{1}{2!} \boldsymbol{\beta}^{(2)} \boldsymbol{EE} \\ \langle \boldsymbol{p}^{(3)} \rangle &= \frac{1}{3!} \boldsymbol{\beta}^{(3)} \boldsymbol{EEE}, \end{aligned} \tag{1.4}$$

where $\boldsymbol{\alpha}^{(1)}$ is the first-order polarizability of the molecular dipole, $\boldsymbol{\beta}^{(2)}$ is the second-order polarizability, and $\boldsymbol{\beta}^{(3)}$ is the third-order polarizability [65]. Each of these terms describes a charge oscillation in the molecule. With respect to the presented framework, second harmonic generation stems from the second-order polarization $\boldsymbol{P}^{(2)}$, which can be described as:

$$\boldsymbol{P}^{(2)} = \epsilon_0 \boldsymbol{\chi}^{(2)} \boldsymbol{EE} \sim N \langle \boldsymbol{p}^{(2)} \rangle . \tag{1.5}$$

Based on Eq. 1.5, the second-order nonlinear susceptibility $\boldsymbol{\chi}^{(2)}$ is dependent on the second-order polarizability $\boldsymbol{\beta}^{(2)}$, the density of molecules, and their orientational distribution [102]. Within the dipole approximation [103, 104], second-order optical effects are forbidden in a centrosymmetric medium. On one side, this is a restriction, as the SHG can't be used for studying bulk materials that contain an inversion symmetry. On the other hand, the centrosymmetry at the interface between two isotropic media is broken along the interface normal; therefore, allowing for SHG. This implication is particularly powerful, as it renders the SH surface-specific. One of the first experimental reports about SHG was done on a flat surface by Brown et al. more than a half-century ago, where the authors investigated the effect of adsorbed surface layers altering the SH signal [105]. It became apparent afterward that molecules adsorbed on the surface modify the SH signal. To avoid the influence of surface-adsorbed impurities, ultrahigh purity chemicals should be used in SH experiments. Another way how to circumvent impurities was demonstrated much later in 1996 by Wang et al., where authors measured the SH signal from the surface of centrosymmetric particles in isotropic solution, which increased the effective surface area by several orders of magnitude [106].

SHG can originate from two types of processes, as shown in Fig. 1.2. The first one is called a resonant process (Fig. 1.2A). Here, two fundamental incident photons at an angular frequency ω bring the system to an excited state through a virtual intermediate state. Upon relaxation, the system transitions from the excited state into the ground state, emitting a SH photon with double energy and a double angular frequency of the fundamental photons. The second type of SH signal is non-resonant, see Fig. 1.2B. The main difference is in the

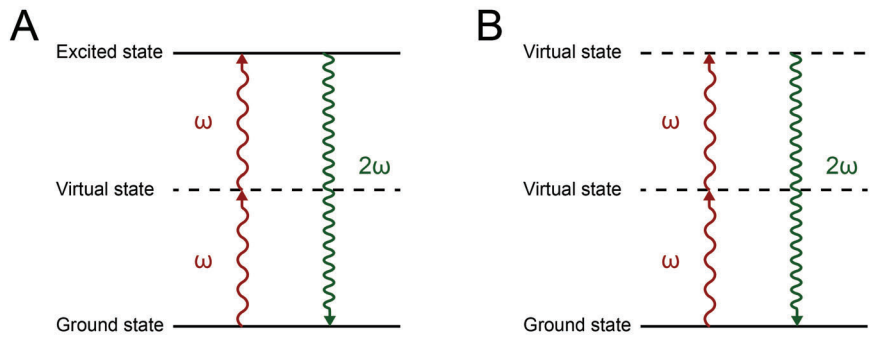

Figure 1.2 – Energy-level diagram describing the second harmonic generation. (A) Diagram of a resonant SH generation, where two incident photons of angular frequency ω (red color) excite the system to a real excited electronic state. Once the energy stored in the excited state relaxes back to the initial ground state, the energy difference is emitted as a photon with twice the angular frequency 2ω (green color). (B) Diagram of non-resonant SH generation, analogous to (A). The main difference is that the system is actually excited to a virtual state instead of an excited electronic state.

excitation, as both the intermediate and the final states are virtual. Such process is elastic with all the participating photon wavelengths far away from any electronic resonance of the material. Non-resonant SHG is, therefore, especially favorable for biological samples due to no absorption of photons; i.e., low photo-toxicity. The SHG material response, according to Eq. 1.5, depends on the value of $\chi^{(2)}$, which is generally on the order of $\sim 10^{-12}$ m/V [66].

1.3.2 Influence of surface potential on the SH signal

So far, we have considered SH generation to be given purely as a second-order process. However, other processes can contribute to the second-order polarization as well, and therefore contribute to the SH signal. At solid/liquid interfaces, the nonlinear polarization responsible for generating SH photons at planar interfaces is composed of two terms: a second-order polarization $\boldsymbol{P}^{(2)}(2\omega)$ and a third-order polarization $\boldsymbol{P}^{(3)}(2\omega)$. In a mathematical perspective, this translates to:

$$\boldsymbol{P}^{NL}(2\omega) = \epsilon_0 \boldsymbol{\chi}_s^{(2)} : \boldsymbol{E}(\omega)\boldsymbol{E}(\omega) + \epsilon_0 \boldsymbol{\chi}^{(3)'} : \boldsymbol{E}(\omega)\boldsymbol{E}(\omega)\boldsymbol{E}_{DC}(z), \tag{1.6}$$

where $\boldsymbol{\chi}_s^{(2)}$ is the second-order surface susceptibility, $\boldsymbol{\chi}^{(3)'}$ is the effective third-order susceptibility including all the contributions associated with the electric field at the interface $\boldsymbol{E}_{DC}(z)$. $\boldsymbol{\chi}_s^{(2)}$ is dependent on the second-order polarizability $\boldsymbol{\beta}^{(2)}$, the density of non-centrosymmetric molecules at the interface, and their orientational distribution. Considering a liquid of polar solvents, such as water, where every water molecule is a (non-centrosymmetric) dipole, the SH signal from surface species will be dominated by the SH contribution from interfacial water molecules due to their higher number of density [107, 108]. The second term in Eq. 1.6 shows that SH signal is also influenced by the $\boldsymbol{E}_{DC}(z)$. This is caused by the presence of

interfacial charges, which create a surface potential $\Phi(z)$ (z = 0 defined at the interface). The surface potential is related to the electric field at the interface through the Gauss law as $\boldsymbol{E}_{DC}(z) = -\nabla\Phi(z)$. Surface potential influences water molecules in the vicinity of the interface by changing their orientation.

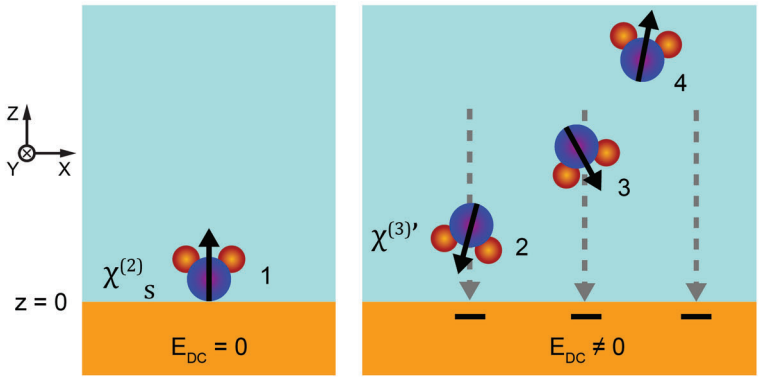

Figure 1.3 – Molecular sources for possible second harmonic scattering. (1) SH signal originating from the non-centrosymmetry of interface through $\boldsymbol{\chi}_s^{(2)}$ considering no electrostatic field. Contribution of SH signal originating from the water molecules reoriented by electrostatic field in the vicinity of the surface (2) and in the bulk (3). Last SH contribution (4) is associated with the third-order response of isotropic molecules $\left(\boldsymbol{\beta}^{(3)}\right)$, which is usually extremely small. Gray lines represent the field-lines.

Fig. 1.3 illustrates the various SH contributions at a planar interface. Apart from the inherent SH contribution of centrosymmetry breaking at the interface (marked as 1), there are three more SH contributions associated with $\boldsymbol{\chi}^{(3)'}$: the contribution from oriented water molecules in the vicinity of the interface (marked as 2), the contribution from oriented water molecules in bulk (marked as 3), and the contribution from $\boldsymbol{E}_{DC}(z)$ interaction with the isotropic third-order susceptibility of bulk water (marked as 4). Contributions 2) and 3) are related to $\boldsymbol{\beta}^{(2)}$ of water, but contribution 4) depends on $\boldsymbol{\beta}^{(3)}$. The presented mechanism implies that polar liquids, such as water, can be used as a probe for tracking the interfacial processes and their dynamics [109, 110].

Lastly, it is important to mention that the SH photons can be generated coherently or incoherently. The degree of coherency is given by the phase relationships between the molecules generating SH photons. If the non-centrosymmetric molecules have a fixed phase relationship, for instance by belonging to the same interface, the resulting SH signal is coherent, and its intensity scales quadratically with the number density of molecules [111]. On the other hand, generating SH photons from isotropically distributed non-centrosymmetric molecules, such as bulk water, will yield an incoherent SH signal. The resulting SH intensity then scales linearly with the number density of the molecules. This type of SH scattering is known as Hyper-Rayleigh Scattering.

1.4 Second harmonic generation at aqueous interfaces

In this thesis, we focused on studying the surface chemistry at two solid/liquid interfaces by means of second harmonic microscopy. These interfaces are the silica glass/electrolyte interface and the polycrystalline gold/electrolyte interface, which are two widely studied model systems used for various industrial applications, such as water-repellent coatings, thermostable general-duty lubricants, electrodeposition, nanoparticle catalysts, electrochemical sensors, etc. [112, 113]. To pave the way for Chapters 3-5, we introduce here the underlying mechanisms of how the SH signal is generated from these interfaces and how this signal is related to meaningful surface properties.

1.4.1 Silica glass - aqueous interface

Silicon dioxide (silica) is an oxide of silicon with chemical formula SiO_2. Silica is the most abundant solid compound in the Earth's crust, which causes it to be a low-cost material. Being optically transparent in the visible range, silica is used as the major component for various types of amorphous glasses in the optical industry. Another interesting property of silica in a glass form is the chemical resistance, making this material widely utilized in the chemical industry. In the nano- to micro-particle form, colloidal suspensions of SiO_2 are broadly used for separation, heterogeneous catalysis, and as major components for ceramics and coatings [112].

When silica is in contact with an aqueous solution, surface SiO_2 groups react with water molecules and form silanol groups (SiOH) [114]. The basic silanol groups are displayed in Fig. 1.4. In general, silanol groups are amphoteric, which means that they can release or accept protons into or from the solution depending on the local pH condition at the interface [115]. For instance, at high local pH, i.e., low proton concentration, protons on the silanol groups are unstable and are prone to be released into the solution. Thus, the surface becomes composed of negatively charged silanol groups (see the silanol group on the right in Fig. 1.4), which results in a negatively charged overall surface. Different silanol groups impose chemical equilibrium at different pH values [107]. This is largely determined by the local network of hydrogen bonds between neighboring silanol groups [116]. In a vicinal silanol group, the proton of one silanol interacts with the oxygen atom of an adjacent silanol through the hydrogen bonding. The proton is, therefore, less prone to be released into the solution, with logarithm of acid dissociation constant ($pK_{a,s}$) ~ 2.7 [116]. In an isolated silanol group, adjacent silanols are further apart, so the proton can be easier released into the solution resulting in a lower local pH (more acidic), and a $pK_{a,s}$ ~ 10.3. Different $pK_{a,s}$ values and their assignment to specific silanol groups is, however, still being debated in the research community [117].

The surface of silica glass containing different silanol groups displays heterogeneity in surface charge density [118]. As described in Section 1.3.2, interfacial water molecules reorient their dipole moment in the vicinity of surface charges, in this case, mirroring the distribution of surface charges. This induces a heterogeneity in the degree of interfacial centrosymmetry

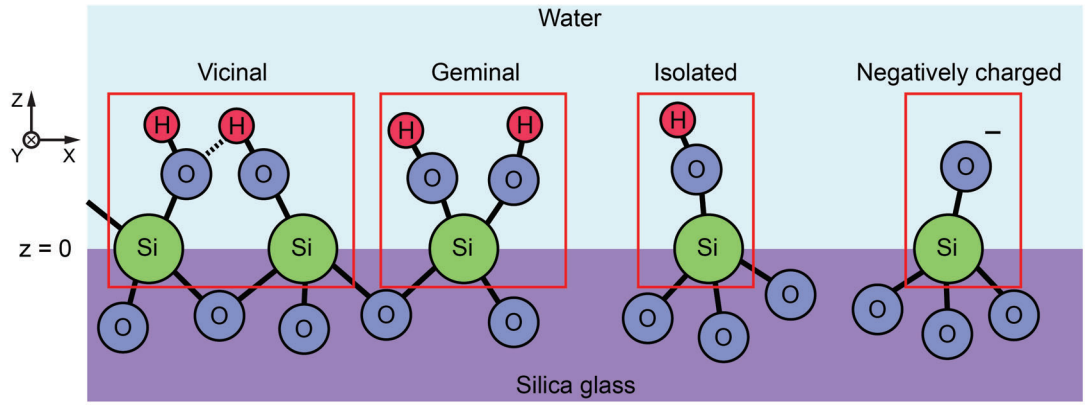

Figure 1.4 – Silanol groups at the silica/water interface. The schematics depicts the basic silanol groups: vicinal, geminal, isolated, and negatively charged group, marked with red rectangles. Si, O, and H represents the silicon, oxygen, and hydrogen, respectively.

breaking, which can be monitored by the SHG. One of the first SH experiments on the silica/water interface was performed by Ong et al. in 1992 [107], where the authors measured the SH signal from a flat surface as a function of bulk pH. Indeed, the increase of SH signal with increasing pH of the bulk solution was attributed to different ratios of SiOH vs. SiO- silanol groups at the surface. The authors also demonstrated that the SHG technique can be used for determining the equilibrium constant at the interface.

Using the SH signal to track the distribution of surface silanol groups at the silica/water interface became a key concept essential for SH studies because it demonstrated how to link the SH signal to other surface-related quantities, such as the surface potential, or $pK_{a,s}$. Surprisingly, since this concept was published in 1992, there is still an ongoing debate about reported $pK_{a,s}$ values from different research groups, that seem to be contradictory [107, 116–118]. In Chapter 3 we will examine the surface potential and related $pK_{a,s}$ values of a glass/electrolyte interface by performing a SH microscopy, and see, if the spatial resolution that has been absent in the previous experimental studies will bring new insights into contradictory results.

1.4.2 Gold - aqueous interface

Gold has the electronic configuration $[Xe]4f^{14}5d^{10}6s^{1}$, and its atomic number is 79, which indicates that this element is born during supernova explosions in the universe. One of the unique characteristics of gold is that the 4f electrons under-screen the 5d and the 6s,p electrons from the nuclear charge, resulting in an effect analogous to lanthanide contraction, which is further superimposed with an onset of relativistic effects [113, 119]. As a result, the atom radius is ~20% smaller, and gold is the most electronegative metal on a Pauli scale [119]. The high corrosion resistance of gold is due to a very high first ionization potential (9.2 eV). On the other hand, the well-defined band-edge at ~2.4 eV is responsible for the strong yellow color of

bulk gold [113]. Gold metal assembles its atoms into a face-centered-cubic (fcc) crystal lattice.

In the language of nonlinear optical processes, the gold structure is centrosymmetric; hence, the SHG is forbidden from the bulk material. However, the centrosymmetry is broken at the interface, making gold a suitable material for SHG surface studies [120]. Unlike the previously discussed amorphous silica glass that inherently possesses morphological surface heterogeneities, here, an ideal single-crystal gold surface appears periodically homogeneous. However, even single crystal gold can possess surface structural variations, such as terraces that will alter its local surface properties at an Å scale [121]. Such a small length scale can be properly studied only by scanning probe microscopies. The polycrystalline gold, on the other hand, contains a large number of different types of defects that span from Å to mm length scale, creating complex structural and chemical surface heterogeneities [14]. While understanding these heterogeneities is important to understand reactivity at the interface and electrochemical reactions, the polycrystalline gold is seldom used for deterministic studies due to the difficulty of experimentally mapping the complex morphology. Hence, there is a room for research in this area yet to be filled.

SHG from gold/electrolyte interface differs from the silica/electrolyte interface because gold is a conductor and possesses free electrons. Free electrons cause a substantially stronger centrosymmetry breaking at the interface than in the case of dielectric material [122, 123]. Therefore, the SH contribution from the interfacial reoriented water molecules will not be so strongly dominating the overall SH signal in this case. The presence of free electrons also means that plasmons can be generated by laser light wavelengths of < 500 nm, which should be considered when designing a SHG experiment. Propagating surface plasmons can be excited with laser light only by using a prism or a grating, while localized surface plasmons can be excited on local surface irregularities alone [124, 125].

Generating SH light from a gold/electrolyte interface is largely determined by the symmetries of gold facets. Thus, the SH signal displays an azimuthal anisotropy [126]. Monitoring the SH anisotropy of a single-crystal gold surface under electrochemical conditions has proven to be particularly useful for studying the surface adsorption or the surface reconstruction effects as these effects modify the surface symmetry, altering the SH anisotropy pattern [127]. Performing SHG on the gold/electrolyte interface under applied bias shows that the SH signal increases with increasing positive applied potential, as a result of positive surface charging [128]. This trend ceases upon reaching the oxidation potential, which starts at ~1.2 V vs. reversible hydrogen electrode (RHE). By further increasing the potential, the SH signal starts to decrease due to the oxide layer effectively removing the excess charge of the metal. Surface adsorption and reconstruction will further modify the trend of the SH-potential dependent signal, which is likely to occur at surface heterogeneities [129]. By tracking the SH potential-dependent signal during cyclic voltammetry, a local comparison of surface sites can be made, revealing areas of strong surface reconstruction. Identifying these areas is further explored in Chapter 4.

1.5 This Thesis

In this thesis, we studied the chemical heterogeneity of solid/liquid interfaces with high-throughput wide-field second harmonic microscopy. We employ this imaging technique to study the spatial distribution and magnitude of acid dissociation constants at the silica/electrolyte interface with sub-second temporal resolution. We demonstrate that SH imaging is capable of identifying surface areas prone to reconstruction under potential cycling at the polycrystalline gold/electrolyte interface, as well as identifying different types of active sites responsible for O_2 bubble evolution. The thesis is structured as follows:

- Chapter 2 contains a detailed description and characterization of the wide-field SH microscope used for this thesis. The chapter further contains key theoretical and practical concepts for maximizing the efficiency of generating the SH signal, discussing the importance of various imaging parameters. The last section gives information on the sample preparation, and additional technical details.
- In Chapter 3, we performed SH imaging of the silica/electrolyte interface with sub-second temporal resolution, revealing heterogeneity in the values of the acid dissociation constant of silica groups along the interface, ranging from $pK_a = 2.3$ to $pK_a = 10.7$. Furthermore, we demonstrated the possibility to image microscopically-confined bulk water molecules that rotate along an oscillating external electric field.
- In Chapter 4, we studied the gold/electrolyte interface by applying SH imaging combined to cyclic voltammetry to polycrystalline and nanocrystalline gold electrodes. Processing the acquired SH data by two different approaches yields mutually supporting results, granting SH imaging an ability to identify surface areas/spots that undergo surface restructuring under potential cycling, without any a priori knowledge of surface morphology.
- In Chapter 5, we show that by combining SH imaging with in-situ voltammetry/chronoamperometry, we were able to identify two types of active sites for the evolution of molecular oxygen at the polycrystalline gold/electrolyte interface. The first type is restricted to <1% of the total gold surface (tens of μm^2), starts at potentials positive of the onset of the oxygen evolution reaction (OER), and requires a structural defect. The second type starts before the onset of the OER, and is unstable under potential cycling.
- Chapter 6 contains the summary of the findings of this thesis, and provides an outlook of future directions and applications using non-resonant SH imaging of solid/liquid interfaces.

This thesis is based on various publications by the author. The details of the publications are given at the end of the thesis.

2 Experimental Details & Methodology

This chapter provides a detailed description of the wide-field second harmonic (SH) microscope used in this thesis to collect all the SH data. The first section describes the operation principle and the characterization of the SH microscope with emphasis on the high imaging throughput allowing for tracking the dynamics of surface processes on the order of ms to µs. The second section offers general insights for designing a SH imaging experiment, revealing which parameters of the system are crucial and how they can limit the overall performance. The last section gives details on sample preparation and assembly of experimental parts before the imaging in an electrochemical cell.

The wide-field SH microscope used in this thesis was built by Dr. Carlos Macias Romero, a former postdoc in the Laboratory for Fundamental Biophotonics (LBP). Furthermore, the theoretical calculation and experimental characterization of the imaging throughput in Section 2.1.4 was also done by Dr. Romero.

2.1 SH Microscope

In this section, first the wide-field SH microscope and its underlying principle of operation are described, followed by characterizing the fundamental beams, their propagation through the microscope, and the optical fluence deposited on the sample. Next, the variable 3D illumination of the microscope is described emphasizing the importance of the light polarization direction. Experimental details on how to align and match respective fundamental and SH polarization combinations are presented. The chapter continues with an explanation and evaluation of why the wide-field configuration can be orders of magnitude faster in acquiring the same SH intensity as a raster scanning configuration.

2.1.1 Optical setup

The optical setup description is divided into two parts, starting with the description of the experimental assembly and composition of optical elements. The following part focuses on explaining the principle of how the variable 3D illumination in the SH microscope is generated.

General Concept

Figure 2.1 shows the schematic of the wide-field emission multiphoton microscope that can operate in the second harmonic (SH) regime and in the two-photon fluorescence regime. Two different schemes for collecting the signal from the sample are possible: the transmission mode (fully described here) as well as the reflection mode (this sub-configuration is detailed in Section 4.2.3). Fig. 2.1 shows the setup in the transmission mode. The light source is a Yb:KGW femtosecond laser (Light Conversion Ltd., model Pharos SP-1.5), which delivers < 190 fs pulses centered at 1028 ± 5 nm at a maximum output power of 6 W and variable repetition rates between 1 kHz - 1 MHz. The laser system is set to a repetition rate of 200 kHz. All microscope mirrors on the path are protected silver mirrors (Thorlabs, PF10-03-P01). The achromatic lenses and other optical elements on the illumination path (1030 nm) are near-infrared antireflection coated (Thorlabs, B), while the optical elements on the detection path (515 nm) are antireflection coated for the visible region (Thorlabs, A).

We use a spatial light modulator (Holoeye Pluto-NIR-015), which is a phase-only device coated for near-infrared wavelengths, to modify the illumination pattern of the laser beam. The spatial light modulator has a 1920 x 1080 pixel resolution and an 8 µm pixel pitch. A diffraction grating is displayed on the SLM, shaping the reflected laser light in distinct diffraction orders that are focused in the Fourier plane. At the Fourier plane, only the $+1^{st}$ and -1^{st} orders are allowed to pass. The two orders are eventually focused in the back focal plane of the illumination microscope objective (OBJ1), which results in two collimated beams overlapping at the sample in a wide-field configuration. The illumination water-immersion microscope objective (Olympus, LUMPLFLN 60XW) has 60x magnification with a numerical aperture of NA = 1.0, providing a working distance of 2 mm. The laser is set to deliver a peak power density of 34.6 GW/cm^2 (6.7 mJ/cm^2 fluence) at the sample, on a field of view with a diameter of 82 µm full-width at half maximum. Once the SH photons are generated at the sample, they are collected by a water-immersion microscope objective (Olympus, LUMFLN 60XW) with high NA of 1.1 that possesses a collar for variable coverslip correction. The working distance of this objective is 1.5 mm. The collected SH light is projected on a back-illuminated electron-multiplied and intensified CCD camera with 512x512 pixels (Princeton Instruments, PI-MAX4: 512EM-HBf P46 GEN III). The size of a single pixel corresponds to ~400x400 nm in the sample plane. The basic acquisition time of the SH image is 5 µs, and the setting can be adjusted to deliver the final SH image as a sum or an average of

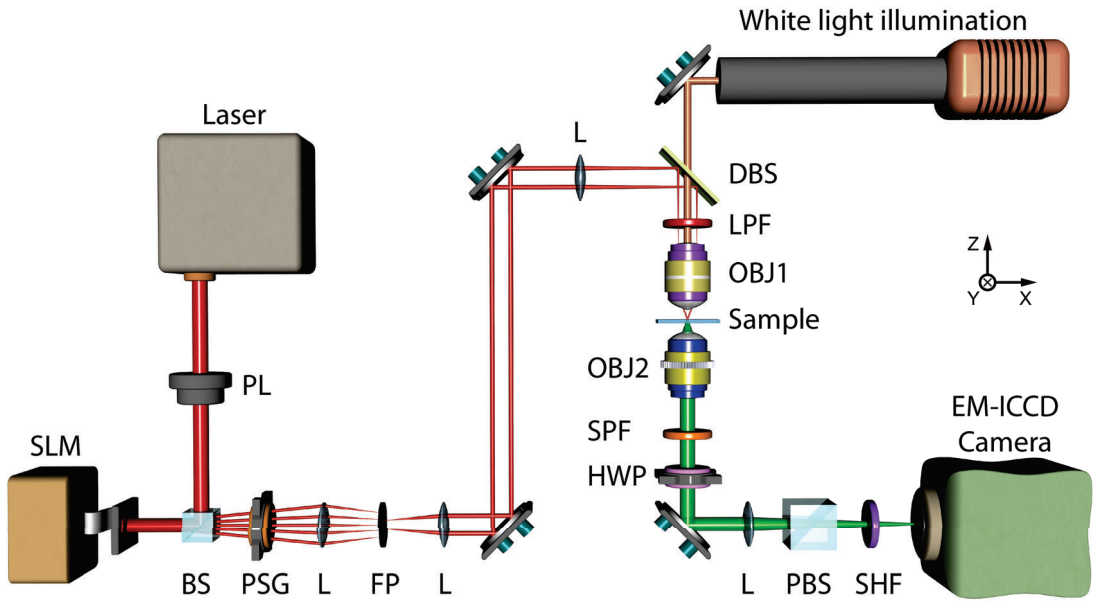

Figure 2.1 – Schematic of the second harmonic microscope in the transmission mode of operation. SLM – spatial light modulator, BS – beam splitter, PL – polarizer, PSG – polarization state generator, L – achromatic lens, FP – Fourier plane, DBS - dichroic beam splitter, LPF - long-pass filter, OBJ1 – microscope objective, SPF – short-pass filter, HWP – half-wave plate, PBS – polarizing beam splitter, SHF – second harmonic band-pass filter, EM-ICCD – electron multiplying gated camera.

multiple basic acquisitions.

The position of the sample is manipulated by an XYZ translation stage (Asi Imaging, PZ-2000), where the XY-axes are controlled by actuators with a 10 cm travel range, while the Z-axis is moved by a piezoelectric stage with 300 µm travel range. As a complementary feature of this positioning system, both microscope objectives are mounted on Z-axis actuator stages (Asi Imaging, LS-200), offering an individual alignment of each microscope objective.

An essential feature of the SH microscope is the ability to perform polarimetric measurements. Here, we use a polarization state generator composed of a zero-order quarter-wave plate (Thorlabs, WPQ05M-1030) followed by a zero-order half-wave plate (Thorlabs, WPH10M-1030) to modify the polarization state of the laser light. Long-pass filter (Thorlabs, FEL0750) before the top microscope objective ensures that only the laser light is illuminating the sample. The polarization state of the emitted SH light is analyzed with a zero-order half-wave plate (Thorlabs, WPH10M-514) followed by a polarizing beam splitter (Thorlabs, PBS252). A short-pass filter (Thorlabs, FES0750) and a 515 nm SH band-pass filter (Omega Optical, 10 nm) after the bottom microscope objective ensure that only the SH photons are collected by the camera.

Variable illumination angle in 3D

Nowadays, spatial light modulators (SLM) are widely utilized in microscopic applications due to their versatility to modulate the laser light in the system [130–132]. In laser scanning microscopes, the speed of image acquisition depends on the physical response of the scanner and also on the imaging

process detecting a sufficient signal in each pixel. At the same time, the intensity of the confocal illumination must be below the photodamage threshold of the sample. To increase the speed of such imaging, it would be necessary to parallelize the imaging with multiple scanning laser beams. Laser beam multiplexing can be easily achieved by using an SLM eliminating the complexity of any moving scanning parts [133]. SLMs are also used for phase and orientation alterations of the illumination pattern to yield a sub-diffraction resolution without mechanical calibration [134]. Furthermore, SLMs are used as optical wavefront shapers as well as filters in the Fourier plane capable of correcting for many types of aberrations in the transmitted beam due to any refractive index mismatches [130].

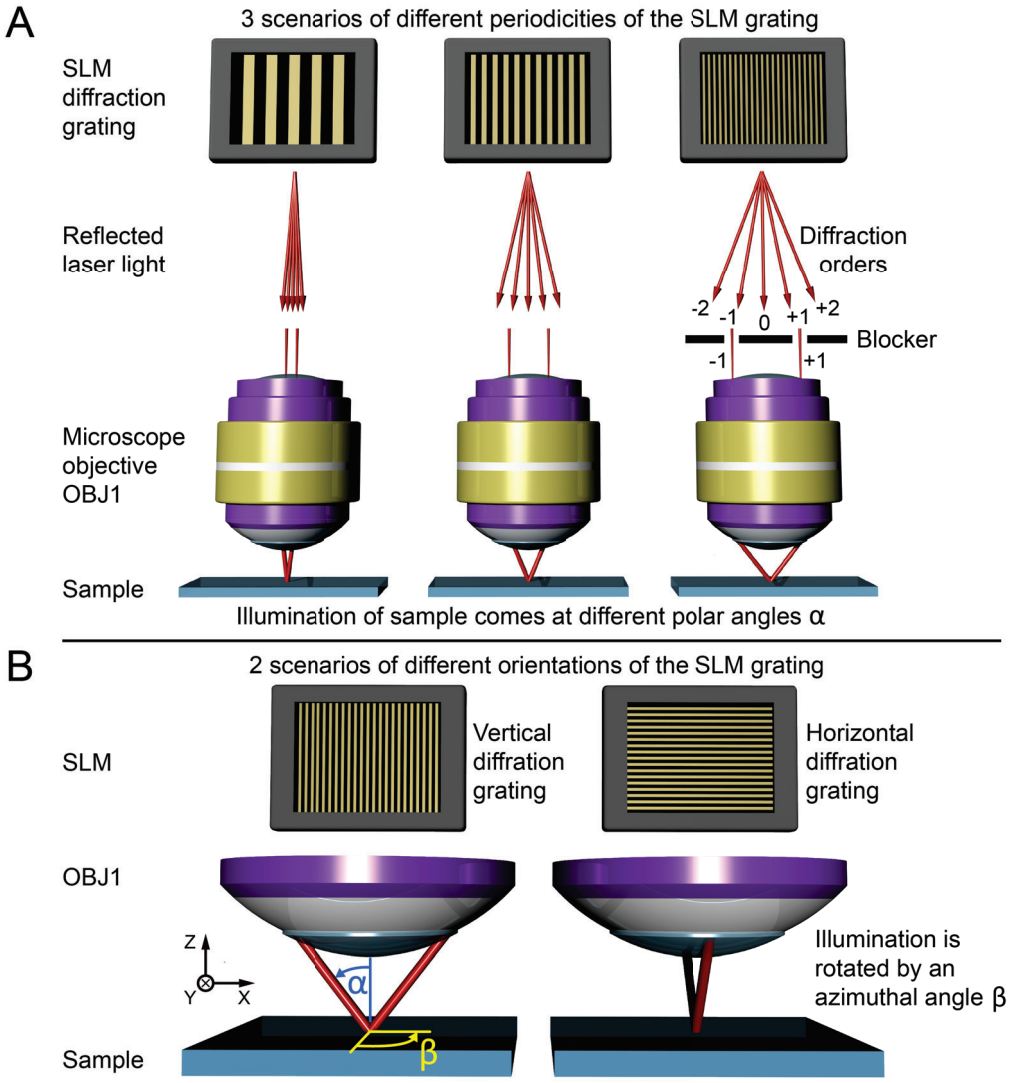

Figure 2.2 – Variable 3D illumination angle. (A) Laser light reflected from an SLM grating generates a diffraction pattern of multiple diffraction orders. Only the -1st and +1st order pass into the microscope objective illuminating the sample. The polar angle of illumination (α in (B)) is dependent on the periodicity of the SLM grating. (B) Comparison of sample illumination using vertical vs. horizontal SLM grating. The azimuthal angle of illumination (β) depends on the rotation of the SLM grating.

In our microscope, we utilize the SLM with the purpose to modify the fundamental beam illumination on the sample. A computer-generated grating is projected on the SLM, where it becomes a

phase grating of aligned liquid crystal molecules acting as a diffraction grating for the laser light, see Fig. 2.2A. The resulting diffraction pattern propagates to the Fourier plane where all the diffraction orders are blocked except the 1^{st} and the -1^{st} order. The periodicity of the grating dictates the angular spread of the orders that are focused in the back focal plane of the illumination-microscope objective. The light from the objective is then illuminating the sample with a Fourier transformed image of the back focal plane, which are two collimated beams overlapping at the sample. To conclude on the influence of the SLM grating on the final 3D illumination angle; the polar angle α from Fig. 2.2B (angle between the illumination beam and the surface normal) is given by the periodicity of SLM grating, while the azimuthal angle β (angle between YZ plane and the plane of incidence) is given by the rotation of SLM grating.

Using the SLM in the described way grants easy access to variable polar and azimuthal angles of illumination without any moving mechanical parts, that could introduce inconsistency. It is noteworthy to mention that the polar illumination angles are limited only by the transfer function of the microscope objective. Furthermore, the redistribution of energy in the diffraction orders differs for different SLM gratings. For instance, using a harmonic, binary, or blazed phase-grating (which produces only one diffraction order) can theoretically convert 33.9%, 40%, and 100% of laser energy into the $+1^{st}$ diffraction order, respectively.

2.1.2 Characterization of the SH microscope

SH and fundamental beam spectra

The spectra of the fundamental beam and the SH light were characterized by a USB spectrometer (Ocean optic, USB4000) with a 0.2 nm spectral resolution in the range of 345 - 1034 nm. The SH spectrum, shown in Fig. 2.3, was measured from the SH light generated by placing a BBO crystal into the path of the fundamental beam. Black dots represent the data, and the red curve represents the Gaussian fit. The SH peak is centered at 515.1 nm. The spectrum of the fundamental beam is shown in the inset; however only up to to 1034 nm, as this is the cutoff wavelength of the spectrometer. The fundamental spectrum is centered at 1031 nm with a full width at half maximum (FWHM) of 9.9 nm, also referred to as the wavelength bandwidth. This is equivalent to 2.8 THz of frequency bandwidth.

Fundamental beam pulse duration

The pulse duration profile of the fundamental beam was measured right after the laser with an auto-correlator as 257 fs at the FWHM. However, this value has to be further divided by $\sqrt{2}$ yielding a final Gaussian pulse of 180 fs at the FWHM for the fundamental beam. The time-bandwidth product of the fundamental beam is 0.50 (2.8×10^{12} Hz x 180 fs). This value indicates how close is the pulse to the transform limit. For a bandwidth-limited Gaussian pulse, the theoretical value is ~0.44. Therefore, the fundamental beam is of good quality.

In order to estimate the pulse duration of the fundamental beam at the plane of the sample, we measured the pulse duration in an optical setup adjacent to our SH microscope, however, using the same laser. The geometry of sample illumination in the optical setup is shown in Fig. 2.4A. This setup was used due to its ability to modify the time delay in one of the two fundamental beam paths illuminating the sample, a requirement for determining the pulse duration through the measurement of an auto-correlation. The optical setup contains a similar optical path and number of optical elements;

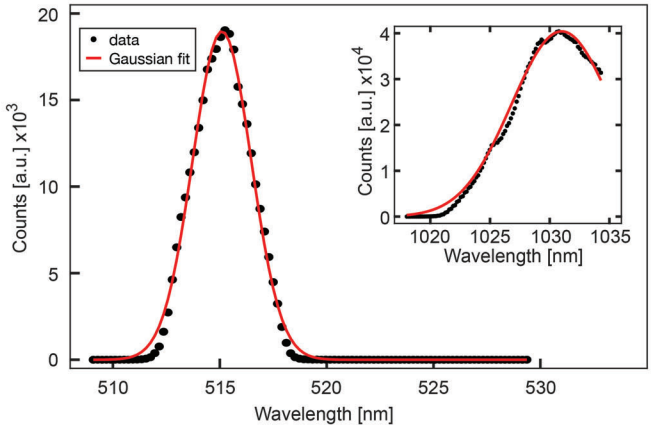

Figure 2.3 – Characterization of the fundamental and second harmonic spectra. Second harmonic spectrum generated from the BBO crystal with a center at 515.1 nm wavelength. The black dots represent the measured data, and the red curve is the Gaussian fit. The inset shows the fundamental beam spectrum.

thus, the presented measurement provides a good approximation of pulse duration at the focus of our SH microscope. SH auto-correlation signal $I_{SH}(\tau)$ was recorded from 50 nm $BaTiO_3$ nanoparticles as a function of temporal delay, displayed in Fig. 2.4B. The $I_{SH}(\tau)$ is given as:

$$I_{SH}(\tau) = \int_{-\infty}^{\infty} G(t)G(t-\tau)dt, \tag{2.1}$$

where τ stands for the temporal delay and function $G(t)$ represents the optical field of the fundamental beam at the sample plane. This equation can also be used for an n-order auto-correlation if the function $G(t)$ corresponds to an n-order multiphoton process. Here, $BaTiO_3$ nanoparticles were generating a second-order auto-correlation signal $I_{SH}(\tau)$. The SH pulse width was determined at the FWHM, assuming a Gaussian pulse. The FWHM of the fundamental beam pulse $\tau^{FWHM}_{fundamental}$ was then related to the FWHM of SH auto-correlation signal τ^{FWHM}_{SH} by using an equation given by [135]:

$$\tau^{FWHM}_{fundamental} = \frac{\tau^{FWHM}_{SH}}{\sqrt{2}}. \tag{2.2}$$

The illustration of the experiment is shown in Fig. 2.4A. A fundamental beam is first split by the beam splitter into two beams of equal intensities. The two beams are then reflected from the mirrors and overlap at $\alpha = 45°$ in the sample plane. The temporal delay is introduced by translating the left mirror by a distance x, which modifies the spatial path length difference Δ as $\Delta = \sqrt{2}x$. The temporal delay is related to Δ as $\tau_{delay} = \Delta/c$, where c is the speed of light in air. The optical system ensures fundamental beams overlap at the sample when the left mirror is being translated. Fig. 2.4B displays the auto-correlation intensity as a function of temporal delay τ_{delay} in fs. The data were fitted by a Gaussian function yielding a FWHM of 276 fs. Inserting this value into the Eq. 2.2 we obtain the pulse duration of the fundamental beam at the sample plane as 195 fs. Comparing this pulse duration with the pulse duration just after the laser (~180 fs) shows that the temporal spread is minimal.

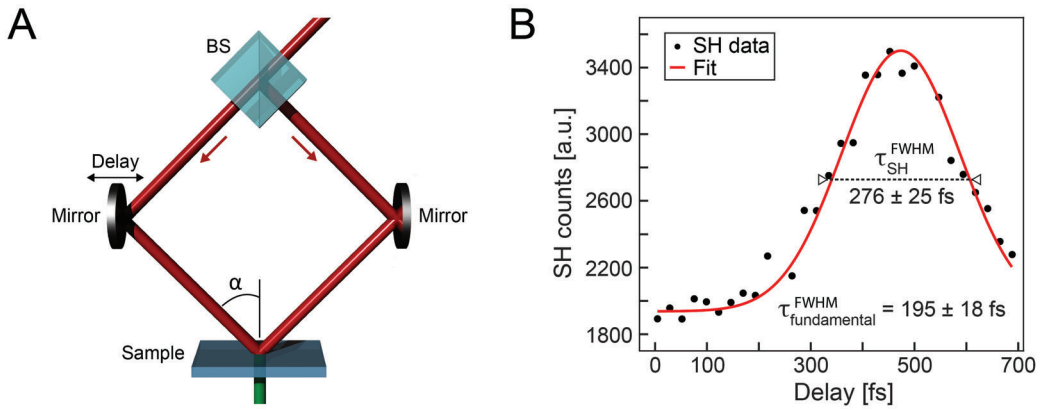

Figure 2.4 – Laser pulse duration. (A) Schematics of an optical setup adjacent to the SH microscope presented in this thesis using the same laser source. BS = beam splitter. (B) The pulse duration of the laser was determined by measuring 50 nm $BaTiO_3$ nanoparticles. Displayed data (black points) represents auto-correlation SH intensity as a function of temporal delay. The red curve represents a Gaussian fit.

Laser fluence at sample

The optical power of the laser can be varied between 0.4 - 3.5 W. The laser output beam is split in two separate beams with equal intensities, powering two different optical setups (the main SH microscope described in this chapter, and the optical setup illustrated in Fig. 2.4A). The deposited optical power on the sample in the SH microscope is substantially lower than the optical power entering the SH microscope due to the loses of propagation through different optical elements. The main drops in power happen when: i) the beam is focused through the pinhole for a wavefront cleaning; ii) the diffraction orders are blocked in the Fourier plane, iii) the beam is being transmitted through the microscope objective illuminating the sample. The optical power throughout the SH microscope is documented in Tab. 2.1 displaying the four most frequent laser powers used for aligning the microscope and for performing experiments. This table further shows the computed energy of the laser pulse (E_p) and fluence (F) at the sample, given by:

$$\begin{aligned} E_p &= \frac{\langle P \rangle}{f}, \\ F &= \frac{E_p}{A_{eff}}, \end{aligned} \tag{2.3}$$

where $\langle P \rangle$ is the average power in Watts, f is the repetition rate of the laser in Hz, and A_{eff} is the effective area of laser illumination. The f of the microscope is set to 200 kHz, and the A_{eff} of Gaussian beams is $\sim 1.52 \cdot 10^{-4}$ cm^2.

Characterization of the polar illumination angles on the sample

As described in Fig. 2.2, the SLM grating periodicity (in SLM pixels) impacts the polar illumination angle α. The angle α can be directly determined from the periodicity of the interference fringes at the

Table 2.1 – Measurements of laser power and fluence in the SH microscope. FP means Fourier Plane, OBJ1 is the microscope objective illuminating the sample, see Fig. 2.1.

Laser transmission	Power at laser [W]	Power after FP [W]	Power before OBJ1 [W]	Power at sample [W]	Pulse energy at sample [J]	Fluence at sample [mJ/cm^2]	Peak intensity at sample [GW/cm^2]
10%	0.42	0.024	0.023	0.013	0.6 x10^{-8}	0.8	4.2
40%	1.54	0.089	0.084	0.046	2.3 x10^{-7}	3.0	15.5
70%	2.65	0.150	0.141	0.078	3.9 x10^{-7}	5.1	26.2
100%	-	0.200	0.187	0.103	5.2 x10^{-7}	6.7	34.6

sample, as shown in Fig. 2.5A. The calculation of α follows the equation

$$\alpha = \arcsin\left(\frac{\lambda}{2\,\Lambda}\right), \tag{2.4}$$

where λ is the fundamental wavelength, and Λ is the period of the interference fringes [125]. In a real experiment, a reference to known distances is required to determine the illumination angles correctly. For this purpose, we imaged a resolution target (Thorlabs, R1L3S6P) with the smallest grating of 250 black lines per mm, see Fig. 2.5B (white light image). From this image, we obtained the magnification of the SH microscope correlating 1 pixel on camera to ~ 400x400 nm at the sample plane. Figure 2.5C displays a SH image of the resolution target, where the vertical lines represent the interference fringes of fundamental beams. The experimental results of angle α measured for SLM gratings with periodicity from 9 to 25 SLM pixels are shown in Fig. 2.5D. The red curve, representing the experimental data, shows a good match with the blue curve, representing the theory.

2.1.3 Polarization sensitivity of the SH microscope

SH microscopy, as an optical technique, has the benefit of being non-invasive. Additionally, compared to linear light scattering microscopy techniques, it further provides structural information about the sample. SH processes are sensitive to a breaking in the spatial centrosymmetry; therefore, the main requirement is that the sample possesses a non-centrosymmetric feature. This feature is most commonly the non-centrosymmetry of the sample's crystalline structure or the non-centrosymmetry at the interface of the sample and its environment, inherent to all materials. Furthermore, non-centrosymmetry is specific to certain spatial directions depending on the nature of the sample and its geometry. Therefore, the oscillation direction of the electric field of the fundamental beam illuminating the sample will significantly influence the efficiency of generating SH light. This is widely utilized in nonlinear polarimetry, where the relation of SH intensity vs. the polarization direction of light can reveal information about: i) structural organization, such as supramolecular assembly of collagen in tissues [136–138], or ii) changes in the non-centrosymmetry at the interface, such as tracking neuronal membrane potentials [139–141].

To demonstrate the power of nonlinear polarimetry in practice, Fig. 2.6 shows SH data of single-layer molybdenum disulfide (MoS_2) flakes measured at different azimuthal angles β (see Fig. 2.2). The imaged sample in Fig. 2.6A-B contains four MoS_2 flakes [1] rotated by 90° from each other. Imaging the sample with a fundamental beam of vertically oscillating electric field in the sample plane, see Fig. 2.6A,

[1] The MoS_2 samples were kindly provided by the laboratory of professor Aleksandra Radenovic.

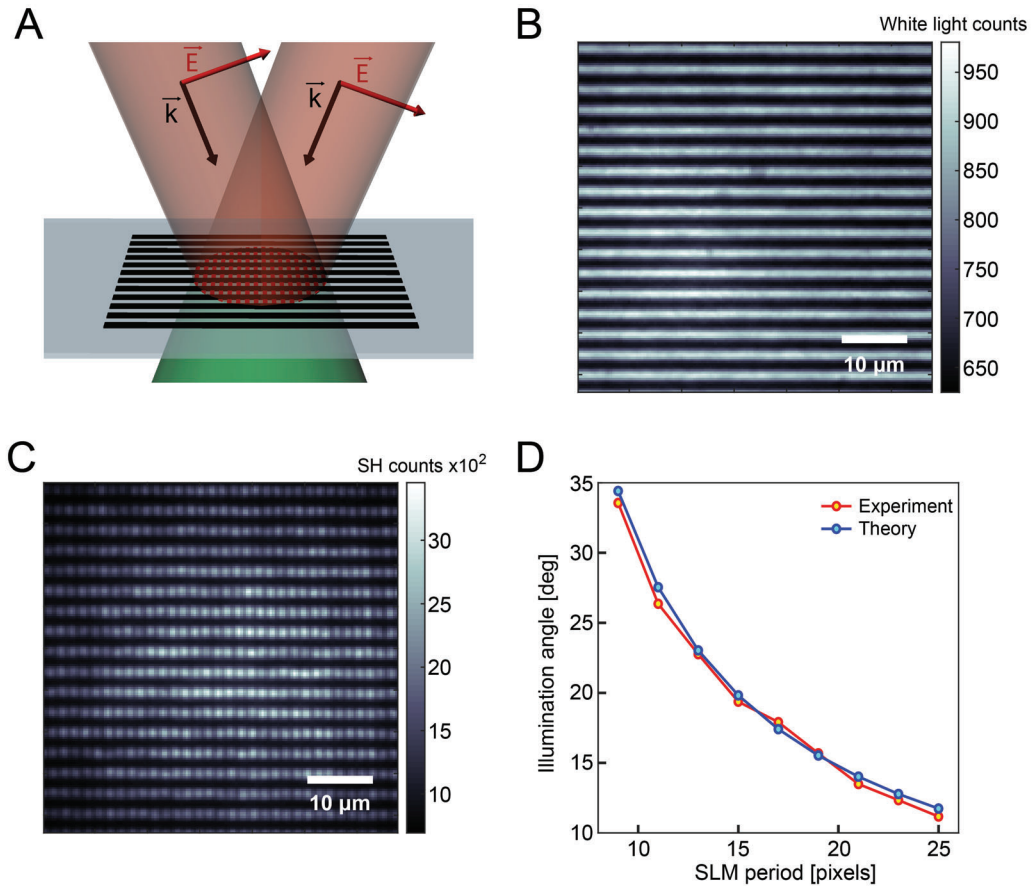

Figure 2.5 – Characterization of the polar illumination angles. (A) Schematics of two fundamental beams illuminating a resolution target. $\vec{E}$ represents the electric field oscillation direction, and $\vec{k}$ is the wave vector determining the direction of propagation. (B) White light image of the resolution target with a periodicity of 250 black lines per mm. (C) SH image of resolution target showing the vertical interference fringes of two fundamental beams. (D) Experimental and theoretical comparison of the polar angle α dependent on the SLM periodicity.

yield SH signal only from two MoS_2 flakes. On the other hand, employing a horizontally oscillating electric field reveals in Fig. 2.6B different two MoS_2 flakes. This is due to the directionality of the non-centrosymmetry of the sample, as discussed above. MoS_2 is a transition metal dichalcogenide with hP6 crystal structure according to Pearson notation. The MoS_2 structure is shown in Fig. 2.6C, where each molybdenum atom exists at the center of a trigonal prismatic coordination sphere covalently bonded to six sulfide ions. The red sets of arrows mark the armchair directions of the structure. Azimuthal SH measurement from a different MoS_2 flake [2] is shown in Fig. 2.6D exhibiting a six-fold anisotropic pattern. In fact, each intensity maximum points to an armchair direction [142] (matched to Fig. 2.6C), because while a bulk MoS_2 crystal has an inversion symmetry, MoS_2 monolayer is non-centrosymmetric due to inversion symmetry breaking via stacking termination along the surface normal (c-axis) [143, 144].

Nonlinear SH polarimetric measurements require that the polarization directions of both the fundamental and the SH light are well defined at the sample plane. In our SH microscope, the illumi-

[2] The MoS_2 sample was kindly provided by the laboratory of professor Guillermo Villanueva.

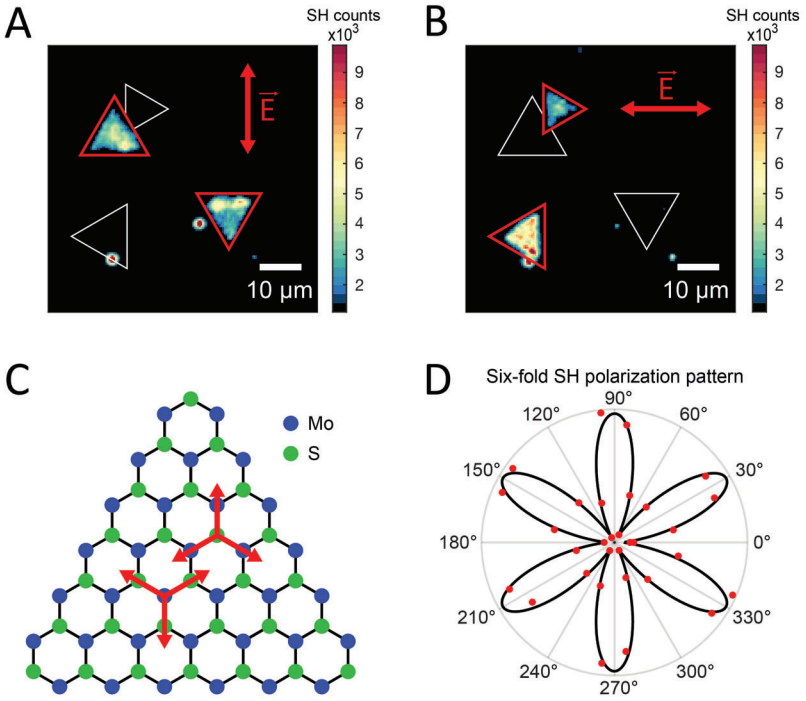

Figure 2.6 – Azimuthal dependence of SH intensity in MoS_2 sample. (A) SH image of triangular MoS_2 flakes. The direction of the electric field oscillation of the fundamental beam is shown as a red vertical line with arrows. The red triangles highlight the MoS_2 flakes visible for the current polarization of light. The white triangles feature MoS_2 flakes that yield no SH signal for the current polarization of light. (B) is analogical to (A) displaying the same sample, however, with a horizontal direction of electric field oscillation. (C) Top view of MoS_2 monolayer structure. The red sets of arrows mark the armchair directions. (D) Azimuthal SH measurement of MoS_2 sample not shown here. The red dots are the average SH intensity of a region of interest. The black curve represents the theoretical fit.

nation angle of the sample can vary in 3D (azimuthal and polar angle). It is not trivial in this case to track the mutual alignment of the fundamental and SH polarization directions. Fig. 2.7A shows an illustration of sample illumination with an extra yellow clock pattern as an azimuthal guide matching the clock patterns in Fig. 2.7B, C. The polarization direction of fundamental light can be azimuthally rotated in the sample plane with the polarization state generator in a clockwise direction, see Fig. 2.7B. On the other hand, the polarization direction of SH light is rotated by the half-wave plate in the anti-clockwise direction, as depicted in Fig. 2.7C. Another parameter influencing polarization directions is the geometry of the fundamental beams shown in Fig. 2.7D. Two examples are given below to explain how to obtain different polarization combinations.

Light polarizations are given here either as S, or P signifying that the electric field oscillation is perpendicular or parallel to the plane of incidence, respectively. Polarization combinations are noted with three letters, such as SPP, where the first letter represents the polarization state of the SH light, and the last two letters represent the polarization state of the fundamental beam. The SSS polarization combination can be obtained by setting the: i) geometry of beams (azimuthal angle β) to 0°, ii) polarization of laser light to 45°, and iii) polarization of SH light to 0°. The resulting SSS polarization will be oscillating between 3 to 6 o'clock in the clock pattern. The SPP polarization combination can be obtained by setting the: i) geometry of beams to 90°, ii) polarization of laser light to 45°, and iii)

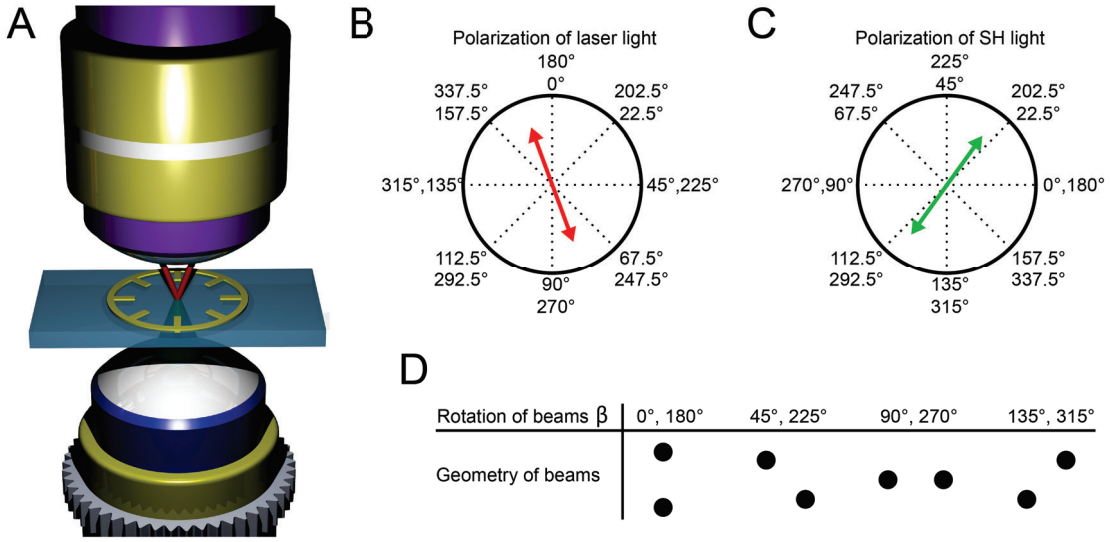

Figure 2.7 – Synchronization of fundamental and SH polarization directions in the microscope. (A) Illustration of sample illumination with two fundamental beams. The yellow clock pattern on the glass coverslip is a visual guide matching the clock patterns in (B) and (C). (B) Polarization directions of fundamental light in the sample plane. The red arrow shows an example direction of electric field oscillation of the fundamental beam. Displayed degrees correspond to the values set on the polarization state generator (PSG, Fig. 2.1). (C) Polarization directions of SH light in the sample plane. The green arrow shows an example direction of electric field oscillation of the SH light. Displayed degrees correspond to the values set on the half-wave plate (HWP, Fig. 2.1). (D) Spatial geometry of two fundamental beams illuminating the sample based on the rotation parameter of SLM generated grating.

polarization of SH light to 45°. The SH S polarization oscillates between 6 to 12 o'clock in the clock pattern; however, the fundamental PP polarizations oscillate between 3 to 6 o'clock in the clock pattern at a polar tilt equal to angle α derived from the used periodicity of SLM grating. Such tilt is shown in Fig. 2.5A.

So far, we discussed the ability of the presented SH microscope to illuminate the sample at variable polar and azimuthal angles, as well as the importance of using a proper polarization combination in order to maximize the amount of generated SH light. However, we have not discussed the Achilles heel of SH microscopy yet: SH signal is generally extremely weak, which makes the SH acquisition times on the order of seconds to minutes. This issue is addressed in the following Section 2.1.4.

2.1.4 Increasing the imaging throughput of the SH microscope

As mentioned in the previous section, the acquisition of SH images on traditional microscopes is typically between seconds to minutes [145–147], making dynamic measurements of interfaces unfeasible. In this section, we discuss the factors that can speed up SH imaging, bringing the acquisition times eventually down to microseconds, enabling SH imaging of dynamical processes in biology, material science, or clinical applications [27, 148, 149].

The conventional configuration of the SH microscopes are of the rastering type [137, 141], where

the laser beam is focused to a spot, close to the diffraction limit, and a set of image-relayed scan mirrors scan this laser spot throughout the sample. The detection is carried out by a photon counter PMT module having only a single area ("pixel") of detection. The final image is therefore obtained as a montage of individual measurements. The advantage of this approach is that the scanning systems and the PMT modules have been on the market for decades, and are readily available for a reasonable price.

Two approaches can be taken to make the SH imaging faster, i.e., to improve the imaging throughput, which is defined as the number of detected photons per image per second [150, 151]. Firstly, the scanning speed can be improved by a faster repetition rate of laser sources [152, 153]. Secondly, the imaging process can be parallelized [154]. In principle, both approaches can be realized by using a wide-field illumination of the sample and a PMT camera to image the whole surface at a single instance. However, it was only in the last two decades that there has been a tremendous development in ultrafast laser sources [155, 156], enabling the optical power-demanding wide-field SH configuration. The next paragraph will discuss how to quantify the improvement in SH imaging throughput between the scanning and the wide-field configuration.

The number of photons produced per second per illuminated area is given by [154] as:

$$N_i \propto |\Gamma^{(2)}|^2 \frac{E_{p,i}^2}{\tau_i A_i} f_i, \tag{2.5}$$

where $\Gamma^{(2)}$ is the effective second-order surface susceptibility of the probed (curved) surface, $E_{p,i}$ is the pulse energy, τ_i is the pulse duration, A_i is the illumination area, and f_i is the repetition rate of the laser. The subscript i represents the two configurations: wide-field (wf) and scanning (s). As N_i depends upon the size of illumination area A_i, it is essential to take into account the ratio between the illumination area and the size of the scanned sample. It is assumed that the scanning rate for the scanning system is one image frame per second and that this image is composed of n scanning points (pixels) as $n = A_{wf}/A_s$. Presuming that the fluence ($F = \frac{E_p}{A}$) and wavelength are equal for both the wide-field and the scanning system, it is evident that $E_{wf} = n.E_s$ and $\tau_{wf} = \tau_s$. The throughput ratio can be then compared as:

$$\frac{N_{wf}}{N_s} = n\frac{f_{wf}}{f_s}. \tag{2.6}$$

Interpreting this equation means that for an image with 1000 x 1000 scanning points ($n = 10^6$) and a scanning repetition rate of f_s = 100 MHz, the wide-field system detects more photons if $f_{wf} > 0.1$ kHz. Considering a repetition rate of 100 kHz for the wide-field system, the imaging throughput for the wide-field system then shows an increase of 10^3. At the same time, by decreasing the repetition rate of the laser, the generated heat at the sample has more time to dissipate into the environment around it, which is crucial mainly to biological samples [157, 158]. Fig. 2.8 shows a comparison of imaging contrast for three different illumination conditions in two SH microscopes; one scanning system and one wide-field system. The wavelength (1028 nm) and pulse duration (190 fs) were kept constant in all measurements. The SH contrast was evaluated from images of 50 nm $BaTiO_3$ nanoparticles. The highest image contrast is observed for the wide-field system with a repetition rate of 200 kHz (blue and red curve). The contrast decreases dramatically when the repetition rate is only 1 kHz. On the other

hand, a standard scanning system with a repetition rate of 88 MHz displays 2-3 orders of magnitude slower acquisition of equivalent SH intensity. An additional difference between the blue, red, and green curve is that the SH signal was recorded with the i) EM-ICCD camera with the intensifier and the electronic amplification turned on, ii) EM-ICCD camera with only the intensifier turned on, and iii) CCD camera with a quantum efficiency of 50%.

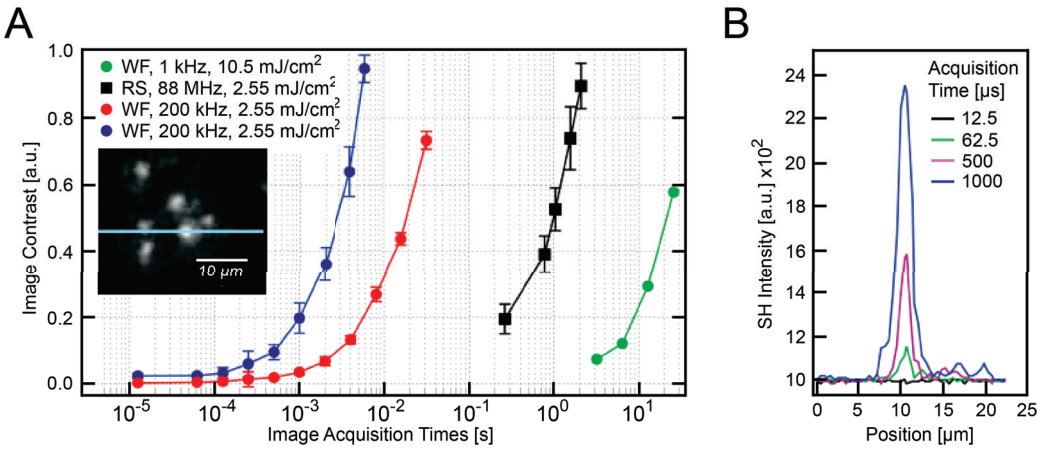

Figure 2.8 – Comparison of imaging throughput between different SH microscopes. (A) Measured contrast in the images recorded from the same position of the same sample in different systems: wide-field (SH microscope developed in our laboratory, 200 kHz, gated detection, blue and red curves), a scanning microscope (Leica TCS SP5 with 1028 nm, 88 MHz, 190 fs laser pulses illumination, a 1.2 NA 20x water immersion objective, a scanning rate of 1000 Hz/line, image size of 256 x 256 pixels, and collecting NA of 0.9), and a wide-field (SH microscope developed in our laboratory, 1 kHz geometry with a regular CCD camera). The used pulse power and repetition rate are given in the legend. The blue data points were recorded with the intensifier, and the electronic amplification of the camera both turned on, while the red data points were recorded with only the intensifier on. The inset shows an image of the nanoparticle sample corresponding to the largest red data point. The horizontal blue line indicates the position for which the intensity cross-sections are displayed in (B). (B) Intensity (raw data) versus position for various acquisition times corresponding to the red data points in (A). This figure is courtesy of Dr. Macias Romero, and can be found in a modified version in reference [154].

Measurements in this thesis are performed with a SH microscope equivalent to the wide-field system presented in Fig. 2.8 with red line. By using a medium repetition rate of 200 kHz and wide-field illumination, we were able to study dynamic processes of surface chemistry on a millisecond time scale [27].

2.2 Important factors influencing the SH signal

In this section, we discuss and quantify the influence of the electric field oscillation direction on the SH yield at interfaces, inspecting the Fresnel factors. This aims to give a more fundamental point of view on the significance of polarization combinations in SH measurements, introduced in Section 2.1.3. Further, we examine the experimental restrictions for not being able to achieve the largest theoretical SH signal. Finally, we discuss how the SH intensity from different measurements should be scaled and compared.

2.2.1 Influence of Fresnel factors on the SH yield

As shown in Section 2.1.3, the efficiency of generating SH photons from a solid crystalline material is dependent on both the azimuthal and polar angle of laser illumination. This angular dependence is not just the property of solids, but it also extends to interfaces (here considering solid/liquid), where the centrosymmetry is broken. At interfaces, the polar illumination angle specifically plays a crucial role in the overall magnitude of the generated SH signal. To quantify this dependence, a simulation inpired by Liljeblad et al. [159] was performed for a model system, see Fig. 2.9, consisting of ultrapure water, a self-assembled silane monolayer (octadecyltrichlorosilane), and fused silica glass. This system is close to our routine reflection measurements, where the microscope objective is immersed in the ultrapure water, illuminating the glass coverslip. The main difference compared to the transmission

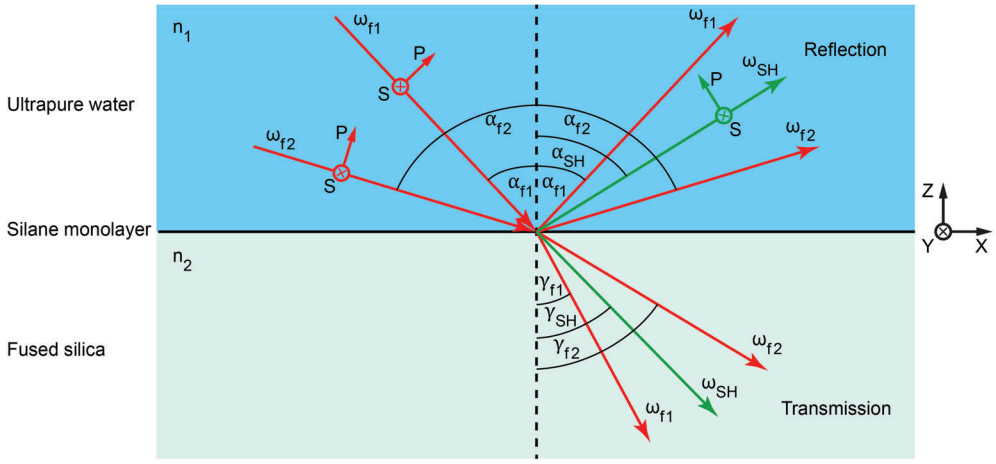

Figure 2.9 – Generation of SH light from a dielectric interface. Two fundamental beams are illuminating the interface of ultrapure water and fused silica in a copropagating geometry. Fundamental beams and SH beam are displayed in red (angular frequency ω_{f1}, ω_{f2}) and green (angular frequency ω_{SH}), respectively. Incident angles are equal to the reflected angles; therefore, designated by a mutual letter α. Transmission angles are denoted by letter γ. Index of refraction is indicated as n_1 and n_2 for the ultrapure water and fused silica, respectively. Letter P symbolizes the P polarization, and letter S symbolizes the S polarization.

configuration is that the illumination microscope objective is also used as a lens to image the generated SH photons on the EM-ICCD camera (for more details see Section 4.2.3). Considering a copropagating geometry of fundamental beams, the SH intensity is given as:

$$I(\omega_{SH}) = \frac{8\pi^3\omega_{SH}^2}{c^3 n_1(\omega_{SH}) n_1^2(\omega_1)\cos(\alpha_{SH})^2} |\chi_{eff}^{(2)}|^2 I(\omega_{f1}) I(\omega_{f2}), \tag{2.7}$$

where ω_1 is the angular frequency of the fundamental beams, ω_{SH} is the angular frequency of the SH beam, n_1 is the refractive index of ultrapure water, $\chi_{eff}^{(2)}$ is the effective susceptibility tensor incorporating all partial contributions, and $I(\omega_{f1})$ & $I(\omega_{f2})$ are the intensities of the fundamental beams [159].

For the PPP polarization combination the tensor $\chi^{(2)}_{eff}$ is related to the tensor $\chi^{(2)}$ as:

$$\begin{aligned}\chi^{(2)}_{eff,PPP} = &-L'_{xx}(\omega_{SH})L'_{xx}(\omega_{f1})L'_{zz}(\omega_{f2})\cos(\alpha_{SH})\cos(\alpha_{f1})\sin(\alpha_{f2})\chi^{(2)}_{xxz}\\ &- L'_{xx}(\omega_{SH})L'_{zz}(\omega_{f1})L'_{xx}(\omega_{f2})\cos(\alpha_{SH})\sin(\alpha_{f1})\cos(\alpha_{f2})\chi^{(2)}_{xzx}\\ &+ L'_{zz}(\omega_{SH})L'_{xx}(\omega_{f1})L'_{xx}(\omega_{f2})\sin(\alpha_{SH})\cos(\alpha_{f1})\cos(\alpha_{f2})\chi^{(2)}_{zxx}\\ &+ L'_{zz}(\omega_{SH})L'_{zz}(\omega_{f1})L'_{zz}(\omega_{f2})\sin(\alpha_{SH})\sin(\alpha_{f1})\sin(\alpha_{f2})\chi^{(2)}_{zzz},\end{aligned} \tag{2.8}$$

where index jj represents xx, yy, or zz. Values $L'_{jj}(\omega)$ can be calculated as a product of macroscopic Fresnel factors $L_{jj}(\omega)$ and the microscopic local field factors $l(\omega)$. However, $l(\omega)$ are independent of the angles of incidence (AOI). Using the macroscopic three-layer model originally proposed by Shen and Heinz, an infinitely thin polarization sheet sandwiched between two bulk media has an assigned index of refraction n' [160, 161]. n' can be interpreted as the ratio of the microscopic local field factors, $l_{xx} = l_{yy}$ over l_{zz} [162]. The macroscopic Fresnel factors $L_{jj}(\omega)$ can then be written:

$$\begin{aligned}L_{xx}(\omega_i) &= \frac{2n_1(\omega_i)\cos(\gamma_i)}{n_1(\omega_i)\cos(\gamma_i) + n_2(\omega_i)\cos(\alpha_i)}\\ L_{yy}(\omega_i) &= \frac{2n_1(\omega_i)\cos(\alpha_i)}{n_1(\omega_i)\cos(\alpha_i) + n_2(\omega_i)\cos(\gamma_i)}\\ L_{zz}(\omega_i) &= \frac{2n_2(\omega_i)\cos(\alpha_i)}{n_1(\omega_i)\cos(\gamma_i) + n_2(\omega_i)\cos(\alpha_i)}\left(\frac{n_1(\omega_i)}{n'(\omega_i)}\right)^2,\end{aligned} \tag{2.9}$$

where index i represents the chosen beam (fundamental 1, fundamental 2, or SH). The presented mathematical framework was taken from reference [159]. Performed simulation is showing the SH yield in PPP polarization for a reflection geometry in Fig. 2.10. According to Eq. 3.2, the SH signal in PPP polarization is composed of four terms - xxz, xzx, zxx, and zzz. Their respective dependence of SH yield on the angle of incidence (AOI) is shown in Fig. 2.10A-D. The SH intensity varies there over six orders of magnitude, with zzz component being the strongest. The total SH intensity in PPP polarization incorporating all four prefactors (Fig. 2.10A-D) is shown in Fig. 2.10E. Here, the plot displays a sharp line of minimal SH intensity, making the choice of incident angles crucial. For the case of both fundamental beams having an equal AOI (blue line in Fig. 2.10E), Fig. 2.10F shows the corresponding SH intensity with a logarithmic scale. If the SH microscope would illuminate the sample at a polar angle $\alpha = 0°$, the SH counts would be on the order of 10^{-4} in the presented scale. Opening the AOI to ~20° results in improving the SH intensity by more than three orders (SH counts ~0.6). This is followed by a dip at ~35° lowering the signal back again to $1.2{*}10^{-4}$ counts. The SH counts grow from there until reaching a maximum at ~73.5° (SH counts ~77).

From the trend presented in Fig. 2.10F, it is apparent that careful choice of fundamental beams AOI is necessary for imaging of flat interfaces. Choosing an inappropriate polar AOI will not just prolong the SH imaging due to the lower signal, but it will also decrease the signal to noise ratio. Such an effect can make the observation of surface dynamics impossible. Note should be taken that the results presented here are valid for the water/fused silica interface only, and need to be calculated for each specific sample.

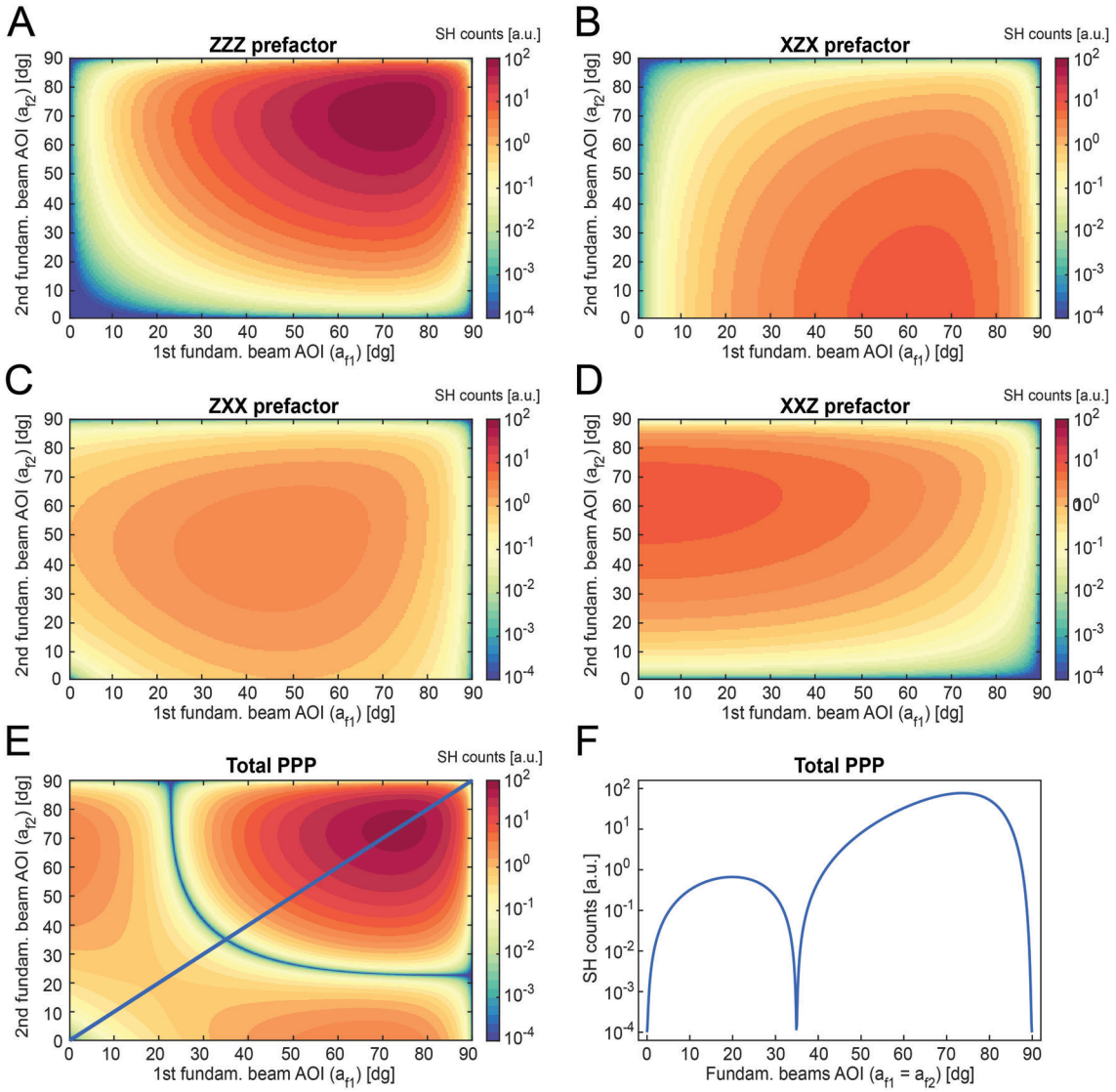

Figure 2.10 – Angular dependence of SH generation for PPP polarization in reflection. (A-E) represent the SH yield from a model interface, shown in Fig. 2.9, in a reflection geometry considering only PPP polarization combination. The angle of incidence (AOI) for the first and second fundamental beam marked as a_{f1} and a_{f2} correspond to Fig. 2.9. (A-D) show four different components of the PPP polarization corresponding to the four terms in Eq. 3.2. (E) display the total SH yield for PPP. All plots (A-E) share a common logarithmic color band scale normalized to the highest value observed for a zzz prefactor in (A). (F) displays the diagonal SH intensity in (E) marked with the blue line. The coded mathematical framework from reference [159] was a courtesy of Prof. Eric Tyrode. This code has been rewritten and modified for the purposes of this figure.

2.2.2 Illumination limits in the SH wide-field imaging

In contrast to the linear scattering microscopy techniques, where the main focus is to have the best contrast to be able to resolve small details, SH intensity carries additional information about the structure of the imaged material. This structure can be linked to a crystalline solid, to an interface, or

to a polar liquid under a strong electric field [27, 65, 66, 163]. The information about the structure is tied to the 3D orientation of the sample; therefore, it depends on what illumination angles are used at the sample. In spectroscopy, where effectively only a single "spatial" pixel is collected, the polar illumination angle can be arbitrary, up to α ~90° (see Fig. 2.9). The situation is quite different for wide-field imaging. Considering a colinear illumination and the fundamental beams at high angles of α ~75°, the highest SH intensity is in the reflected direction at ~75°. Inserting a lens in this reflection direction could provide a collection of the SH signal from the surface. The lens would have to have a longer focal length, i.e., a larger depth of focus in order to collect the SH signal from the tilted surface. The issue with this approach is that the lens would create significant aberrations in the final image. For imaging with minimal/no optical aberrations, the use of a well-designed microscope objective is necessary. Modern microscope objectives are designed to image plane perpendicular to their optical axes, so tilting the objective with respect to the sample surface is not an option.

Considering now conventional imaging with a microscope objective (optical axes of an objective is colinear with the normal of the imaged surface), the maximum illumination/collection angle, α_{max}, is limited due to the finite numerical aperture (NA) of the objective. α_{max} is given by:

$$\alpha_{max} = \arcsin\left(\frac{\mathrm{NA}}{n_1}\right), \tag{2.10}$$

where n_1 is the refractive index of a medium between the objective and the sample. In order to image liquid/solid interfaces, for example in an electrochemical or biological context, water immersion microscope objectives are commonly used. Considering such objectives with a NA = 1.1 and NA = 1, and a refractive index of water n_1 = 1.33, the α_{max} ~55.8° and α_{max} ~48.8°, respectively. To optimize the microscope resolution and SH intensity, the illumination/collection angle α should be well below this limit, in order not to lose higher spatial frequencies in the Fourier plane that compose the fine optical resolution of the microscope. Inspecting now the Fig. 2.10F again reveals that a microscope illuminating the sample at α between 30° - 40° will yield a limited SH intensity for the presented interface. This limitation can be overcome by optimizing the geometry of the experiment and sample, such as in Chapter 3, which allows for optimization of the polar angle α. Despite this limitation, considering the optical power and repetition rate of modern lasers, as well as the development of novel electron-multiplying gated cameras, the SH intensity can be still efficiently collected in wide-field configuration offering a µs to ms time resolution for image acquisition.

2.2.3 Scaling of SH signal with imaging parameters of the optical system

SH counts can be used as an indicator for measuring and tracking the changes in surface properties, such as surface potential. SH intensity can be linked to surface potential through an appropriate model (see Section 3.5.2), but in order to get absolute values, one needs to tie the SH intensity to "boundary" conditions, such as when the average surface potential is zero, or when the average surface potential is maximized (maximum surface charge density). Such conditions, however, cannot be experimentally reached for an arbitrary sample. Modifications of surface charge density can lead to instability; for instance, biological cells are quite sensitive to pH changes. Therefore, a question arises if one can use the knowledge of linked SH intensity to absolute values of surface potential in one sample to map the surface potential in another sample. The answer is, in principle, yes; however, great caution should be taken.

The main requirement is that the laser fluence on both samples is identical. At the same time, the relationship between the SH intensity and the imaging parameters (for instance electron-multiplying gain of the camera) needs to be known, as the imaging parameters are often different experiment to experiment in order to optimize the image contrast and signal to-noise-ratio. Therefore, a calibration between SH intensity and imaging parameters is necessary to qualitatively compare images obtained at different imaging parameters.

We mapped the imaging parameters in our SH microscope by imaging a sample composed of $BaTiO_3$ nanoparticles sandwiched between two glass coverslips (for preparation procedure see Section 2.3.3). The imaging parameters that we investigated were the gain on our EM-ICCD camera and the pulse duration of the laser, see Fig. 2.11. Fig. 2.11A shows the dependence of SH counts on the intensifier gain of the camera for four different laser pulse durations. The data displays a linear behavior with the largest SH counts corresponding to the shortest laser pulse duration of 180 fs (measured at the laser output), which is expected, because decreasing the pulse duration results in increasing the energy density; therefore, increasing the SH signal. Fig. 2.11B is analogous to Fig. 2.11A, however, here also the electron multiplier on the camera is turned on yielding an order of magnitude stronger SH signal. The laser fluence was kept constant at 6.7 mJ/cm^2 in the sample plane.

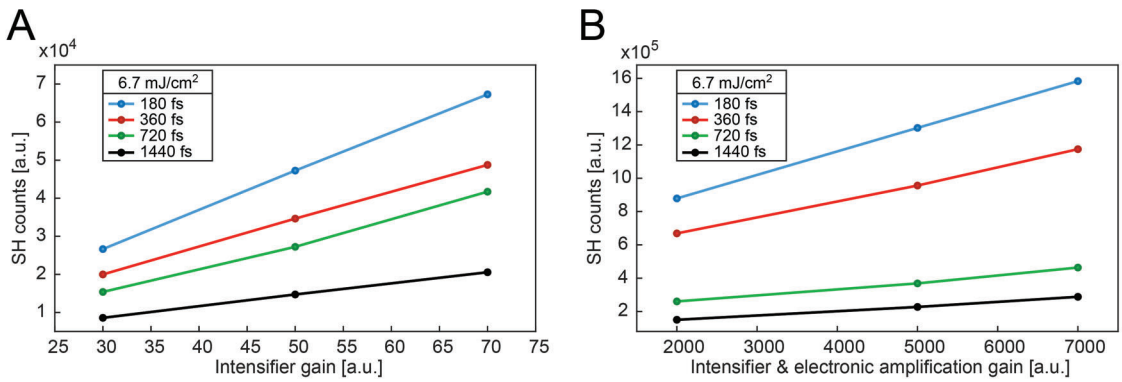

Figure 2.11 – Dependence of the SH intensity on imaging parameters. (A) SH counts from a $BaTiO_3$ nanoparticles sample with respect to the set intensifier gain on the EM-ICCD camera in our SH microscope for four different laser pulse durations. Displayed SH values are taken as average values of the measured images. Laser fluence was fixed at 6.7 mJ/cm^2 in the sample plane. The used $BaTiO_3$ nanoparticles sample is shown in Fig. 2.14B. (B) is analogous to (A) with additional electron multiplier gain turned on.

To optimize the comparison of SH intensity coming from various samples, the SH intensity should be measured at least for three different values of camera gain to establish a proper scaling. At the same time, while scaling the SH intensity between different samples can always be done, interpreting the surface properties by using one measurement as a reference for another should be done with great care, considering the SH nature and all contributions to the signal. In this thesis, all the experiments were performed with the laser pulse duration of 180 fs, measured at the laser output.

2.3 Samples preparation and experimental details

2.3.1 Cleaning of the glassware

SH signal originating from a solid/electrolyte interface contains information about surface properties. These properties, such as surface potential, are influenced by surface-adsorbed species; therefore, it is important that the studied interface is free of chemical impurities. These chemical impurities might be synthetic residues in the as-received chemicals or related to insufficient cleaning of components that are in contact with the electrolyte. To give an example, a solution of 1 mL and 1 mM of 99.5% pure chemical include sufficient amount of impurity molecules to spread over an area of 15 - 30 cm^2 expecting the worst scenario where all the impurities are surface-active with a molecular area of 50 - 100 $Å^2$ [164]. This type of impurity can be significantly reduced by buying chemicals with high purity (ultrahigh purity is given in order of 99.999%). The second type of impurity can originate from a deficient cleaning of glassware used in the experiment. In our case, that would be primarily the glass coverslip supporting the sample and the electrolyte.

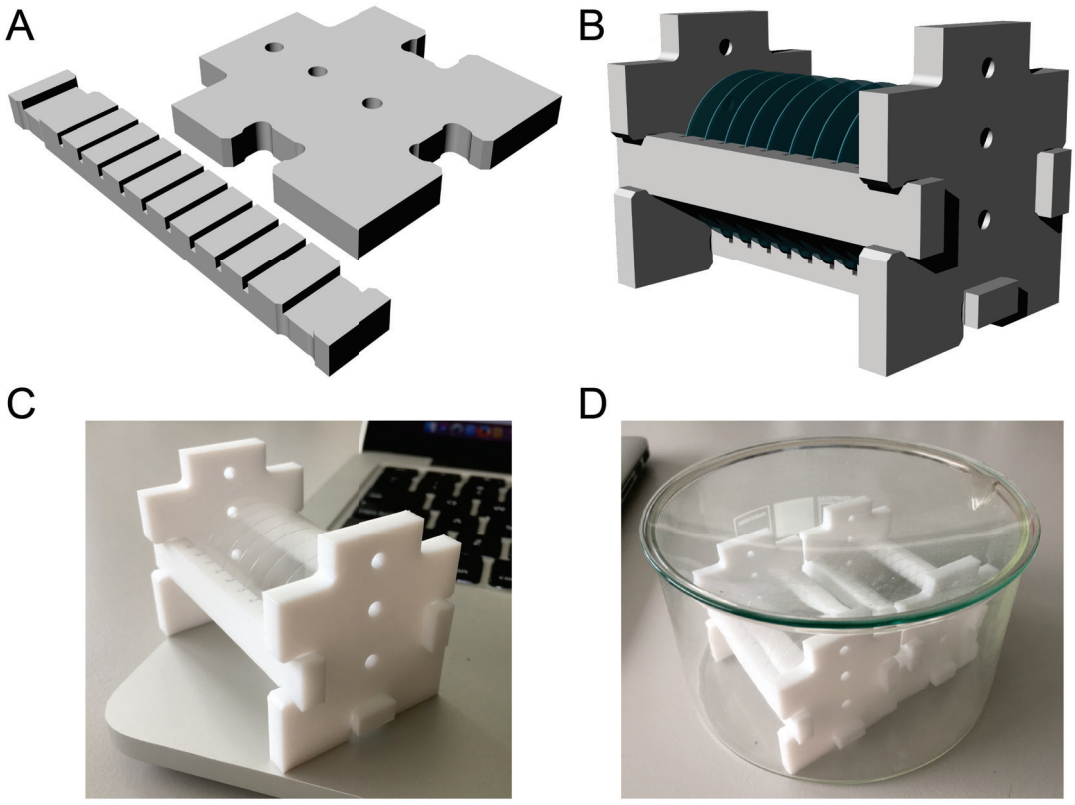

Figure 2.12 – In-house manufactured PTFE compartment to clean glass coverslips. (A) 3D model of basic parts of the coverslip rack. (B) The model of assembled coverslip rack. (C) CNC machined version of PTFE rack filled with glass coverslips. (D) Glass compartment accommodating two racks for chemical cleaning.

To ensure cleanness, coverslips with a diameter of 30 mm are cleaned in acidic piranha solutions, then thoroughly rinsed with ultra-pure water (H_2O, Milli-Q UF plus, Millipore, Inc., resistivity of 18.2 MΩ.cm) and stored sealed in ultra-pure water for a maximum of few days prior to experiments. The

coverslips are thoroughly rinsed in ultra-pure water again just before the experiment. This procedure is performed in a In-house manufactured rack from a PTFE material holding the coverslips, see Fig. 2.12. The PTFE rack is composed of 4 parts clicked together by pressure, as no additional screws or glues are allowed to be in contact with the piranha solution. Holes in the rack (Fig. 2.12C) can be used to grab it for a transfer. Fig. 2.12D shows two racks filled with coverslips fitted in a glass container, which is usually filled with ultra-pure water, and sealed.

2.3.2 Assembly of electrochemical cell

In chapters 4, and 5, we studied the gold/electrolyte interface during (electro)chemical conversion with the aim to map and quantify the spatial extent of surface reconstruction during potential cycling. These measurements were performed in a home-made electrochemical cell allowing for simultaneous SH imaging and cyclic voltammetry.

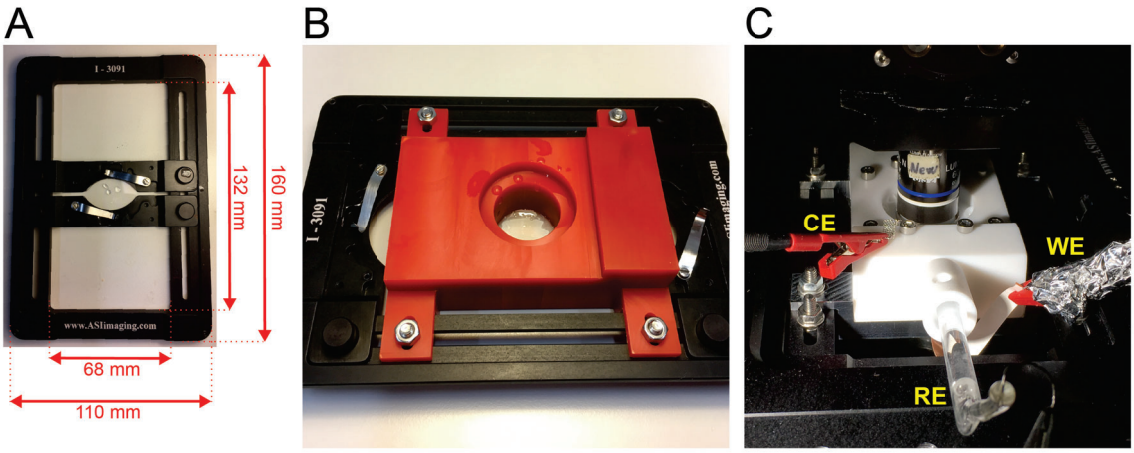

Figure 2.13 – Assembly of electrochemical cell. (A) Slide insert used in our SH microscope for holding glass coverslips. (B) Modified slide insert holding a plastic model of designed electrochemical cell manufactured for testing purposes prior to real electrochemical experiments. (C) Assembly of PTFE electrochemical cell with three electrodes: WE - working electrode, CE - counter electrode, and RE - reference electrode. The cell was designed by Gregor Zwaschka from Fritz Haber Institute of the Max Planck Society in Berlin.

The cell was developed in collaboration with the group of Professor R. Kramer Campen (Fritz Haber Institute of the Max Planck Society, Berlin, Germany). The main design was done by Gregor Zwaschka, see Fig. 2.13B,C. In order to perform the electrochemical measurements, the bottom microscope objective was removed for gaining extra space in the sample plane, and measurements were done in reflection geometry (see Section 4.2.3). This means that the same microscope objective was illuminating the sample and collecting the reflected SH signal, as shown in Fig. 2.13C. Fig. 2.13C also displays the placement of electrodes. The cavity where the microscope objective is immersed into is sealed from the bottom with a gold sample backed with a borofloat glass, all clamped together by an aluminum base. The cavity is filled with an electrolyte of choice.

2.3.3 $BaTiO_3$ sample preparation

Barium titanate ($BaTiO_3$) is a non-centrosymmetric crystal widely used in the electronic industry [165], and recently it has been demonstrated that $BaTiO_3$ nanoparticles can be used in SH bio-imaging due to their strong second-order nonlinear optical property with diameters below 50 nm [148, 166]. Here, we describe how the $BaTiO_3$ nanoparticles film was prepared for Fig. 2.11. Due to the random orientation of nanoparticles in the film, which effectively yields a quasi-homogeneous SH response from the imaged area, the $BaTiO_3$ sample can be used for aligning purposes, and also for scaling the SH intensity between different SH measurements, see Section 2.2.3.

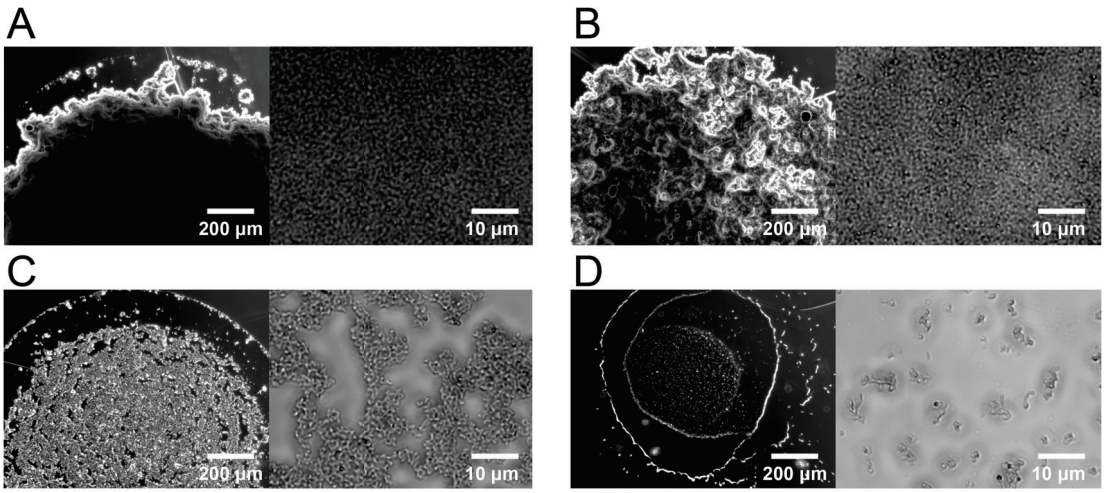

Figure 2.14 – $BaTiO_3$ sample prepared at different concentrations. (A-D) White light images of $BaTiO_3$ nanoparticle film sandwiched between glass coverslips. Prior to sandwiching, a liquid droplet containing $BaTiO_3$ nanoparticles was deposited on the bottom coverslip, and the water was allowed to evaporate. The concentrations of $BaTiO_3$ in (A-D) are 270 mM, 27 mM, 2.7 mM, and 270 µM, respectively. Left and right sides of images correspond to magnifications of 40x and 4x, respectively.

The $BaTiO_3$ (100 nm, US Research Nanomaterials) nanoparticles were first sonicated in a 1 M HCl solution for 10 minutes and afterward centrifuged at 8000 rpm for 10 minutes. The pellet was collected and successively redispersed in a basic 1 mM NaOH solution. The sample was further precipitated and redispersed in ultrapure water. The nanoparticles were stirred in a vortex for 10 min and then sonicated for 20 min. The final concentration of the $BaTiO_3$ nanoparticles sample was 270 mM. Three more solutions were diluted from this main solution with concentrations of 27 mM, 2.7 mM, and 270 µM. From these four solutions, the $BaTiO_3$ nanoparticle films were made by depositing a droplet on a coverslip, and after the water evaporated, dried films were sandwiched with a top coverslip. Resulting films are shown in Fig. 2.14A-D.

3 Optical imaging of surface chemistry at the glass-electrolyte interface

The interfacial structure and dynamics of water in a microscopically confined geometry is imaged in three dimensions and on millisecond time scales, using a 3D wide-field second harmonic microscope developed in our laboratory that employs structured illumination. We image pH-induced chemical changes on the curved and confined inner and outer surfaces of a cylindrical glass micro-capillary immersed in aqueous solution. The image contrast reports on the orientational order of interfacial water, induced by charge-dipole interactions between water molecules and surface charges. The images constitute surface potential maps. Spatially resolved surface $pK_{a,s}$ values are determined for the silica deprotonation reaction. Values range from $2.3 < pK_{a,s} < 10.7$, highlighting the importance of surface heterogeneities. Water molecules that rotate along an oscillating external electric field are also imaged. With this approach, real-time movies of surface processes that involve flow, heterogeneities and potentials can be made, which will further developments in electrochemistry, geology, catalysis, biology, and microtechnology.

This chapter is based on the author's journal article: Macias-Romero, C.; **Nahalka, I.**; Okur, H. I.; Roke, S. Optical Imaging of Surface Chemistry and Dynamics in Confinement, *Science*, **2017**, *357*, 784–788.

3.1 Introduction

Microscopic and nanoscopic structural heterogeneities, confinement, and flow critically influence surface chemical processes in electrochemical, geological, and catalytic reactions. Recently, there has been an advance in understanding some of these mechanisms, which are being utilized in micro- and nanotechnology driven research [167–171]. For instance, micro- and nanocapillaries in combination with interfacial voltage gradients are used in the fabrication, manipulation, and characterization of droplets and interfaces [172–175] and highly amorphous materials [176]. An electrostatic field gradient in a narrow channel can be used to separate [177] and identify analytes [178]. Naturally occurring pores and interfaces employ extremely high electric field gradients to separate and transport chemicals from one aqueous phase to another [179]. Artificial nanopores have recently been used to generate liquid jets [180] and electric power [181, 182]. The increase in complexity of new materials and nano- and microtechnological developments [183] requires technology that can track, in real time, three dimensional spatial changes in the molecular structure of confined systems, such as curved interfaces and pores, as well as the response to electrostatic fields of these systems.

With this need in mind, a high-throughput structured illumination second harmonic microscope was constructed in our laboratory to perform real-time 3D chemical imaging of surfaces and confined geometries. Non-resonant coherent second harmonic (SH) generation occurs only when non-centrosymmetric molecules, such as water, are oriented non-centrosymmetrically [66]. This selection rule allows for probing just several monolayers at the interface. We use this property to image the orientational order of water molecules at the inner and outer surfaces of a glass micro-capillary immersed in aqueous solution. The surface chemistry of the micro-capillary is altered by changing the bulk pH of the solution. The images are converted in maps of the surface potential and surface chemical equilibrium constants. Although average surface $pK_{a,s}$ values agree with literature, a clear structural interfacial heterogeneity is apparent with $pK_{a,s}$ values ranging from 2.3 to 10.7. Dynamical structural changes induced by an external oscillating electrostatic field are also imaged on millisecond time scales and in three dimensions. The observed structural fluctuations at the interface and in the < 1 μm tip opening originate from water molecules that interact with the external electrostatic field.

3.2 Materials and Methods

3.2.1 Chemicals

NaCl (99.999%, 38979 Sigma-Aldrich), NaOH (99.99%, 306576 Sigma-Aldrich), and HCl (37 wt. % in H_2O, 99.999% trace metals basis, 339253 Sigma-Aldrich) were used as received without further purification. All samples were made by dissolving the electrolytes in degassed 18.2 MΩ·cm ultrapure water that was obtained from a Milli-Q UF plus instrument (Millipore, Inc.). The electrolyte solution with pH 2 was obtained by adding 10 mM of HCl to ultrapure water. The pH neutral solution was obtained by adding 10 mM of NaCl to ultrapure water. The solution with pH 12 was obtained by adding 10 mM of NaOH to ultrapure water.

3.2.2 Optical setup

The same optical setup (see Chapter 2.1 for details) was used for SH imaging. The laser source was operated at 1030 nm wavelength with a repetition rate of 200 kHz delivering ~ 195 fs pulses at an

optical fluence of 3.6 mJ/cm^2 at the sample. The field of view on the sample was determined by the spot size on the SLM and the overall magnification of the relay system with the spatial frequency σ of the interference pattern determining the angle of incidence of the beams on the sample. The sample was illuminated by a water immersion microscope objective (Olympus, LUMPLFLN 60x). All images were recorded with a water-immersion microscope objective (Olympus, LUMFLN 60x) with high NA of 1.1. The sample was imaged onto an EM-ICCD camera. Nonlinear polarimetry [184] was performed by controlling and analyzing the polarization state of the illuminating and emitted beams.

3.2.3 Imaging of surface chemistry and surface dynamics

The micro-capillary (MGM-1x, FIVEphoton biochemicals) was filled with the electrolyte solution, placed on a glass coverslip, mounted on the microscope stage and immersed in the electrolyte solution with the same pH; the pH is the same on the inside and the outside (Fig. 3.2 and 3.3). For Fig. 3.2A each image was obtained with an acquisition time of 5 s and HiLo processed. The optical fluence on the sample was 3.6 mJ/cm^2 and the gain of the camera was set to 7000x in automatic mode (i.e. setting the optimum gain between the intensifier and electron multiplier internally).

For the flow experiments (Fig. 3.2B) a capillary was connected to silicon tubes attached to a syringe pump (Harvard Apparatus PHD 2000). The diameter of the capillary was 100 µm were the images were taken, and the diameter at the tip was 30 µm to enable a steady flow. With a flow rate of 50 µL/min a shear rate of 8.5·10^3 s^{-1} was achieved, resulting in a laminar flow. Starting with a pH neutral solution with 10 mM NaCl to obtain a reference, the solution was changed to pH = 2 that was flown at a speed of 0.5 mL/min for 5 minutes to completely protonate all surface silica groups. SH images were recorded with 250 ms acquisition time, using σ = 1.04 µm^{-1}, where σ is the spatial frequency of the interference pattern determining the angle of incidence of the laser beams on the sample. The data was not HiLo processed and the SH signal was integrated along the y-axis direction to improve the signal-to-noise ratio. The optical fluence on the sample was 3.6 mJ/cm^2 and the gain of the camera was set to 70x using only the intensifier gain. The bulk pH of the solution was determined as a function of time by repeating the flow experiment on the same spot of the same capillary inside a UV/Vis spectrometer (Varian Cary 50 Bio) adding a few drops (250 µL) of pH indicator dye to the solution, as specified (Honeywell Fluka 31282, Universal indicator solution).

For the dynamics experiments (Fig. 3.3) the micro-capillary was filled with and immersed in pH neutral degassed ultrapure water containing 10 mM of NaCl. An Ag/AgCl wire electrode (36 AWG, WPI) was placed inside the capillary and an AG/AgCl pellet electrode (EP05, WPI) was placed in the liquid facing the small opening of the capillary (Fig. 3.3A). The micro-capillary and electrodes were placed on a glass coverslip, and mounted on the microscope stage. The electrode placed outside the micro-capillary was held at 0 V and the electrode inside the micro-capillary was set to $\Delta V = V_0 \sin(\nu t)$ with ν = 0.05 Hz and V_0 = 10 V using a function generator (Hewlett-Packard 3312A). The SH images were recorded with 250 ms integration time and HiLo processed. The optical fluence on the sample was 3.6 mJ/cm^2 and the gain of the camera was set to 70x using only the intensifier gain.

3.3 Results & Discussions

3.3.1 Mapping the heterogeneity of surface chemical equilibrium constants

3D imaging is not possible in a wide-field illumination geometry because the beam(s) are too wide. To achieve 3D imaging and to improve the transverse spatial resolution [185], we use an adapted HiLo imaging procedure [186–191]. Note, that HiLo microscopy is different from Higly Inclided and Laminated Optical (HILO) sectioning microscopy. Here, HiLo relies on partial spatial coherence introduced by the interaction of a chirped illuminating pulse with the sample. The procedure uses Fourier filtering to reject out of focus SH light present in samples thicker than a few µm. The interference grating provides a reference spatial frequency for the filtering procedure, using a cosine intensity pattern. With this pattern, structured images I_n and $I_{n'}$ are produced, the latter being phase shifted by $\pi/2$. The filtering is done with a uniformly illuminated image ($I_u = I_n + I_{n'}$), and the structured illuminated image (I_n), using a HiLo algorithm [186, 187, 190, 192, 193].

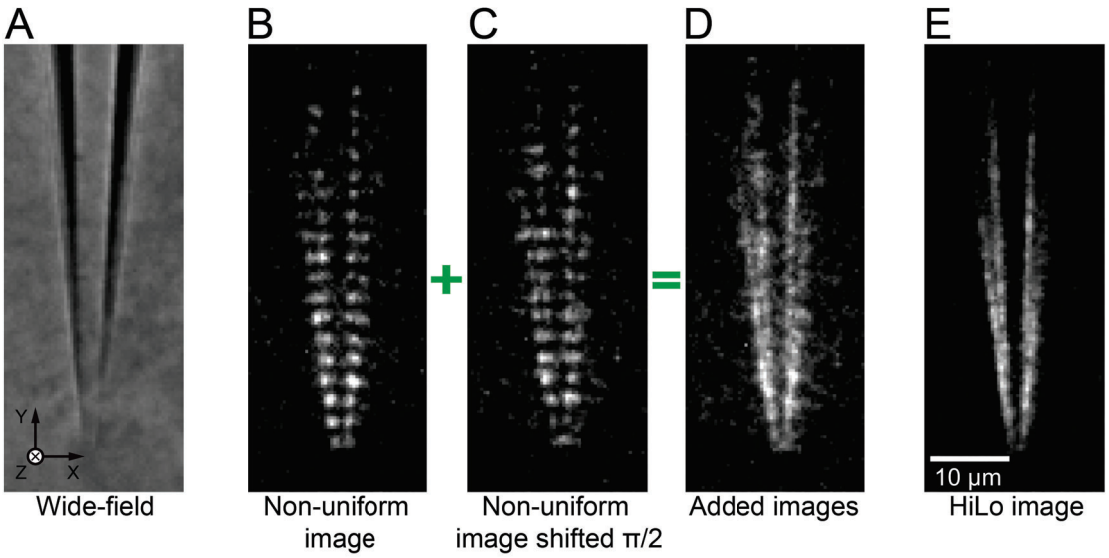

Figure 3.1 – Micro-capillary HiLo imaging.(A) Phase contrast image of the micro-capillary in aqueous solution (obtained by placing a white light source in the beam path). (B), (C) SH structured image without, and with the pattern phase shifted by $\pi/2$. (D) Sum of (B) and (C). (E) HiLo image obtained after applying the HiLo algorithm [191] on (B) and (D). The SH intensity is only detectable if the polarization combination is in the x-axis direction, i.e. along the surface normal.

Fig. 3.1A shows a phase contrast image. Fig. 3.1B-E show SH images of a glass micro-capillary immersed in an aqueous solution of pH neutral ultrapure water with 10 mM NaCl. The structured SH images I_n and $I_{n'}$ are shown in Fig. 3.1B and C, respectively. Fig. 3.1D shows the uniformly illuminated image that is obtained from $I_u = I_n + I_{n'}$. Using the algorithm of Mertz and Kim [191] we obtain the final HiLo image of Fig. 3.1E. It can be seen from comparing Fig. 3.1D (unprocessed, not cross-sectioned) and 3.1E (HiLo processed) that the background rejection results in an image with a much better contrast. The SH intensity is emitted in the x-axis polarization combinations, i.e. with all beams polarized and analyzed in a direction perpendicular to the main symmetry axis of the micro-capillary (Fig. 3.1B). Light polarized along the interface does not generate SH photons.

Surface chemical changes are induced on the glass micro-capillary surface by changing the pH

of the solution. SH surface images are made of three different micro-capillaries. The silica surface in contact with a solution of pH = 2 is on average charge neutral, with the vast majority of the silanol groups in the protonated -SiOH state [194, 195]. Increasing the bulk pH of the solution increases the fraction of surface SiO^- groups, resulting in a predominantly negatively charged surface (with average charge densities of -2 μC/cm^2 under pH neutral conditions and <-17 μC/cm^2 at pH = 12 [194, 195]. Upon increasing the net surface charge by deprotonation, the interfacial electrostatic field E_{DC} grows in magnitude. Interaction of this field with the dipole moment of water results in a distortion of the orientational distribution of water molecules. In absence of any external forces there is no net directionality of the water molecules (and thus no coherent SH is generated by them). In the presence of an interfacial electrostatic field the orientational distribution of water molecules changes. The dipole moment of the water molecules aligns with the electrostatic field, allowing for SH photons to be generated [107]. This electric-field induced SH generation [196] can be used to probe aqueous silica interfaces [107, 197]. Time- and spatially-averaged spectroscopic SH measurements have shown that even though the breaking of centrosymmetry occurs over a distance of only a few nm and involves only a very small fraction of all water molecules, it is enough to result in a detectable SH intensity. The spatially and temporally integrated SH intensity can be correlated to the surface potential (Φ_0) : $I_{2\omega} \sim \left|\boldsymbol{\chi}_s^{(2)} + \boldsymbol{\chi}^{(3)'}\Phi_0 f_3\right|^2$ [107, 163], which originates from:

$$I(2\omega, x, y, t) \sim I(\omega, x, y, t)^2 \left|\chi_s^{(2)}(x, y, t) + \chi^{(3)'} f_3 \int_0^\infty E_{DC}(x, y, z)\, dz\right|^2, \tag{3.1}$$

where x, y, z represent the local surface coordinate system, with z being the surface normal, $E_{DC}(x, y, z)$ relates to the electrostatic potential change (Φ) via $-\nabla\Phi(x, y, t)$, $\chi_s^{(2)}$ is a value of the second-order susceptibility of the capillary silica/water surface, and f_3 is an interference term which has the value 1 for SH transmission experiments [163]. $\chi^{(3)'}$ is a value of an effective third-order susceptibility that contains different contributions (Section 3.5.2) of which the reorientation of water molecules in the electric double layer is the largest one ([163], here ~99%, Section 3.5.2). This response can be used to determine changes in the surface potential (Φ_0).

When imaging three different systems consisting of a solution with a different bulk pH value (pH = 2, pH neutral, and pH = 12) and a micro-capillary immersed in it, we observe very different SH responses as shown in Fig. 3.2A. Note that the ionic strength is kept constant at 10 mM (by adding NaCl). It can be seen that the average intensity increases in the order pH(2) < pH(neutral) < pH(12), in agreement with expectations from spectroscopic measurements [107, 117, 198–200]. Using Eq. 3.1 we convert the SH intensity in the images of Fig. 3.2A to a change in the surface potential (Φ_0). Although it is not possible to determine absolute values for the surface potential in this experiment [163], assuming that $\langle\Phi_0\rangle = 0$ at pH = 2 and that the average charge density under pH neutral condition is -2 μC/cm^2 [194, 195] we can construct a scale for Φ_0 using the Gouy-Chapman-Stern model to provide reference values [195]. The retrieved values are given by the color bar in Fig. 3.2A. The average values of Φ_0 agree well with literature values [117, 195, 198, 199]. The variation in the spatial distribution of intensities/surface potentials values is, however, significant reaching values of ~$3\langle\Phi_0\rangle$. This variation reflects the diverse values reported in literature [117, 195, 198, 199] and indicates that the surface is structurally not uniform, for example in terms of the distribution of charged SiO^- or the nanoscopic surface geometry imposed by the production procedure of the capillary. Indeed, experimental reports have been made of mono-, bi-, or trimodal deprotonation behavior, with surface pK_a values of 6.8 [201], 4.8, 8.5 [107], or 3.8, 5.2, and ~9, as well as a dependence on the pH history of the sample [117]. Computations show

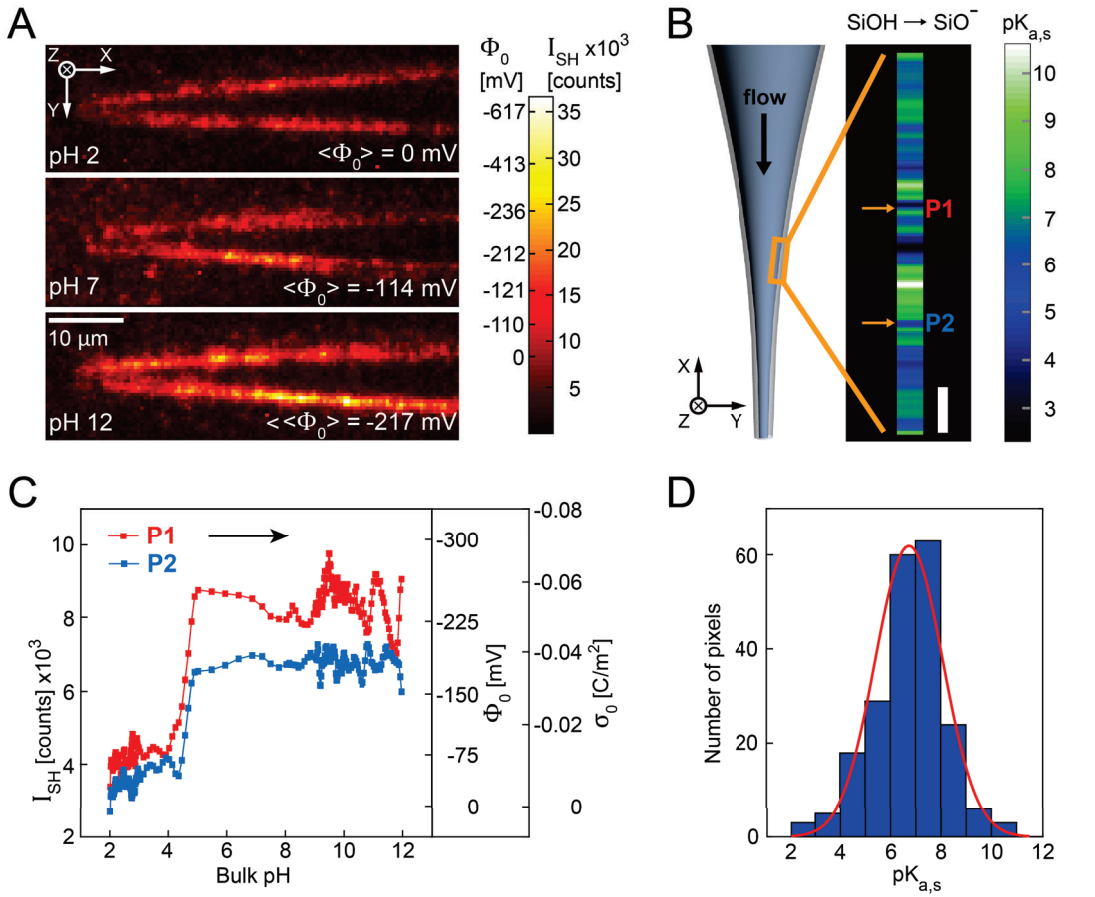

Figure 3.2 – Imaging of surface chemistry and potential. (A) SH cross-sectioned images (2 µm thick) using the x-axis polarization combination for different pH values of the electrolyte solution, recorded with 5 s acquisition time per image. The color bar reports on the intensity as well as the calculated change in the surface potential (Φ_0). (B) $pK_{a,s}$ values for the deprotonation reaction of the silica/water interface along the wall of a 100 µm wide capillary, obtained by imaging the change in the surface potential while changing the pH under laminar flow from 2 → 12. The pH is determined using a solution of pH indicator dyes in a separate experiment (Section 3.2.3). Note that the values are integrated along the X direction. Scale bar: 10 µm. (C) The change in SH intensity as a function of pH for two different points in (B), $pK_{a,s}$(P1) = 3.8 and $pK_{a,s}$(P2) = 5.9. The extracted surface potential and computed surface charge density values are displayed as right vertical axes. (D). Histogram of obtained $pK_{a,s}$ values, reflecting the variance in surface reactivity. The red line represents a Gaussian fit.

that the local chemical structure and hydrogen bonding environment, as well as strains or defects in the surface structures all contribute [116, 118]. Given the importance of silica as one of the most abundant minerals on planet earth, it makes sense to extend these studies beyond the time- and spatially-averaged mean field behavior to explain this large discrepancy. We therefore determine the $pK_{a,s}$ values for the $SiOH_{(s)} + H_2O \equiv SiO^-_{(s)} + H_3O^+_{(s)}$ reaction by flowing a pH = 12 solution over an on average charge-neutral capillary Fig. 3.2B-D, using a shear rate of $8.5 \cdot 10^3$ s^{-1}. We then image surface potential changes every 250 ms. The pH of the solution was determined with a pH indicator dye solution, as detailed in Section 3.2.3. Knowing the bulk pH value inside the capillary we can determine

the $pK_{a,s}$ value of every pixel using:

$$K_{a,s} = \left[H_3O^+_{(b)}\right] \frac{\left(N_{\equiv SiO^-_{(s)}}\right)}{\left(N_{\equiv SiOH_{(s)}}\right)} \exp\left(-\frac{e\Phi_0}{k_bT}\right), \qquad pK_{a,s} = -\log\left[K_{a,s}\right], \tag{3.2}$$

with $\frac{\left(N_{\equiv SiO^-_{(s)}}\right)}{\left(N_{\equiv SiOH_{(s)}}\right)}$ the ratio of deprotonated over protonated groups, which can be derived from Φ_0 (using Gouy-Chapman-Stern theory [202], Section 3.5.3). Fig. 3.2B shows the distribution of $pK_{a,s}$ values for the deprotonation reaction, integrated along the x-axis direction. Fig. 3.2C displays the surface potential and derived corresponding surface charge density for two pixels as a function of pH (with $pK_{a,s}$(P1) = 3.8 and $pK_{a,s}$(P2) = 5.9). Fig. 3.2D displays histograms of the obtained $pK_{a,s}$ values with an average of 6.7. The chemical reactivity varies spatially from 2.3 < $pK_{a,s}$ < 10.7 (following a Gaussian distribution). The average value agrees with reference [201] but the significant variation in chemical reactivity across the surface is remarkable. It explains why different studies (even employing the same methods [107, 117]) find different average $pK_{a,s}$ values. Further details on the spatial and the temporal heterogeneity can be found in the appendix, Section 3.5.4.

3.3.2 Imaging the dynamical structural changes of bulk water under electrostatic field

To further image dynamical changes at interfaces and in confinement, two Ag/AgCl electrodes are placed in a pH neutral solution that also contain the micro-capillary and 10 mM NaCl as sketched in Fig. 3.3A. The electrode outside the capillary is grounded and the external electrostatic potential difference ΔV is varied sinusoidally on the inner electrode from 10 V to -10 V with a frequency of 0.05 Hz (~1 V/s). The spacing between the electrodes is 1 cm, and we image the 60 µm long edge that has an opening with a < 1 µm radius. According to the theoretical simulations of Macias-Romero [27], the electrostatic field strength reaches more than 10^6 V/m in the interfacial region and in the tip of the micro-capillary. As ΔV is cycled from 10 V to -10 V, the electrostatic field at the surface (z = 0) of the micro-capillary changes as the distribution of Na^+ and Cl^- ions in the electric double layer changes.

Water molecules that are dynamically oriented by the interfacial DC field can be probed with the polarization combination along the y-axis, see Fig. 3.3. Another place where the electrostatic field reaches similarly high values is inside the < 1 µm radius opening of the micro-capillary [203]. According to the theoretical simulations of Macias-Romero [27], here, the E_{DC} oscillates between $0.75{\cdot}10^6$ V/m and $-1.15{\cdot}10^6$ V/m, which corresponds to a fraction of $5{\cdot}10^{-4}$ oriented water molecules that are fully aligned by it (Section 3.5.2), or, equivalently, ~1 million aligned water molecules per pixel. These aligned water molecules can be probed with the polarization combination along the x-axis, that is, with all beams polarized and analyzed along the main symmetry axis of the capillary.

To image the change in the orientational order of water molecules in both regions as a function of time and applied potential, we recorded SH images with 250 ms integration time in different polarization combinations (along y-axis to probe the interfacial water and along x-axis to probe the water in the tip). Fig. 3.3B shows the applied potential difference ΔV (green curve) and the

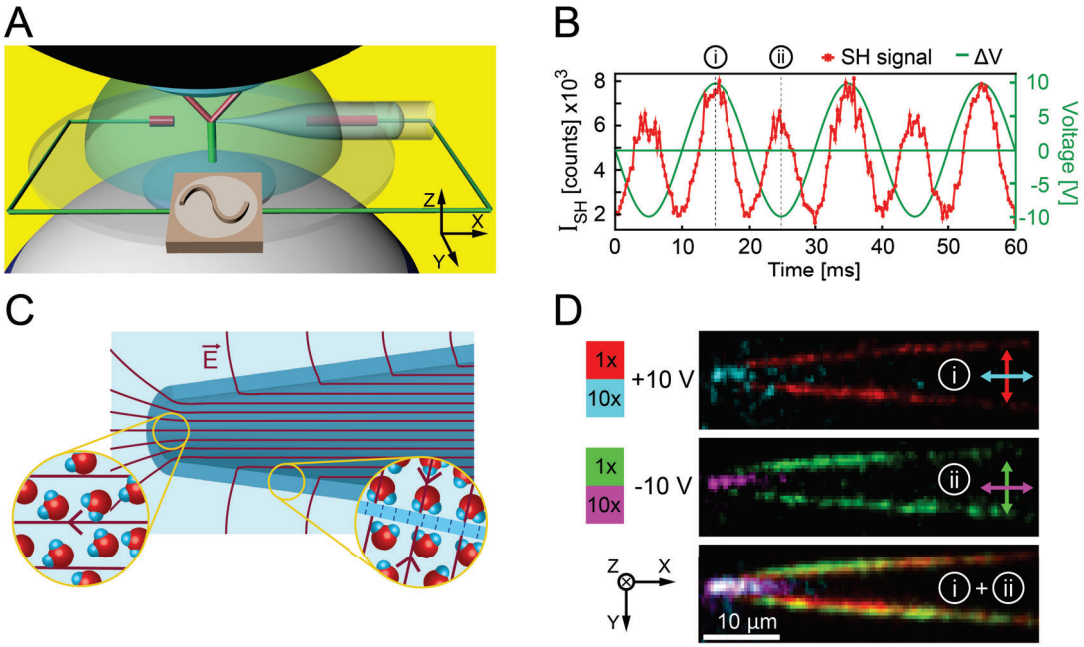

Figure 3.3 – Dynamic imaging of surface chemical changes. (A) Illustration of the experiment: a micro-capillary is immersed/filled with 10 mM NaCl solution and two electrodes are positioned inside/outside of the micro-capillary to apply bias. (B) Time-dependent applied potential (ΔV, green curve) and the corresponding spatially integrated SH intensity (polarization along y-axis, red curve). (C) Illustration of the external field lines for ΔV > 0. (D) Snapshots of movie M1, recorded with 250 ms acquisition time for different values of applied potential (10 V, i; -10 V, ii; composite of 5 frames each, i+ii). The M1 movie can be found at: "https://science.sciencemag.org/content/suppl/2017/07/20/science.aal4346.DC1". All images were normalized with respect to the illuminating beam profile.

corresponding spatially averaged SH intensity of the interfacial water (polarization along the y-axis, red curve). Fig. 3.3C illustrates the external field lines for ΔV > 0 showing water molecules orientation. Fig. 3.3D displays 250 ms snapshot cross-sections for ΔV = 10 V (i) and -10 V (ii) and their overlap (averaging 5 frames). The 250 ms acquisition time is enough to resolve the interfacial water as well as the ~10^6 oriented water molecules in the tip. Inspecting the surface response in these images, it can be seen that the intensity distribution is not uniform. This difference points towards local variations in the surface structure, potential and chemical reactivity similar to those observed in Fig. 3.2.

With this experiment, we demonstrated the ability to probe the bulk water structure in the confinement of a glass micro-capillary tip under external electric field. The future aim will be to study the water structure dependence on the applied field and the size of glass capillary opening, with spatio-temporal resolution, focusing on nanoscale-sized capillary tips, i.e., solid-state nanopores. This system has been lately gaining attention for investigating the behavior of charged polymers [204], and also for characterizing electroosmotic nanojets [180].

3.4 Summary and Conclusions

Dynamical interfacial changes as well as small amounts of oriented confined water can be imaged in three dimensions and on millisecond timescales. The real-time observation of heterogeneity/transient structures in the surface charge distribution, chemical reactivity, and/or the spatial variations in flow are evidence that surface chemical processes heavily depend on local structural/chemical fluctuations on sub-micron length scales. By using the Gouy-Chapman-Stern theory, we spatially resolved $pK_{a,s}$ values for the silica deprotonation reaction that ranged from 2.3 to 10.7. This extended range is in contrast with the reported average $pK_{a,s}$ values (6.8 [201]; 4.8, 8.5 [107]; 3.8, 5.2, 9 [117]), highlighting the importance of having a tool that can resolve locally the differences in $pK_{a,s}$. It is for the first time that a whole spectrum of $pK_{a,s}$ values is reported, encompassing different $pK_{a,s}$ values in the literature both from experimental [107, 117, 201], and from theoretical studies [116, 118]. Being able to non-invasively observe such variations optically, label-free, and in-situ in a confined geometry that is difficult to access, will advance our understanding of surface chemistry beyond that of idealized interfaces, and of mean-field models. This is especially necessary for the development of micro- and nanotechnology that critically relies on local structural and dynamical processes [177], but also for geochemistry, catalysis, electrochemistry (such as in fuel cells) [171, 177, 180, 183], and processes using electrokinetic phenomena, in micro- and nanofluidic environments [205]. Being able to image ~10^6 oriented water molecules per pixel, and knowing that electrostatic fields of the order of 10^9 V/m are predicted in pores that are ~1-10 nm wide [179], we estimate that water in such nanopores can easily be imaged on sub-second time scales. The possibility to image the orientational order of water in confinement has great merit as the water structure can be used to non-invasively report on the structure of other macro-molecules, such as lipids, DNA and proteins, or on potential gradients. The current interest in nano-confinement [206, 207] and the technological development and use of artificial [178, 180, 208] or natural [179] nanopores and capillaries for synthesis [209], chemical separation [177], and even power generation [181, 182] will benefit from it.

3.5 Appendix

3.5.1 HiLo routines for SH imaging

The 3D imaging is achieved by implementing an adapted HiLo imaging procedure [186–191, 193]. In this procedure a first image (I_n) is recorded with the sample being illuminated with a patterned intensity distribution (typically with a single spatial frequency). A second image (I_u) is then obtained but with the sample illuminated with a uniform intensity distribution. The Z-sectioned image is created from these two images with the aid of the algorithm of reference [191] in which low (I_{Lo}) and a high (I_{Hi}) spatial frequency content images are obtained from:

$$\begin{aligned} I_{Lo} &= F_2\{|F_1 I_u - I_n|\}\,, \\ I_{Hi} &= F_2^* I_u\,. \end{aligned} \tag{3.3}$$

Here $F_1\{\}$ denotes a high-pass filter operator intended to center I_u - I_n around zero, $F_2\{\}$ denotes a low-pass Gaussian filter operator and $F_2^*\{\}$ is its conjugate (high-pass) operator. The cut-off frequency of $F_2\{\}$ is typically set at half of the spatial frequency of the illumination pattern. The HiLo image (of

Fig. 3.1D) is then given by:

$$I_{HiLo} = I_{Hi} + \mu I_{Lo}\,, \tag{3.4}$$

where μ is a parameter chosen empirically to aid the transition between low and high frequencies [191]. The image I_n is recorded with a cosine phase grating and $I_{n'}$ is recorded with the same grating shifted by a quarter of a period ($\pi/2$). Adding them results in the uniform image (I_u), as $\cos^2(\sigma x) + \cos^2(\sigma x) + \frac{\pi}{2} = 1$. This is different from HiLo procedures reported in the literature, where the uniform and structured images are obtained by changing the angle of incidence of the light or by randomizing the wave front [187, 192, 193, 210]. These approaches cannot be used with pulsed illumination.

HiLo procedures are based on Fourier filtering and are typically applied for fluorescence imaging. For this type of imaging the emitted light is spatially incoherent. This incoherent nature of the fluorescent signal ensures that outside of the focus, the interference fringes decay rapidly in the axial (z-axis) direction. This process is illustrated in Fig. 3.4. The rapid decay is essential to obtain cross-sectioned images with maximum axial resolution.

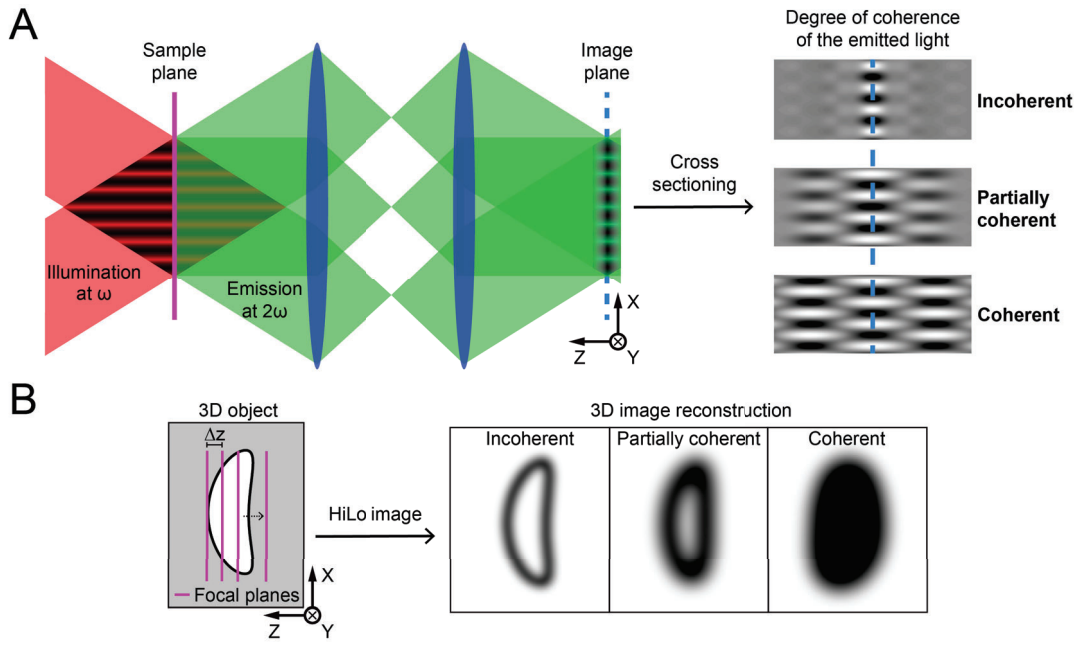

Figure 3.4 – Degree of coherence of the emitted SH light vs. the imaging process. The axial resolution is expected to vary with the amount of coherence in the emitted light. The incoherent emission has the best axial resolution, while the fully coherent light has poor/no axial resolution.

If the emitted light is spatially coherent, interference fringes will persist and modify the axial resolution. Fig. 3.4 also illustrates what will happen for the case of fully coherent emission. Here, an interference pattern is created along the axial direction, which will not decay, and thus no cross-sectioning capabilities are achieved. If the emitted light is only partially coherent, we expect that there will be some intermediate scenario, with some amount of spatial coherence present in the emitted light. In this case, there are fringes, and they do decay but over some distance (illustrated in the middle panel of Fig. 3.4B). In this case HiLo imaging can still be performed but with a lower axial resolution

than for fluorescence imaging.

To understand the changes in axial resolution due to the different degrees of coherence, consider imaging a 10 μm thick sample that is illuminated with a single wavelength plane-wave and emits SH light with a certain degree of coherence. Due to the thicker sample, the SH light will be generated from multiple axial planes with a given spatial offset in phase and all the light will be propagated through the system and focused on the imaging plane (camera). In terms of lateral resolution, the SH light from each plane can be decomposed into a series of plane-waves arriving at different angles that add up in magnitude based on their phase. If the sample is illuminated with a cosine pattern, this pattern will always be present at the focus of the image. In terms of axial resolution, the visibility of interference pattern along z-axis depends on the presence of planes that add up in phase. Therefore, with a decreasing degree of coherence, the visibility of the fringes along the z-axis reduces, resulting in a reduction of the side lobes seen in Fig. 3.4A, and hence an increase in the axial resolution compared to fully coherent light. In the extreme scenario of fully incoherent light, as it is the case for two photon fluorescence (TPF), the axial distribution results in a single peak. The axial resolution also depends on the spatial frequency. In general, wide spectrum of frequencies lead to larger opening angles 2δ (via $\sin(2\delta) = \sigma\lambda$), narrower interference fringes, and higher resolution [211]. Here, the SH imaging ranges with the axial resolution between 1.1 and 4.3 µm, using $0.41 < \sigma < 0.83$ µm^{-1}. For the measurements of Fig. 3.2A and Fig. 3.3 we used the encircled value of $\sigma = 0.64$ µm^{-1}.

3.5.2 The SH response

From the theory of second harmonic generation we have for the SH intensity [66, 163]:

$$I \propto \varepsilon_0^2 \left| \boldsymbol{\chi}^{(2)} : \boldsymbol{E}_1(\omega)\boldsymbol{E}_2(\omega) + \boldsymbol{\chi}^{(3)'} : \boldsymbol{E}_1(\omega)\boldsymbol{E}_2(\omega)\boldsymbol{E}_{DC} \right|^2 , \tag{3.5}$$

where $\boldsymbol{E}_{DC}$ is an electrostatic field, $\boldsymbol{E}_1$ and $\boldsymbol{E}_2$ are the electric fields of the light oscillating at a frequency ω, and $\boldsymbol{\chi}^{(2)}$ and $\boldsymbol{\chi}^{(3)'}$ are the second- and effective third-order susceptibility tensors of the material in question, respectively [163, 212]. For the effective third-order susceptibility we have [212]:

$$\chi^{(3)'}_{ijkz} = g\beta^{(3)}_{ijkz} + \frac{2\mu_z}{3kT} h_1 \beta^{(2)}_{s,ijk} + \frac{2\mu_z}{3kT} h_2 \beta^{(2)}_{ijk} , \tag{3.6}$$

where g and h are constants that are determined by spatially averaging the orientational distribution of water molecules and the number of water molecules present, $\beta^{(3)}_{ijkz}$ is the third-order bulk hyperpolarizability of water, $\beta^{(2)}_{s,ijk}$ is the second-order hyperpolarizability of water at the surface (which contributes in the range $0 < z <\sim 0.3$ nm), $\beta^{(2)}_{ijk}$ is the second-order hyperpolarizability of bulk water (which contributes in the range $z > 0.3$ nm). It is commonly assumed that $\beta^{(2)}_{s,ijk} \cong \beta^{(2)}_{ijk}$. h_1 and h_2 are different since the orientational distribution of water is different. It was recently estimated that the contribution of $\beta^{(3)}_{ijkz}$ is negligible compared to the other two (0.15 %) [213].

The time varying component of the intensity normal to the walls at the surface can be written as (Eq. 3.1). For non-resonant SHG we can expect that the value of $\chi^{(3)'}$ is the same as for other aqueous systems as it reports on the second-order hyperpolarizability and dipole moments of pure water [27, 163]. The value for $\chi^{(2)}_s$ will be interface-dependent. To retrieve changes in the surface

potential (Fig. 3.2) we use Eq. 3.1 with the assumption that at pH = 2 the average charge density on the surface is zero [194, 195]. The remaining response then originates from $\chi_s^{(2)}$. Assuming an average charge density at pH neutral conditions of -2 μC/cm^2 [194, 195], and the Gouy-Chapman-Stern model [214] that is commonly applied for the silica-water interface [195], a value of -114 mV is found for the average surface potential under pH neutral conditions and an ionic strength of 10 mM. The spatially averaged ratio $\frac{\chi_s^{(2)}}{\chi^{(3)'}}$ will then be -0.28. Using $\chi^{(3)'}$ = 10.3·10^{-22} m^2/V^2 for water from [108](29), we obtain $\chi_s^{(2)}$ = -2.85·10^{-22} m^2/V.

3.5.3 Determining the surface chemical reaction equilibrium constant

The surface of glass is populated with $\equiv SiOH$ and $\equiv SiO^-$ groups. At the glass/water interface, the population of these groups depends on the pH of the aqueous solution in contact with the surface via the following chemical equilibrium:

$$\equiv SiOH_{(s)} + H_2O \overset{K_{a,s}}{\leftrightarrows} \equiv SiO^-_{(s)} + H_3O^+_{(s)}\,, \tag{3.7}$$

where $\equiv SiOH_{(s)}$ and $\equiv SiO^-_{(s)}$ are the protonated and deprotonated surface sites, respectively. $H_3O^+_{(s)}$ is the interfacial hydronium ion concentration. $K_{a,s}$ denotes the equilibrium constant for the surface (s) chemical reaction, which can be expressed as follows:

$$K_{a,s} = \frac{\left[H_3O^+_{(s)}\right]\left(N_{\equiv SiO^-_{(s)}}\right)}{\left(N_{\equiv SiOH_{(s)}}\right)}\,, \tag{3.8}$$

where $\left[H_3O^+_{(s)}\right]$ refers to the H_3O^+ interfacial ion concentration $\left(N_{\equiv SiO^-_{(s)}}\right)$ and $\left(N_{\equiv SiOH_{(s)}}\right)$ represents the number of deprotonated and protonated groups per unit area. The H_3O^+ ion concentration near the surface cannot be measured directly but it can be estimated if we know the bulk pH and the surface potential (Φ_0) of the glass surface. The surface H_3O^+ concentration is related to the bulk H_3O^+ concentration by:

$$\left[H_3O^+_{(s)}\right] = \left[H_3O^+_{(b)}\right]\exp\left(-\frac{e\Phi_0}{k_bT}\right), \tag{3.9}$$

where $\left[H_3O^+_{(b)}\right]$ is the bulk aqueous H_3O^+ ion concentration, e, k_b and T denote the elementary charge, the Boltzmann constant and the temperature, respectively. Combining both expressions we get [107]:

$$K_{a,s} = \frac{\left[H_3O^+_{(b)}\right]\left(N_{\equiv SiO^-_{(s)}}\right)}{\left(N_{\equiv SiOH_{(s)}}\right)}\exp\left(-\frac{e\Phi_0}{k_bT}\right), \tag{3.10}$$

The $pK_{a,s}$ of this chemical equilibrium can be obtained via $pK_{a,s} = -\log K_{a,s}$. To find the value for $pK_{a,s}$, we need to know at which pH 50 % of the available sites have been deprotonated (that is, when

$\frac{\left(N_{\equiv SiO^-_{(s)}}\right)}{\left(N_{\equiv SiOH_{(s)}}\right)} = 1$).

As described above, the SH intensity scale can be converted into a surface potential scale. Knowing the values of Φ_0 from our images, it is possible to compute the surface charge density (σ_0) per pixel using the Gouy-Chapman-Stern model [214]:

$$\Phi_0 = \frac{\sigma_0 d_s}{\varepsilon_0 \varepsilon'_r} + \frac{2k_b T}{e} \sinh^{-1}\left(\frac{\sigma_0}{\sqrt{8000 k_b T N_A c \varepsilon_0 \varepsilon_r}}\right), \tag{3.11}$$

with ε_0, ε'_r, ε_r, d_s, N_A, c the permittivity of vacuum, the dielectric constant in the Stern layer, the dielectric constant of water, the Stern layer thickness, Avogadro's number, and the ionic strength in the solution in mol/L. Taking the Stern layer thickness at d_s = 0.91 nm, and the dielectric constant in the Stern layer as ε'_r = 43 from reference [202], we can convert the values of Φ_0 into values of σ_0. Knowing then Φ_0 and σ_0 as a function of time and bulk pH, we can find the corresponding point of σ_p where $\frac{\left(N_{\equiv SiO^-_{(s)}}\right)}{\left(N_{\equiv SiOH_{(s)}}\right)} = 1$ as $\sigma_p = \frac{1}{2}\left(\sigma_{pH=12} - \sigma_{pH=2}\right) + \sigma_{pH=2} = \frac{1}{2}\sigma_{pH=12} + \frac{1}{2}\sigma_{pH=2}$. The final chemical surface reaction constants are calculated as:

$$\begin{aligned} K_{a,s} &= \left[H_3O^+_{(b)}\sigma_{(p)}\right] \exp\left(-\frac{e\Phi_0(\sigma_{(p)})}{k_b T}\right), \\ pK_{a,s} &= -\log\left[K_{a,s}\right]. \end{aligned} \tag{3.12}$$

3.5.4 Spatial and temporal heterogeneity

The spatial heterogeneities in the images of Fig. 3.2A can be estimated by averaging the intensity values within squares of different pixel areas in the image and calculating the standard deviation of these larger squares throughout the mosaicked image. The standard deviation as a function of the size of the integration area is plotted in Fig. 3.5A. It can be seen the standard deviation becomes a factor of 1.9 smaller when the integrated area is increased from 0.16 µm^2 to ~20 µm^2, where it levels off. The transition occurs at ~10 µm^2. The spatial extent of the heterogeneity thus comprises ~125 pixels. This value of ~10 µm^2 suggests that the spatial heterogeneities observed here are connected to the surface roughness, which typically occurs over a length scale on the order of a micron and likely originates from the production process of the micro-capillary. Applying an external potential difference (Fig. 3.3) results in an initially ~20 % larger spread in the computed surface potential values. This suggests that the spatial heterogeneity is not only connected to the surface roughness but also to the distribution of ions in the electric double layer, as the external bias modifies this distribution

To investigate the temporal behavior of the observed heterogeneity in Fig. 3.2A we compute the standard deviations of the intensity/pixel for the pH neutral case. Fig. 3.5B shows two examples of different distributions with 1 s and 5 s integration times. Fig. 3.5C shows the standard deviation divided by the steady state standard deviation as a function of time. It can be seen that taking snapshots of 1 s instead of 5 s results in a bigger distribution of surface potential values. This time scale of a few seconds is much longer than the timescale of diffusion in the electric double layer from where the SH

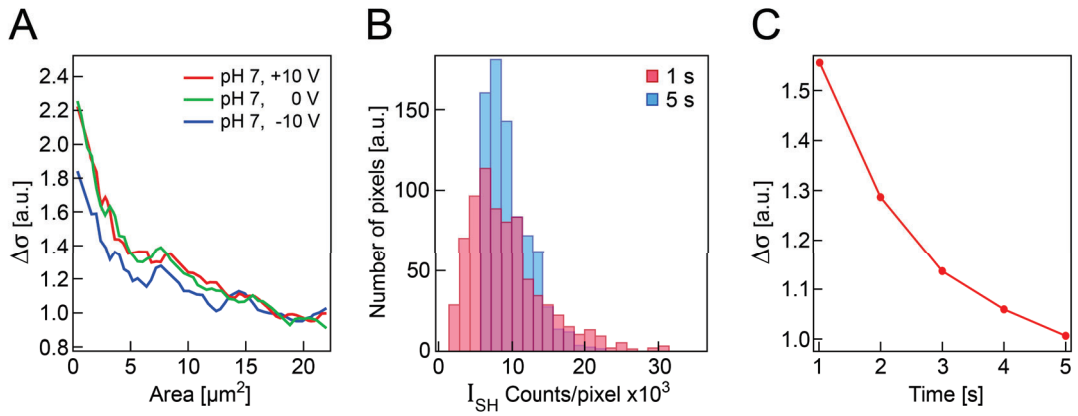

Figure 3.5 – Spatial and temporal heterogeneity. (A) Standard deviation in the intensity as a function of integration area (pH neutral, Fig. 3.2A and Fig. 3.3). (B) Histogram of SH counts/pixel for a 1 s and a 5 s integration time (pH neutral, Fig. 3.2A). (C) Change in the standard deviation as a function of integration time (Fig. 3.2A, pH neutral). The data in panels (A) and (C) is normalized to the steady state standard deviation.

intensity originates.

Interpretation. It has been shown that silica in contact with water undergoes several chemical reactions [215], of which the dissolution of silica and the deprotonation of surface OH^- groups are most important [200]. These reactions occur at different speeds, depending on the local pH and surface structure and determine the charge on the surface. The speed of these reactions (investigated on a fused silica crystal surface) depends on the ionic strength, the pH of the solution, and the flow rate of the liquid [200, 216]. It is clear from the experiments shown here that the structure of the capillary is heterogeneous on a micron length scale, with patches that have vastly different surface potentials, and as a consequence, different surface chemical reaction equilibria constants for the deprotonation reaction (with an average $pK_{a,s}$ of ~6.7 and limiting values of 2.3 and 10.7). This shows there is a complex surface charge distribution varying across the interface that drives an ionic flux (of all ionic species) along the surface plane. This ionic flux in turn influences the chemical conversion of the silica groups (as evidenced by the effect on the bias on the spread in surface potential values in Fig. 3.5A). The establishment of the local chemical reaction equilibria (and their cross-talk) occurs on a much slower time scale than the diffusion. Areas with a high reactivity will convert more quickly into other species, which explains why the distribution in Fig. 3.5B, C narrows.

4 Mapping Electrochemical Heterogeneity at Gold Surfaces

Designing efficient catalysts requires correlating surface structure and local chemical composition with reactivity on length scales from nanometers to tens of microns. While much work has been done on this structure/function correlation on single crystals, comparatively little has been done for catalysts of relevance in applications. Such materials are typically highly heterogeneous and thus require methods that allow mapping of the structure/function relationship during electrochemical conversion. Here, we use optical second harmonic imaging combined with cyclic voltammetry to map the surface of gold nanocrystalline and polycrystalline electrodes during electrooxidation and to quantify the spatial extent of surface reconstruction during potential cycling. The wide-field configuration of our microscope allows for real-time imaging of an area ~100 µm in diameter with submicron resolution. By analyzing the voltage dependence of each pixel, we uncover the heterogeneity of the second harmonic signal and quantify the surface domains where it follows a positive quadratic dependence with increasing bias. There, the second harmonic intensity is mainly ascribed to electronic polarization contributions at the metal/electrolyte interface. Additionally, we locate areas where the second harmonic signal follows a negative quadratic dependence with increasing bias, which also show the largest changes during successive cyclic voltammetry sweeps as determined by an additional correlation coefficient analysis. We assign these areas to domains of higher roughness that are prone to potential-induced surface restructuring, and where anion adsorption occurs at lower potentials than expected based on the cyclic voltammetry of the whole gold electrode.

This chapter is based on the author's journal article: **I. Nahalka**[1], G. Zwaschka[1], R. K. Campen, A. Marchioro, and S. Roke, Mapping Electrochemical Heterogeneity at Gold Surfaces: A Second Harmonic Imaging Study, Submitted (2020).

4.1 Introduction

The surface structure of a catalyst has a tremendous impact on its activity [217–219]. Therefore, revealing catalysts surface heterogeneity is of major importance. This is particularly true for catalysis at the liquid/solid interface, which is essential for many energy conversion and storage processes, e.g., water electrolysis. Much past work has tried to establish the relationship between surface structure and activity. Such efforts are challenging for a variety of reasons, as for example: (1) the presence of defects or grain boundaries can significantly alter the local reactivity by changing the surface charge density or the local conductivity [220, 221], (2) the surface strain of metal catalysts has been demonstrated to be correlated with catalytic activity [15, 16], and (3) restructuring of the surface under operating conditions can also contribute to changes in local activity [222–224]. Designing an efficient catalyst thus requires correlating surface structure and the nature of the catalytically active sites with activity on submicron length scales under operating conditions. For electrocatalysis this challenge can be addressed by experimental techniques that collect both the electrochemical response and the topography/local chemical composition *operando*.

Several techniques can be used to probe the topography, the local activity and the compositional spatial heterogeneity under operating conditions. Electrochemical atomic force microscopy (EC-AFM) can be used to investigate changes in electrode morphology during an electrochemical reaction, with a resolution in the nm to µm range [47, 48]. Scanning electrochemical microscopy (SECM) and variations of this technique have proven very valuable in the study of electrochemical processes at various interfaces, by probing both the topography and the local reactivity with sub-µm spatial resolution [225, 226]. It has been recently shown that electrochemical scanning tunneling microscopy (EC-STM) can map the catalytic activity of surfaces with sub-nm to nm spatial resolution by comparison of local fluctuations in the tunneling current above reactive and non-reactive nanoscale surface sites [18]. Chemical specificity can be obtained by electro-chemical tip-enhanced Raman spectroscopy (EC-TERS), which shows great promise to map active-site chemistry with a precision of 10 nm by combining Raman spectroscopy with EC-STM [31]. However, none of these techniques would be suitable to study systems where electro-chemical reactions produce, for example, gas bubbles. In addition to this limitation, all these techniques rely on a rastering scheme, where the signal is collected pixel by pixel. This scheme implies a time delay in collecting the signal from different areas, which prevents monitoring of large-scale changes in real time. It also becomes time-consuming if applied to large surface areas (in the hundreds of µm range), which can be a drawback in an application-oriented context where large-scale screening of samples is needed. As all practical (photo)electrocatalysts are extremely heterogeneous due to their large surface areas, the ability of large-scale screening of the surface is desirable to localize the presence of “hot spots” of increased reactivity.

Imaging of surfaces in real time (i.e., without employing a rastering scheme) can be obtained by high-throughput wide-field second harmonic (SH) microscopy. We have recently reported a study of the silica/water interface where we imaged the interfacial structure and dynamics of water in a microscopically confined geometry, using a structurally-illuminated SH wide-field microscope [27]. Dissociation constants for the silica surface deprotonation could be extracted from surface potential maps employing a suitable model relating surface potential, charge and chemistry, and were found to change over 9 orders of magnitude along the surface of a single capillary because of surface heterogeneity. Contrarily to conventional rastering SH microscopes, here the wide-field configuration enables the imaging of spatial heterogeneity in real-time for areas of 100 µm in diameter and enables imaging of planar surfaces with detection along the surface normal. Furthermore, the imaging throughput is improved by 2-3 orders of magnitude compared to a point-scan imaging [154], bringing the image

acquisition time down to ms [27] or even µs [148, 227]. Such a short acquisition time is extremely valuable for dynamical imaging [27], where surface changes could be monitored with µs to ms time resolution.

The advantages of this wide-field microscopy configuration are further combined with second-harmonic generation (SHG), which has been used to study the electrode-electrolyte interface for decades [126, 228–237]. SHG is an optical, non-invasive and label-free technique and only requires a broken centrosymmetry of the media to generate a signal, making it interface-specific [160]. This requirement makes SH particularly suitable for studying centrosymmetric metal electrodes such as gold or silver, where the SH signal mainly arises from the broken symmetry at the electrode/electrolyte interface. In these experiments there are a number of contrast mechanisms: the SH light response is complex and influenced by many factors. For metals, the SH primarily originates from the charge gradient at the interface and is consequently sensitive to modifications of this gradient. The applied voltage modifies the surface charge density at the interface and therefore the SH intensity. At sufficiently positive potentials, the formation of oxide layers on the surface will then start to quench the SH signal by reducing the free charge density [128, 230, 238]. This quenching is particularly strong if the SH signal is partially resonant due to a surface plasmon resonance (that disappears upon oxidation), as for example on gold [230]. Besides the exposed surface structure (for example (111) vs. (110)) [126, 239], ion sorption (adsorption and desorption) [127, 238], surface reconstruction [233, 238, 240], and water orientation in the adjacent electrolyte solution [241] can all contribute to the SH response and are all a function of surface structure. Lastly, illumination angle [242], and wavelength, as well as SH wavelength will influence the SH intensity [128, 129, 233, 243, 244].

In this chapter, we use wide-field high throughput SH imaging combined with cyclic voltammetry (CV) to study the spatial extent of gold surface chemistry on nanocrystalline and polycrystalline electrodes during metal electrooxidation. Understanding metal electrooxidation is desirable, because it precedes the oxygen evolution reaction (OER), the oxidative half-cell reaction of water electrolysis. The OER is performance-limiting in virtually every electrolyser [245] and finding better catalysts for it is (among other factors) complicated by our lacking understanding of the oxidation process and the resulting oxide formation. Using two different types of image analyses and without any *a priori* knowledge of the surface structure, we show that the SH response as a function of applied potential in polycrystalline electrodes displays strong heterogeneity on the order of µm as opposed to the nanocrystalline electrodes with sizes of single grains below the imaging resolution, which show a uniform SH vs. potential profile across the entire field of view. Analyzing the voltage dependence of each pixel on the polycrystalline electrode, we identify areas on the sample where the SH signal follows a positive quadratic dependence with increasing bias. There, the SH intensity is mainly attributed to electronic polarization contributions at the metal/electrolyte interface. Additionally, we identify areas where the SH signal follows a negative quadratic dependence with increasing bias. These latter sites correspond to areas that show the largest changes in successive CV sweeps, as corroborated by correlation coefficient analysis. We assign these areas to domains of higher roughness that show an anion adsorption behavior distinctively different from the average, and are more prone to potential-induced surface reconstruction. Rough and dynamic surfaces are often correlated to catalytic activity [14, 246]. Lastly, we show that those same areas appear as the brightest in the PSS polarization combination for our experimental conditions.

4.2 Materials and Methods

4.2.1 Chemicals and gold electrodes preparation

Sodium phosphate monobasic monohydrate (NaH_2PO_4, ≥ 99.0% purity, Sigma-Aldrich), hydrogen peroxide (30% Reactolab SA), and sulfuric acid (95-97%, ISO, Merck) were used as received. All aqueous solutions were made with ultrapure water (H_2O, Milli-Q UF plus, Millipore, Inc., resistivity of 18.2 MΩ·cm).

4.2.2 Sample preparation

The nanocrystalline gold thin-film sample was obtained by physical vapor deposition of 200 nm of gold on an optically flat glass substrate with a 30 Å layer of Cr for increased adhesion (Fig. 4.1C). The polycrystalline gold foils were purchased from Sigma-Aldrich (0.025 mm thickness, 99.99% trace-metal basis) and annealed at 500 °C for 2 h (with linear heating and cooling ramps) to achieve a grain size distribution characteristic of many practically relevant catalysts and suitable for our microscope (Fig. 4.1D). Before use, both electrodes were cleaned using the following procedure: copiously rinsed in acetone, copiously rinsed with Milli-Q water, exposed to ozone for 5 min in a UV ozonator, copiously rinsed with Milli-Q water, copiously rinsed with electrolyte, and annealed electrochemically until the CV was stable (generally 20-30 cycles of cyclic voltammetry). After this procedure, no organic contamination is apparent in the CV. The counter electrode was a Pt mesh, which was cleaned identically to the Teflon cell. A self-made reversible hydrogen electrode was employed as reference [247]. The potential cycling ranged from 0 to 1.7 V vs. the reversible hydrogen electrode (RHE) for the nanocrystalline gold film; and from 0.1 to 1.6 V vs. RHE for the polycrystalline gold foil.

4.2.3 Optical setup

The SH microscope has been described in detail for the transmission geometry in Chapter 2. Here, we use the reflection geometry displayed in Fig. 4.1A. The laser source is operated at 1030 nm wavelength with a repetition rate of 200 kHz delivering ~ 195 fs pulses at an optical fluence of 3.4 mJ/cm^2 at the sample. The microscope objective illuminates the sample (Olympus, LUMPFLN 60XW, NA = 1, WD = 2 mm) at a polar angle α = 34° (see Fig. 2.1) in a one-beam reflection geometry. Once the SH photons are generated, they are collected by the same microscope objective used for illumination and further projected on a back-illuminated electron-multiplied and intensified CCD camera with 512x512 pixels (PI-MAX4: 512EM-HBf P46 GEN III). The polarization state of the emitted light is analyzed with a half-wave plate followed by a polarizing beam splitter. All SH videos were acquired with 0.25 s acquisition time per frame either in PPP, or PSS polarization combinations, where the first letter stands for the polarization state of the SH light and the last two letters stand for the polarization state of the two fundamental beams illuminating the sample. S polarization signifies that the electric field is perpendicular and P polarization that it is parallel to the plane of incidence. The plane of incidence is defined as the plane containing the incoming and reflected rays as well as the normal to the sample surface. Here, the two fundamental beams are identical, as we use a one-beam reflection geometry. We chose here a slower acquisition in order to have an optimum CV shape, however, it is possible to decrease the acquisition time down to 10 ms while still retaining an optimum SH signal-to-noise ratio.

4.2.4 Cyclic Voltammetry in a PTFE cell

CV measurements were performed simultaneously with the SH imaging in a custom-designed PTFE cell. As shown in Fig. 4.1B, the gold electrode was sandwiched between the substrate borofloat glass and PTFE cell. The phosphate buffer solution NaH_2PO_4 of pH = 2.8 was on top of the gold electrode immersing the microscope objective, the platinum counter electrode and the reversible hydrogen reference electrode. The cell was cleaned by immersion in Piranha solution overnight and repeated supersonication in Milli-Q water before the experiment. Details of the cleaning procedure can be found in our previous work [248]. The absence of traces of chloride and sulfate ions was crosschecked in separate experiments where we intentionally introduced those contaminants on the gold electrode (Section 4.5.1), which showed that our 0.5 M (NaH_2PO_4) electrolyte is not contaminated with chloride or sulfate ions.

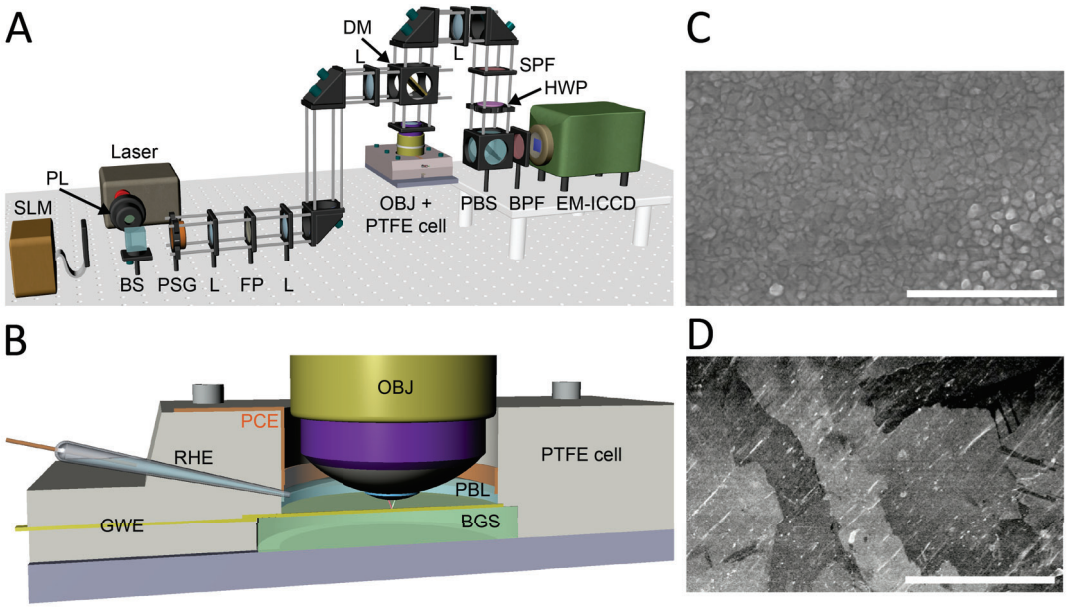

Figure 4.1 – Experimental setup and gold samples. (A) Schematic of the second harmonic microscope in reflection mode of operation; SLM – spatial light modulator, PL – polarizer, BS – beam splitter, PSG – polarization state generator, L – achromatic lens, FP – Fourier plane, DM – dichroic mirror, OBJ – microscope objective, SPF – short pass filter, HWP – half wave plate, PBS – polarizing BS, BPF – second harmonic band-pass filter, EM-ICCD – electron multiplying gated camera. (B) PTFE cell for SH and CV measurements; GWE – gold working electrode, RHE – reversible hydrogen electrode, PCE – platinum counter electrode, PBL – phosphate buffer liquid, BGS – borofloat glass substrate. (C), (D) Gold nanocrystalline and polycrystalline samples imaged by scanning electron microscopy, respectively. Scale bar is 50 μm.

4.2.5 The SH response

As described in the introduction of this chapter, the SH response from gold has a complicated nature involving multiple SH contributions that are often difficult to disentangle. A model for characterizing the SH response from metals was proposed by Lee et al. [196] in 1967. The authors found that, under certain conditions, the SH intensity produced in reflection from a silver surface could be described as a quadratic function of the applied potential, and that the surface susceptibility varied linearly

with the applied potential. This was further validated by later work [128, 229, 243]. The nonlinear polarization can be described, analogously to Eq. 1.6, as the sum of dipolar electric polarizations and static dc-field-induced polarizations:

$$\boldsymbol{P}(2\omega) = \epsilon_0 \left[\boldsymbol{\chi}^{(2)} : \boldsymbol{E}(\omega)\boldsymbol{E}(\omega) + \boldsymbol{\chi}^{(3)'} : \boldsymbol{E}(\omega)\boldsymbol{E}(\omega)\boldsymbol{E}_{DC} \right] , \tag{4.1}$$

where $\boldsymbol{\chi}^{(2)}$ is the total second-order nonlinear susceptibility from both surface and bulk (for gold, the surface term dominates over the bulk term) [249] and $\boldsymbol{\chi}^{(3)'}$ is the effective total third-order nonlinear susceptibility. The effective third-order nonlinear susceptibility includes both the material's response as well as the contribution of all oriented dipoles (mainly solvent) in the solution. In the case of gold, the dipole response is much smaller than the gold response. $\boldsymbol{E}(\omega)$ is the electric field associated with the fundamental laser beam, and $\boldsymbol{E}_{DC}$ is a static electric field across the interface. The intensity of the SH signal $I(2\omega)$ can then be written as proportional to:

$$I(2\omega) \sim \left| \boldsymbol{\chi}^{(2)} + \boldsymbol{\chi}^{(3)'} \Phi_0 \right|^2 I(\omega)^2 , \tag{4.2}$$

where Φ_0 is the potential drop across the metal surface (the difference in potential between the gold surface and bulk electrolyte), and $I(\omega)$ is the intensity of the fundamental beam [128]. Here, $\boldsymbol{\chi}^{(2)}$ and $\boldsymbol{\chi}^{(3)'}$ are assumed to be potential-independent. This can be reduced to a parabolic equation:

$$I(2\omega) \sim \left(\boldsymbol{\chi}^{(3)'} \boldsymbol{\chi}^{(3)*'} \right) \Phi_0^2 + \left(\boldsymbol{\chi}^{(2)} \boldsymbol{\chi}^{(3)*'} + \boldsymbol{\chi}^{(2)*} \boldsymbol{\chi}^{(3)'} \right) \Phi_0 + \left(\boldsymbol{\chi}^{(2)} \boldsymbol{\chi}^{(2)*} \right) = Q\Phi_0^2 + L\Phi_0 + C , \tag{4.3}$$

where Q , L, and C are the quadratic, linear, and constant coefficient, respectively. We assume that the potential drop at the metal surface is:

$$\Phi_0 = V - V_{PZC} , \tag{4.4}$$

where V is the applied potential and V_{PZC} is the potential of zero charge. Based on the estimate for the third-order susceptibilities of gold within Miller's rule (Section 4.5.7), we find that the imaginary part of the third-order susceptibility is negligible at the fundamental wavelength used in this study, which simplifies Eq. 4.3 to:

$$\frac{Q}{L} \sim \frac{\mathrm{Re}\left(\chi^{(3)'}\right)}{\mathrm{Re}\left(\chi^{(2)}\right)} . \tag{4.5}$$

For simplicity, from now on we will omit the real part notation and refer to the values of $\mathrm{Re}(\chi^{(3)'})$ and $\mathrm{Re}(\chi^{(2)})$ in the rest of the manuscript as $\chi^{(3)'}$, $\chi^{(2)}$, respectively. If value of $\chi^{(3)'} \gg \chi^{(2)}$, then the signal is parabolic with a minimum at the V_{PZC}. Conversely, if value of $\chi^{(3)'} \ll \chi^{(2)}$, the signal is no longer parabolic and dominated by second-order contributions of surface and bulk. If value of $\chi^{(3)'} \approx \chi^{(2)}$ then the signal is parabolic with a minimum shifted away from the V_{PZC}. It is important to note that

the assumptions in Eqs. 4.2 and 4.4 are only valid in the absence of specifically adsorbing ions, or in a potential region where no specific ion adsorption occurs, i.e., when tuning the electrode potential is analog to changing the charge density on a bare metal capacitor. Additionally, Guyot-Sionnest et al. [128] have shown that for fundamental wavelengths with photon energies within the free-electron regime, where only intraband transitions can occur, the third-order contribution is important, while this contribution becomes negligible for photon energies that allow for interband transitions (for gold, this corresponds to wavelengths below ~ 500 nm [113]). In the interband transition regime, the second-order susceptibility is predominant.

4.3 Results & Discussions

4.3.1 SH imaging of nanocrystalline and polycrystalline electrodes

The surface of a nanocrystalline gold electrode is imaged with the SH microscope in a phosphate buffer electrolyte (0.5 M NaH_2PO_4, pH = 2.8) while performing CV. Phosphate ions were chosen because of their rather low propensity to adsorb on the surface [250] and to ensure pH stability during measurements. During potential cycling, the increasing of potential towards positive values is referred to as the forward scan, and the decreasing of potential towards negative values as the reverse.

Fig. 4.2A displays an SH image taken at 1.2 V during the forward scan. All potentials are given with respect to the RHE. The color scale is chosen for comparison with upcoming figures that show a larger spread of SH counts. The SH image does not have any specific features and the SH signal is homogeneous with small stochastic deviations in its magnitude. The black line indicates the position of the line scan displayed in Fig. 4.2B. This line scan shows that the SH counts across the image range from $7.0{\cdot}10^3$ to $9.7{\cdot}10^3$ with a standard deviation of ~ $0.5{\cdot}10^3$. Fig. 4.2C shows the cyclic voltammogram (black curve) together with the mean SH signal of the whole image as a function of the applied potential (SH-V). Just before the SH imaging, the gold electrode was electrochemically cleaned by cycling through oxidizing and reducing potentials, until we obtained a stable cyclic voltammogram, as described in section 4.2.4. The cyclic voltammogram shows the features that are expected for gold electrodes [113,251] and three different regions can be identified in the forward scan. The first region is termed the polarization or double layer charging region (0 to 0.4 V) [252] with no/minor surface anion adsorption (for the weakly adsorbing ions we employ here) [250,253]. In this range, only a change in the electrostatic charge on the metal and corresponding change in double layer structure is expected [251]. The second region (0.4 to 1.2 V) is a region of further polarization where anion adsorption starts after the point of zero charge (in our case 0.4 V) [252] with strong adsorption of phosphate species occurring between 0.7 – 1.2 V [253]. The third region corresponds to oxide growth (1.2 to 1.7 V) [254]. It has been shown that low-coordinated gold atoms exhibit lower activation barriers [20]. Polycrystalline gold generally exhibits a large number of surface defects, and we expect that a considerable amount of these defect will be low-coordinated gold surface atoms. Therefore, the slight peak in the CV near 1.2 V in the forward scan is likely caused by the pre-monolayer oxidation of surface steps and defects [255]. The peaks above 1.35 V are the result of oxidation of the first full layer of metal atoms including terraces, which happens by replacement of adsorbed anions by either O, or OH, and subsequent site exchange of the oxygen species with metal ions [256–259], while subsequent layers of oxide are only expected to grow at higher potentials. In the reverse scan, the peak around 1.1 V results from the reduction of the oxide. The small peak around 0.4 V is due to a minor impurity (see section 4.5.2). The slight bend in the cyclic voltammogram from 0 to 0.5 V is due to the presence of oxygen that causes a negative current due to the oxygen reduction reaction [245].

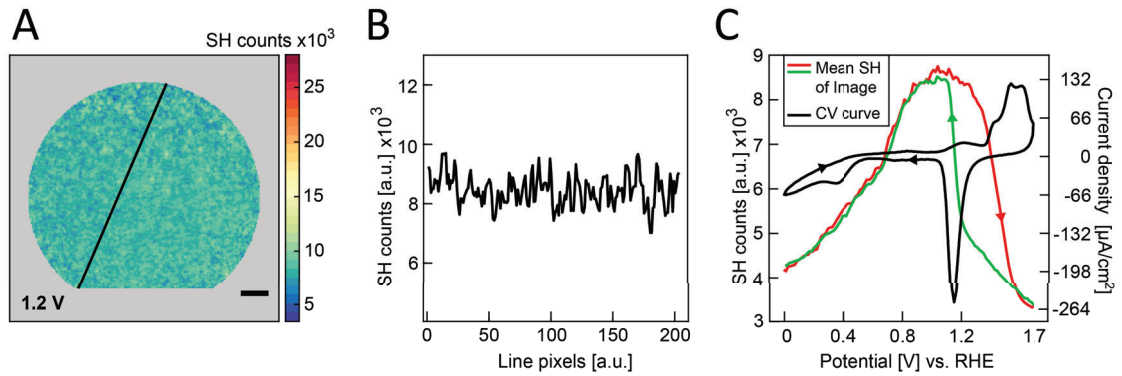

Figure 4.2 – Second harmonic imaging and cyclic voltammetry of the nanocrystalline gold. (A) The SH image at 1.2 V vs. RHE during the forward scan. The SH image is a frame extracted from a SH video recorded with 0.25 s acquisition time per frame. The CV sweeping rate was set to 60 mV/s and the electrolyte was 0.5 M NaH_2PO_4. (B) The variation of SH counts across the image was obtained from the black line scan in (A). (C) Cyclic voltammogram (black curve) displayed with the mean SH signal of the whole image. The red and green traces are recorded during the forward and reverse scan, respectively. The SH data was obtained in PPP polarization combination. The potential values are given with respect to the RHE. Scale bar is 10 μm.

During the forward scan, the spatially-averaged SH intensity increases and eventually reaches a maximum around 1.1 V (Fig. 4.2C). The SH intensity then decreases from 1.2 to 1.7 V. In the reverse scan, the SH signal recovers to its initial highest value once the surface oxide is fully reduced at 1.1 V vs. RHE, displaying a pronounced hysteresis. Note that during forward and reverse scans an identical parabolic behavior of SH intensity can be observed as a function of applied bias between 0 and 0.9 V. The mean SH signal intensity of the nanocrystalline electrode as a function of applied voltage shows similar features to what has been already reported in the literature for both silver and gold electrodes [128, 129, 243] and matches well with the CV data: from 0 to 1.2 V the SH intensity is expected to increase with increasing positive bias due to the increasing (positive) charge density at the metal surface. The subsequent decrease with increasing positive bias above 1.2 V is the result of gold surface oxidation [128, 230].

Fig. 4.3A, B, and C show the SH images of the polycrystalline gold electrode recorded during CV at 60 mV/s in a phosphate 0.5 M NaH_2PO_4 buffer solution (pH = 2.8) at three different potentials during the forward scan: 0.2 V, 1.2 V and 1.51 V vs. RHE. The SH images were recorded in the PPP polarization combination. The SH signal in all three images, Fig. 4.3A, B, and C, display strong spatial heterogeneity. The color scale is identical to the color scale of Fig. 4.2A, offering a direct comparison of the nanocrystalline vs. the polycrystalline gold electrode. The line scan in Fig. 4.3B shows the variation of the SH counts across the image ranging from $4.4{\cdot}10^3$ to $50{\cdot}10^3$ with a standard deviation of ~ $7.6{\cdot}10^3$ and an average value of ~ $8.4{\cdot}10^3$ counts. For the polycrystalline gold electrode, clear areas with SH intensity per pixel above 10^4 counts spanning several tens of microns can be identified, while no such areas are visible on the nanocrystalline gold electrode, where the line scan across the image is flat and the SH intensity has an average value of ~ $8.4{\cdot}10^3$ counts. The mean SH intensity of the entire field of view shown in the second panel of Fig. 4.3D (black curve) has a maximum around 1 V and is qualitatively very similar to the mean SH intensity recorded for the nanocrystalline electrode shown in Fig. 4.2C, with a maximum around 1.1 V. However, it is interesting to note that different spots on the surface show distinct SH behavior as a function of applied potential, therefore suggesting that looking only at the averaged SH signal obscures the local variations. This is demonstrated in Fig. 4.3D, where

the SH intensity dependence on the applied potential is shown for three representative pixels, P1 (blue lines), P2 (red lines), and P3 (green lines) for three consecutive CV cycles, named CV1, CV2 and CV3. Pixels P1 and P3 are from neighboring bright (higher signal intensity) and dark (lower signal intensity) SH patches, respectively. Pixel P2 lies on their border. For further analysis, we highlight two regions of interest: the polarization region (PR), marked in yellow in Fig. 4.3D and the oxide growth (OG) region, marked in orange. Only the forward scan will be considered here. In the PR, the SH intensity of pixel P1 increases with applied potential, the SH intensity of pixel P3 slightly decreases with increasing potential, and the SH signal for pixel P2 increases slightly. On the other hand, in the OG region, all three pixels exhibit qualitatively similar SH behavior, i.e. the SH intensity decreases with increasing potential. Lastly, inspecting the SH signal on the whole forward scan (0.1 – 1.6 V), it appears that the borderline pixel P2 shows an intermediate SH behavior between pixels P1 and P3, suggesting that this transition region is an average between two opposite trends. The nanocrystalline sample at three different potentials during the forward scan can be found in Section 4.5.3 (Fig. 4.8) for comparison. The SH intensity quadratically increases with increasing bias in the PR for the three pixels displayed.

Prior work has established that the efficiency of SH generation is highly dependent on the exposed surface structure ((111) vs. (110) facet, for example) and for a given facet it is also strongly dependent on the azimuthal orientation of the facet [127, 239]. This could possibly explain the difference of overall magnitudes in SH-V curves belonging to the three different pixels in Fig. 4.3D. However, this alone is unlikely to explain why some pixels display a decreasing SH signal with increasing bias in the PR region. An interpretation for the behavior of these pixels will be discussed in the next Section 4.3.2. Interestingly, the voltage dependence in the OG region appears to be common to all pixels, indicating that once the oxide is starting to grow, the characteristics of the surface, such as the roughness, grain boundaries, or other sorts of large-scale defects, do not significantly influence the SH signal.

4.3.2 SH dependence on the voltage

Characterizing the SH signal and all of its contributions is a difficult task even on well-defined single crystal samples. Here, the situation is even more complicated as we use polycrystalline gold with no prior knowledge about the gold morphology at each pixel. In spite of this complication, we can still extract useful information about the surface changes as a function of potential by analyzing the SH data within the mathematical framework described above. In Fig. 4.4 we show a pixel-wise fitting of the SH-V data model based on Eq. 4.3, see Section 4.2.5. As described by this equation, the SH intensity can display a parabolic shape with a minimum at the potential of zero charge when $\chi^{(3)'} \gg \chi^{(2)}$ [128]. The reason for this SH-V behavior is related to the increase in surface charge density: by increasing the applied potential on the electrode, the (positive) surface charge density at the metal surface increases. This increases the charge gradient at the interface, which results in a quadratic increase of the SH intensity with applied bias [27]. The minimum of the parabola can be displaced from the V_{PZC} when the relative strength of $\chi^{(3)'}$ decreases with respect to $\chi^{(2)}$. In this case, the signal with increasing applied potential up to V_{PZC} is due to a superposition of an increase in (positive) surface charge density (although the charge gradient is here reduced as we are below V_{PZC}) and of the $\chi^{(2)}$ contribution. In our case, the fundamental wavelength of our laser is 1030 nm, and the gold response is free electron-like (no interband transition) at this wavelength. We therefore expect a significant $\chi^{(3)'}$ contribution [128]. However, by examining Fig. 4.3D, we can already expect a significant amount of $\chi^{(2)}$ contribution. Considering the half-parabola in the potential range we investigate (from 0.1 to 0.4 V), it can be seen that the minimum is not located at V_{PZC} but rather shifted to more negative bias (not visible in our experiment).

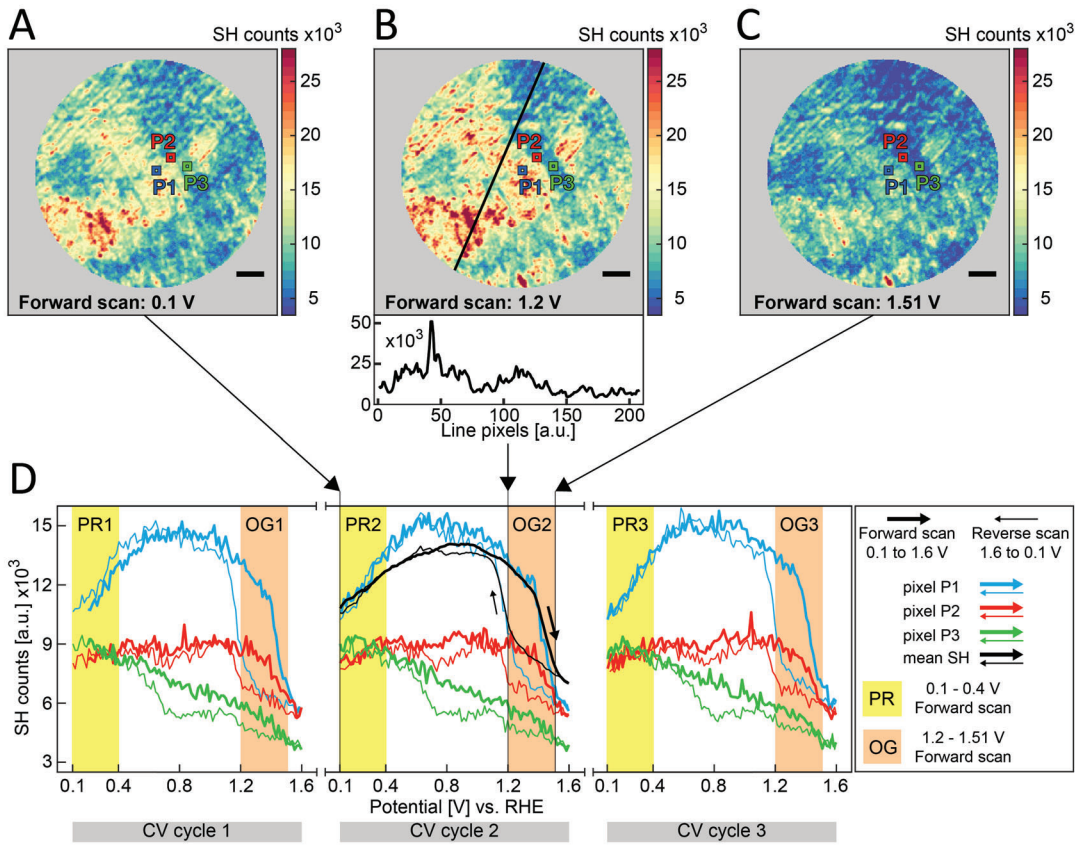

Figure 4.3 – Second harmonic imaging of the polycrystalline gold electrode as a function of applied voltage. (A), (B), (C) SH images at 0.1 V, 1.2 V, and 1.51 V vs. RHE during the forward 60 mV/s scan. The SH images are frames extracted from a SH video recorded with 0.25 s acquisition time per frame. Points P1, P2, and P3 mark the chosen single pixel locations. The color scale is identical to Fig. 4.2A. In (B) the black line shows variation in SH counts across the image. (D) SH intensity as a function of the potential applied to the gold electrode in three continuous CV cycles. The blue curve corresponds to pixel P1; the red curve corresponds to pixel P2; and the green curve corresponds to pixel P3. The black line in the second image corresponds to the average SH signal of the whole image in CV cycle 2. The thick lines correspond to the forward scan, while the thin lines correspond to the reverse scan. The polarization region (PR, 0.1-0.4 V) is marked in yellow for all three cycles while the oxide growth regions (OG, 1.2-1.51 V) is marked in orange. The SH data was obtained in PPP polarization combination. The potential values are given with respect to the reversible hydrogen electrode. Scale bar is 10 µm.

The SH-V signal is fitted in the PR with a parabola according to Eq. 4.3 at every pixel resulting in a quadratic (Q), a linear (L) and a constant (C) coefficient. Eq. 4.3 is applied to the PR potential interval as the approximation made in Eq. 4.4 is only valid in absence of strong anion adsorption [128]. For the fitting procedure, the knowledge of V_{PZC} is necessary. A large range of V_{PZC} values has been reported in the literature for different gold facets [251, 260]. Our polycrystalline gold electrode was prepared with the same procedure as reported by Mariano et al. [221], where the gold surface contained almost exclusively (111) and (110), but almost no (100) facets. We chose for the V_{PZC} a value of 0.4 V vs. RHE, because it appears to be the average of the values reported in the literature. This choice will be further commented here below. Fig. 4.4A, B, C, and D were calculated from the PR2 (see Fig. 4.3D) thus the quadratic and linear coefficients have been labeled as Q_2 and L_2. Fig. 4.4A and B show respective maps

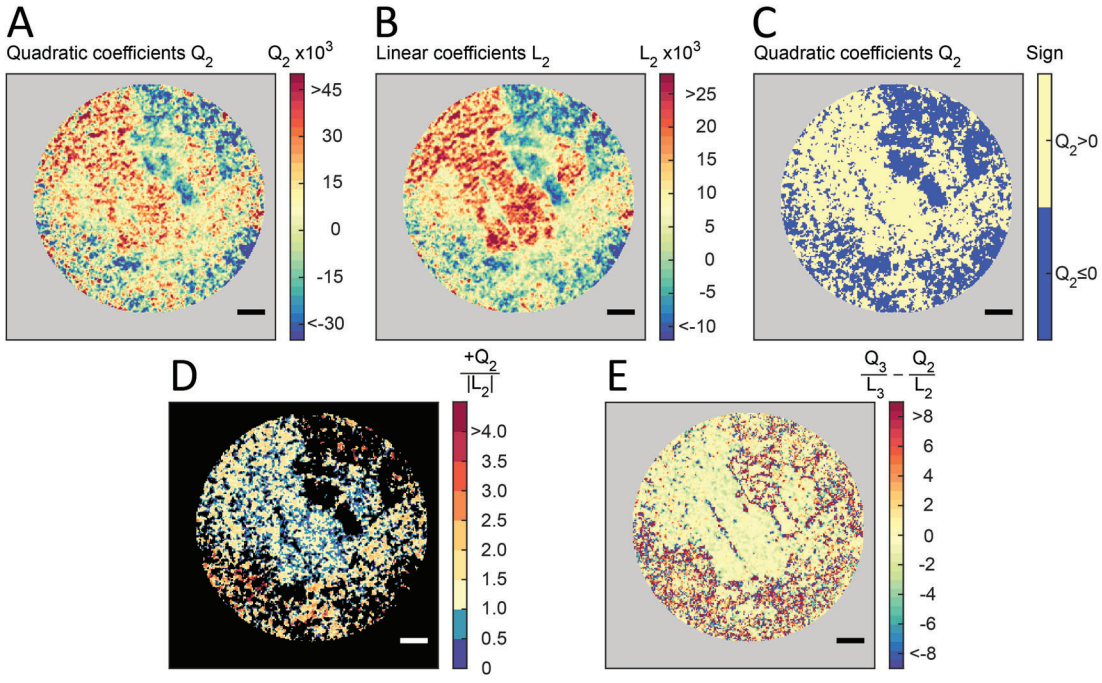

Figure 4.4 – Fitting of the second harmonic signal in the PR as a function of applied potential for polycrystalline gold electrode. Second harmonic PPP polarization signal corresponding to potential interval PR2 (see Fig. 4.3D) is fitted by a polynomial of 2nd degree with point of zero charge offset common to all pixels. This yields a map of fitted quadratic coefficients Q_2 in (A) and a map of fitted linear coefficients L_2 in (B). (C) Map of quadratic coefficients Q_2 with a binary color-code of yellow ($Q_2 > 0$) and blue ($Q_2 \leq 0$). (D) Division of Q_2 map over the absolute value of L_2 map. Pixels where $Q_2 \leq 0$ are not considered here. (E) Difference of quadratic over linear coefficients ratios obtained from potential interval PR3 minus PR2 (see Fig. 4.3 D). Scale bar is 10 µm.

of the quadratic and linear fit coefficients. These two maps look qualitatively similar; however, their scale differs. The map of linear coefficients shows much clearer large-scale features, while the map of quadratic coefficients reveals more signal variation within these features.

Fig. 4.4C displays again the map of quadratic coefficients, however, this time with a color coding separating the $Q_2 > 0$ and $Q_2 \leq 0$. The regions where $Q_2 > 0$ account for 59.7% of the total surface, while the regions where $Q_2 \leq 0$ represent 40.3% of the total surface. The negative Q_2 values are present both in larger patches as well as in smaller spots distributed across most of the surface. The areas where $Q_2 \leq 0$ indicate that there is no increase in the SH intensity with increasing potential, but rather a decrease, implying that in these areas the increase in (positive) surface charge density caused by the increasing potential is counteracted by another effect. We hypothesize that anion adsorption at potentials below the V_{PZC} could occur in these areas, leading to charge screening at the gold surface and therefore to a decrease in SH intensity. Additionally, anion adsorption can drive or influence electro-chemical processes at potentials in the PR (a potential window much below the actual oxygen evolution reaction) such as surface reconstruction [256, 257, 263] or oxidation of metastable surface states [264], with a corresponding modification of the SH intensity.

While phosphate ions, at the pH of our experiment specifically dihydrogen phosphate ions ($H_2PO_4^-$) are not expected to strongly adsorb on the surface [250], they are still expected to be better

sorbents than very weakly adsorbing ions, as for example ClO_4^- ions [261]. As such, phosphate adsorption in some areas cannot be totally excluded. It is important to note here that model we employ assumes no/minor adsorption of ions in order to fit the regions $Q_2 > 0$. Deviations from the model (regions where $Q_2 < 0$) indicate that, in those regions, the SH intensity as a function of applied potential in the PR cannot be interpreted within the framework established by Eq. 4.5. Therefore, the anomalous behavior of those specific areas can be tied to ion adsorption. This phenomenon could be the manifestation of a local V_{PZC} being different than the average V_{PZC} we have assumed for our sample [262]. As the choice of the average V_{PZC} was made for the purpose of the fitting, any deviations from it have to be interpreted as local variations from this average value that we arbitrarily chose, which indicate that the point of zero charge is not a homogeneous quantity across the surface but has to be treated as a spatially-dependent parameter [262].

Having considered the positive and negative values of Q_2, we also define the regions where Q_2 is close to zero. To specifically identify these pixels, we first need to define a threshold. Considering that the maximum Q_2 values are close to $40{\cdot}10^3$, a threshold value of $|Q_2| \leq 1000$ represents 2.5% of the maximum Q_2 values, and all the pixels with values below this threshold can be considered as having negligible Q_2. Only a small number of pixels where Q_2 is close to zero (~ 3.8% of the total surface) is found and an even smaller number of pixels where Q_2 and L_2 are both close to zero (~ 2.4% of the total surface when $|Q_2|$ and $|L_2| \leq 1000$), reflecting that there are only very few areas on the surface where the SH signal linearly depends on the voltage $\left(\chi^{(2)} \gg \chi^{(3)'}\right)$, or where the SH signal remains insensitive to the applied voltage, respectively.

For comparison, the SH-V dependence of the nanocrystalline sample mostly shows regions where the SH intensity quadratically increases with increasing bias in the PR, with only a negligible number of pixels with an inverted potential-dependence scattered across the image (Section 4.5.4, Fig. 4.9).

Having determined the surface areas where the SH intensity quadratically increases with the applied potential and the ones where this is not the case, we can now correlate these voltage-dependent behaviors with specific surface characteristics. In Fig. 4.4D we examine the results of fitting the data to Eq. 4.3 as the ratio of the Q_2 map over the absolute value of the L_2 map. The absolute value of L_2 is chosen here to focus on the Q_2/L_2 ratio without distinctions between $\pm L_2$ (the sign of L_2 is related to the sign of the surface susceptibility, which for simplicity we do not consider in this analysis). By inspecting the ratio $Q_2/|L_2|$ of different pixels, we can compare the relative strength of $\chi^{(3)'}$ over $\chi^{(2)}$ between these pixels according to Eq. 4.5. Only pixels with $Q_2 > 0$ are considered here, as pixels with $Q_2 < 0$ do not satisfy the assumptions of Eq. 4.5. As a reference value, the magnitude of $\chi^{(2)}$ for gold at 1064 nm was reported to be close to $2{\cdot}10^{-19}$ m·V^{-1} [249], which is close to the magnitudes reported for $\chi^{(3)}$ for gold, in the range of $2{\cdot}10^{-19}$ to $7{\cdot}10^{-19}$ m·V^{-1} at 1030 nm [265]; $\chi^{(3)}$ is not equal to $\chi^{(3)'}$ but is considered to be in the same order of magnitude for a metal [128]. The ratio $Q/|L|$ is then expected to be in the range of 0-10, which agrees with our data showing the majority of the pixels displaying a ratio between 0 and 4. Values below 1 (20.65% of the total surface) are colored in blue and values above 1 (79.35% of the total surface) are colored in yellow to red. A detailed breakdown of the percentage of pixels per location is presented in Table 4.1. These percentages show that pixels with higher second-order surface susceptibility ($Q_2/|L_2| < 1$) tend to accumulate at the edges of distinct surface features and at the borderline with the greyed areas ($\pm Q_2$ boundary). On the other hand, the areas where $Q_2/|L_2| > 1$ are more evenly distributed over the image and there is not as much specific accumulation at the $\pm Q_2$ boundary.

From these results we see that, in the areas with $Q_2 > 0$, the majority of the pixels (79.35%) display a relatively stronger $\chi^{(3)'}$ contribution, indicating that the SH signal is dominated by variations of

Table 4.1 – Percentage of pixels in Fig. 4.4D according to the fitting the SH data of polycrystalline gold to Eq. 4.3.

$Q_2 > 0$, $Q_2/\|L_2\| > 1$			$Q_2 > 0$, $Q_2/\|L_2\| < 1$		
Total	± Q_2 boundary	elsewhere	Total	± Q_2 boundary	elsewhere
79.35%	40.68%	38.67%	20.65%	14.21%	6.44%

surface charge density. A minority of pixels in the $Q_2 > 0$ areas display a stronger $\chi^{(2)}$ contribution (20.65%), which indicates that the signal is dominated by variations of the surface term and it is likely accompanied by a rise in the excitation of a local surface plasmon (LSP) [128]. While surface plasmons in general cannot be excited by transverse electromagnetic waves by a simple one-beam reflection on a perfectly flat gold surface, the presence of irregularities at the surface can facilitate the excitation of the LSP [266, 267]. Thus, we can assign the areas with the highest $\chi^{(2)}$ contribution ($Q_2/|L_2| < 1$) to various defects, grain boundaries, or small roughened parts that are spread over the polycrystalline surface. This is further supported by the observation of the majority of the pixels with stronger $\chi^{(2)}$ contribution accumulating at the edges between surface features displaying different SH intensity, i.e. grain boundaries (14.21% out of 20.65% total pixels).

Regions where $Q_2 < 0$ (SH intensity decreases with potential) cannot be interpreted within the framework established by Eq. 4.5, as we hypothesized that the initial assumption of no (strong) anion adsorption is not met in those specific areas. A decreasing SH intensity as a function of applied bias, or almost flat voltage dependence in the PR, such as shown in pixels P3 and P2 respectively (Fig. 4.3), could indicate the adsorption of anions at the surface, thus effectively screening the electric field at the interface. We can further speculate about the nature of these areas by inspecting Fig. 4.4E. Fig. 4.4E shows the Q_3/L_3 - Q_2/L_2 difference maps for PR3 and PR2 with no distinctions between $Q > 0$ or $Q \leq 0$. Here, a higher difference, either positive or negative, indicates that the shape of the SH-V curve has significantly changed between CV2 and CV3 cycle. This map evidences that the areas with the largest heterogeneity and the largest changes cycle to cycle are the borders of +Q/-Q areas. As a quantitative example, we estimate the percentage of pixels with values > 2 or < -2 to be 40%, which correlates well with the percentage of pixels where $Q_2 < 0$ (40.3%), as determined above. A detailed breakdown of the percentage of pixels per location is presented in Table 4.2 and highlights that the borderline regions are prone to change cycle to cycle, which is a similar observation as in Fig. 4.4D. On the other hand, the areas in Fig. 4.4E that change the less cycle to cycle match well with the regions where $Q_2 > 0$ (yellow areas in Fig. 4.4C).

Table 4.2 – Percentage of pixels in Fig. 4.4E according to the fitting the SH data of polycrystalline gold to Eq. 4.3.

$\left(\frac{Q_3}{L_3} - \frac{Q_2}{L_2}\right) > 2$ or < -2		
Total	± Q_2 boundary	elsewhere
40.0%	27.2%	12.8%

The observation of large differences from cycle to cycle, together with a higher heterogeneity, in most of the areas where the quadratic coefficient is negative suggests that these surface areas undergo dramatic structural changes while potential cycling. These findings support our hypothesis hereabove, where anion adsorption below the average V_{PZC} could be the cause for increased surface reconstruction. Indeed, surface reconstruction induced by specific adsorption of ions has been previously observed

by SHG on gold samples [238, 239]. LSP excitation, related to the second-order susceptibility, is also possible in these regions, but is difficult to quantify in this case using the linear coefficient L, which in practice indicates the position of the minimum of the parabola. As a matter of fact, the position of this minimum could also be shifted as a result of anion adsorption [129] and not only due to LSP excitation.

4.3.3 Correlation coefficient analysis

The analysis of the data with Eq. 4.3 is limited to the PR and Q > 0 regions where Eq. 4.4 holds. We now describe an alternative image processing method in order to support our findings from above and that can be applied to other potential intervals than the PR. The aim of this method is to distinguish the differences in shapes of two SH-V signals in the same potential interval, however, from two consecutive CV cycles. Such a method can identify which pixels show different SH-V behavior in one CV cycle compared to the previous CV cycle, pointing to potential-dependent surface changes. For this reason, we chose to calculate the correlation coefficient for every pixel as follows:

$$\text{CorrCoeff}(A,B)_{per\ pixel} = \frac{\text{cov}(A,B)}{\sigma_A \sigma_B}\,, \tag{4.6}$$

where A is the respective SH-V signal intensity at a given pixel, and B is the mean SH-V signal intensity of the whole image, both for a given potential interval. cov(A,B) is the covariance of A and B, σ_A is the standard deviation of A and σ_B is the standard deviation of B. The correlation coefficient is a measure for the correlation of A and B as a function of voltage. Its output value ranges from -1 to 1. A value of 1 expresses an ideal correlation between A and B: for a positive increase in A - there is also a positive increase in B. The other extreme of -1 expresses an ideal inverse correlation between A and B: for a positive increase in A - there is a decrease in B. A value of 0 implies that there is no correlation between A and B.

Using Eq. 4.6, we calculated the correlation coefficient for every pixel using SH-V curves from 3 CV cycles. The results are displayed in Fig. 4.5A. The red to orange areas display the strongest correlation, thus indicative of the regions where the SH-V data at each pixel behaves similarly to the averaged SH-V signal. Note that there are similarities between the red regions in Fig. 4.5A and the areas displayed in yellow on Fig. 4.4C (i.e. areas where $Q_2 > 0$). On the other hand, the yellow to blue areas indicate regions where the SH-V data deviates from the averaged SH-V signal. Those areas match well with blue regions in Fig. 4.4C ($Q_2 < 0$ areas).

We obtain additional information by performing the correlation coefficient analysis also on the PR and OG potential intervals (see Fig. 4.3D). As mentioned above, the first potential interval (0.1 – 0.4 V) was chosen as the potential interval corresponding to double layer charging, where on average no/minor ion adsorption is expected. The OG region spans from 1.2 to 1.51 V for the polycrystalline sample. In this potential interval, the first layer of oxide is growing and eventually fully covering the surface [256, 259]. Correlation coefficient maps are calculated for both PR and OG potential intervals in the second CV cycle (PR2, OG2) and third CV cycle (PR3, OG3). By looking at the map of the absolute difference of correlation coefficient (designated here as |ΔCorrCoeff|), we can locate surface areas where the SH-V behavior is the same, or is different, from one cycle to the other. The correlation coefficient maps are calculated for a specific interval, however, their difference retains the full history of the sample. For example, a large value of |ΔCorrCoeff| (PR3-PR2) indicates that changes have occurred between PR3 and PR2, however these changes could have originated at any point in the cycle and

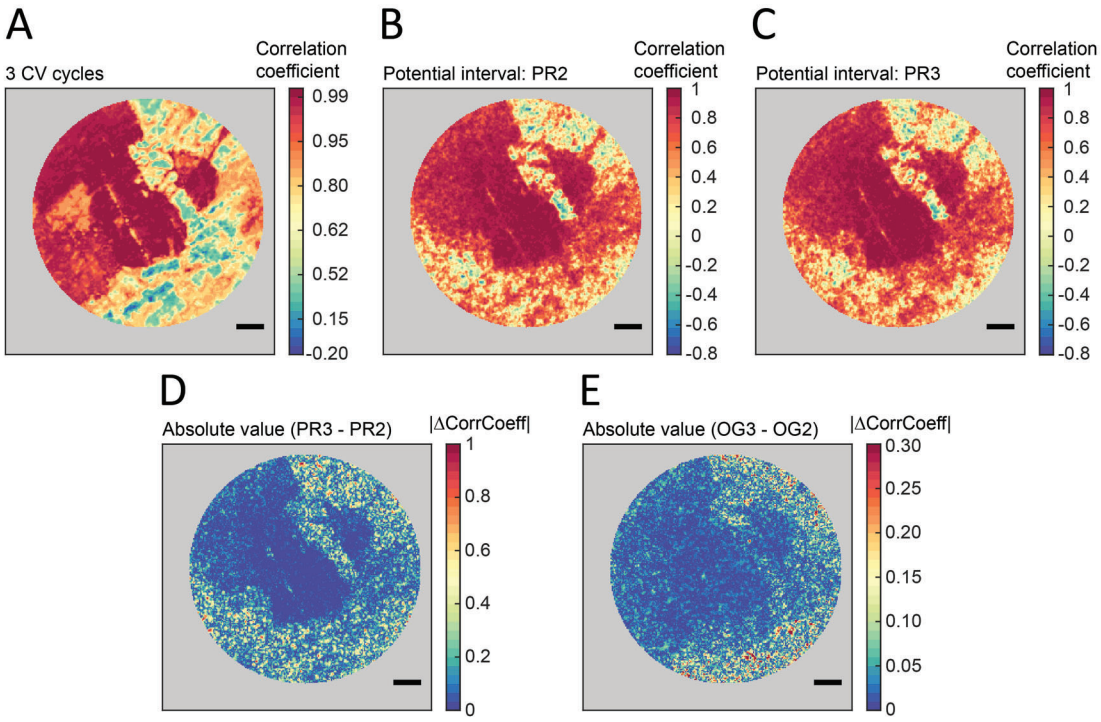

Figure 4.5 – Correlation coefficient analysis. (A) Correlation coefficient map of the polycrystalline gold electrode calculated from three full CV cycles. (B), (C): Correlation coefficient maps calculated from PR2 and PR3 potential intervals, respectively. (D) Absolute value of the difference between (B) and (C). (E) Absolute value of the difference between two correlation maps calculated in potential intervals OG3 and OG2. SH data was recorded in the PPP polarization combination. Scale bar is 10 µm.

not only in PR2 or PR3 (also during OG2 or reduction, for example). Analogously, a large value of |ΔCorrCoeff| (OG3-OG2) indicates that changes have occurred between the OG3 and OG2 region, but those changes could have originated either during the oxide growth (OG2 or OG3), or during the successive reduction and polarization of the sample in PR3 [1]. Note that here we consider the difference, so both correlation coefficients have to be calculated with respect to the same reference curve B in Eq. 4.5. Here, we chose a simple y = x curve as reference [2]. We applied this approach to the polycrystalline gold sample and present the results in Fig 4.5B-F. Fig. 4.5B,C show the calculated correlation maps from PR2 and PR3 potential intervals, which are qualitatively similar to the map calculated with respect to the average SH-V signal in Fig. 4.5A. Fig. 4.5D then shows the absolute value of the difference between Fig. 4.5B and C.

The |ΔCorrCoeff| map shown in Fig. 4.5D shows large spatial heterogeneity over the surface. As mentioned above, the areas with largest values of |ΔCorrCoeff| indicate that more changes are occurring in those areas over one full cycle. We take |ΔCorrCoeff| > 0.1 as an indication for substantial changes occurring to the surface (the error on |ΔCorrCoeff| is estimated to ± 0.04, see Section 4.5.8). Fig. 4.5E

[1] The correlation coefficient analysis can only be used to compare the relative shape of the SH-V curves; it cannot be used directly to examine if a certain process started at a lower or higher potential.

[2] This ensures that the SH-V signal will be correlated against the same reference curve, therefore, exposing mutual differences. The mean SH-V signal of the whole image is not appropriate here because it can vary cycle to cycle.

also shows spatial heterogeneity in |ΔCorrCoeff| calculated for the OG region. While the magnitude of the |ΔCorrCoeff| cannot be directly compared for the PR and OG region [3], we can compare the spatial extent of the changes on both potential intervals. In the OG region, values of |ΔCorrCoeff| > 0.05 (the error on |ΔCorrCoeff| is estimated to ± 0.02, see Section 4.5.8), indicating areas with changes occurring over one full cycle, are found with a similar spatial distribution as Fig. 4.5D. The percentage of the total surface displaying changes of |ΔCorrCoeff| > 0.1 in the PR interval is 39.7%. For comparison, the percentage of the total surface displaying changes of |ΔCorrCoeff| > 0.05 in the OG interval is 22.7%. The nature of the changes associated with larger |ΔCorrCoeff| values will be addressed below. Results for the polycrystalline sample can be compared with the nanocrystalline gold sample shown in Section 4.5.5. This comparison highlights that no specific surface feature can be observed in the nanocrystalline electrode within our submicron resolution, while for the polycrystalline sample we can clearly distinguish areas whose SH-V profiles change cycle to cycle and areas that do not.

Given that the potential interval PR in Fig. 4.5D corresponds to the same potential interval considered in Fig. 4.4, we now can compare the correlation coefficient analysis in the PR with the analysis based on Eq. 4.3. The correlation coefficient analysis reveals that changes in the SH-V shape from one cycle to the next (regions with higher value of |ΔCorrCoeff|) occur in the same spatial regions where the analysis based on Eq. 4.3 (the result of which are shown in Fig. 4.4) yields negative quadratic coefficients. There is indeed a remarkable agreement between the percentage of total surface displaying changes of |ΔCorrCoeff| > 0.1 in the PR interval (39.7 %) and the percentage of total surface where Q < 0 (40.3 %) obtained from the analysis of Fig. 4.4. At the same time, the areas with the largest Q_3/L_3 - Q_2/L_2 values shown in Fig. 4.4E, indicating the largest changes cycle to cycle, also match well with the areas displaying the largest |ΔCorrCoeff| values in Fig. 4.5D. It is therefore reasonable to assume that the correlation coefficient analysis can be used to further investigate the areas where Q < 0, a prospect that the analysis with Eq. 4.3 does not offer. Areas displaying a higher value of |ΔCorrCoeff| (i.e. |ΔCorrCoeff| > 0.1) imply a change in the surface structure/chemistry during the electrochemical cycling, which alters the SH-V behavior from one cycle to the next. On the other hand, the areas with lower values of |ΔCorrCoeff| indicate that the SH-V behavior in a given potential interval is similar after one cycle. We do not expect electrochemical reactions to happen in the potential interval of 0.1 – 0.4 V and therefore assume that the largest values of |ΔCorrCoeff| (PR3-PR2) in Fig. 4.5D originate from surface restructuring during one entire potential cycle, likely roughening the surface by oxidation and reduction. This further supports the hypothesis formulated within the SH-V analysis of Fig. 4.4E, where the regions with $Q_2 < 0$ correspond to the areas with the largest surface changes during electrochemical cycling.

Note also that the observation of similar areas of considerable correlation differences (|ΔCorrCoeff| > 0.05) in the OG potential interval (Fig. 4.5E) indicates that the SH-V behavior during oxide growth does experience changes from one cycle to the next. We speculate that the SH-V behavior during oxide growth is also affected by surface topographical changes due to potential-induced surface reconstruction. These surface topographical changes may already happen before the OG region and are possibly a consequence of surface reconstruction [256, 257, 263] or oxidation of metastable surface states [264], processes that are very likely strongly influenced by anion adsorption. These processes could also explain areas with elevated |ΔCorrCoeff| in the OG region. Because anion desorption precedes oxide growth (as detailed in Section 4.3.1), we assume that a different local potential is required to initiate oxide growth in areas where anions behave different from the average (e.g. in Q < 0 areas). Such a behavior would also affect the SH-V curve and modify the distribution of |ΔCorrCoeff| values in the OG

[3] While the |ΔCorrCoeff| can be calculated for each of these regions, comparing their magnitudes is challenging as the possible contributions to the SH signal are likely potential dependent.

region. On the other hand, the rest of the areas show an identical SH-V behavior in the oxide growth region from one cycle to the next.

The difference of the correlation coefficient analysis over the analysis based on Eq. 4.3 is that, as far as the electrochemical behavior of the sample of interest is known, the correlation coefficient analysis can be performed in any potential interval of interest and is not limited to the PR.

4.3.4 PSS/PPP polarization combination ratio

Here we present a way of identifying regions more prone to surface reconstruction during potential cycling, which possibly have a higher catalytic activity, that does not require a lengthy image analysis but relies purely on a measurement. The SH intensity from a given polarization combination is composed of multiple contributions, that unfortunately we cannot separate in our SH data. However, different facets on the surface can have a different response as a function of the incoming beam polarization. Fig. 4.6 shows two different polarization combinations: PPP, PSS, and their ratio for the polycrystalline gold electrode. It can be observed that these two polarization combinations appear to be complementary: the regions of highest SH intensity in the PPP polarization combination are also the regions of lowest SH intensity in the PSS polarization combination, and vice-versa. Furthermore, the areas with the strongest SH intensity signal in PPP polarization combination in Fig. 4.6A bear some spatial similarities to the blue areas in Fig. 4.5D with the lowest correlation difference between CV cycle 2 and 3, while the areas with the strongest SH intensity signal in PSS polarization in Fig. 4.6B display some spatial similarities with the areas of highest correlation difference in Fig. 4.5D. Division of PSS by PPP polarization shown in Fig. 4.5C presents the relative strength of the SH signal in PSS polarization in comparison with PPP polarization and visually intensifies various features at the surface. The cropping of Fig. 4.5C is a consequence of unintentionally shifted illumination when switching the polarization combinations. Here, we see that this ratio displays almost identical features as the PSS polarization combination in Fig. 4.5B. Indeed, the regions with a higher PSS contribution (given as PSS/PPP > 0.1) visually correlate with the regions of higher difference in correlation coefficient observed in Fig. 4.5D. We estimate that 39.4% of the surface has a PSS/PPP ratio above or equal to 0.1. Comparing this number to the ones found above for the pixels with negative quadratic coefficient (40.3%) and the pixels showing the largest correlation difference above 2 or below -2 (40%), we conclude that all three methods to visualize the data identify similar surface areas. No specific features can be seen on the nanocrystalline sample presented in the Section 4.5.6 (Fig. 4.11) in both polarization combinations.

We note that the SH image of the PSS polarization combination in Fig. 4.6B is not directly superimposable with the results of the model described by equations 4.3 and 4.5 and the correlation analysis (obtained on images recorded in the PPP polarization combination). Some of the most apparent mismatches are the sharp diagonal thin lines in the PSS polarization combination, which we presume are due to surface scratches. The SH intensity of PPP and PSS polarization combinations are dependent on amplitudes of the isotropic, onefold, twofold and threefold symmetry contributions [239]. The difference is, these amplitudes are different for these polarization combinations. Therefore, the SH intensity is dependent on the azimuthal angle of laser illumination [126, 236]. On top of that the SH intensity is dependent on many factors, such as i) the given polycrystalline gold surface facet and its orientation in a given pixel [127]; ii) occurrence of surface reconstruction [238, 239]; iii) anion adsorption and desorption [127]; iv) LSP excitation [267], etc. Considering all these factors that contribute differently to the SH-V shape and absolute SH signal intensity, it is interesting to see that the images in the PSS polarization combination show a fair amount of similarities to the results of the

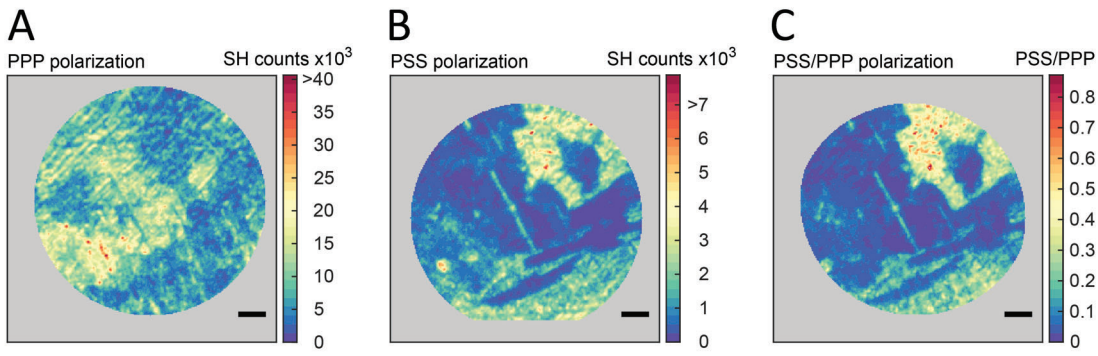

Figure 4.6 – Second harmonic images of polycrystalline gold in different polarization combinations. All three images represent the mean image averaged from the video frames corresponding to PR2 potential interval. (A), (B), and (C) correspond to PPP, PSS, and PSS divided by PPP polarization combinations for the polycrystalline gold electrode, respectively. Scale bar is 10 µm.

parabolic model and the correlation analysis. While the model based on Eq. 4.3 and the correlation analysis were comparing two different CV cycles in PPP polarization combination, the SH image of PSS polarization shown in Fig. 4.6B is from a single CV cycle. This suggests that the SH PSS polarization combination on this particular electrode/electrolyte system is inherently more sensitive to the areas with irreversible surface chemistry in CV cycling on Au electrodes than the PPP polarization combination. Further work would be necessary to establish if there is a correlation between a high contrast mechanism in a specific polarization combination and areas prone to potential-induced reconstruction also for other metal/electrolyte systems. Such a general correlation could then be used as a basis for large-scale material screening with the goal to locate parts of the surface that are more prone to potential-induced surface reconstruction. This is of interest for studying corrosion and potentially for studying catalytic activity, as rough and dynamic surfaces are often catalytically active.

4.4 Summary and Conclusions

In summary, optical second harmonic (SH) imaging in a wide-field configuration combined with in-situ cyclic voltammetry is used here to investigate surface reconstruction during potential cycling of gold nanocrystalline and polycrystalline electrodes. Our findings show that, while the average SH intensity as a function of applied bias follows a similar trend as reported in prior studies, it varies drastically on the (sub)micron level for polycrystalline electrodes: Spatial averaging obscures qualitative differences in the SH response. In contrast, images of nanocrystalline electrodes show no such heterogeneity. Fitting the SH signal as a function of potential in the polarization region (0 – 0.4 V vs. RHE), where no electrochemical reactions occur and no specific ion adsorption is expected, reveals two distinct dependences on the applied potential. On the majority of the surface (~ 60%), the SH intensity is found to quadratically increase with increasing bias ($Q > 0$). This is in line with results of previous SH spectroscopy studies, where only the average SH response of the surface was probed. On the rest of the surface (~ 40%), the SH intensity quadratically decreases with increasing bias ($Q < 0$), which has not been reported before. In areas where $Q > 0$, we can quantify on a pixel-wise level the extent of the contributions from the second- and third-order susceptibilities. This analysis reveals that regions with higher second-order susceptibility, indicating a higher surface plasmon contribution, tend to be located at the boundaries between areas with ($Q > 0$) and ($Q < 0$). Furthermore, these boundary

pixels display also the highest changes in the ratio of third-order susceptibility over second-order susceptibility between successive potential cycles, showing that surface reconstruction must occur here during the potential cycling. On the other hand, areas with higher third-order susceptibility contribution appear to display minimal changes from one cycle to the next, and here, the SH signal as a function of applied bias can be explained mainly by reversible changes in surface charging. For the areas where the SH intensity quadratically decreases with increasing bias, we attribute this inverse behavior to anion adsorption at potentials below the average potential of zero charge, which is possibly facilitated by a rough and non-equilibrated surface structure, and therefore particularly susceptible to surface reconstruction during potential cycling. Interestingly, no such areas are identified on the nanocrystalline sample within our sub-micron resolution.

This hypothesis is corroborated by a correlation coefficient analysis. The correlation coefficient analysis reveals that the strongest changes in the SH-V shape from one cycle to the next (regions with higher value of |ΔCorrCoeff|) occur in the same spatial regions where the fit of the SH dependence as a function of potential yields Q < 0. We find that the percentage of the total surface area that is undergoing substantial changes cycle to cycle, where |ΔCorrCoeff| > 0.1 in the PR interval, is in good agreement with the percentage of total surface where Q < 0 (39.7% and 40.3%, respectively). At the same time, the areas with the largest Q_3/L_3 - Q_2/L_2 values, indicating the largest changes cycle to cycle, also match well with the areas displaying the largest |ΔCorrCoeff| values. We therefore assign these largest values of |ΔCorrCoeff| to originate from structural modifications occurring over one entire electrochemical cycle, likely roughening the surface. A similar spatial distribution of the highest |ΔCorrCoeff| values is also obtained for the correlation coefficient analysis in a potential region where surface oxide is expected to grow, adding further evidence that Q < 0 regions are particularly prone to surface reconstruction during potential cycling. Comparison to the nanocrystalline sample highlights that no specific spatial area of increased surface reconstruction can be observed in the nanocrystalline electrode within our submicron resolution. This finding suggests that the extent of areas with a rough and non-equilibrated surface is dependent on the grain size.

Lastly, the areas with the largest SH intensity in the PSS polarization combination match reasonably well with the above identified areas that are particularly prone to surface reconstruction during potential cycling. Following this observation, we will further investigate SH wide-field imaging in various polarization combinations on other metal/electrolyte systems. Establishing a correlation between a high contrast mechanism in a specific polarization combination and areas prone to potential-induced surface reconstruction would be a valuable tool for the investigation of certain aspects of surface chemistry, like corrosion, or potentially catalytic activity on a polycrystalline sample without any *a priori* knowledge of its surface structure.

This study demonstrates the applicability of a new imaging modality to the operando characterization of electrocatalysts on hundreds of µm length scales. Due to its speed and sub-micron resolution, this technique could be utilized to correlate various parameters of the surface (for example it could be potentially used to map out the local V_{PZC}) and chemical reactivity in an application-oriented context.

4.5 Appendix

4.5.1 The effect of surface contamination

The purity of the chemical compounds used in the experiments was crosschecked in separate measurements where we intentionally introduced contaminants, such as chloride and sulfate ions, on the gold electrode. We first prove that our measurement conditions are stable by showing a series of 25 CV cycles of our polycrystalline Au electrode in 0.5 M (NaH_2PO_4) in Fig. 4.7A. The CVs are virtually identical and no fluctuations from cycle to cycle are apparent. The peak at 0.5 V in the reverse scan (0.4 V for the nanocrystalline electrode in Fig. 4.2C) is discussed in the next section 4.5.2.

Whether a possible chloride contamination is relevant for our measurements was investigated in a second experiment. For this experiment, the polycrystalline Au electrode was again examined by cyclic voltammetry in 0.5 M NaH_2PO_4, but this time not with a reversible hydrogen electrode (RHE) as reference electrode, but with a Ag/AgCl micro reference electrode. From the Ag/AgCl micro reference electrode, chloride anions slowly contaminated the electrolyte, leading to an increase in chloride concentration with time, see Fig. 4.7B. CVs taken every 3 min reveal the influence of the increasing chloride ion concentration on the CV. In the forward scan, an additional peak around 1.4 V vs. RHE grows with time. Additionally, the surface oxidation peak around 1.5 V vs. RHE grows and narrows. In the reverse scan, the oxide reduction peak around 1.15 V vs. RHE shrinks, but an additional reduction current from 1.15 to ~0.4 V vs. RHE arises. The CVs of our electrodes during the optical measurements are stable and do not change with time, see Fig. 4.7A. Furthermore, we neither see the additional peak in the forward scan at 1.4 V vs. RHE, not the additional reduction current from 1.15 to ~0.4 V vs. RHE in the reverse scan. We therefore conclude that our electrolyte is not contaminated with chloride ions.

Whether a possible sulfate contamination is relevant for our measurements was investigated by cyclic voltammetry of the polycrystalline Au electrode in 0.5 M Na_2SO_4 + 0.001 M H_2SO_4 (the objective of our microscope cannot withstand concentrated mineral acids). The CV can be seen in Fig. 4.7C. Compared to the phosphate buffer solution, the surface oxidation peak is strongly anodically shifted to ~1.95 V vs. RHE. The oxide reduction peak remains at the same position, 1.1 V vs. RHE. However, an additional cathodic peak is apparent in the reverse scan around 0.85 V vs. RHE. From the absence of this second cathodic peak in the CVs that we show in Fig. 4.7A and the positions of the surface oxidation peaks in phosphate buffer and sulfate solution, we conclude that our 0.5 M NaH_2PO_4 electrolyte is not contaminated with sulfate ions.

4.5.2 CV reduction peak at 0.4 V for nanocrystalline electrode

The CV of the nanocrystalline electrode in Fig. 4.2C shows the presence of a peak in the reverse scan at 0.4 V. Organic impurities are neither likely after electrode treatment in the plasma cleaner, nor obvious from the CV. The most probable candidate for an inorganic impurity is platinum from the counter electrode, although throughout all the experiments we made sure not to reach potentials where platinum could dissolve. However, we believe that the presence of platinum does not directly influence the SHG measurements, but only the CV, based on the geometry of our experiment. The CV records the signal from the whole surface, while in our experiment the SH signal was only collected in the center of our round electrode. The platinum counter electrode had a circular shape with a diameter of ~22 mm, while the gold circular sample centered below had a diameter ~17 mm. We imaged the center of the gold electrode with a ~100 μm field of view. The imaging field of view was, therefore, 10 mm away from

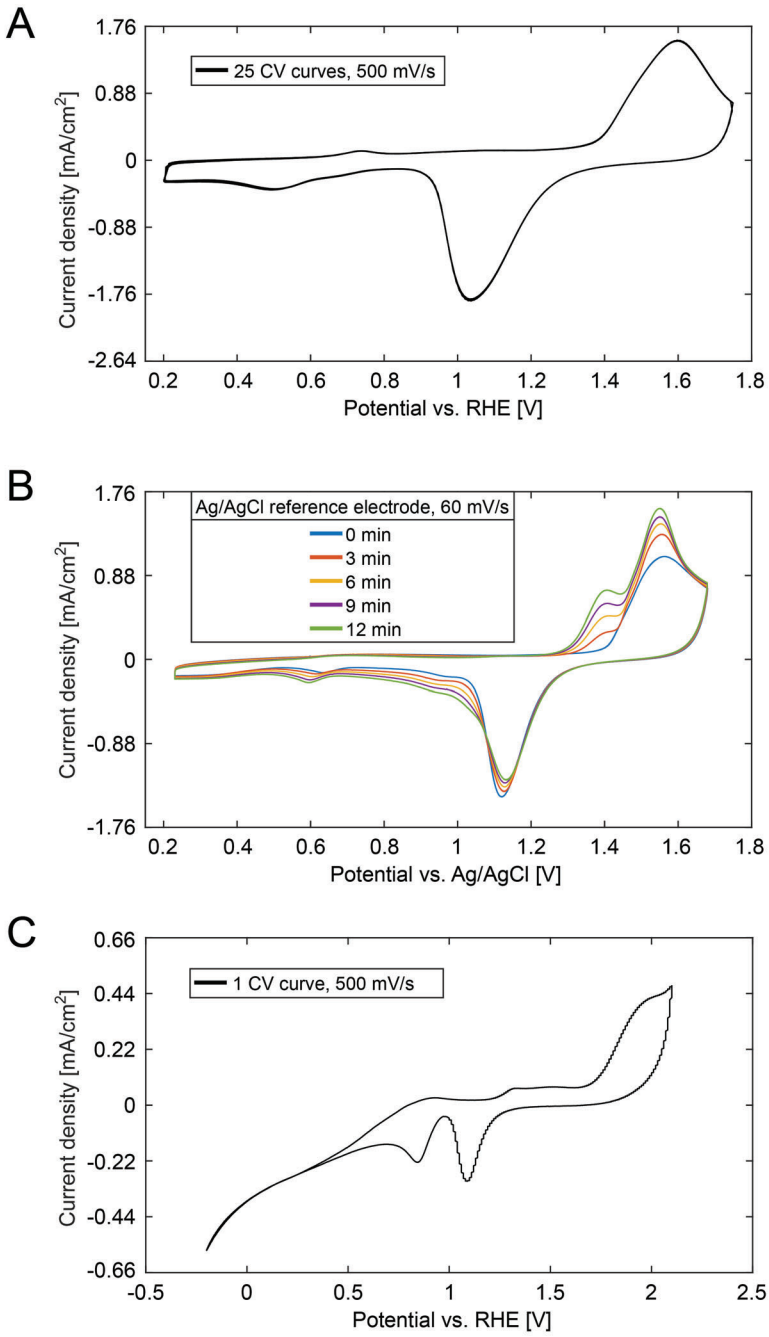

Figure 4.7 – The effect of surface contamination on the CV. (A) 25 cyclic voltammograms (CVs) of the polycrystalline Au electrode in 0.5 M NaH_2PO_4. (B) CVs taken every 3 min reveal the influence of increasing chloride ion concentration on the CV. (C) Au electrode in 0.5 M Na_2SO_4 + 0.001 M H_2SO_4.

the counter electrode. The presence of small platinum residuals is likely to deposit at the edges of the electrodes, therefore not influencing the center of the electrode where the actual SH signal is collected. Additionally, we have evidence that this possible contaminant does not influence the SH data: Indeed, we do not observe any abrupt change in the trend of the SH-V data (Fig. 4.2C) around 0.4 V. Hence, the

presence of inorganic contaminants from the counter electrode can be excluded on the areas where the SH-V signal is collected.

Additionally, we do not observe any abrupt change in the trend of the SH-V data around 0.4 V. For this reason, we do not believe the SH signal is impacted by the presence of inorganic contaminants from the counter electrode.

4.5.3 SH imaging of nanocrystalline gold

Fig. 4.8A, B, and C show the SH images of the nanocrystalline gold electrode recorded during cyclic voltammetry at 60 mV/s in a phosphate buffer solution (pH = 2.8) at three different potentials during the forward scan: 0.2 V, 1.2 V and 1.51 V. The SH images were recorded in the PPP polarization combination. All three images, Fig. 4.8A, B, and C, lack spatial heterogeneity in the SH signal due to the nanocrystalline nature of the sample. The color scale is identical to the color scale of Fig. 4.3A in the main text, offering a direct comparison of the nanocrystalline vs. the polycrystalline gold electrode. Different spots on the surface show the same SH behavior as a function of applied potential. This is demonstrated in Fig. 4.8D, where the SH intensity dependence on the applied potential is shown for three pixels, P1 (blue lines), P2 (red lines), and P3 (green lines) for three consecutive CV cycles, named CV1, CV2 and CV3. In the PR, the SH intensity increases with applied potential for all pixels. In the OG region, all pixels exhibit again qualitatively the same SH behavior, i.e. the SH intensity decreases with increasing potential.

4.5.4 SH dependence on the voltage for nanocrystalline gold

Fig. 4.9A, B, C, and D were calculated from the potential interval of 0 – 0.4 V in the forward scan of the second CV cycle using Eq. 4.3. The quadratic and linear coefficients have been labeled as Q_2 and L_2. Fig. 4.9A and B show respective maps of the quadratic and linear fit coefficients. These two maps look qualitatively similar, but their scale differs. Fig. 4.9C displays again the map of quadratic coefficients, however, this time with a color coding separating the $Q_2 > 0$ and $Q_2 \leq 0$. The regions where $Q_2 \leq 0$ represent 8.8% of the total surface, while the regions where $Q_2 > 0$ account for 91.2% of the total surface. The pixels with negative Q_2 values are scattered across the image with increasing occurrence towards the edges of the image. This spatial distribution matches with the spatial distribution of error bars, that also increase towards the edges of Gaussian illumination. The error bars for nanocrystalline gold are much more pronounced in comparison with the polycrystalline gold because of the nature of the sample. A single camera pixel is imaging ~ 40 gold nanocrystals that all contribute to the final observed SH signal. Only a small number of pixels where Q_2 is close to zero (~ 5.84% of the total surface where $|Q_2| \leq 1000$) is found and an even smaller number of pixels where Q_2 and L_2 are both close to zero (~ 0.04% of the total surface when $|Q_2|$ and $|L_2| \leq 1000$).

4.5.5 Correlation coefficient analysis of nanocrystalline gold

In order to have a reference for the correlation coefficient analysis, we compare the results obtained on the polycrystalline sample to the results obtained on the nanocrystalline gold sample. Fig. 4.10A, B display the correlation map difference analogous to Fig. 4.5D, E and show a rather homogeneous surface map with no specific features. The larger values of |ΔCorrCoeff| towards the edges of the image in Fig. 4.10A, B are solely due to the increasing error bar towards the edges of the Gaussian illumination

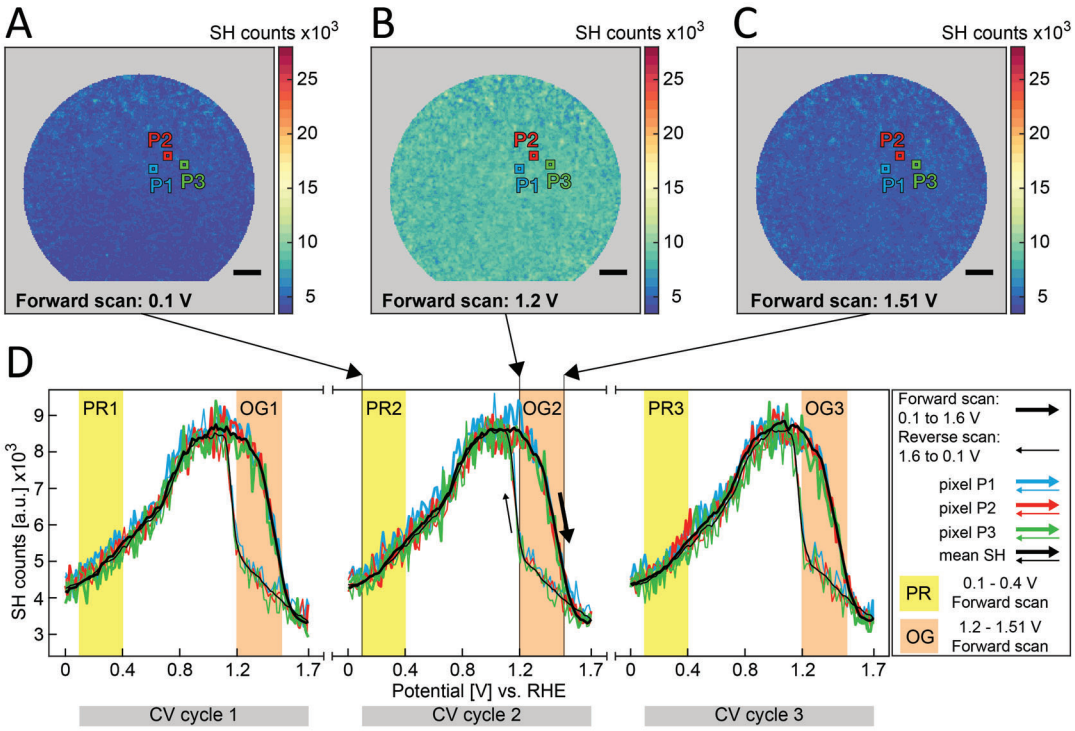

Figure 4.8 – Second harmonic imaging of the nanocrystalline gold electrode as a function of applied voltage. (A), (B), (C) SH images at 0.1 V, 1.2 V, and 1.51 V vs. RHE during the forward 60 mV/s scan. The SH images are frames extracted from SH video recorded with 0.25 s acquisition time per frame. Points P1, P2, and P3 mark the chosen single pixel locations. The color scale is identical to Fig. 4.2A. (D) SH intensity as a function of the potential applied to the gold electrode in three continuous CV cycles. The blue curve corresponds to pixel P1; the red curve corresponds to pixel P2; and the green curve corresponds to pixel P3. The black line corresponds to the average SH signal of the whole image. The thick lines correspond to the forward scan, while the thin lines correspond to the reverse scan. The polarization region (PR, 0.1-0.4 V) is marked in yellow for all three cycles while the oxide growth regions (OG, 1.2-1.51 V) is marked in orange. The SH data was obtained in PPP polarization combination. The potential values are given with respect to the reversible hydrogen electrode. Scale bar is 10 µm.

beam. Note that the same scale is used for Fig. 4.5D and Fig. 4.10A, as well as for Fig. 4.5E and Fig. 4.10B. No specific surface feature can be observed in the nanocrystalline electrode within our sub-micron resolution. It is reasonable to expect such a homogeneous distribution, because the grain size of the nanocrystalline sample is much smaller than the pixel area, with ~ 40 grains/pixel. On the other hand, for the polycrystalline sample shown in the main text we can clearly distinguish areas whose SH-V profiles change cycle to cycle from areas which do not experience any change.

4.5.6 PSS and PPP polarization combination for the nanocrystalline gold

Fig. 4.6 in the main text shows the PPP and PSS polarization combination SH images for polycrystalline gold in PR2. Analogically, Fig. 4.11 shows the results for the nanocrystalline gold. Division of PSS by PPP polarization shown in Fig. 4.11C presents the relative strength of the SH signal in PSS polarization in comparison with PPP polarization. The cropping of Fig. 4.11C is a consequence of unintentionally shifted illumination when switching the polarization combinations. Here, we can see that Fig. 4.11C is

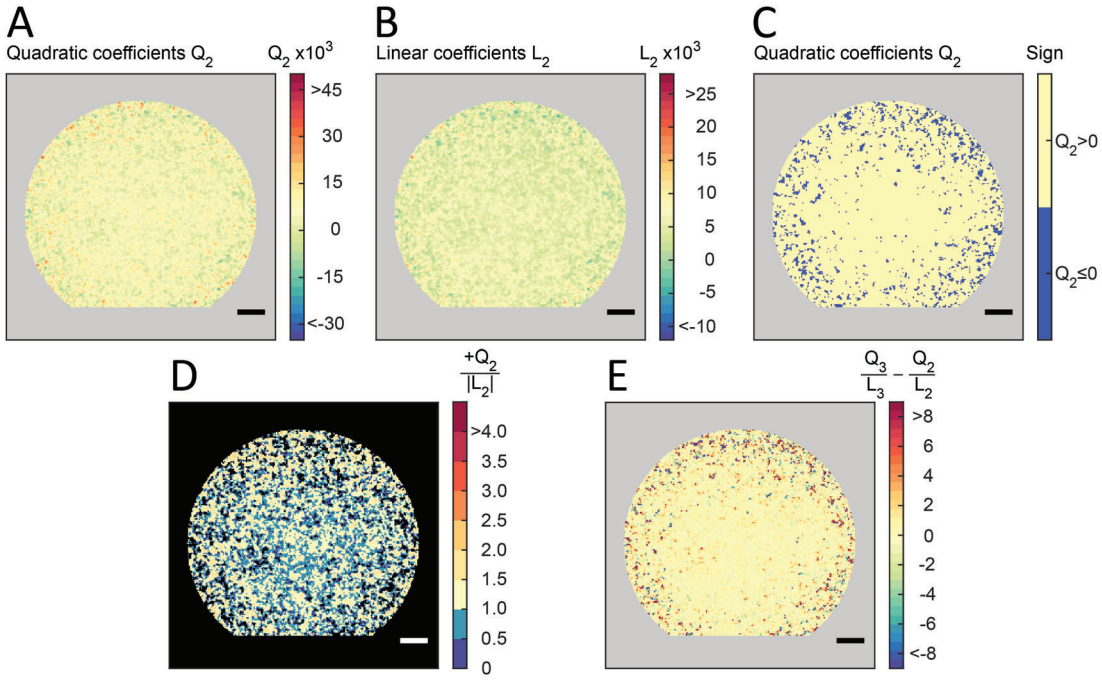

Figure 4.9 – Fitting of the SH signal in the PR as a function of applied potential for nanocrystalline gold electrode. Second harmonic PPP polarization signal corresponding to the potential interval PR2 (see Fig. 4.8) is fitted by a polynomial of 2nd degree with point of zero charge offset common to all pixels. This yields a map of fitted quadratic coefficients Q_2 in (A) and a map of fitted linear coefficients L_2 in (B). (C) Map of quadratic coefficients Q_2 with a binary color-code of yellow ($Q_2 > 0$) and blue ($Q_2 \leq 0$). (D) Division of Q_2 map over the absolute value of L_2 map. Pixels where $Q_2 \leq 0$ are not considered here. (E) Difference of quadratic over linear coefficients ratios obtained from the potential interval PR3 vs. PR2 (see Fig. 4.8). Scale bar is 10 µm.

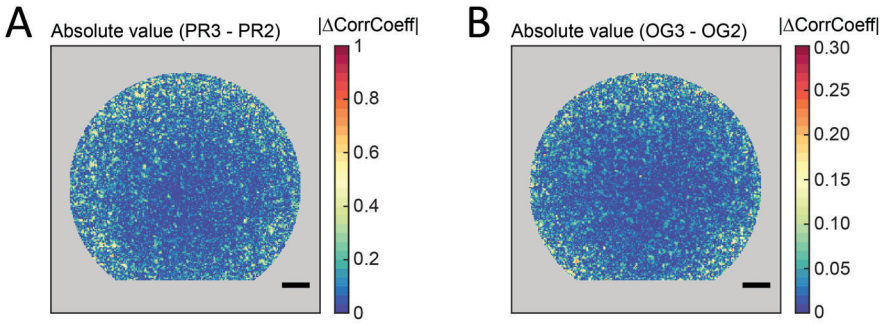

Figure 4.10 – Correlation coefficient analysis of nanocrystalline gold. (A) Absolute value of the difference between the correlation coefficient map calculated for the PR2 and PR3. (B) Absolute value of the difference between the correlation coefficient map calculated for the OG2 and OG3. SH data was recorded in the PPP polarization combination. Scale bar is 10 µm.

not displaying any significant spatial features. This is in accordance with the previous nanocrystalline results presented above.

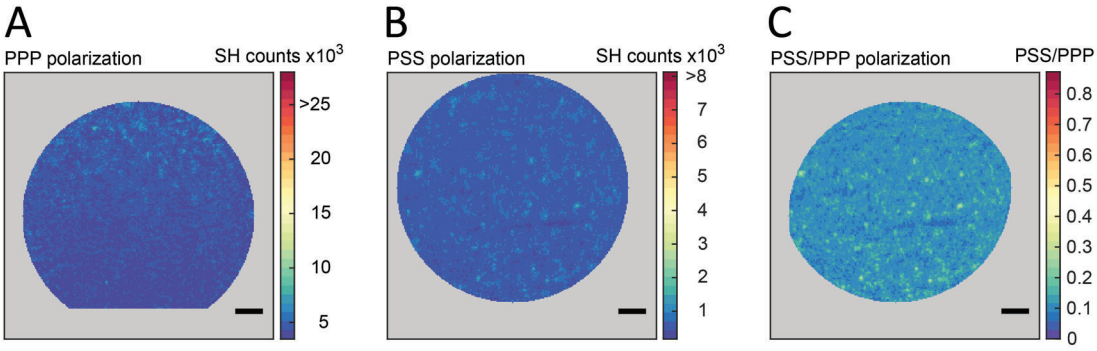

Figure 4.11 – SH images of PPP and PSS polarization combinations for the nanocrystalline gold. All three images represent the mean image averaged from the video frames corresponding to PR2 potential interval. (A), (B), and (C) correspond to PPP, PSS, and PSS divided by PPP polarization combinations for the nanocrystalline gold electrode, respectively. Scale bar is 10 µm.

4.5.7 Third-order nonlinear susceptibility of gold

Miller's rule can be employed to predict the second-order nonlinear optical properties of a broad range of materials. Miller's rule can be also generalized for the third-order nonlinear optical interactions in the form of:

$$\boldsymbol{\chi}^{(3)}(\omega_2,\omega_1,\omega_1,\omega_1) = B\boldsymbol{\chi}^{(1)}(\omega_2)\boldsymbol{\chi}^{(1)}(\omega_1)\boldsymbol{\chi}^{(1)}(\omega_1)\boldsymbol{\chi}^{(1)}(\omega_1)\,, \tag{4.7}$$

where $\omega_2 = 3\omega_1$, and where B is a proportionality constant that is assumed to be frequency independent and nearly the same for all materials [66]. In our case, the fundamental wavelength ω of our laser is 1030 nm. We can use Miller's rule to predict the ratio of $\mathrm{Re}(\chi^{(3)})$ and $\mathrm{Im}(\chi^{(3)})$ values, which is then given as:

$$\frac{\mathrm{Re}\left(\chi^{(3)}\right)}{\mathrm{Im}\left(\chi^{(3)}\right)} \sim \frac{\left(\varepsilon_2'-1\right)\left(\varepsilon_1'-1\right)\left(\varepsilon_1'-1\right)\left(\varepsilon_1'-1\right)}{\varepsilon"_2\varepsilon"_1\varepsilon"_1\varepsilon"_1}\,, \tag{4.8}$$

where ε_2' and $\varepsilon"_2$ correspond to the dielectric permittivity of gold for the wavelength ω_2. ε_1' and $\varepsilon"_1$ correspond to the dielectric permittivity of gold for the wavelength ω_1.

Calculating this ratio for $\omega_1 = 600$ nm and $\omega_1 = 630$ nm yields twice the value as reported experimentally in [265], confirming the validity of Miller's rule to predict the magnitude of the third-order susceptibility. The experimental value of $\frac{\mathrm{Re}(\chi^{(3)})}{\mathrm{Im}(\chi^{(3)})}$ for 600 nm is ~ 12 and for 630 nm is ~ 18. Extrapolating the calculation for $\omega_1 = 1030$ nm yields ratio of $\mathrm{Re}(\chi^{(3)})$ and $\mathrm{Im}(\chi^{(3)})$ ~ 1180. Therefore, we expect that $\mathrm{Im}(\chi^{(3)})$ is negligible compared to $\mathrm{Re}(\chi^{(3)})$.

4.5.8 Determining the error bars

SH PPP polarization combination error bars. SH-V signal of every pixel was smoothed (across the applied potential) by a moving average method in MATLAB with a span of 10 neighboring data points. We obtained the absolute difference of smoothed SH-V signal and original SH-V signal per pixel, from which we calculated the standard deviation (STD). In this manner we calculated the STD for every pixel getting a map of SH error bars. The error bars are smallest in the center of Gaussian illumination, but increase towards the perimeter of the SH image due to the flat-fielding. Therefore, we estimated the error bars from three areas: A1 – center area of the image, A2 – middle-ring area of the image, and A3 – perimeter area of the image. For these areas we obtained the average SH intensity as well as average SH error bar values. Their division yields an average SH error bar for: A1 as 1.3%, A2 as 1.6%, and A3 as 2.6%. In other words, SH error bars for pixels in the center of the image are ~ 1.3% of the average SH signal in the center of the image. The SH error bars for the pixels at the perimeter of the image are ~ 2.6% of the average SH signal at the perimeter of the image.

Correlation coefficient error bars. This section concerns SH-V data in the PPP polarization combination. Correlation Coefficient maps of |ΔCorrCoeff| (PR3-PR2) (Fig. 4.5D main text) and |ΔCorrCoeff| (OG3-OG2) (Fig. 4.5E main text) were obtained as discussed in the main text (Results & Discussions: Correlation coefficient analysis). For determining the correlation coefficient error bars, the original SH-V data was modified by adding/subtracting a random noise (within limits of SH error bar calculated for a given pixel). This was done for all the SH images corresponding to different applied potentials. With this noise-modified SH-V signal we calculated the $|\Delta\text{CorrCoeff}|_{NOISE}$ (PR3-PR2) and $|\Delta\text{CorrCoeff}|_{NOISE}$ (OG3-OG2). We compared the difference of |ΔCorrCoeff| with and without added noise for both (PR3-PR2) and (OG3-OG2) as follows;

$$\begin{aligned} \Delta_{PR} &= |\Delta\text{CorrCoeff}|\,(\text{PR3}-\text{PR2}) \;-\; |\Delta\text{CorrCoeff}|_{NOISE}\,(\text{PR3}-\text{PR2})\,, \\ \Delta_{OG} &= |\Delta\text{CorrCoeff}|\,(\text{OG3}-\text{OG2}) \;-\; |\Delta\text{CorrCoeff}|_{NOISE}\,(\text{OG3}-\text{OG2})\,. \end{aligned} \tag{4.9}$$

Final correlation coefficient error bar for the PR was obtained as an average value of ΔPR from the center area of the image, where the |ΔCorrCoeff| (PR3-PR2) display small values. The value of the final correlation coefficient error bar for the PR is 0.04.

Final correlation coefficient error bar for the OG was obtained as an average value of ΔOG from the center area of the image, where the |ΔCorrCoeff| (OG3-OG2) display small values. The value of the final correlation coefficient error bar for the OG region is 0.02.

In the main text, we chose a threshold value for |ΔCorrCoeff| of at least twice the correlation coefficient error bar estimated here, ensuring that |ΔCorrCoeff| values above the threshold represent meaningful changes to the surface from one cycle to the next.

5 Imaging the Heterogeneity of the Oxygen Evolution Reaction on Gold Electrodes Operando: Activity is Highly Local

Understanding the mechanism of the oxygen evolution reaction (OER), the oxidative half of electrolytic water splitting, has proven challenging. Perhaps the largest hurdle has been gaining experimental insight into the active site of the electrocatalyst used to facilitate this chemistry. Decades of study have clarified that a range of transition metal oxides have particularly high catalytic activity for the OER. Unfortunately, for virtually all of these materials, metal oxidation and the OER occur at similar potentials. As a result catalyst surface topography and electronic structure is expected to continuously evolve under reactive conditions. Gaining experimental insight into the OER mechanism on such materials thus requires a tool that allows spatially-resolved characterization of the OER activity. In this study, we overcome this formidable experimental challenge using second harmonic microscopy and electrochemical methods to characterize the spatial heterogeneity of the OER activity on polycrystalline Au working electrodes. At moderately anodic potentials we find that the OER activity of the electrode is dominated by < 1% of the surface area and that there are two types of active sites. The first type is observed at potentials positive of the OER onset and is stable under potential cycling (and thus presumably extends multiple layers into the bulk gold electrode). The second type occurs at potentials negative of the OER onset and is removed by potential cycling (suggesting it involves a structural motif only 1-2 Au layers deep). This type of active site is most easily understood as the catalytically active species (hydrous oxide) in the so-called incipient hydrous oxide/adatom mediator model of electrocatalysis. We demonstrate here that combining the ability to characterize the spatial heterogeneity of the OER activity with a systematic program of electrode surface structural modification offers the possibility of creating a new generation of OER electrocatalysts with unusually high activity.

This chapter is based on the author's journal article: G. Zwaschka[1], **I. Nahalka**[1], A. Marchioro, Y. Tong, S. Roke, and R. K. Campen. Imaging the Heterogeneity of the Oxygen Evolution Reaction on Gold Electrodes Operando: Activity is Highly Local, *ACS Catalysis*, **2020**, *10*, 6084–6093.

5.1 Introduction

It is increasingly clear that a global energy economy based on hydrocarbon combustion has adverse consequences for the climate, the earth surface environment and human health. An economy instead based on the combustion of H_2 would avoid virtually all of these consequences. Perhaps the best candidate to produce H_2 sustainably is (photo)electrochemical water splitting (where the large energy input required for the reaction comes from a renewable source). While finding catalysts that are active, stable and inexpensive for both halves of this redox reaction is challenging, the oxidation half of water splitting, the oxygen evolution reaction (OER), is currently rate limiting in most devices [245]. The relative sluggishness of the OER is a kinetic limitation: the high overpotential necessary to drive it is a result of a high activation barrier. In principle, choice of an appropriate electrocatalyst should be able to lower the overpotential. However, the rational design of an efficient OER catalyst is hampered by our incomplete understanding of the reaction mechanism. This lack of understanding is linked to the OER's complexity: it requires the transfer of 4 electrons and involves an unknown number of corresponding intermediates.

Past work, principally in gas phase heterogeneous catalysis, has shown that catalyst surface atomic structure can be often correlated with activity [167]: certain atomic-scale structural motifs outperform others by many orders of magnitude (e.g. steps vs. terraces). Quantifying such structure/reactivity correlations is powerful, as it makes it possible to infer the identity of catalytically active sites [268]. It is perhaps not surprising that the identity of the active site depends on the reaction, catalyst, and catalyst surface structure, which are all tied to the mechanism of the reaction of interest: predicting the active site of a particular catalyst for a particular reaction has therefore proven to be extremely challenging.

Most studies that have shown clear correlations between surface atomic structure and catalytic activity, whether in gas phase or electrocatalysis, have done so on single crystals [269–271]. Because surface structure and bonding can be well characterized on such substrates, they are useful systems to demonstrate differences in activity of terraces and steps for different crystal faces (e.g. (111) vs. (100) terraces and/or steps). Such comparisons can be done indirectly by comparing the activity of stepped and unstepped surfaces in an (electro)catalytic experiment [269–271], or directly by operando imaging of the activity of steps and adjacent terraces [18]. While the reactivity of single crystals is not generally of practical interest, some more complex catalysts, e.g. shape-selected supported nanoparticle systems, have reactivities that can be rationalized as a linear combination of the reactivity of the crystal faces of which their surface is composed [272].

Unfortunately, virtually all candidates for efficient electrocatalytic materials have a complexity that cannot be directly understood as a linear combination of features apparent in idealized model systems: e.g. for the great majority of catalysts relevant in industrial contexts, both surface structure and catalytic activity have been shown to be heterogeneous on length scales from nm to µm [13, 14]. This structural heterogeneity is thought to influence reactivity in at least four ways: i) grain boundaries (or other microscopic defects) stabilize reactive atomic defects or high step densities that can not exist on extended surfaces [221]; ii) differences in local conductivity [220]; iii) heterogeneity in transport (e.g. local turbulent flow or nonuniform diffusion) and iv) a resulting spatial heterogeneity in the extent to which the catalyst restructures under reactive conditions [14]. It therefore seems clear that optimizing catalyst performance requires operando imaging of reactivity on the nm-µm spatial scales of structural heterogeneity. In this study we meet this challenge by imaging the OER activity and structural heterogeneity of polycrystalline Au electrodes on the 100 nm - 100 µm length-scales of

particular relevance for this material.

Understanding the OER on noble metals in general, and Au in particular, is important both for possible applications and as a useful model system in OER electrocatalysis. Despite decades of study, neither for the OER, nor for the electrooxidation of Au (which begins at potentials cathodic of and continues through potentials relevant to the OER) does a universally accepted picture exist. It is generally accepted that at sufficiently low potentials the Au surface is covered with anions [258, 259] and that, as potential is scanned increasingly positively, the first step of surface oxidation is the reversible replacement of anions with either O or OH [245, 256–259]. While less work exists on the subsequent stages of oxidation, increasing the potential is thought to lead, after completion of the oxygen species monolayer, to site exchange of the oxygen-containing species with gold atoms [273] and the formation of a quasi three-dimensional hydroxy-oxide film [258, 259, 274] in which the oxidation state of gold is +3 [275]. Koper and coworkers have found that further increasing the potential does not change oxidation state of gold, but rather dehydrates the film towards Au_2O_3 [245]. This dehydration cannot be complete, as pure gold oxide is not stable thermodynamically under oxygen evolution conditions [276]. Regardless of their detailed structure the first three layers of oxide are typically termed α-oxide and thought to be compact [277], while the following layers, termed β-oxide, have increased porosity/hydration as the number of layers increases [275,277]. For the actual OER, Koper and coworkers presented evidence from online electrochemical mass spectrometry that the first molecular oxygen, evolved as α-oxide (thought to be formed from the the first three layers of Au as one goes from bulk H_2O to bulk Au), is transformed to β-oxide at 2 V vs. the reversible hydrogen electrode (RHE) in 1 M $HClO_4$ [245]. Burke and coworkers also found 2 V vs. RHE to be the onset potential for the OER on Au in basic electrolyte [278]. At even more positive potentials, other mechanisms for the OER may be active where, for example, one oxygen atom of an O_2 molecule comes from the surface oxide and the other from the electrolyte [279–281]. While the onset potential of the OER appears to be relatively insensitive to electrolyte pH, much work has clarified that the OER activity is not: most OER catalysts are more active in alkaline media (IrO_x is a notable exception) [282].

This body of prior work clarifies that, if we are to understand the spatial heterogeneity of the OER on Au we also need to understand the spatial heterogeneity of Au surface oxidation: we require an imaging technique sensitive to both processes that can be employed operando. This requirement is nontrivial for at least two reasons: i) prior work has clarified that oxidation (and subsequent reduction) lifts atomic order even for initially well-defined Au single crystals [256], and ii) it implies that methods, which use electrons as probes (e.g. STM) or use the optical response of the metal to enhance a photon-based observable (e.g. SEIRAS or SERS) are not applicable.

Here we apply second harmonic microscopy (SHM) to image two different Au electrodes under reactive conditions as Au is oxidized and oxygen bubbles are produced. SHM is a nonlinear optical technique that is surface specific by its symmetry selection rules. This surface specificity allows for a precise alignment of the microscope focal plane with the Au/electrolyte interface to monitor the surface processes [154]. Using SHM on our Au electrodes under reactive conditions, we find the OER activity to be highly local and to occur in two distinct types of active areas. The first type is observed at potentials anodic (i.e. positive) of the OER onset and is stable with respect to surface atom reconstruction during repeated potential cycling. This localization of bubble formation, and its stability with respect to potential cycling, is consistent with a scenario in which bubble formation occurs at a defect that is oxidized and penetrates through the surface into the bulk (potential cycling Au electrodes leads to surface reconstruction of the first 2-3 Au layers [256]). The relative coverage of the surface with active areas of this type is comparable to the relative coverage of active sites found in gas phase heterogeneous

catalysis, but lower than in other heterogeneous (electro)catalysis studies that probe active sites by indirect means [1]. The current that is passed through this type of active site at potentials anodic of the OER onset can quantitatively explain the current we measured across the entire working electrode. The second type of active area is observed at potentials cathodic (i.e. negative) of the OER onset and is not stable with respect to surface atom reconstruction during potential cycling. This instability is most easily understood if it is the result of a highly-active surface motif. Such active sites have been invoked to explain unusually reactive noble metal surfaces in a variety of electrocatalytic reactions in the incipient hydrous oxide/adatom mediator model of electrocatalysis [255, 264, 283].

The wide-field imaging of two distinct types of OER active sites on spatially heterogeneous Au offers an essential tool for both fundamental and applied studies: e.g. the systematic dependence of active site distribution on electrolyte and the possibility of engineering novel Au samples that stabilize few atom layer thin, highly active sites for application in electrolyzers.

5.2 Materials and Methods

5.2.1 Chemicals and gold electrodes preparation

Sodium phosphate dibasic (Na_2HPO_4, ≥ 99.999% purity, Fluka Analytical), hydrogen peroxide (30% Reactolab SA), and sulfuric acid (95-97%, ISO, Merck) were used as received. All aqueous solutions were made with ultrapure water (H_2O, Milli-Q UF plus, Millipore, Inc., resistivity of 18.2 MΩ·cm).

The nanocrystalline gold sample was obtained by physical vapor deposition of 200 nm of gold on an optically flat glass substrate with a 30 Å layer of Cr for increased adhesion (Section 4.2.2, Fig. 4.1C). The nanocrystalline gold is homogeneous on the scale of the SH microscope resolution (~ 400 nm). The polycrystalline gold foils were purchased from Sigma-Aldrich (0.025 mm thickness, 99.99% trace metal basis) and annealed at 500 °C for 2 h (with linear heating and cooling ramps) to achieve a grain size distribution in the order of tens of micrometers (Section 4.2.2, Fig. 4.1D). The gold electrodes were sonicated in acetone, rinsed thoroughly with Milli-Q water followed by three times sonicating in fresh Milli-Q water. Subsequently, the gold electrodes were cleaned in an ozonator, rinsed thoroughly with Milli-Q water and then inserted into the PTFE cell where the exposed electrode surface was rinsed again repeatedly with Milli-Q water and then electrolyte.

5.2.2 Optical setup

The SH microscope has been described in detail for the transmission geometry in Chapter 2. Here, we use a one beam-reflection geometry configuration and parameters identical to that in Section 4.2.3.

[1] A similar relative coverage of active sites is expected for different reactions and surfaces because the activity of a particular site is related to the adsorption energy of the reaction intermediate in an exponential fashion: small differences in adsorption energy result in drastic differences in reactivity. The great majority of industrially-relevant catalytic materials are not flat, well-defined surfaces. They are rough over multiple length scales with a large range of adsorption sites and energies [246].

5.2.3 Electrochemistry

A homebuilt Teflon cell (Sections 2.3.2, and 4.2.4) was used for the SH microscopy experiments under cyclic voltammetry (CV) potential control. The cell was cleaned by immersion in Piranha solution overnight and repeated ultrasonication in Milli-Q water before the experiment. The electrodes were cleaned using the following procedure: copiously rinsed in acetone, copiously rinsed with Milli-Q water, exposed to ozone for five minutes in a UV ozonator, copiously rinsed with Milli-Q water, copiously rinsed with electrolyte and annealed electrochemically until the CV was stable (generally 20-30 cycles of cyclic voltammetry). After this procedure no organic contamination is apparent in the CV (see Figure S3 in the Supporting Information) The counter electrode was a Pt mesh and cleaned identically to the Teflon cell. A self-made reversible hydrogen electrode was employed as reference.

5.3 Results & Discussions

5.3.1 Active sites observed at potentials positive of the oxygen evolution reaction onset that are stable under the potential cycling

We initially examined a polycrystalline gold foil working electrode in 0.5 M Na_2HPO_4 (to ensure stable conditions throughout the optical measurements), pH = 9, and collected SH images while conducting linear sweep voltammetry from 1.8 to 2.2 V vs RHE. The range of the sweep was chosen to start well before oxygen evolution commences (at 2.0 V vs RHE) and to end at a potential where oxygen evolution is fast enough to produce macroscopic O_2 bubbles (as showcased in Fig. 5.1), whose growth rate allows real-time imaging of bubble growth and detachment (given the 0.25 s necessary to acquire an image at sufficient signal/noise). The potential sweep is displayed from 1.9 V in Fig. 5.2B-D in red. In the SH images, structural heterogeneity with a length scale of 10-50 μm is apparent if the potential is kept below the oxidation threshold (see Fig. 5.6 in Section 5.5.2 for results). Ex-situ scanning electron microscopy (SEM) images show structural heterogeneity on similar length scales (see Fig. 4.1D in Section 4.2.2), implying that we observe the metal's grain structure in our SH images.

At potentials above oxidation, the different domains can no longer be distinguished clearly and SHM images appear almost featureless, as shown for 1.8 V in Fig. 5.2A. However, as the potential is increased positively, bubbles appear, grow, and detach from the electrode. On the left of Fig. 5.2A, the entire field of view is displayed as a grayscale image with red dots indicating sites of O_2 bubble formation above 2.0 V vs RHE. Figure 5.2B contains the measured current density of the whole electrode for applied potentials between 1.9 - 2.2 V vs. RHE (red curve). We approximate the position of each bubble's formation site from the first frame in which a bubble is clearly discerned with a bubble radius on the order of few μm; further details can be found in Section 5.5.3. As is apparent from Fig. 5.2A, the vast majority of bubbles appear within a highly confined active area encircled in purple. As can be seen, in a single potential sweep at some spots only a single bubble appeared (such as "a-d"), while in others spots (such as "e" and "f"), multiple bubbles appeared either in direct succession or with a pause in between. With increasing potential, oxygen bubbles start to appear at more spots. The first bubble "a" is observed at 0.07 V higher in potential than the onset of the OER at 2 V. This offset can be rationalized by insufficient current densities, close to the onset potential of O_2 formation, to locally supersaturate the electrolyte with O_2. While the SH images in Fig. 5.1B show that bubble appearance is strongly localized, they do not demonstrate whether activity is localized: whether the current flow necessary to explain bubble production is a significant portion of the measured current flow through the whole electrode.

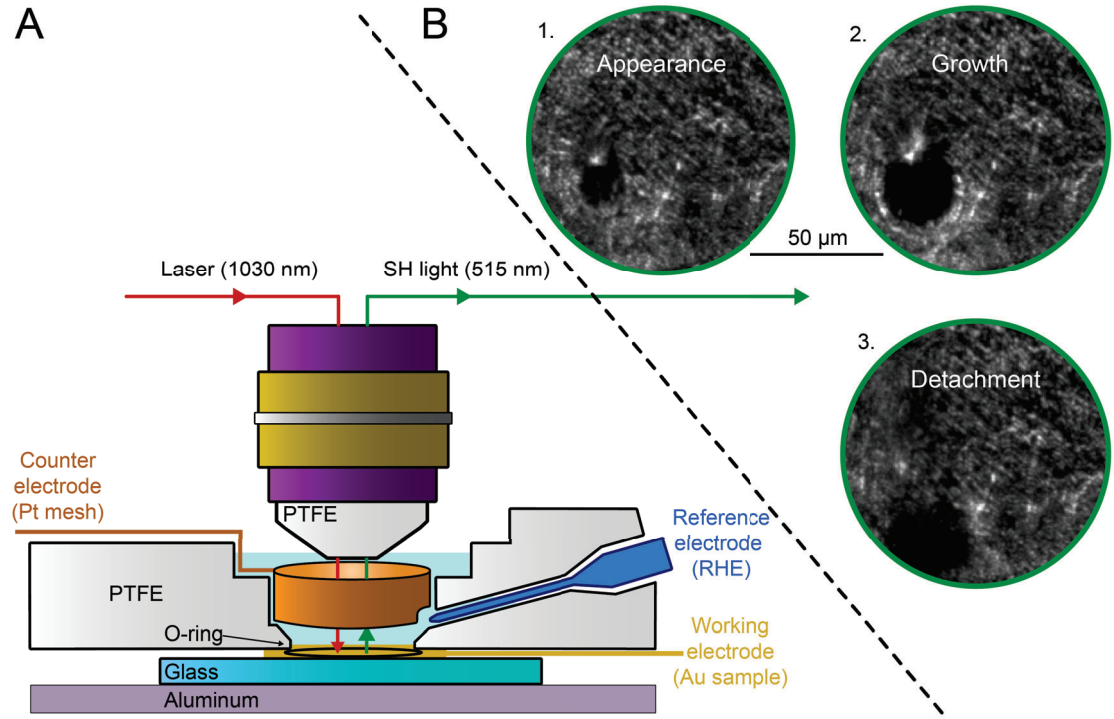

Figure 5.1 – Experimental setup for imaging oxygen bubbles. (A) Schematic of the SH/cyclic-voltammetry microscopy experiment. (B) SH images of the life-cycle of an oxygen bubble: appearance, growth and detachment. The color scale represents SH intensity from low values (black) to high values (white).

To answer this question, we estimate the number of O_2 molecules necessary to explain the observed bubbles by measuring the diameter of each bubble in the frame where it detaches from the surface, assuming the bubble is formed of 1 atm of O_2 and using the ideal gas law. We then compare this estimated bubble-related current to the current expected to flow through the imaging field of view, which is based on the current measurement from the whole electrode. If the current necessary to produce the O_2 bubbles is large with respect to the current flowing through the field of view, it suggests that O_2 generation that does not result in bubble formation, as well as Au oxidation, do not contribute significantly to the measured electrode current. For the results shown in Fig. 5.2 this condition is clearly met: the current required to generate the O_2 bubbles in Fig. 5.2B, C, and D is 188, 195, and 134 % of the current expected to flow through an area the size of the field of view, respectively. Clearly, under the conditions of this linear sweep voltammetry, current flow is dominated by electrochemical oxygen evolution resulting in bubble formation.

The local, high density of sites at which oxygen bubbles appear can be rationalized either as the result of transport or of chemistry. In other words, we observe either an active area for bubble nucleation from a neighboring electrolyte supersaturated with O_2 or an active area for O_2 generation. As we show in detail in Section 5.5.4, the high time-resolution of our approach allows us to finely resolve bubble growth rate, and to show that its time dependence is incompatible with a diffusion-limited scenario, where the growth rate would scale with the surface area of the bubble. The fact that bubble growth rate is independent of the bubble surface area suggests that, for bubbles of radius ≥4 µm, the O_2 responsible for bubble growth is produced locally from the active sites.

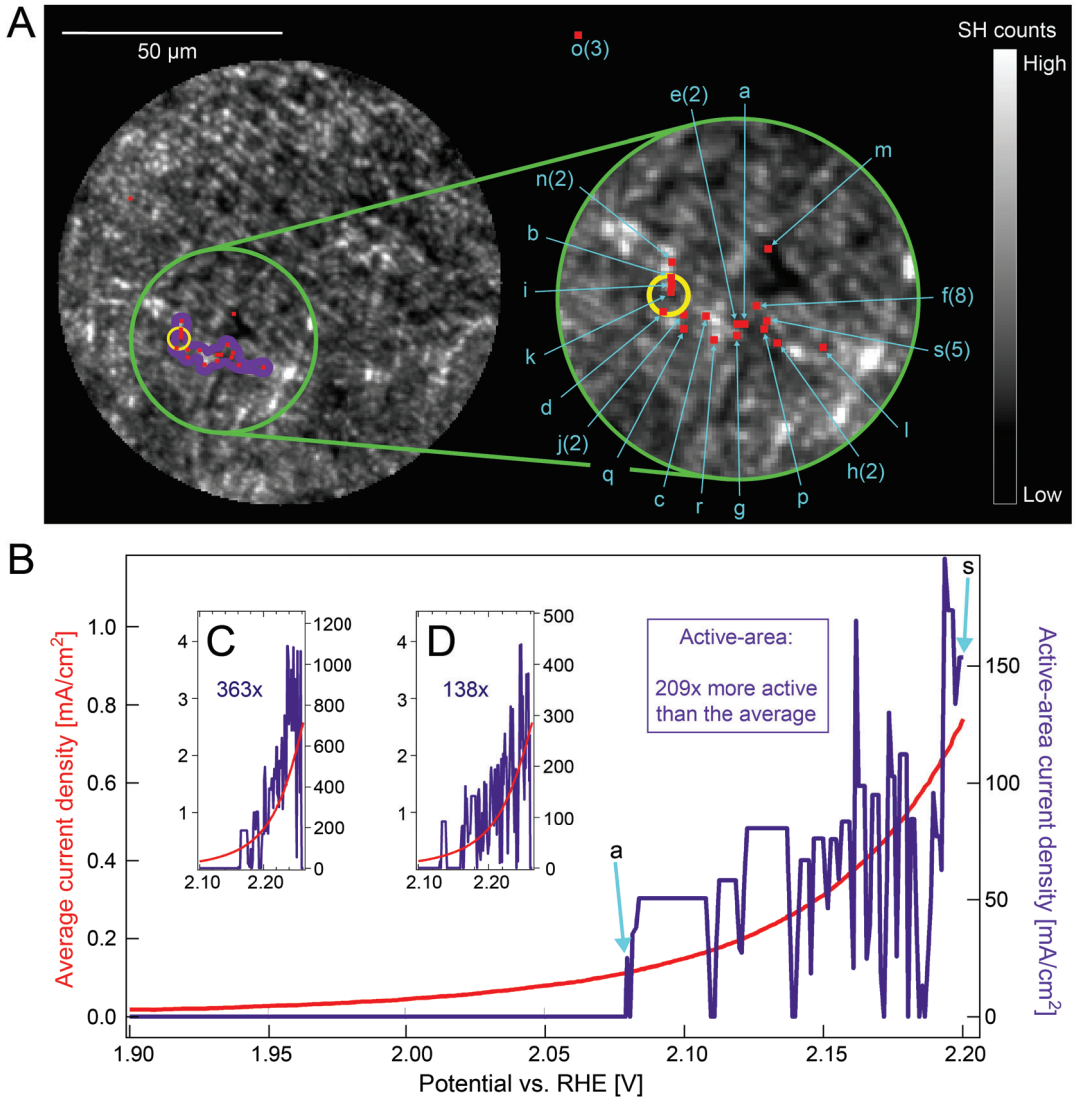

Figure 5.2 – Localized nucleation sites of O_2 bubbles vs. the current density. (A) On the left side is the circular field of view of the polycrystalline gold electrode at 1.8 V vs. RHE in our SH microscope. Red dots indicate sites at which O_2 bubbles nucleated during the linear potential sweep shown in (B). On the right side is a magnified area that contains the nucleation sites (red dots). The letters assigned to the dots designate the order in which bubbles appeared from the respective spots during the potential sweep. The number in brackets denotes the number of O_2 bubbles that emerged from each site. The yellow circle denotes the area from which the first O_2 bubbles emerged when repeating the experiment after potential cycling. (B) Shows the current density of the average electrode (in red) and the active area (in purple, calculated as discussed in the text) as a function of potential during a linear sweep from 1.9 to 2.2 V vs. RHE with a sweep rate of 1 mV/s. "a" and "s" denotes the first, and the last bubble in (A). Insets (C) and (D) show comparable current density vs. potential plots for two more spots on the same electrode that were the sole active areas in different field of views during repeated experiments. The electrolyte was 0.5 M Na_2HPO_4.

Much prior work suggests that the bubbles we observe nucleate at length scales much smaller than those accessible by our SH microscope. For example, White and coworkers have extensively

studied electrochemically generated nanobubbles of a variety of gasses, i.e. H_2, N_2 and O_2, on Pt nanoelectrodes as well as on microelectrodes in confinement [284–287]. These studies suggest that, on Pt nanoelectrodes, bubble nucleation occurs with a critical size as small as 4-5 nm [288] and is driven by a strong supersaturation of the electrolyte close to the electrode with the respective gas (up to 300 times larger than the saturation concentration under standard conditions [289]) rather than local differences in activity. Work by others suggests that the necessary degree of supersaturation is extremely sensitive to details of the surface. For larger Pt microelectrodes, the reported supersaturation values for nucleation ranged from 1.5 to 24 times the standard concentrations [290, 291]. For other surfaces, the formation of surface nanobubbles without supersaturation of the electrolyte with gas has been reported [292, 293].

Clearly, the 4-5 nm length scale of bubble nucleation is not observable in our SH microscope, and thus it is difficult to draw conclusions about the nucleation and growth mechanisms. Our results are consistent with one of two scenarios: i) the nucleation of O_2 bubbles occurs inside of nanopores in the surface that enable local supersaturation of the electrolyte with O_2 even at minute current densities (e.g. 0.11 mA/cm^2 during the observation of bubble "a" in Fig. 5.2A), or ii) a much lower supersaturation is required on our macroscopic electrode due to heterogeneous bubble nucleation at larger structural motifs, such as grain boundaries. Regardless of the mechanism of bubble nucleation, however, as soon as bubbles are large enough to be observed in our microscope, we find bubble growth to be driven not by mass transport from solution via diffusion, but by local electrochemical O_2 evolution.

To quantify the reactivity of these active areas with respect to the OER we need to convert the O_2 bubble-related current into current-density. We estimated the geometric surface area of the active sites as 69.9 μm^2 for Fig. 5.2B. Detailed description of calculating the surface of the active area, considering the sensitivity of our SH microscope, can be found in Section 5.5.5. After this, we calculated the current density simply by dividing the O_2 bubble-related current by the surface of the active area. The resulting current density is plotted in Fig. 5.2B as a purple curve, starting at around 2.07 V vs. RHE (position of bubble "a"), and is denoted as “active area current density”. Its increase with potential correlates well with the potential-dependent behavior of the average electrode (red curve), but its current density is significantly higher. Integrating the current density from active area over the course of the experiment (from "a" - "s") and comparing it to the integrated current density of the entire electrode (during the same period), we find that the active area’s charge density is 209x higher than the electrode’s average charge density. To validate this result, we performed the same experiment and calculation on two more different field of views on the same electrode, see Fig. 5.2C-D. The corresponding integrated current densities of the active areas are 363x, and 138x times higher than the electrode average.[2] Assuming that the field of views we measured are representative of the electrode as a whole, the active areas in Fig. 5.2 are 138-363 times more active than the electrode average, and the measured current results from surface area of 0.28-0.72 % of the electrode.

While the molecular level structure of an active site is substrate- and reaction-dependent for both electro- and gas phase catalysis, our estimate for the fractional coverage of the surface with active areas (0.28-0.72 %) compares well with active site coverages from gas phase catalysis studies, but is considerably lower than ex-situ estimates of active site coverages in electrocatalytic systems. Studies of gas phase catalysis, e.g. the catalytic dissociation of NO [294] and N_2 [295] on well-defined single crystals and propene metathesis on less well defined metal oxides [296], find active site coverages of 1-2 %. The similarity of these estimates to our 0.28-0.72% active area is consistent with our conclusion that we observe active sites for O_2 generation. In contrast, previous estimates for the fraction of active

[2] The area that was used to calculate the charge density was 72.8 μm^2 for Fig. 5.2C and 38.7 μm^2 for Fig. 5.2D.

sites on Au electrocatalysts for hydrogen evolution, determined from the spontaneous deposition of Ag, Pd and Pt at active sites to poison the surface, find ~5 % [297–299] of the surface to be active. These differences in active site coverage may be partially the result of the means of characterization: while in the electrocatalysis studies active site coverage was determined by ex-situ methods, both in our and the metathesis study active site coverages were determined operando. Prior work, much of it on gas-phase catalytic chemistry, has emphasized the importance of active site characterization operando because active sites evolve [300, 301] or even only appear [14] under reaction conditions. As described above, prior works characterizing active site abundances in electrocatalysis are largely either indirect, i.e. inferred from current voltage measurements of well-defined single crystal surfaces, or ex-situ, i.e. measured by offline mass spectrometry of adsorbed metal. Our SH imaging of active sites overcomes both of these shortcomings.

Having observed an active area for electrochemical O_2 bubble formation, we next investigated the stability of the active area. As has been demonstrated by prior authors in a variety of electrochemical STM studies, cycling the bias across an Au electrode between 0 and 1.7 V vs. RHE, i.e. repeatedly oxidizing and reducing the surface, results in surface reconstruction [256]. While the extent of reconstruction is a function of scan rate and time spent at oxidizing potentials, current features that persist after such cycling are presumably related to structural motifs that are insensitive to surface reconstruction. In other words, if the activity of the active area was the result of a specific arrangement of surface atoms only, one might expect that the active area for bubble generation would shift with every oxidation/reduction cycle. Repeating the experiment after restructuring the electrode surface yields bubble growth from the same active area: the yellow ring shown in Fig. 5.2A. Given that O_2 bubble formation only starts close to 2.1 V vs. RHE, our data are thus consistent with a scenario in which highly active sites for the OER are the result of an oxidized structural defect penetrating into the bulk.

The polycrystalline gold foil makes validation of this conclusion challenging. We do not know from the SH images alone, how deeply the structural features of active sites might penetrate. As discussed above, observing the active area before or after the electrochemical cycling with an experimental technique that offers nanoscale insight into surface structure usually involves ex-situ conditions, and the character of the active are is likely to change under these conditions. Therefore, we approach this problem from the sample side by examining a different gold sample, obtained by physical vapor-deposition of gold on an optically smooth glass surface. This gold electrode is mirror smooth and comprised of ~ 50 nm clusters (see Section 4.2.2, Fig. 4.1C for an SEM micrograph of the as-prepared sample). On this electrode we found a surface defect, that we imaged with second harmonic microscopy, while we ramped the bias from 0 - 2.3 V vs. RHE with a scanning speed of 60 mV/s, and then held it at 2.3 V for two minutes. Figure 5.3 captures this experiment, showing the SH image of the defect in (A), and the SH image of O_2 bubble formation at the defect in (B). The respective SH intensity profile of the defect, vs. a regular surface spot is shown in Fig. 5.3C, together with the current of the imaged field of view (estimated from the measured current of whole electrode) vs. the O_2 bubble related-current.

The measured current in Fig. 5.3C clarifies that scanning the bias from 0 - 2.3 V vs. RHE produces the expected oxidation current feature at 1.5 V: from an electrochemical point of view the surface is clearly oxidized when it reaches 2.3 V. Figure 5.3C shows the average SH intensity per pixel for areas on and away from the defect. Two characteristics of these curves are evident from inspection: i) both increase up to the oxidation current peak and decrease rapidly thereafter, and ii) the SH intensity on the defect appears to be offset positively from that in the surroundings. Both observations are consistent with previous literature: for a wide variety of Au electrodes and electrolytes, the SH intensity has been

observed to increase with increasing potential up to oxidation and decrease thereafter [128, 230], while at a given potential, the SH intensity on Au has been found to be a function of surface structure and even azimuthal angle for a given surface structure [302].

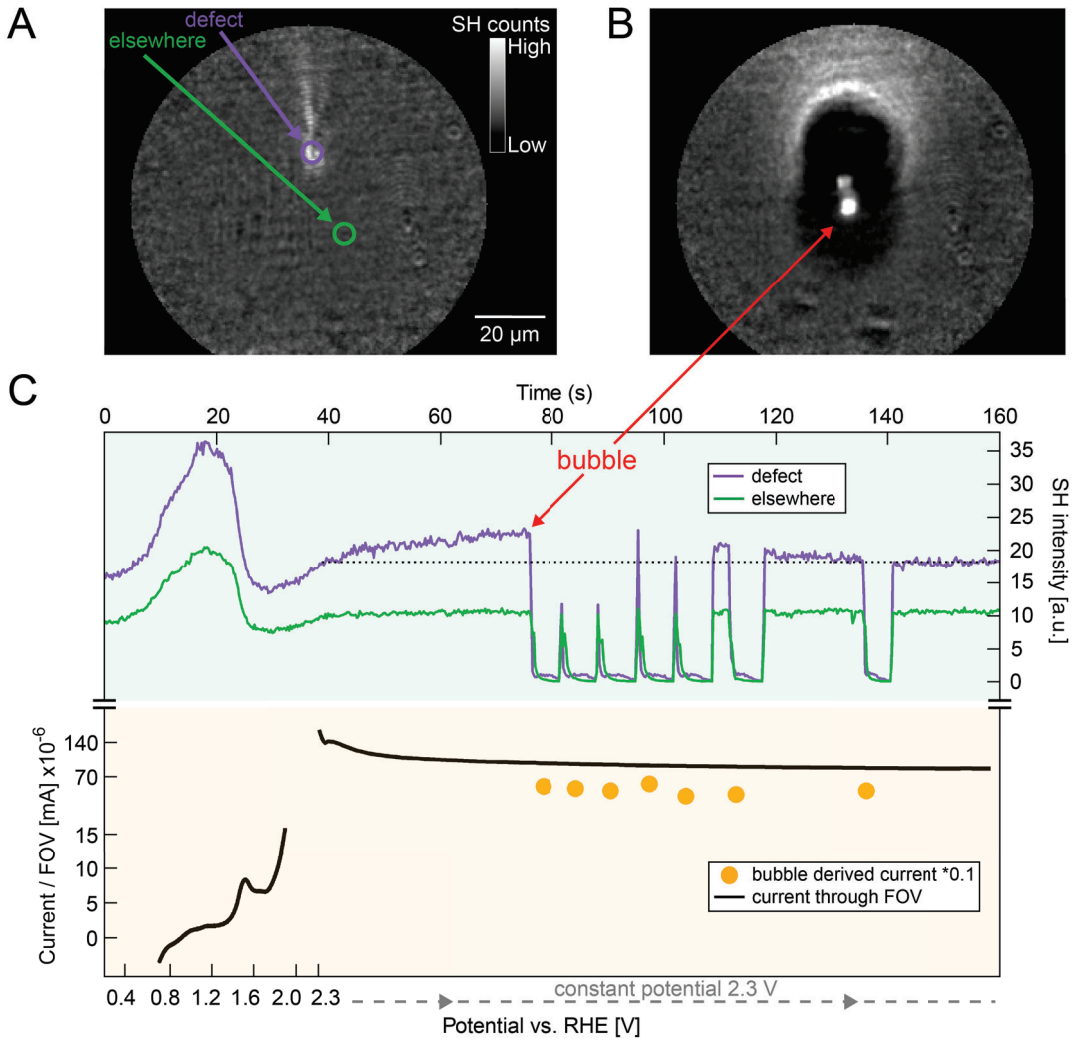

Figure 5.3 – O_2 bubbles originating from a defect in homogeneous (nanocrystalline) gold. (A) The circular field of view of a physical vapor deposited gold electrode at 2.3 V vs. RHE, including a defect, as observed within our SH microscope. (B) The same view as in (A) showing an oxygen bubble forming from the defect. (C) SH intensity profile of the defect (purple) vs. a regular surface spot (green) shows there are several O_2 bubbles produced, corresponding to the SH peaks. The SH peaks in green curve are artificial as a result of defect-bubble physically shielding the imaged green circle spot. The current corresponding to the imaged field of view (calculated from the size of the field of view vs. the geometric area of the electrode) during the linear potential sweep up to 2.3 V and the potentiostatic experiment at 2.3 V are labeled in black. The O_2 bubble related-current after the first 75 s is labeled in yellow. The scanning speed of the linear sweep was 60 mV/s and the used electrolyte was 0.5 M Na_2HPO_4.

After the bias reached 2.3 V vs. RHE in Fig. 5.3C, the sample was maintained under potentiostatic control. Under these conditions the measured current is constant, the SH intensity off the defect is also constant and that on the defect slowly increased up to ~ 75 s. While understanding this potential-

induced change in local SH contrast is challenging, the different behavior is most easily rationalized if under these electrochemical conditions local structure near the defect continues to evolve while that away from the defect is stable. Thirty-six seconds after the potential has been fixed at 2.3 V v. RHE, O_2 bubbles start to emerge at the defect. As these bubbles grow, detach and diffuse out of the field of view, the local SH signal decreases due to scattering and then recovers as the bubble diffuses away. The first five bubbles emerge from the defect in rapid succession with no waiting period in between. Between bubbles five and six there is a waiting period of ~ 5 s. Between bubbles six and seven this waiting period grows to almost 20 s. The SH intensity on the defect during the waiting periods and after bubble seven is decreased with respect to its value before the first bubble. The current passed in order to create the bubbles is shown as golden dots in the lower panel of Fig. 5.3C, with the current passed through the field of view as a reference, showed in black. As expected for these potentiostatic conditions, the current is approximately constant. In contrast to the polycrystalline Au electrode shown in Fig. 5.2, here the bubble estimated current exceeds the expected current for an area the size of the field of view by 10x (bubble derived current is scaled by 0.1x to fit on the same plot). This result reflects that these defects are relatively uncommon on the physical vapor-deposition sample, i.e. the great majority of field of views we observed did not have them, and thus, the field of view showing the data in Fig. 5.3A-B is not representative of the electrode as a whole.

The increase in waiting time and the decrease of the SH intensity on the defect after the fifth bubble is consistent with a scenario in which the structure of the active area evolves and its reactivity decreases under OER conditions. The former conclusion is consistent with the results of much prior works (although only through indirect means at solid/liquid interfaces): catalyst active sites are dynamic under reaction conditions [300, 301, 303]. We rationalize the apparent decrease in reactivity by noting that the OER on Au is known to occur on an increasingly oxidized surface due to the thermodynamic instability of the oxygen anion in the metal oxide lattice [276]. Together with the observation that metal corrosion accompanies the OER [304], the data displayed in Fig. 5.3 are thus consistent with a scenario in which the OER at 2.3 V consumes catalytically active, partially oxidized, Au cations more quickly than they are created.

5.3.2 Active sites observed at potentials negative of the oxygen evolution reaction onset that are removed by the potential cycling

We also observed a second type of dynamic active area behavior on the polycrystalline Au electrodes, qualitatively different from that shown in Fig. 5.2. This type of active area differs from that described previously in two ways: i) oxygen bubbles appear at these sites at potentials lower than 2 V and ii) these sites disappear after potential cycling (presumably they are not stable with respect to potential induced surface reconstruction). A representative series of experiments are shown in Fig. 5.4A. Here, three experiment, each with four cyclic voltametries (CVs) were collected, using the polycrystalline electrode of Fig. 5.2, but imaging a different field of view with second harmonic microscopy. In every experiment the four CVs following one after another start at 0 V vs. RHE, and the potential is ramped up to 1.6, 1.75, 1.9, and 2.05 V vs. RHE, respectively. In experiment 1, for example, an O_2 bubble was produced in the penultimate cycle at 1.9 V and in the last cycle at 2.05 V. The potentials at which bubbles were produced are marked in the respective voltammogram by stars that have a separate color for each experiment. In experiment 2, a bubble was only produced at 2.05 V. Experiment 3 and following cyclic voltammetry experiments did not yield bubble growth at all. In Fig. 5.4B, the locations of bubble nucleation from experiment 1 and 2 are marked with red and turquoise stars. This behavior is unexpected, as prior empirical work [245], and our findings discussed above, suggest that O_2 should

be generated on polycrystalline Au only anodic of 2 V vs. RHE. The observation of O_2 bubble formation under conditions in which the electrode as a whole is clearly not active with respect to the OER is most easily understood if the indicated spots/areas with stars are active with respect to electrochemical O_2 production. That is, the observation of bubbles from forming on these sorts of dynamic active areas is extremely unlikely to be the result of just bubble nucleation from a supersaturated solution.

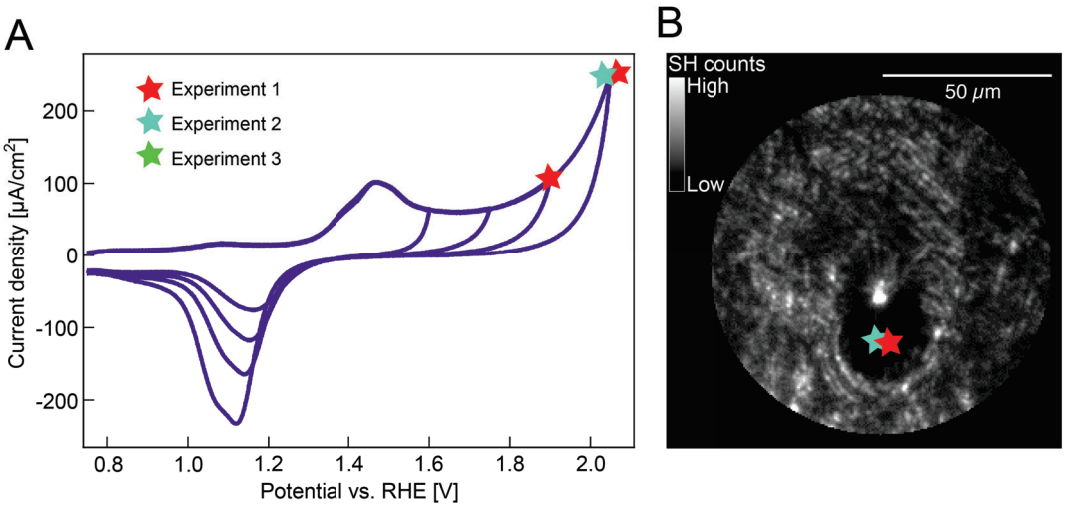

Figure 5.4 – O_2 bubbles at polycrystalline gold electrode during consecutive increasing CVs. (A) Cyclic voltammograms (CV) collected in three separate experiments on the polycrystalline Au electrode, also used in Fig. 5.2. In each experiment, four CVs are collected in order: 0-1.6, 0-1.75, 0-1.9 and 0-2.05 V vs. RHE. For all CVs the scan rate was 60mV/s, and the used electrolyte was 0.5 M Na_2HPO_4 with pH = 9. (B) The formation of a bubble during the experiment. The SH image shown was collected during experiment 1 at 1.9 V vs. RHE. The nucleation sites during experiment one and two are shown as colored stars. The field of view here was different from the three fields of view summed up in Fig. 5.2.

In chronoamperometric experiments analogous to the experiments shown in Fig. 5.3, but at a potential of 1.9 V vs. RHE (i.e. before the expected onset of the OER) on a polycrystalline gold, formation of a single bubble per experiment was observed in two successive experiments, but not subsequently. The bubbles formed in the chronoamperometric and cyclic voltammetry experiments originated from spots that lie outside the active area of Fig. 5.2. Corresponding SH count vs. potential curves, that show the signature of bubble formation, can be found in Section 5.5.6, Fig. 5.10.

Given the body of prior work discussed earlier, and our results shown in Fig. 5.2 and 5.3, Au oxidation is clearly a prerequisite to O_2 evolution. The metastable active sites shown in Fig. 5.4 are consistent with a scenario in which high energy, high reactivity sites exist on our polycrystalline Au that are oxidized, and begin to emit O_2, at potentials cathodic of O_2 evolution observed by both us and others on more homogeneous surfaces [245]. Because these sites appear to be largely removed on voltammetric cycling, such defects are likely surface bound. Oxygen evolution from such transient surface sites, 200 mv before the regular onset of the OER, has previously been observed, indirectly, by Burke et al. [305].

Despite being the noblest of metals and relatively inert with respect to chemisorption, Au electrodes show surprising activity in a variety of oxidation and reduction reactions [278]. Burke et al. hypothesized that this activity could be explained by the presence of surface bound undercoordinated metal species (adatoms, clusters) that are oxidized at potentials substantially below that of the bulk

metal. The result of this premonolayer oxidation, a minority species called "incipient hydrous oxide", is argued to be the catalytically active entity of Au, and noble metal electrodes in general, for a wide variety of different reactions [255]. In order to correlate the presence of the incipient hydrous oxide with catalytic activity, electrode pretreatment protocols to increase the abundance of this minority species were designed. Such protocols allowed these authors to observe anodic features in the bilayer region of the first CV scan, which were assigned to the formation of the incipient hydrous oxide (structurally distinct from α- and β-oxide) [264, 283]. Surfaces with stronger anodic features in the bilayer region showed an increased catalytic activity. These experiments suggested what Burke and coworkers termed an “Incipient Hydrous Oxide/ Adatom Mediator” (IHO/AM) model of noble metal electrocatalysis. Such a pretreatment also significantly enhanced the oxygen gas evolution from transient sites at around 1.8 V vs. RHE [305], linking the IHOAM model also to fully oxidized surfaces and the OER.

As noted above, the approach of Burke and coworkers to characterize this “incipient hydrous oxide” was indirect: the electrode structure was perturbed sufficiently, such that a minority species becomes a majority and the presence of this species was apparent in electrochemical observables. This approach greatly complicates insight into what the high energy sites actually are, or which underlying structure produces them. Our imaging approach circumvents this problem by virtue of its local character: we characterize the transient reactivity of surface species with extremely low coverage. In the case of the first produced bubble in experiment 1 of Fig. 5.4, the current at 1.9 V vs. RHE is on the same level as for the monolayer oxidation and no oxygen evolution would be expected, yet we are able to detect local oxygen production. The production of a bubble under conditions in which no clearly assignable OER current is apparent from voltammetry is consistent with the presence of such transient strongly catalytically active sites on our electrode. Current work in our laboratories focuses on connecting the potential-dependent local Au oxidation SH signal studied in Chapter 4, to these transient OER active sites. Such a connection would clarify the nature of this incipient hydrous oxide to the bulk electrode oxidation.

From a more practical point of view, the observation of OER activity 100 mV prior to 2 V vs. RHE, on what presumably is a highly active surface defect, demonstrates the possibility of highly active catalysts that are only a few (1-3) atomic layers thick. Clearly, higher spatial resolution probes, and subsequent physics-directed electrode engineering to stabilize these sites, would be of great benefit in enhancing the kinetics of a variety of electrocatalytic processes.

5.4 Summary and Conclusions

In this study, we characterized heterogeneous polycrystalline gold foils with a grain sizes of tens of µm and gold electrodes composed of 50 nm clusters grown by physical vapour deposition with second harmonic generation microscopy (SHM) while performing voltammetry and chronoamperometry in 0.5 M Na_2HPO_4 solution, pH = 9. The use of SHM enabled us to directly identify and characterize active sites/areas operando at the interface of an oxidized, non-ideal electrode and a liquid phase. At potentials positive of the onset of the oxygen evolution reaction (OER), we observed that the evolution of O_2 bubbles is restricted to highly active areas on the polycrystalline foil with small surface area of tens of μm^2 (0.28-0.72 % of the total electrode surface area). The current required for O_2 bubble formation quantitatively explains the current we measure over the entire electrode over a range of moderately anodic potentials. Our finding of the relative area covered by active sites is consistent with prior in-situ and operando works in gas phase catalysis, but considerably lower than the active site estimate for electrocatalysts from ex-situ studies. Because understanding the relationship of local

oxidation and O_2 bubble formation on heterogeneous Au foils is challenging, we conducted similar experiments on a physical vapour deposition gold sample at a potential high enough for a steady state OER current, but low enough to avoid widespread bubble formation on the smooth surface. In this bias window only at a single defect (that was stable with respect to repeated surface atom rearrangement during electrochemical cleaning) and after the formation of a sufficiently thick oxide layer, did bubbles appear. The results of both experiments suggest that this class of highly active areas/active sites for the OER on gold need a structural defect penetrating to the bulk and a sufficiently thick layer, or specific type, of oxide to form. Finally, in a third type of experiment, the production of O_2 bubbles was observed on the polycrystalline foil at potentials below the onset of the OER, in active areas that were unstable under potential cycling. Such metastable active sites are consistent with those suggested by Burke and coworkers, as the catalytically active entity in the incipient hydrous oxide/adatom mediator (IHOAM) model of electrocatalysis.

Our study is, to our knowledge, the first to describe the spatial heterogeneity of an electrocatalytic reaction at the electrode/aqueous electrolyte interface under reaction conditions through wide-field imaging of product formation. Because of its practical importance and significance for a variety of applications, we interrogated the electrooxidation and OER on polycrystalline Au. While the spatial resolution of the microscope precludes molecular level structural insight into the composition of the active sites and, presumably nm-scale bubble nucleation, our results clearly suggest that a combined program of higher resolution, near-field, operando microscopy and systematic electrode modification holds out the hope of understanding the relationship of surface structure and active site abundance (in the frame of the IHOAM model of electrocatalysis). Doing so will help create Au electrodes with dramatically enhanced reactivity. The particular issues we address in this study - separating the spatial heterogeneity of oxidation and the OER on Au - are obstacles in the optimization of essentially all practical OER catalysts. As a result, and because the operando SHM approach we describe is not restricted to Au or electrooxidation/OER (another important application is the investigation of bubble formation and surface wetting behavior of bubbles in water electrolysers [306]), we expect this study to be of wide interest.

5.5 Appendix

5.5.1 Full cyclic voltammogram and integrated SH vs. applied potential

Prior work on the oxygen reduction reaction (ORR) on gold has shown that this reaction leads to a cathodic current starting at 0.9 V vs. RHE that increases with decreasing potentials in alkaline media, in the absence of mass transfer limitations. This reaction is irreversible at 0.9 V and below and thus is expected to add a negative 'tilt' to all CVs on Au in which O_2 is present in the electrolyte [307]. We see such a 'tilt' at potentials 0.7 V vs. RHE and below, suggesting that our electrochemical cell contains dissolved O_2 (see Fig. 5.5). Between 0.7 V vs. RHE and the start of oxidation at ~ 1.3 V, our CV appears to show small current features. Similar features have been observed previously they are generally more pronounced in alkaline electrolyte than acid [308, 309] – and attributed to surface defects, or non-equilibrated surface domains [264, 283].

The spatially integrated second harmonic intensity is plotted as a function of potential (along with the CV) in Fig. 5.5. Clearly, the SH intensity increases with increasing potential up to 0.85 V vs. RHE, then it is relatively stable between 0.85 and 1.1 V, and drops abruptly at potentials above 1.3 V: the onset of oxidation. In the cathodic scan, the SH signal recovers at 1.15 V vs. RHE (with the dissolution

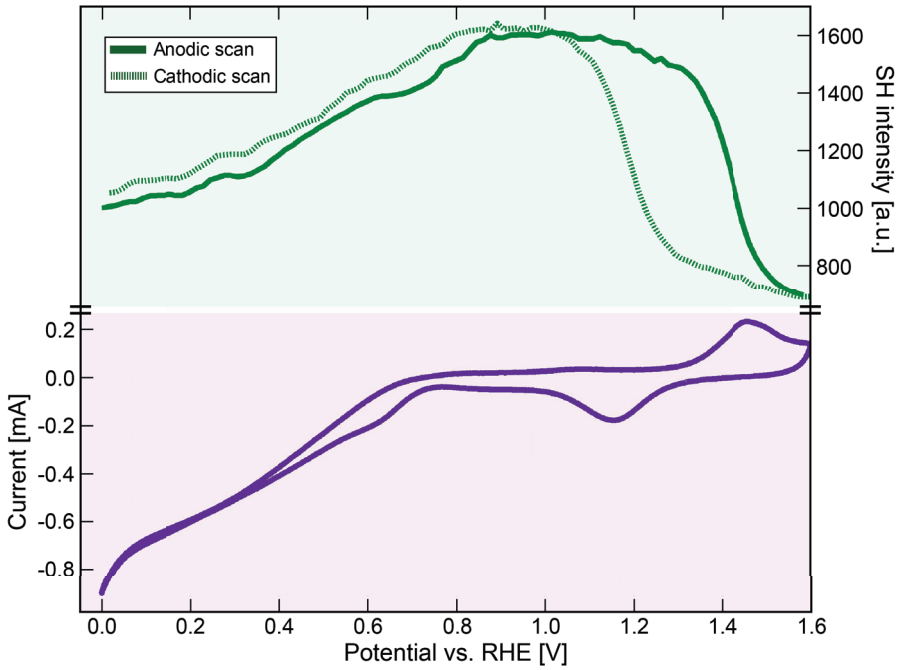

Figure 5.5 – Full cyclic voltammogram and mean SH signal vs. applied potential. SH potential-dependent intensity averaged over the entire field of view (green), and corresponding cyclic voltammogram (purple). Sample was a polycrystalline gold surface with an electrolyte of 0.5 M Na_2HPO_4, pH = 9, at 60 mV/s.

of the oxide), and is afterward reversible. This general behavior of the SH signal is in agreement with previous reports [128, 230]: at comparable fundamental wavelengths, these authors also found an approximately linear increase of SH intensity with increasing potential until the oxidation of the surface where a sharp drop in intensity was reported.

5.5.2 Surface heterogeneity of SH images during potential cycling cathodic of Au oxidation

The SH images at potentials below oxidation show features on a length scale of tens of µm, see Fig. 5.6. The length scales of these features are similar to those observed in SEM images (Section 4.2.2, Fig. 4.1D). Interestingly, as shown in Fig. 5.6, the dependence of SH intensity on potential varies widely from surface spot to surface spot. Prior work suggests a variety of possible reasons why SH intensity vs. potential profiles on Au might show such strong spatial variability. Polycrystalline gold typically exhibits facets of (111)- or (110)-like surfaces [221]. These crystal faces have strongly distinctive work functions, solvation structures, ion sorption behavior and oxidation/reduction characteristics. These differences are reflected in electrochemical observables such as the point of zero charge (PZC) for gold single crystal electrodes. The PZC can vary with surface structure up to 400 mV [310, 311]. Adding to the complication, we expect that in addition to having both (111)- and (110)-like crystal faces, our sample may contain domains of either type that are rotated with respect to each other. A strong azimuthal dependence of SH intensity vs. potential profiles has been demonstrated for gold single crystal electrodes, demonstrating that the histogram of domain orientation with respect to the laboratory reference frame will strongly influence the measured second harmonic intensity [302].

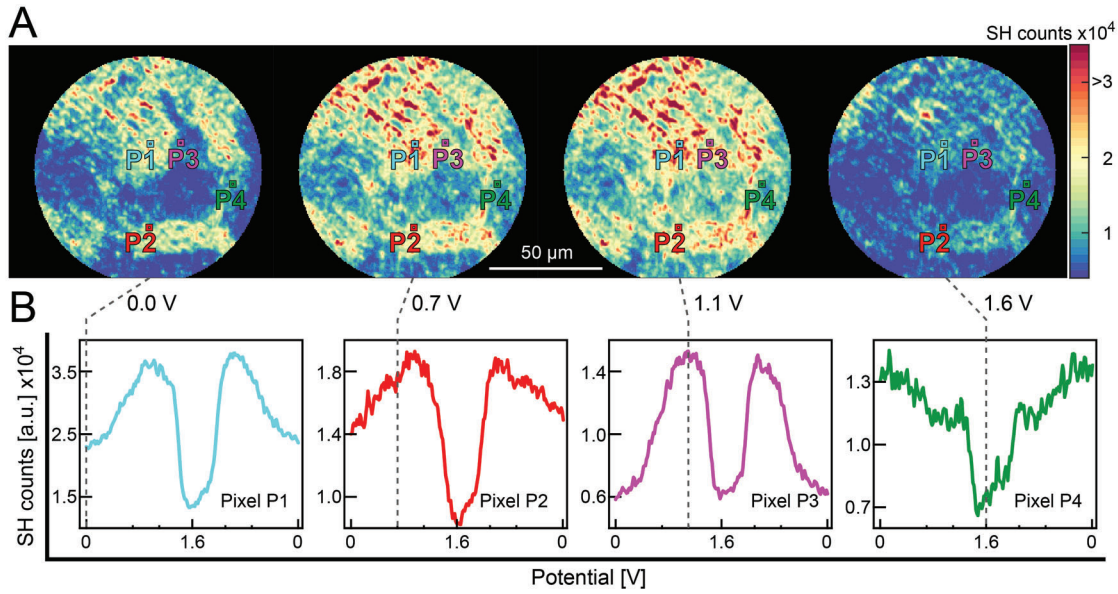

Figure 5.6 – Surface heterogeneity displayed by SH-potential dependent images. (A) SH images of polycrystalline gold electrode at 0, 0.7, 1.1, and 1.6 V, respectively, showing the surface heterogeneity. Four pixels chosen on the surface are marked as P1, P2, P3, and P4. (B) SH-potential dependent curves of pixels P1, P2, P3, and P4, respectively. The electrolyte was 0.5 M Na_2HPO_4, pH = 9, and the scanning speed was set to 60 mV/s.

5.5.3 Calculating the O_2 bubbles volume and their corresponding charge

Increasing the potential positive of 2 V vs. RHE leads to the formation of oxygen bubbles on the electrode surface. We monitor this formation by observing the bubbles and the shadows they cast on the imaged gold/electrolyte surface. In most cases, the bubble itself is hardly visible because it extends well above the focal plane (which we place on the Au/electrolyte interface) and is thus out of focus. In contrast, the shadow is always in focus, because it lies in the plane of the electrode surface. An example where bubble and shadow can be seen together is Fig. 5.3. An illustration can be seen in Fig. 5.7, showing that the real position of the bubble and the center of the shadow is offset. This offset was taken into account by determining the center of a bubble's shadow and then correcting for it in MATLAB, assuming a spherical bubble and accounting for the 34° angle of incidence. The shadows are slightly elliptical due to illumination at 34°, therefore, for calculation of bubble's volume we used the shadow's diameter perpendicular to the direction of illumination.

The amount of charge that is passed in order to form a O_2 bubble was calculated as follows. Given the measured diameter of a bubble, we calculated its (assumed spherical) volume. The volume is then used to calculate the amount of oxygen molecules inside the bubble assuming pure oxygen and a pressure of 1 atm. It is worth noting that 1 atm is a lower bound of bubble pressure: bubbles with a radius of ~ 10 µm (the average size of the detaching bubbles evaluated for Fig. 5.2) will have slightly higher pressure due to the Laplace pressure. However, this additional pressure is only 0.14 atm (with larger bubbles having even lower pressures). From the amount of oxygen molecules we calculated the number of electrons consumed per bubble and then convert this number into a current. The conversion from the current into a current density requires the knowledge of the active area's surface (which is further discussed in Section 5.5.5).

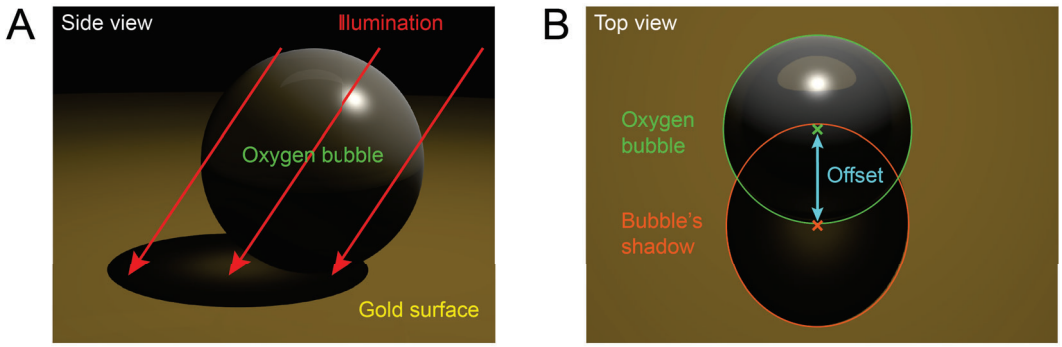

Figure 5.7 – Illustration of an oxygen bubble on the gold surface. (A) shows a bubble and its shadow in side view along with the collimated illumination at 34°. (B) The surface, bubble and shadow are seen from above. It is apparent, that the real center of the oxygen bubble is shifted from the center of the shadow by a size specific offset.

5.5.4 Dominating factor influencing the bubble growth

As discussed in the main text of this chapter, it is not immediately apparent that the formation of bubbles exclusively in the active area is actually a consequence of its superior activity compared to the surroundings. One might alternatively imagine that bubble nucleation occurs from a supersaturated solution at nucleation sites that are particularly active because of roughness, or a specific composition. In this scenario, bubble growth would be dictated by mass transport of O_2 molecules from electrolyte into the growing O_2 bubble. In such a scenario, the growth rate of the bubble is expected to be a function of bubble's surface area. Evaluating the growth rate of a bubble over the course of 26 s during the linear sweep experiment of Fig. 5.2 clarifies that this is not the case. Within experimental error, the growth rate is relatively insensitive to the bubble size, as shown in Fig. 5.8. Note that the possible slight increase in the growth rate for large bubbles may be the result of the increase in bias during the course of bubble growth. As it is a linear sweep experiment with a sweep rate of 1 mV/s, the potential at the end of the bubble growth will be 26 mV higher than at the start. We take this argument to suggest that the growth of bubbles, and the activity of the active area, are a consequence of the high intrinsic OER activity of the active area.

5.5.5 Determination of the active area size

Nucleation initially leads to bubbles that are only a few nanometers large [288], well below the resolution limit of the microscope. While such bubbles cannot be resolved, we can identify their presence by intensity fluctuations of a few pixels against an otherwise static background. As might be expected, these fluctuations are spread over a circular area with a radius of 1-2 µm, but at this stage, no clear spherical shape can be identified and the center of the bubble can not be determined reliably. The bubbles grow further, and at around 3-5 µm in radius, they can be identified. In Fig. 5.2, the center of each bubble's nucleation sphere was marked with a red dot. Here, we show a more detailed SH image, where the centers are marked with red dots and white crosses, see Fig. 5.9. In the early stage of bubble growth (before it can be discerned as spherical), the bubble's geometry is ill defined, and it is reasonable to assume an area for the bubble nucleation. For this purpose, we assume a circular nucleation area around each center (green circle), whose radius is defined by the standard deviation of a bubble radius. This standard deviation was determined by fitting the size of the bubble nine times by hand. The

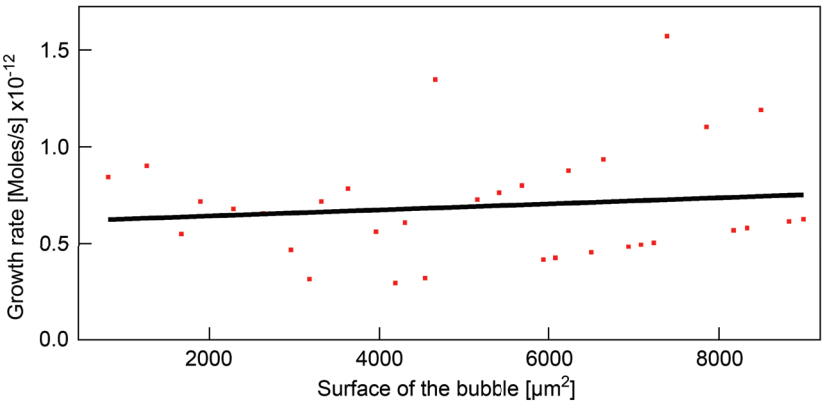

Figure 5.8 – Growth rate of a bubble versus its surface area during the bubble growth. The bubble was part of the linear sweep experiment depicted in Fig. 5.2, nucleated at ~ 2.08 V vs. RHE and grew for about 26 s before detaching. The experiment was conducted in 0.5 M Na_2HPO_4 (pH = 9) with a sweep rate of 1 mV/s.

resulting standard deviation was 1.8 µm. Mostly all nucleation sites lie in a close vicinity to each other, most nucleation areas overlap with neighboring ones. The green area was termed an "active area", because with few exceptions, every bubble originated from there. An estimate for the geometrical area of this active area is then obtained by choosing an envelope that contains all nucleation areas for which it appears sensible to be grouped together. This envelope is shown in thin yellow line, wrapping the green area in Fig. 5.9. The resulting area is 69.9 µm^2.

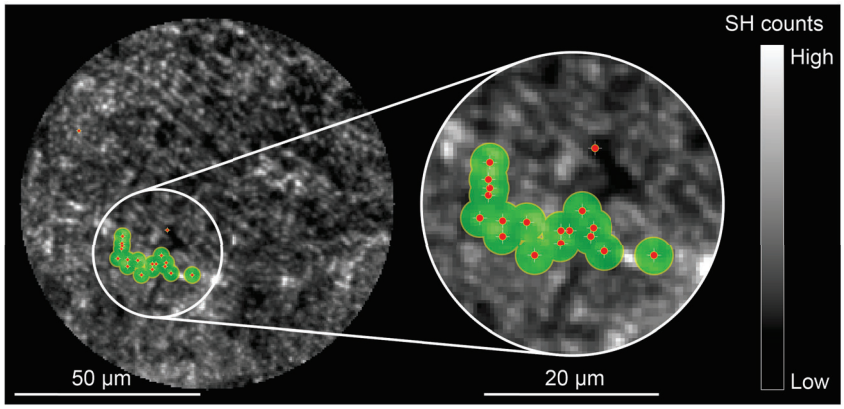

Figure 5.9 – Determination of the active area size. The surface of the active areas was determined by assuming a radius of bubble nucleation of 1.8 µm around every nucleation center (red dot with white crosses). Overlapping these areas (green circles) and taking the envelope (thin yellow line) yields 69.9 µm^2. The radius of nucleation was determined from the standard deviation of how precisely we can determine a bubble's size.

It is obvious that the calculated active area will linearly affect the current densities that are plotted in Fig. 5.2, and that it depends to some degree on our choice of the envelope (yellow line). However, this does not affect the argumentation in the result section for two reasons: i) the assumption of a spherical nucleation area with a radius of 1.8 µm is an overestimate that we are using because our microscope does not resolve the bubble nucleation on the sub-micron scale; ii) choice of a different envelope with the same nucleation areas (green circles) would result in an active area that varies by ± 10%, which

would in turn alter the current density by a similar percentage. However, this can not explain the two orders of magnitude difference between the current densities of active areas and the average electrode.

5.5.6 SH data for the active sites occurring at potentials negative of the OER onset

This section contains SH potential-dependent data supporting the observed active sites that occur at potentials < 2 V vs. RHE, see Fig. 5.10.

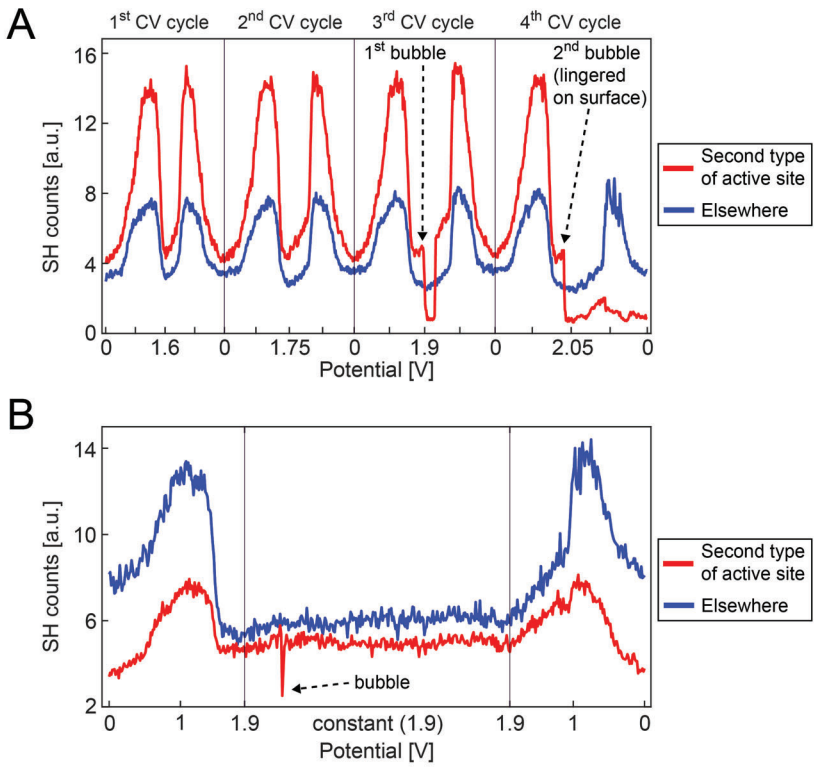

Figure 5.10 – Observation of active site at < 2 V vs. RHE potential. (A) Corresponds to experiment 1 of Fig. 5.4. SH-potential dependent curves of the active site vs. a regular surface spot are colored in red, and blue, respectively. The consecutive CV cycles increase by 0.15 V. The scanning speed was set to 60 mV/s. (B) A different prior experiment performed on the same polycrystalline gold as Fig. 5.4. The potential was linearly increased to 1.9 V, then hold constant, and finally, linearly decreased back to 0 V. SH-potential dependent curves of the active site/elsewhere are colored in red, and blue, respectively. The scanning speed prior to and after the potentiostatic period was 60 mV/s. The electrolyte in (A) and (B) was 0.5 M Na_2HPO_4 with pH = 9.

5.5.7 Processing of the SH data

Measured second harmonic data in form of videos were first stabilized in ImageJ with the plugin "Image Stabilizer" using the Lucas-Kanade algorithm, the parameters that were used are: Transformation: Translation; Maximum Pyramid Levels: 1; Template Update Coefficient: 0.99; Maximum Iterations: 200; Error Tolerance 0.0000001. The stabilization was used as the sample displayed random movements in the lateral plane on the order of a few hundreds of nanometers over the course of a measurement.

After image stabilization we performed a flat-fielding procedure in MATLAB. The SH data is collected by a wide-field second harmonic (SH) microscope. As opposed to a rastering SH microscope, where every pixel is illuminated with the same laser fluence, here we illuminate and collect the SH intensity from the whole imaged area at the same time. The benefits of the wide-field approach are: i) we can effectively deliver more laser power to the sample during the time equal to one rastering cycle, which enables our approach to be orders of magnitude faster; ii) SH intensity from all pixels are comparable in real time in every image as there is no rastering delay between different pixels. The downside of the wide-field configuration is that the illumination has a Gaussian like intensity distribution in the x and y direction, i.e. in the plane of the surface, and therefore, does not deliver the same laser fluence to every pixel of the field of view. To compensate for this we use a flat-fielding procedure to simulate a homogeneous illumination so we can directly compare the SH intensity pixel to pixel. For this reason, we acquire the SH beam profile immediately before every experiment. The flat-fielding procedure is then a simple division of acquired SH images with the SH beam profile image.

6 Summary & Outlook

In this thesis, we used high-throughput wide-field second harmonic (SH) microscopy to study the surface chemistry at solid/liquid interfaces. The sub-second time resolution of our SH microscope allowed for tracking the spatio-temporal dynamics of the observed surface chemistry. We find structural heterogeneity on sub-μm to tens of μm length scales. This heterogeneity alters the local properties and largely the surface function with respect to chemical reactions. For example, local defect structures on gold can display a decreased reaction barrier enabling surface chemical reactions (such as the oxygen evolution reaction) to take place at lower applied potentials than the rest of the surface. Such mechanisms play a crucial role in material science, where surface engineering can greatly improve the efficiency of catalysts and electrocatalysts.

6.1 Summary

In Chapter 2, we presented the SH microscope setup used for experiments in this thesis. An improvement of 2-3 orders of magnitude in the throughput of our microscope compared to commercial raster-scanning SH microscopes originates from: i) a high-intensity laser, ii) the wide-field illumination configuration, and iii) an electron-multiplying *gated* camera. We characterized the SH microscope by measuring the laser wavelength, the laser pulse duration, the laser power distribution in the system, the range of laser incidence angles on the sample, and the polarization sensitivity. Furthermore, we discussed important factors influencing the SH intensity generated from solid/liquid interfaces, and how to experimentally optimize these parameters. Lastly, we designed an electrochemical cell that enabled in-situ SH imaging during various electrochemical experiments. The versatility of this system paved the way for dynamic imaging of surface (electro)chemical heterogeneity.

In Chapter 3, we investigated the structure and dynamics of water at the glass/aqueous solution interface. We imaged pH-induced chemical changes on the curved and confined inner- and outer-surfaces of a cylindrical glass micro-capillary. The resulting SH images report on the ordering of interfacial water under the electric field caused by surface charges. By using the Gouy-Chapman-Stern theory, we converted the SH images to surface potential maps, and to surface charge density maps. The acquired pixel-wise knowledge of the surface potential, the surface charge density, and the average measured pH of the solution allowed us to calculate surface $pK_{a,s}$ values for the silica deprotonation reaction. Spatially resolved $pK_{a,s}$ values range from 2.3 to 10.7. This extended range of $pK_{a,s}$ values is in stark contrast with the reported average mono-modal $pK_{a,s}$ (6.8) [201], bi-modal $pK_{a,s}$ (4.8, 8.5) [107],

or tri-modal $pK_{a,s}$ (3.8, 5.2, 9) [117], highlighting the importance of having a tool that can resolve locally the differences in $pK_{a,s}$. It is for the first time that a whole spectrum of $pK_{a,s}$ values is reported, encompassing different $pK_{a,s}$ values in the literature both from experimental [107, 117, 201], and from theoretical studies [116, 118]. We attribute the spectrum of measured $pK_{a,s}$ values to the fact that in our experiment we were able to spatially resolve details small as ~ 400x400 nm, while previous studies measured mainly the spatially-averaged surface response from a single spot. In Chapter 3, we also demonstrated the ability to image the orientation of bulk water molecules under an externally-applied electric field in the 1 μm-sized pore of the glass microcapillary in real time with 250 ms resolution.

In Chapter 4, we combined SH imaging with cyclic voltammetry to map the surface of gold polycrystalline and nanocrystalline electrodes during electro-oxidation, and to quantify the spatial extent of surface reconstruction during potential cycling. We analyzed the voltage-dependence of the SH signal on a pixel-wise level for the polycrystalline gold, uncovering heterogeneity in the form of two types of surface areas. The first type comprises ~ 60% of the surface, and the SH signal has a positive quadratic dependence with increasing bias in the potential range of 0 - 0.4 V vs. the reverse hydrogen electrode (RHE), reported also in prior studies. The SH intensity here is related to the electronic polarization contributions at the metal/electrolyte interface. The second type composes ~ 40% of the surface, and the SH signal has a negative quadratic dependence in the same potential range, which has not been reported before. Interestingly, no such areas are observed on the homogeneous (nanocrystalline) gold surface. We find that the second type shows the largest changes during successive cyclic voltammetry (CV) sweeps. This is further confirmed by the correlation-coefficient analysis, which correlates the SH potential-dependent signal in the successive CV sweeps on a pixel-wise level. To our knowledge, this is the first study applying the correlation-coefficient analysis to the SH imaging. We assign these second type of gold surface areas, which are prone to potential-induced surface restructuring, to domains of higher roughness where anion adsorption occurs at lower potentials than expected, based on the cyclic voltammetry of the whole gold electrode. Our analysis further reveals that the boundary between the first and second type of surface area displays higher second-order susceptibility, as well as the highest changes in the ratio of the second- vs. the third-order susceptibility between successive potential cycles, indicating a strong potential-dependent surface reconstruction.

In Chapter 5, we combined SH imaging and electrochemical methods to study the oxygen evolution reaction (OER) activity on polycrystalline gold working electrodes. We find that the OER displays a strong spatial heterogeneity, as < 1% of the electrode surface is active with respect to the OER. Additionally, we reveal that there are two types of active sites for oxygen evolution. The first is observed at potentials positive of the OER onset, and is stable under potential cycling; thus, we presume it extends multiple layers into the bulk gold electrode. The second type is observed at potentials negative of the OER onset, and is removed by potential cycling, suggesting it involves a structural motif only 1-2 gold layers deep. The second type of active site is most easily understood as the catalytically active species (hydrous oxide) in the so-called incipient hydrous oxide/adatom mediator model of electrocatalysis. In this study, we address the issue of separating the spatial heterogeneity of oxidation and the OER on gold, which is a crucial element for optimization of OER catalysts.

6.2 Outlook

The optimization of (electro)catalysts' efficiency is nowadays still approached mostly on an empirical level. The missing key is the lack of knowledge to tie specific surface structures to specific mechanisms of chemical reactions. This is due to the fact that research reports generally focus on model systems, i.e.,

crystal structures. However, virtually all the industrially-used (electro)catalysts display very complex and morphologically rough surfaces. This thesis is a step towards understanding the relationship of surface structure vs. chemical function by studying the surface heterogeneity and its spatio-temporal evolution on complex surfaces.

In Chapter 3, we showed how surface heterogeneity at the glass/electrolyte interface influences the local properties: locally-resolved acid dissociation constants $K_{a,s}$ for the silica deprotonation reaction vary over 9 orders of magnitude. Considering such large heterogeneity is important in the industrial context where surface engineering of glass can determine its function; it could be of particular interest for functional glass-ceramic applications [312], smart windows [313], or possibly liquid crystal displays [314]. Therefore, our future aim will be to characterize planar, rather than curved, glass/electrolyte interfaces. Additionally, in Chapter 3, we demonstrated the ability to probe bulk water structure in the confinement of a glass micro-capillary tip under an external electric field. This model system makes a good candidate for studying the properties of confined water molecules, such as in cells or characterizing electroosmotic nanojets [180].

In Chapter 4, we demonstrated the ability of SH imaging to distinguish between polycrystalline gold surface areas undergoing surface reconstruction. The identifying of areas that undergo surface reconstruction was achieved without the exact knowledge of the surface structure. However, a better understanding of specific surface adsorption effects would be possible if we also combine our SH analysis with the knowledge of the material's structure, as for example the crystalline facets [127, 238, 239]. The issue with this approach is that the surface structure would have to be obtained in-situ in the electrochemical cell, as it can reconstruct under different conditions. To solve this problem, our future aim will be to perform an additional step of nonlinear azimuthal polarimetry in our measurements that could spatially resolve surface symmetries, therefore, estimating the corresponding surface facets.

In Chapter 5, we showed that there are two types of active sites for OER on the polycrystalline gold electrode. The first type is observed at potentials > 2 V vs. RHE (the onset of OER); therefore, it is not energetically appealing for industrial purposes, unless the surface could be densely populated with these active sites. The second type is observed at potentials < 2 V vs. RHE, and thus, holds great promise for industrial applications. However, the second type is not stable under electrochemical cycling. The crucial step will be to first engineer the catalyst surface in a manner that the second type of active sites persists during the potential cycling. An idea for such a mechanism is hypothesized here: active sites could potentially traverse on the surface by surface reconstruction at every electrochemical cycle; this would, of course, require an appropriate surface engineering. Future hypothesis and experimental testing will require a tool to identify the second type of active sites before they participate in the OER. It would be, therefore, interesting to see in our future experiments if surface spots identified based on the analysis presented in chapter 4 would coincide with the active sites for the OER in Chapter 5. Such an agreement would make the wide-field SH imaging an indispensable tool for (electro)chemistry.

Lastly, with the current environmental situation on our planet, we will need to explore new pathways to optimize the energetic consumption of technological processes, and to reduce global warming. Research in this thesis is just a small step among many towards this goal, but it gives hope for a greener future.

7 List of Publications

This thesis is based on the following publications:

Chapter 3

Macias-Romero, C.; **Nahalka, I.**; Okur, H. I.; Roke, S. Optical Imaging of Surface Chemistry and Dynamics in Confinement. *Science.* **2017**, *357*, 784–788.

Chapter 4

I. Nahalka[1], G. Zwaschka[1], R. K. Campen, A. Marchioro, and S. Roke. Submitted (2020).

Chapter 5

Zwaschka[1], **I. Nahalka**[1], A. Marchioro, Y. Tong, S. Roke, and R. K. Campen. Imaging the Heterogeneity of the Oxygen Evolution Reaction on Gold Electrodes Operando: Activity is Highly Local. *ACS Catalysis.* **2020**, *10*, 6084–6093.

Bibliography

[1] Sadhu K. Kolekar, Anjani Dubey, Kalyani S. Date, Suwarna Datar, and Chinnakonda S. Gopinath. An attempt to correlate surface physics with chemical properties: molecular beam and Kelvin probe investigations of $Ce_{1-x}Zr_xO_2$ thin films. *Physical Chemistry Chemical Physics*, 18(39):27594–27602, 2016.

[2] Henry Wise. *Material Concepts in Surface Reactivity and Catalysis*. Academic Press, Inc., 1990.

[3] Junwu Xiao, Qin Kuang, Shihe Yang, Fei Xiao, Shuai Wang, and Lin Guo. Surface Structure Dependent Electrocatalytic Activity of Co_3O_4 Anchored on Graphene Sheets toward Oxygen Reduction Reaction. *Scientific Reports*, 3(1):2300, dec 2013.

[4] John Turner, George Sverdrup, Margaret K. Mann, Pin-Ching Maness, Ben Kroposki, Maria Ghirardi, Robert J. Evans, and Dan Blake. Renewable hydrogen production. *International Journal of Energy Research*, 32(5):379–407, apr 2008.

[5] Steven Chu and Arun Majumdar. Opportunities and challenges for a sustainable energy future. *Nature*, 488(7411):294–303, aug 2012.

[6] Nathan S. Lewis and Daniel G. Nocera. Powering the planet: Chemical challenges in solar energy utilization. *Proceedings of the National Academy of Sciences*, 103(43):15729–15735, oct 2006.

[7] Jose M. Campos-Martin, Gema Blanco-Brieva, and Jose L. G. Fierro. Hydrogen Peroxide Synthesis: An Outlook beyond the Anthraquinone Process. *Angewandte Chemie International Edition*, 45(42):6962–6984, oct 2006.

[8] George .A. Olah, Alain Goeppert, and G.K. Surya Prakash. *Beyond Oil and Gas: The Methanol Economy*. John Wiley & Sons, 2nd edition, 2018.

[9] Zhi Wei Seh, Jakob Kibsgaard, Colin F. Dickens, Ib Chorkendorff, Jens K. Nørskov, and Thomas F. Jaramillo. Combining theory and experiment in electrocatalysis: Insights into materials design. *Science*, 355(6321):eaad4998, jan 2017.

[10] Yan Jiao, Yao Zheng, Mietek Jaroniec, and Shi Zhang Qiao. Design of electrocatalysts for oxygen- and hydrogen-involving energy conversion reactions. *Chemical Society Reviews*, 44(8):2060–2086, 2015.

[11] Jesse D. Benck, Thomas R. Hellstern, Jakob Kibsgaard, Pongkarn Chakthranont, and Thomas F. Jaramillo. Catalyzing the Hydrogen Evolution Reaction (HER) with Molybdenum Sulfide Nanomaterials. *ACS Catalysis*, 4(11):3957–3971, nov 2014.

[12] X. H. Wu, L. M. Brown, D. Kapolnek, S. Keller, B. Keller, S. P. DenBaars, and J. S. Speck. Defect structure of metal-organic chemical vapor deposition-grown epitaxial (0001) GaN/Al_2O_3. *Journal of Applied Physics*, 80(6):3228–3237, sep 1996.

[13] Stephen A. Morin and Song Jin. Screw Dislocation-Driven Epitaxial Solution Growth of ZnO Nanowires Seeded by Dislocations in GaN Substrates. *Nano Letters*, 10(9):3459–3463, sep 2010.

[14] Robert Schlögl. Heterogeneous Catalysis. *Angewandte Chemie International Edition*, 54(11):3465–3520, mar 2015.

[15] M. Mavrikakis, B. Hammer, and J. K. Nørskov. Effect of Strain on the Reactivity of Metal Surfaces. *Physical Review Letters*, 81(13):2819–2822, sep 1998.

[16] Peter Strasser, Shirlaine Koh, Toyli Anniyev, Jeff Greeley, Karren More, Chengfei Yu, Zengcai Liu, Sarp Kaya, Dennis Nordlund, Hirohito Ogasawara, Michael F. Toney, and Anders Nilsson. Lattice-strain control of the activity in dealloyed core–shell fuel cell catalysts. *Nature Chemistry*, 2(6):454–460, jun 2010.

[17] D. Sekiba, Y. Yoshimoto, K. Nakatsuji, Y. Takagi, T. Iimori, S. Doi, and F. Komori. Strain-induced change in electronic structure of Cu(100). *Physical Review B*, 75(11):115404, mar 2007.

[18] Jonas H. K. Pfisterer, Yunchang Liang, Oliver Schneider, and Aliaksandr S. Bandarenka. Direct instrumental identification of catalytically active surface sites. *Nature*, 549(7670):74–77, sep 2017.

[19] Britt Hvolbæk, Ton V.W. Janssens, Bjerne S Clausen, Hanne Falsig, Claus H Christensen, and Jens K. Nørskov. Catalytic activity of Au nanoparticles. *Nano Today*, 2(4):14–18, aug 2007.

[20] N. Lopez, T. V. W. Janssens, B. S. Clausen, Y. Xu, M. Mavrikakis, T. Bligaard, and Jens K. Nørskov. On the origin of the catalytic activity of gold nanoparticles for low-temperature CO oxidation. *Journal of Catalysis*, 223(1):232–235, apr 2004.

[21] H.-J. Qiu, Hai-Tao Xu, Li Liu, and Yu Wang. Correlation of the structure and applications of dealloyed nanoporous metals in catalysis and energy conversion/storage. *Nanoscale*, 7(2):386–400, 2015.

[22] J. Biener, A. Wittstock, L. A. Zepeda-Ruiz, M. M. Biener, V. Zielasek, D. Kramer, R. N. Viswanath, J. Weissmüller, M. Bäumer, and A. V. Hamza. Surface-chemistry-driven actuation in nanoporous gold. *Nature Materials*, 8(1):47–51, jan 2009.

[23] Hai-Jun Jin, Xiao-Lan Wang, Smrutiranjan Parida, Ke Wang, Masahiro Seo, and Jörg Weissmüller. Nanoporous Au-Pt Alloys As Large Strain Electrochemical Actuators. *Nano Letters*, 10(1):187–194, jan 2010.

[24] Ankur Gupta, Kunal Mondal, Ashutosh Sharma, and Shantanu Bhattacharya. Superhydrophobic polymethylsilsesquioxane pinned one dimensional ZnO nanostructures for water remediation through photo-catalysis. *RSC Advances*, 5(57):45897–45907, 2015.

[25] Kingo Itaya and Eisuke Tomita. Scanning tunneling microscope for electrochemistry - a new concept for the in situ scanning tunneling microscope in electrolyte solutions. *Surface Science*, 201(3):L507–L512, jul 1988.

[26] Albertus D. Handoko, Fengxia Wei, Jenndy, Boon Siang Yeo, and Zhi Wei Seh. Understanding heterogeneous electrocatalytic carbon dioxide reduction through operando techniques. *Nature Catalysis*, 1(12):922–934, dec 2018.

[27] Carlos Macias-Romero, Igor Nahalka, Halil I Okur, and Sylvie Roke. Optical imaging of surface chemistry and dynamics in confinement. *Science*, 357(6353):784–788, aug 2017.

[28] R. J. Hamers, R. M. Tromp, and J. E. Demuth. Surface Electronic Structure of Si (111)-(7×7) Resolved in Real Space. *Physical Review Letters*, 56(18):1972–1975, may 1986.

[29] Philippe Wernet. Electronic structure in real time: mapping valence electron rearrangements during chemical reactions. *Physical Chemistry Chemical Physics*, 13(38):16941, 2011.

[30] Sayantan Mahapatra, Yingying Ning, Jeremy F. Schultz, Linfei Li, Jun-Long Zhang, and Nan Jiang. Angstrom Scale Chemical Analysis of Metal Supported Trans - and Cis -Regioisomers by Ultrahigh Vacuum Tip-Enhanced Raman Mapping. *Nano Letters*, 19(5):3267–3272, may 2019.

[31] Jonas H. K. Pfisterer, Masoud Baghernejad, Giovanni Giuzio, and Katrin F Domke. Reactivity mapping of nanoscale defect chemistry under electrochemical reaction conditions. *Nature Communications*, 10(1):5702, dec 2019.

[32] Matthijs A. van Spronsen, Joost W. M. Frenken, and Irene M. N. Groot. Observing the oxidation of platinum. *Nature Communications*, 8(1):429, dec 2017.

[33] Allen J. Bard, Fu Ren F. Fan, Juhyoun Kwak, and Ovadia Lev. Scanning electrochemical microscopy. Introduction and principles. *Analytical Chemistry*, 61(2):132–138, jan 1989.

[34] Shigeru Amemiya, Allen J. Bard, Fu-Ren F. Fan, Michael V. Mirkin, and Patrick R. Unwin. Scanning Electrochemical Microscopy. *Annual Review of Analytical Chemistry*, 1(1):95–131, jul 2008.

[35] Tianhan Kai, Cynthia G. Zoski, and Allen J. Bard. Scanning electrochemical microscopy at the nanometer level. *Chemical Communications*, 54(16):1934–1947, 2018.

[36] Fu-Ren F. Fan, Biao Liu, and Janine Mauzeroll. Scanning Electrochemical Microscopy. In *Handbook of Electrochemistry*, pages 471–540. Elsevier, 2007.

[37] Allen J. Bard and Michael V. Mirkin, editors. *Scanning Electrochemical Microscopy*. CRC Press, apr 2012.

[38] Jiyeon Kim, Christophe Renault, Nikoloz Nioradze, Netzahualcóyotl Arroyo-Currás, Kevin C. Leonard, and Allen J. Bard. Electrocatalytic Activity of Individual Pt Nanoparticles Studied by Nanoscale Scanning Electrochemical Microscopy. *Journal of the American Chemical Society*, 138(27):8560–8568, jul 2016.

[39] Peng Sun, François O. Laforge, Thushara P. Abeyweera, Susan A. Rotenberg, James Carpino, and Michael V. Mirkin. Nanoelectrochemistry of mammalian cells. *Proceedings of the National Academy of Sciences*, 105(2):443–448, jan 2008.

[40] J. R. Hahn and W. Ho. Oxidation of a Single Carbon Monoxide Molecule Manipulated and Induced with a Scanning Tunneling Microscope. *Physical Review Letters*, 87(16):166102, sep 2001.

[41] Paul K. Hansma and Jerry Tersoff. Scanning tunneling microscopy. *Journal of Applied Physics*, 61(2):R1–R24, jan 1987.

[42] Holger Wolfschmidt, Daniel Weingarth, and Ulrich Stimming. Enhanced Reactivity for Hydrogen Reactions at Pt Nanoislands on Au(111). *ChemPhysChem*, 11(7):1533–1541, may 2010.

[43] Ajay Kumar Yagati, Junhong Min, and Jeong-Woo Choi. Electrochemical Scanning Tunneling Microscopy (ECSTM) – From Theory to Future Applications. In *Modern Electrochemical Methods in Nano, Surface and Corrosion Science*. InTech, jun 2014.

[44] Franz J. Giessibl. Advances in atomic force microscopy. *Reviews of Modern Physics*, 75(3):949–983, jul 2003.

[45] Rob Atkin, Sherif Zein El Abedin, Robert Hayes, Luiz H. S. Gasparotto, Natalia Borisenko, and Frank Endres. AFM and STM Studies on the Surface Interaction of [BMP]TFSA and [EMIm]TFSA Ionic Liquids with Au(111). *The Journal of Physical Chemistry C*, 113(30):13266–13272, jul 2009.

[46] Melania Reggente, Daniele Passeri, Marco Rossi, Emanuela Tamburri, and Maria Letizia Terranova. Electrochemical atomic force microscopy: In situ monitoring of electrochemical processes. In *AIP Conference Proceedings*, volume 1873, page 020009, 2017.

[47] Rui Wen, Misun Hong, and Hye Ryung Byon. In Situ AFM Imaging of Li-O_2 Electrochemical Reaction on Highly Oriented Pyrolytic Graphite with Ether-Based Electrolyte. *Journal of the American Chemical Society*, 135(29):10870–10876, jul 2013.

[48] Can Liu and Shen Ye. In Situ Atomic Force Microscopy (AFM) Study of Oxygen Reduction Reaction on a Gold Electrode Surface in a Dimethyl Sulfoxide (DMSO)-Based Electrolyte Solution. *The Journal of Physical Chemistry C*, 120(44):25246–25255, nov 2016.

[49] Ali Eftekhari, editor. *Nanostructured Conductive Polymers*. John Wiley & Sons, Ltd, Chichester, UK, jul 2010.

[50] Z. L. Wang. Transmission Electron Microscopy of Shape-Controlled Nanocrystals and Their Assemblies. *The Journal of Physical Chemistry B*, 104(6):1153–1175, feb 2000.

[51] Ludwig Reimer. *Transmission Electron Microscopy: Physics of Image Formation and Microanalysis*, volume 36 of *Springer Series in Optical Sciences*. Springer Berlin Heidelberg, Berlin, Heidelberg, 1997.

[52] M. H. Nielsen, S. Aloni, and J. J. De Yoreo. In situ TEM imaging of $CaCO_3$ nucleation reveals coexistence of direct and indirect pathways. *Science*, 345(6201):1158–1162, sep 2014.

[53] M. J. Williamson, R. M. Tromp, P. M. Vereecken, R. Hull, and F. M. Ross. Dynamic microscopy of nanoscale cluster growth at the solid–liquid interface. *Nature Materials*, 2(8):532–536, aug 2003.

[54] Byung Hyo Kim, Jiwoong Yang, Donghoon Lee, Back Kyu Choi, Taeghwan Hyeon, and Jungwon Park. Liquid-Phase Transmission Electron Microscopy for Studying Colloidal Inorganic Nanoparticles. *Advanced Materials*, 30(4):1703316, jan 2018.

[55] J. J. De Yoreo and Sommerdijk N. A. J. M. Investigating materials formation with liquid-phase and cryogenic TEM. *Nature Reviews Materials*, 1(8):16035, aug 2016.

[56] John R. Ferraro, Kazuo Nakamoto, and Chris W. Brown. *Introductory Raman Spectroscopy*. Elsevier, 2003.

[57] Robin R. Jones, David C. Hooper, Liwu Zhang, Daniel Wolverson, and Ventsislav K. Valev. Raman Techniques: Fundamentals and Frontiers. *Nanoscale Research Letters*, 14(1):231, dec 2019.

[58] Michiel Müller and Juleon M. Schins. Imaging the Thermodynamic State of Lipid Membranes with Multiplex CARS Microscopy. *The Journal of Physical Chemistry B*, 106(14):3715–3723, apr 2002.

[59] Ji-Xin Cheng, Y. Kevin Jia, Gengfeng Zheng, and X. Sunney Xie. Laser-Scanning Coherent Anti-Stokes Raman Scattering Microscopy and Applications to Cell Biology. *Biophysical Journal*, 83(1):502–509, jul 2002.

[60] Bertrand M. Lucotte, Chloe Powell, Jay R. Knutson, Christian A. Combs, Daniela Malide, Zu-Xi Yu, Mark Knepper, Keval D. Patel, Anna Pielach, Errin Johnson, Lyudmyla Borysova, Kim A. Dora, and Robert S. Balaban. Direct visualization of the arterial wall water

permeability barrier using CARS microscopy. *Proceedings of the National Academy of Sciences*, 114(18):4805–4810, may 2017.

[61] Johanna Trägårdh, Tomáš Pikálek, Mojmír Šerý, Tobias Meyer, Jürgen Popp, and Tomáš Čižmár. Label-free CARS microscopy through a multimode fiber endoscope. *Optics Express*, 27(21):30055, oct 2019.

[62] E. Ploetz, S. Laimgruber, S. Berner, W. Zinth, and P. Gilch. Femtosecond stimulated Raman microscopy. *Applied Physics B*, 87(3):389–393, may 2007.

[63] Christian W. Freudiger, Wei Min, Brian G. Saar, Sijia Lu, Gary R. Holtom, Chengwei He, Jason C. Tsai, Jing X. Kang, and X. Sunney Xie. Label-Free Biomedical Imaging with High Sensitivity by Stimulated Raman Scattering Microscopy. *Science*, 322(5909):1857–1861, dec 2008.

[64] Dan Fu, Fa-Ke Lu, Xu Zhang, Christian Freudiger, Douglas R. Pernik, Gary Holtom, and Xiaoliang Sunney Xie. Quantitative Chemical Imaging with Multiplex Stimulated Raman Scattering Microscopy. *Journal of the American Chemical Society*, 134(8):3623–3626, feb 2012.

[65] Sylvie Roke and Grazia Gonella. Nonlinear Light Scattering and Spectroscopy of Particles and Droplets in Liquids. *Annual Review of Physical Chemistry*, 63(1):353–378, may 2012.

[66] W. Robert Boyd. *Nonlinear Optics*. Elsevier, 3rd edition, 2008.

[67] Shixin Huang, Mohamadamin Makarem, Sarah N. Kiemle, Hossein Hamedi, Moujhuri Sau, Daniel J. Cosgrove, and Seong H. Kim. Inhomogeneity of Cellulose Microfibril Assembly in Plant Cell Walls Revealed with Sum Frequency Generation Microscopy. *The Journal of Physical Chemistry B*, 122(19):5006–5019, may 2018.

[68] Haoyuan Wang, Tian Gao, and Wei Xiong. Self-Phase-Stabilized Heterodyne Vibrational Sum Frequency Generation Microscopy. *ACS Photonics*, 4(7):1839–1845, jul 2017.

[69] Desheng Zheng, Liyang Lu, Kevin F. Kelly, and Steven Baldelli. Chemical Imaging of Self-Assembled Monolayers on Copper Using Compressive Hyperspectral Sum Frequency Generation Microscopy. *The Journal of Physical Chemistry B*, 122(2):464–471, jan 2018.

[70] Katherine A. Cimatu and Steven Baldelli. Chemical Microscopy of Surfaces by Sum Frequency Generation Imaging. *The Journal of Physical Chemistry C*, 113(38):16575–16588, sep 2009.

[71] Elsa C. Y. Yan, Yan Liu, and Kenneth B. Eisenthal. New Method for Determination of Surface Potential of Microscopic Particles by Second Harmonic Generation. *The Journal of Physical Chemistry B*, 102(33):6331–6336, aug 1998.

[72] Raju R. Kumal, Tony E. Karam, and Louis H. Haber. Determination of the Surface Charge Density of Colloidal Gold Nanoparticles Using Second Harmonic Generation. *The Journal of Physical Chemistry C*, 119(28):16200–16207, jul 2015.

[73] Jacek Lipkowski, Zhichao Shi, Aicheng Chen, Bruno Pettinger, and Christoph Bilger. Ionic adsorption at the Au(111) electrode. *Electrochimica Acta*, 43(19-20):2875–2888, jun 1998.

[74] Daniel A Dombeck, Mireille Blanchard-Desce, and Watt W. Webb. Optical Recording of Action Potentials with Second-Harmonic Generation Microscopy. *Journal of Neuroscience*, 24(4):999–1003, jan 2004.

[75] Junhui Shi, Terence T. W. Wong, Yun He, Lei Li, Ruiying Zhang, Christopher S. Yung, Jeeseong Hwang, Konstantin Maslov, and Lihong V. Wang. High-resolution, high-contrast mid-infrared imaging of fresh biological samples with ultraviolet-localized photoacoustic microscopy. *Nature Photonics*, 13(9):609–615, sep 2019.

[76] Xiaowei Liu, Terence T. W. Wong, Junhui Shi, Jun Ma, Qing Yang, and Lihong V. Wang. Label-free cell nuclear imaging by Grüneisen relaxation photoacoustic microscopy. *Optics Letters*, 43(4):947, feb 2018.

[77] Kiran Mathew, Chen Zheng, Donald Winston, Chi Chen, Alan Dozier, John J. Rehr, Shyue Ping Ong, and Kristin A. Persson. High-throughput computational X-ray absorption spectroscopy. *Scientific Data*, 5(1):180151, dec 2018.

[78] Max Wilke, François Farges, Pierre-Emmanuel Petit, Gordon E. Brown, and François Martin. Oxidation state and coordination of Fe in minerals: An Fe K- XANES spectroscopic study. *American Mineralogist*, 86(5-6):714–730, may 2001.

[79] B. E. Etschmann, C. G. Ryan, J. Brugger, R. Kirkham, R. M. Hough, G. Moorhead, D. P. Siddons, G. De Geronimo, A. Kuczewski, P. Dunn, D. Paterson, M. D. de Jonge, D. L. Howard, P. Davey, and M. Jensen. Reduced As components in highly oxidized environments: Evidence from full spectral XANES imaging using the Maia massively parallel detector. *American Mineralogist*, 95(5-6):884–887, may 2010.

[80] Daniela Leanza. *New perception of electrode-electrolyte interfaces in Li-ion batteries enabled by XPEEM spectromicroscopy*. PhD thesis, ETH Zurich, 2019.

[81] Juan J. Velasco-Velez, Verena Pfeifer, Michael Hävecker, Robert S. Weatherup, Rosa Arrigo, Cheng-Hao Chuang, Eugen Stotz, Gisela Weinberg, Miquel Salmeron, Robert Schlögl, and Axel Knop-Gericke. Photoelectron Spectroscopy at the Graphene-Liquid Interface Reveals the Electronic Structure of an Electrodeposited Cobalt/Graphene Electrocatalyst. *Angewandte Chemie International Edition*, 54(48):14554–14558, nov 2015.

[82] Daniela Leanza, Carlos A. F. Vaz, Izabela Czekaj, Petr Novák, and Mario El Kazzi. Solving the puzzle of $Li_4Ti_5O_{12}$ surface reactivity in aprotic electrolytes in Li-ion batteries by nanoscale XPEEM spectromicroscopy. *Journal of Materials Chemistry A*, 6(8):3534–3542, 2018.

[83] M. Salomo, S.E. Pust, G. Wittstock, and E. Oesterschulze. Integrated cantilever probes for SECM/AFM characterization of surfaces. *Microelectronic Engineering*, 87(5-8):1537–1539, may 2010.

[84] Julie V. Macpherson and Patrick R. Unwin. Noncontact Electrochemical Imaging with Combined Scanning Electrochemical Atomic Force Microscopy. *Analytical Chemistry*, 73(3):550–557, feb 2001.

[85] Jeyavel Velmurugan, Amit Agrawal, Sangmin An, Eric Choudhary, and Veronika A. Szalai. Fabrication of Scanning Electrochemical Microscopy-Atomic Force Microscopy Probes to Image Surface Topography and Reactivity at the Nanoscale. *Analytical Chemistry*, 89(5):2687–2691, mar 2017.

[86] Julie V. Macpherson and Patrick R. Unwin. Combined Scanning Electrochemical-Atomic Force Microscopy. *Analytical Chemistry*, 72(2):276–285, jan 2000.

[87] Prabhat Verma. Tip-Enhanced Raman Spectroscopy: Technique and Recent Advances. *Chemical Reviews*, 117(9):6447–6466, may 2017.

[88] Bruno Pettinger, Gennaro Picardi, Rolf Schuster, and Gerhard Ertl. Surface-enhanced and STM-tip-enhanced Raman Spectroscopy at Metal Surfaces. *Single Molecules*, 3(5-6):285–294, nov 2002.

[89] Zhi-Cong Zeng, Sheng-Chao Huang, De-Yin Wu, Ling-Yan Meng, Mao-Hua Li, Teng-Xiang Huang, Jin-Hui Zhong, Xiang Wang, Zhi-Lin Yang, and Bin Ren. Electrochemical Tip-Enhanced Raman Spectroscopy. *Journal of the American Chemical Society*, 137(37):11928–11931, sep 2015.

[90] Kohta Saitoh, Atsushi Taguchi, and Satoshi Kawata. Correlative force and tip-enhanced Raman microscopy. *APL Photonics*, 4(2):021301, feb 2019.

[91] Naresh Kumar, Caterina S. Wondergem, Andrew J. Wain, and Bert M. Weckhuysen. In Situ Nanoscale Investigation of Catalytic Reactions in the Liquid Phase Using Zirconia-Protected Tip-Enhanced Raman Spectroscopy Probes. *The Journal of Physical Chemistry Letters*, 10(8):1669–1675, apr 2019.

[92] M. J. Rost. *High-speed electrochemical STM*. Elsevier, 2018.

[93] Timo Strahlendorff, Gaoliang Dai, Detlef Bergmann, and Rainer Tutsch. Tip wear and tip breakage in high-speed atomic force microscopes. *Ultramicroscopy*, 201(May 2018):28–37, jun 2019.

[94] Nynke A. Krans, N. Ahmad, D. Alloyeau, K.P. de Jong, and J. Zečević. Attachment of iron oxide nanoparticles to carbon nanofibers studied by in-situ liquid phase transmission electron microscopy. *Micron*, 117(October 2018):40–46, feb 2019.

[95] Catarina Costa Moura, Rahul S. Tare, Richard O. C. Oreffo, and Sumeet Mahajan. Raman spectroscopy and coherent anti-Stokes Raman scattering imaging: prospective tools for monitoring skeletal cells and skeletal regeneration. *Journal of The Royal Society Interface*, 13(118):20160182, may 2016.

[96] Li Li, Haifeng Wang, and Ji-Xin Cheng. Quantitative Coherent Anti-Stokes Raman Scattering Imaging of Lipid Distribution in Coexisting Domains. *Biophysical Journal*, 89(5):3480–3490, nov 2005.

[97] Barbara E. Etschmann, Erica Donner, Joël Brugger, Daryl L. Howard, Martin D. de Jonge, David Paterson, Ravi Naidu, Kirk G. Scheckel, Chris G. Ryan, and Enzo Lombi. Speciation mapping of environmental samples using XANES imaging. *Environmental Chemistry*, 11(3):341, 2014.

[98] Lucia Aballe, Michael Foerster, Meritxell Cabrejo, Jordi Prat, Paolo Pittana, Rudi Sergo, Matteo Lucian, Maurizio Barnaba, Tevfik Onur Menteş, and Andrea Locatelli. Pulse picking in synchrotron-based XPEEM. *Ultramicroscopy*, 202(December 2018):10–17, jul 2019.

[99] Srikanth Kolagatla, Palaniappan Subramanian, and Alex Schechter. Nanoscale mapping of catalytic hotspots on Fe, N-modified HOPG by scanning electrochemical microscopy-atomic force microscopy. *Nanoscale*, 10(15):6962–6970, 2018.

[100] Thomas Touzalin, Suzanne Joiret, Ivan T. Lucas, and Emmanuel Maisonhaute. Electrochemical tip-enhanced Raman spectroscopy imaging with 8 nm lateral resolution. *Electrochemistry Communications*, 108(September):106557, nov 2019.

[101] P. A. Franken, A. E. Hill, C. W. Peters, and G. Weinreich. Generation of Optical Harmonics. *Physical Review Letters*, 7(4):118–119, aug 1961.

[102] Orly B. Tarun. *Dynamic Imaging of Lipid Membranes by Means of Water*. PhD thesis, École Polytechnique Fédérale de Lausanne, 2019.

[103] Alex G. Lambert, Paul B. Davies, and David J. Neivandt. Implementing the Theory of Sum Frequency Generation Vibrational Spectroscopy: A Tutorial Review. *Applied Spectroscopy Reviews*, 40(2):103–145, may 2005.

[104] Y. R. Shen. *The Principles of Nonlinear Optics*. Wiley-Interscience, 1st edition, 2002.

[105] Fielding Brown and Masahiro Matsuoka. Effect of Adsorbed Surface Layers on Second-Harmonic Light from Silver. *Physical Review*, 185(3):985–987, sep 1969.

[106] H. Wang, E.C.Y. Yan, E. Borguet, and K.B. Eisenthal. Second harmonic generation from the surface of centrosymmetric particles in bulk solution. *Chemical Physics Letters*, 259(1-2):15–20, aug 1996.

[107] Shaowei Ong, Xiaolin Zhao, and Kenneth B. Eisenthal. Polarization of water molecules at a charged interface: second harmonic studies of the silica/water interface. *Chemical Physics Letters*, 191(3-4):327–335, apr 1992.

[108] Cornelis Lütgebaucks, Grazia Gonella, and Sylvie Roke. Optical label-free and model-free probe of the surface potential of nanoscale and microscopic objects in aqueous solution. *Physical Review B*, 94(19):195410, nov 2016.

[109] Cornelis Lütgebaucks, Carlos Macias-Romero, and Sylvie Roke. Characterization of the interface of binary mixed DOPC:DOPS liposomes in water: The impact of charge condensation. *The Journal of Chemical Physics*, 146(4):044701, jan 2017.

[110] Orly B. Tarun, Christof Hannesschläger, Peter Pohl, and Sylvie Roke. Label-free and charge-sensitive dynamic imaging of lipid membrane hydration on millisecond time scales. *Proceedings of the National Academy of Sciences*, 115(16):4081–4086, apr 2018.

[111] David L. Andrews, Philip Allcock, and Andrey A. Demidov. Theory of second harmonic generation in randomly oriented species. *Chemical Physics*, 190(1):1–9, jan 1995.

[112] Horacio E. Bergna and William O. Roberts, editors. *Colloidal Silica: Fundamentals and Applications*. CRC Press, 1st edition, 2005.

[113] Christopher Corti and Richard Holliday, editors. *Gold: Science and Applications*. CRC Press, 2009.

[114] L.T. Zhuravlev. The surface chemistry of amorphous silica. Zhuravlev model. *Colloids and Surfaces A: Physicochemical and Engineering Aspects*, 173(1-3):1–38, nov 2000.

[115] Xiandong Liu, Jun Cheng, Xiancai Lu, and Rucheng Wang. Surface acidity of quartz: understanding the crystallographic control. *Phys. Chem. Chem. Phys.*, 16(48):26909–26916, nov 2014.

[116] Morgane Pfeiffer-Laplaud, Dominique Costa, Frederik Tielens, Marie-Pierre Gaigeot, and Marialore Sulpizi. Bimodal Acidity at the Amorphous Silica/Water Interface. *The Journal of Physical Chemistry C*, 119(49):27354–27362, dec 2015.

[117] Akemi M. Darlington and Julianne M. Gibbs-Davis. Bimodal or Trimodal? The Influence of Starting pH on Site Identity and Distribution at the Low Salt Aqueous/Silica Interface. *Journal of Physical Chemistry C*, 119(29):16560–16567, 2015.

[118] Kevin Leung, Ida M. B. Nielsen, and Louise J. Criscenti. Elucidating the Bimodal Acid-Base Behavior of the Water-Silica Interface from First Principles. *Journal of the American Chemical Society*, 131(51):18358–18365, dec 2009.

[119] Catherine Louis and Oliver Pluchery, editors. *Gold Nanoparticles for Physics, Chemistry and Biology*. World Scientific, 1st edition, 2012.

[120] N. Bloembergen. Second Harmonic Reflected Light. *Optica Acta: International Journal of Optics*, 13(4):311–322, oct 1966.

[121] A. Mugarza, A. Mascaraque, V. Pérez-Dieste, V. Repain, S. Rousset, F. J. García de Abajo, and J. E. Ortega. Electron Confinement in Surface States on a Stepped Gold Surface Revealed by Angle-Resolved Photoemission. *Physical Review Letters*, 87(10):107601, aug 2001.

[122] Francisco J. Rodriguez, Fu Xiang Wang, and Martti Kauranen. Calibration of the second-order nonlinear optical susceptibility of surface and bulk of glass. *Optics Express*, 16(12):8704, jun 2008.

[123] Debra Krause, Charles W. Teplin, and Charles T. Rogers. Optical surface second harmonic measurements of isotropic thin-film metals: Gold, silver, copper, aluminum, and tantalum. *Journal of Applied Physics*, 96(7):3626–3634, oct 2004.

[124] Jiří Homola. Electromagnetic Theory of Surface Plasmons. Number July, pages 3–44. 2006.

[125] Max Born and Emil Wolf. *Principles of Optics: Electromagnetic Theory of Propagation, Interference and Diffraction of Light*. Cambridge University Press, 1999.

[126] B. Pettinger, J. Lipkowski, S. Mirwald, and A. Friedrich. Specific adsorption at Au(111) electrodes studied by second harmonic generation. *Journal of Electroanalytical Chemistry*, 329(1-2):289–311, jul 1992.

[127] B Pettinger, S Mirwald, and J Lipkowski. In-situ SHG Studies of Ionic and Molecular Adsorption on Surface Structure of Au(111)-Electrodes. *Berichte der Bunsengesellschaft für physikalische Chemie*, 97(3):395–398, mar 1993.

[128] P. Guyot-Sionnest and A. Tadjeddine. Study of Ag(111) and Au(111) electrodes by optical second-harmonic generation. *The Journal of Chemical Physics*, 92(1):734–738, jan 1990.

[129] G L Richmond. Characterization of the silver-aqueous electrolyte interface by optical second harmonic generation. *Langmuir*, 2(2):132–139, mar 1986.

[130] C. Maurer, A. Jesacher, S. Bernet, and M. Ritsch-Marte. What spatial light modulators can do for optical microscopy. *Laser & Photonics Reviews*, 5(1):81–101, jan 2011.

[131] Navid Borhani, Eirini Kakkava, Christophe Moser, and Demetri Psaltis. Learning to see through multimode fibers. *Optica*, 5(8):960, aug 2018.

[132] Yonghong Shao, Wan Qin, Honghai Liu, Junle Qu, Xiang Peng, Hanben Niu, and Bruce Z. Gao. Addressable multiregional and multifocal multiphoton microscopy based on a spatial light modulator. *Journal of Biomedical Optics*, 17(3):030505, 2012.

[133] Volodymyr Nikolenko, O. Brendon Watson, Roberto Araya, Alan Woodruff, S. Darcy Peterka, and Rafael Yuste. SLM microscopy: scanless two-photon imaging and photostimulation using spatial light modulators. *Frontiers in Neural Circuits*, 2(DEC):1–14, 2008.

[134] Bo-Jui Chang, Li-Jun Chou, Yun-Ching Chang, and Su-Yu Chiang. Isotropic image in structured illumination microscopy patterned with a spatial light modulator. *Optics Express*, 17(17):14710, aug 2009.

[135] C Rullière. *Femtosecond Laser Pulses*. Advanced Texts in Physics. Springer New York, New York, NY, 2005.

[136] Warren R. Zipfel, Rebecca M. Williams, R. Christie, Alexander Yu Nikitin, Bradley T. Hyman, and Watt W. Webb. Live tissue intrinsic emission microscopy using multiphoton-excited native fluorescence and second harmonic generation. *Proceedings of the National Academy of Sciences*, 100(12):7075–7080, jun 2003.

[137] P.J. Campagnola and C.-Y. Dong. Second harmonic generation microscopy: principles and applications to disease diagnosis. *Laser & Photonics Reviews*, 5(1):13–26, jan 2011.

[138] Xiyi Chen, Oleg Nadiarynkh, Sergey Plotnikov, and Paul J Campagnola. Second harmonic generation microscopy for quantitative analysis of collagen fibrillar structure. *Nature Protocols*, 7(4):654–669, apr 2012.

[139] Daniel A. Dombeck, Leonardo Sacconi, Mireille Blanchard-Desce, and Watt W. Webb. Optical Recording of Fast Neuronal Membrane Potential Transients in Acute Mammalian Brain Slices by Second-Harmonic Generation Microscopy. *Journal of Neurophysiology*, 94(5):3628–3636, nov 2005.

[140] M. N. Shneider, A. A. Voronin, and A. M. Zheltikov. Action-potential-encoded second-harmonic generation as an ultrafast local probe for nonintrusive membrane diagnostics. *Physical Review E*, 81(3):031926, mar 2010.

[141] Guy Cox. Biological applications of second harmonic imaging. *Biophysical Reviews*, 3(3):131–141, sep 2011.

[142] Jingxin Cheng, Tao Jiang, Qingqing Ji, Yu Zhang, Zhiming Li, Yuwei Shan, Yanfeng Zhang, Xingao Gong, Weitao Liu, and Shiwei Wu. Kinetic Nature of Grain Boundary Formation in As-Grown MoS_2 Monolayers. *Advanced Materials*, 27(27):4069–4074, jul 2015.

[143] D. J. Clark, V. Senthilkumar, C. T. Le, D. L. Weerawarne, B. Shim, J. I. Jang, J. H. Shim, J. Cho, Y. Sim, M.-J. Seong, S. H. Rhim, A. J. Freeman, K.-H. Chung, and Y. S. Kim. Strong optical nonlinearity of CVD-grown MoS_2 monolayer as probed by wavelength-dependent second-harmonic generation. *Physical Review B*, 90(12):121409, sep 2014.

[144] D. J. Clark, C. T. Le, V. Senthilkumar, F. Ullah, H.-Y. Cho, Y. Sim, M.-J. Seong, K.-H. Chung, Y. S. Kim, and J. I. Jang. Near bandgap second-order nonlinear optical characteristics

of MoS_2 monolayer transferred on transparent substrates. *Applied Physics Letters*, 107(13):131113, sep 2015.

[145] Yici Guo, P. P. Ho, H. Savage, D. Harris, P. Sacks, S. Schantz, Feng Liu, N. Zhadin, and R. R. Alfano. Second-harmonic tomography of tissues. *Optics Letters*, 22(17):1323, sep 1997.

[146] J.I. Dadap, X.F. Hu, M. Russell, J.G. Ekerdt, J.K. Lowell, and M.C. Downer. Analysis of second-harmonic generation by unamplified, high-repetition-rate, ultrashort laser pulses at Si(001) interfaces. *IEEE Journal of Selected Topics in Quantum Electronics*, 1(4):1145–1155, 1995.

[147] Mark D. Peterson, Patrick L. Hayes, Imee Su Martinez, Laura C. Cass, Jennifer L. Achtyl, Emily A. Weiss, and Franz M. Geiger. Second harmonic generation imaging with a kHz amplifier. *Optical Materials Express*, 1(1):57, may 2011.

[148] Carlos Macias-Romero, Marie E. P. Didier, Vitalijs Zubkovs, Lucas Delannoy, Fabrizia Dutto, Aleksandra Radenovic, and Sylvie Roke. Probing Rotational and Translational Diffusion of Nanodoublers in Living Cells on Microsecond Time Scales. *Nano Letters*, 14(5):2552–2557, may 2014.

[149] Yuying Zhang, Meredith L. Akins, Kartikeya Murari, Jiefeng Xi, M.-J. Li, Katherine Luby-Phelps, Mala Mahendroo, and Xingde Li. A compact fiber-optic SHG scanning endomicroscope and its application to visualize cervical remodeling during pregnancy. *Proceedings of the National Academy of Sciences*, 109(32):12878–12883, aug 2012.

[150] Peter T.C. So, Elijah Y.S. Yew, and Christopher Rowlands. High-Throughput Nonlinear Optical Microscopy. *Biophysical Journal*, 105(12):2641–2654, dec 2013.

[151] Erich E. Hoover and Jeff A. Squier. Advances in multiphoton microscopy technology. *Nature Photonics*, 7(2):93–101, feb 2013.

[152] Ki Hean Kim, Christof Buehler, and Peter T C So. High-speed, two-photon scanning microscope. *Applied Optics*, 38(28):6004, oct 1999.

[153] Vijay Iyer, Tycho M. Hoogland, and Peter Saggau. Fast Functional Imaging of Single Neurons Using Random-Access Multiphoton (RAMP) Microscopy. *Journal of Neurophysiology*, 95(1):535–545, jan 2006.

[154] Carlos Macias-Romero, Marie E. P. Didier, Pascal Jourdain, Pierre Marquet, Pierre Magistretti, Orly B. Tarun, Vitalijs Zubkovs, Aleksandra Radenovic, and Sylvie Roke. High throughput second harmonic imaging for label-free biological applications. *Optics Express*, 22(25):31102, dec 2014.

[155] W. Sibbett, A. A. Lagatsky, and C. T. A. Brown. The development and application of femtosecond laser systems. *Optics Express*, 20(7):6989, mar 2012.

[156] Ursula Keller. Recent developments in compact ultrafast lasers. *Nature*, 424(6950):831–838, aug 2003.

[157] Daniel A. Dombeck, Karl A. Kasischke, Harshad D. Vishwasrao, Martin Ingelsson, Bradley T. Hyman, and Watt W. Webb. Uniform polarity microtubule assemblies imaged in native brain tissue by second-harmonic generation microscopy. *Proceedings of the National Academy of Sciences*, 100(12):7081–7086, jun 2003.

[158] Periklis Pantazis, James Maloney, David Wu, and Scott E. Fraser. Second harmonic generating (SHG) nanoprobes for in vivo imaging. *Proceedings of the National Academy of Sciences*, 107(33):14535–14540, aug 2010.

[159] Jonathan F. D. Liljeblad and Eric Tyrode. Vibrational Sum Frequency Spectroscopy Studies at Solid/Liquid Interfaces: Influence of the Experimental Geometry in the Spectral Shape and Enhancement. *The Journal of Physical Chemistry C*, 116(43):22893–22903, nov 2012.

[160] Y R Shen. Optical Second Harmonic Generation at Interfaces. *Annual Review of Physical Chemistry*, 40(1):327–350, oct 1989.

[161] T.F. Heinz. Second-Order Nonlinear Optical Effects at Surfaces and Interfaces. In H. E. Ponath and G. I. Stegeman, editors, *Nonlinear Surface Electromagnetic Phenomena*, chapter 5, pages 353–416. North-Holland, Amsterdam, 1991.

[162] Xing Wei, Seok-Cheol Hong, Xiaowei Zhuang, Tomohisa Goto, and Y. R. Shen. Nonlinear optical studies of liquid crystal alignment on a rubbed polyvinyl alcohol surface. *Physical Review E*, 62(4):5160–5172, oct 2000.

[163] Grazia Gonella, Cornelis Lütgebaucks, Alex G. F. de Beer, and Sylvie Roke. Second Harmonic and Sum-Frequency Generation from Aqueous Interfaces Is Modulated by Interference. *The Journal of Physical Chemistry C*, 120(17):9165–9173, may 2016.

[164] Nikolay Smolentsev. *Molecular-level characterization of curved water interfaces with sum frequency and second harmonic scattering*. PhD thesis, École Polytechnique Fédérale de Lausanne, 2017.

[165] J. F. Scott. Applications of Modern Ferroelectrics. *Science*, 315(5814):954–959, feb 2007.

[166] Eugene Kim, Andrea Steinbrück, Maria Teresa Buscaglia, Vincenzo Buscaglia, Thomas Pertsch, and Rachel Grange. Second-Harmonic Generation of Single $BaTiO_3$ Nanoparticles down to 22 nm Diameter. *ACS Nano*, 7(6):5343–5349, jun 2013.

[167] Gerhard Ertl, Helmut Knözinger, Ferdi Schüth, and Jens Weitkamp, editors. *Handbook Of Heterogeneous Catalysis 2., completely revised and enlarged Edition, Vol. 1-8*. Wiley-VCH Verlag GmbH & Co. KGaA, 2009.

[168] John O'M. Bockris and Shahed U. M. Khan. *Surface Electrochemistry: A molecular Level Approach*. Springer US, Boston, MA, 1993.

[169] Barbara Finlayson-Pitts and James Jr. Pitts. *Chemistry of the Upper and Lower Atmosphere*. Elsevier, 1st edition, 2000.

[170] Milan Mrksich. What can surface chemistry do for cell biology? *Current Opinion in Chemical Biology*, 6(6):794–797, dec 2002.

[171] John Zachara, Sue Brantley, Jon Chorover, Robert Ewing, Sebastien Kerisit, Chongxuan Liu, Edmund Perfect, Gernot Rother, and Andrew G. Stack. Internal Domains of Natural Porous Media Revealed: Critical Locations for Transport, Storage, and Chemical Reaction. *Environmental Science & Technology*, 50(6):2811–2829, mar 2016.

[172] Paul J.A. Kenis, Rustem F. Ismagilov, and George M. Whitesides. Microfabrication inside capillaries using multiphase laminar flow patterning. *Science*, 285(5424):83–85, 1999.

[173] Mira T. Guo, Assaf Rotem, John A. Heyman, and David A. Weitz. Droplet microfluidics for high-throughput biological assays. *Lab on a Chip*, 12(12):2146, 2012.

[174] Jean-Christophe Baret and Frieder Mugele. Electrical Discharge in Capillary Breakup: Controlling the Charge of a Droplet. *Physical Review Letters*, 96(1):016106, jan 2006.

[175] Frank H. J. van der Heyden, Derek Stein, and Cees Dekker. Streaming Currents in a Single Nanofluidic Channel. *Physical Review Letters*, 95(11):116104, sep 2005.

[176] Esther Amstad, Manesh Gopinadhan, Christian Holtze, Chinedum O. Osuji, Michael P. Brenner, Frans Spaepen, and David A. Weitz. Production of amorphous nanoparticles by supersonic spray-drying with a microfluidic nebulator. *Science*, 349(6251):956–960, aug 2015.

[177] Richard B.M. Schasfoort, Stefan Schlautmann, Jan Hendrikse, and Albert Van Den Berg. Field-effect row control for microfabricated fluidic networks. *Science*, 286(5441):942–945, 1999.

[178] L. J. Steinbock, O. Otto, D. R. Skarstam, S. Jahn, C. Chimerel, J. L. Gornall, and U. F. Keyser. Probing DNA with micro- and nanocapillaries and optical tweezers. *Journal of Physics: Condensed Matter*, 22(45):454113, nov 2010.

[179] Jie Zheng and Matthew C. Trudeau, editors. *Handbook of Ion Channels*. CRC Press, feb 2015.

[180] Nadanai Laohakunakorn, Benjamin Gollnick, Fernando Moreno-Herrero, Dirk G. A. L. Aarts, Roel P. A. Dullens, Sandip Ghosal, and Ulrich F. Keyser. A Landau–Squire Nanojet. *Nano Letters*, 13(11):5141–5146, nov 2013.

[181] Bruce E. Logan and Menachem Elimelech. Membrane-based processes for sustainable power generation using water. *Nature*, 488(7411):313–319, aug 2012.

[182] Jiandong Feng, Michael Graf, Ke Liu, Dmitry Ovchinnikov, Dumitru Dumcenco, Mohammad Heiranian, Vishal Nandigana, Narayana R. Aluru, Andras Kis, and Aleksandra Radenovic. Single-layer MoS_2 nanopores as nanopower generators. *Nature*, 536(7615):197–200, aug 2016.

[183] Bartosz A. Grzybowski and Wilhelm T. S. Huck. The nanotechnology of life-inspired systems. *Nature Nanotechnology*, 11(7):585–592, jul 2016.

[184] Emma L. DeWalt, Victoria J. Begue, Judith A. Ronau, Shane Z. Sullivan, Chittaranjan Das, and Garth J. Simpson. Polarization-resolved second-harmonic generation microscopy as a method to visualize protein-crystal domains. *Acta Crystallographica Section D Biological Crystallography*, 69(1):74–81, jan 2013.

[185] Mats G. L. Gustafsson, David A. Agard, and John W. Sedat. Doubling the lateral resolution of wide-field fluorescence microscopy using structured illumination. In Jose-Angel Conchello, Carol J. Cogswell, Andrew G. Tescher, and Tony Wilson, editors, *Three-Dimensional and Multidimensional Microscopy: Image Acquisition Processing VII*, volume 3919, pages 141–150, may 2000.

[186] Daryl Lim, Kengyeh K. Chu, and Jerome Mertz. Wide-field fluorescence sectioning with hybrid speckle and uniform-illumination microscopy. *Optics Letters*, 33(16):1819, aug 2008.

[187] Daryl Lim, Tim N. Ford, Kengyeh K. Chu, and Jerome Mertz. Optically sectioned in vivo imaging with speckle illumination HiLo microscopy. *Journal of Biomedical Optics*, 16(1):016014, 2011.

[188] Elijah Y. S. Yew, Colin J. R. Sheppard, and Peter T. C. So. Temporally focused wide-field two-photon microscopy: Paraxial to vectorial. *Optics Express*, 21(10):12951, may 2013.

[189] Chen Yuan Dong, Peter T. C. So, Jerome Mertz, Karsten Koenig, Chris Xu, and Paul Campagnola. Multiphoton Microscopy: Technical Innovations, Biological Applications, and Clinical Diagnostics. *Journal of Biomedical Optics*, 18(3):031101, apr 2013.

[190] Jarett Michaelson, Heejin Choi, Peter So, and Hayden Huang. Depth-resolved cellular microrheology using HiLo microscopy. *Biomedical Optics Express*, 3(6):1241, jun 2012.

[191] Jerome Mertz and Jinhyun Kim. Scanning light-sheet microscopy in the whole mouse brain with HiLo background rejection. *Journal of Biomedical Optics*, 15(1):016027, 2010.

[192] Elijah Y. S. Yew, Heejin Choi, Daekeun Kim, and Peter T. C. So. Wide-field two-photon microscopy with temporal focusing and HiLo background rejection. In Ammasi Periasamy, Karsten König, and Peter T. C. So, editors, *Multiphoton Microscopy in the Biomedical Sciences XI*, volume 7903, page 79031O, feb 2011.

[193] Silvia Santos, Kengyeh K. Chu, Daryl Lim, Nenad Bozinovic, Tim N. Ford, Claire Hourtoule, Aaron C. Bartoo, Satish K. Singh, and Jerome Mertz. Optically sectioned fluorescence endomicroscopy with hybrid-illumination imaging through a flexible fiber bundle. *Journal of Biomedical Optics*, 14(3):030502, 2009.

[194] J. Sonnefeld. Surface charge density on spherical silica particles in aqueous alkali chloride solutions. *Colloid & Polymer Science*, 273(10):932–938, oct 1995.

[195] Matthew A. Brown, Zareen Abbas, Armin Kleibert, Richard G. Green, Alok Goel, Sylvio May, and Todd M. Squires. Determination of Surface Potential and Electrical Double-Layer Structure at the Aqueous Electrolyte-Nanoparticle Interface. *Physical Review X*, 6(1):011007, jan 2016.

[196] C. H. Lee, R. K. Chang, and N. Bloembergen. Nonlinear Electroreflectance in Silicon and Silver. *Physical Review Letters*, 18(5):167–170, jan 1967.

[197] Julianne M. Gibbs-Davis, Jennifer J. Kruk, Christopher T. Konek, Karl A. Scheidt, and Franz M. Geiger. Jammed Acid-Base Reactions at Interfaces. *Journal of the American Chemical Society*, 130(46):15444–15447, nov 2008.

[198] Christopher T. Konek, Michael J. Musorrafiti, Hind A. Al-Abadleh, Paul A. Bertin, Son-Binh T. Nguyen, and Franz M. Geiger. Interfacial Acidities, Charge Densities, Potentials, and Energies of Carboxylic Acid-Functionalized Silica/Water Interfaces Determined by Second Harmonic Generation. *Journal of the American Chemical Society*, 126(38):11754–11755, sep 2004.

[199] Kailash C. Jena, Paul A. Covert, and Dennis K. Hore. The effect of salt on the water structure at a charged solid surface: Differentiating second- and third-order nonlinear contributions. *Journal of Physical Chemistry Letters*, 2(9):1056–1061, 2011.

[200] Dan Lis, E. H. G. Backus, Johannes Hunger, Sapun H. Parekh, and Mischa Bonn. Liquid flow along a solid surface reversibly alters interfacial chemistry. *Science*, 344(6188):1138–1142, jun 2014.

[201] P Schindler and H R Kamber. Die Acidität von Silanolgruppen. Vorläufige Mitteillung. *Helvetica Chimica Acta*, 51(7):1781–1786, oct 1968.

[202] Matthew A. Brown, Alok Goel, and Zareen Abbas. Effect of Electrolyte Concentration on the Stern Layer Thickness at a Charged Interface. *Angewandte Chemie International Edition*, 55(11):3790–3794, mar 2016.

[203] Roman D. Bulushev, Sanjin Marion, and Aleksandra Radenovic. Relevance of the Drag Force during Controlled Translocation of a DNA-Protein Complex through a Glass Nanocapillary. *Nano Letters*, 15(10):7118–7125, 2015.

[204] Nadanai Laohakunakorn, Sandip Ghosal, Oliver Otto, Karolis Misiunas, and Ulrich F. Keyser. DNA Interactions in Crowded Nanopores. *Nano Letters*, 13(6):2798–2802, jun 2013.

[205] Thomas M. Pearce and Justin C. Williams. Microtechnology: Meet neurobiology. *Lab Chip*, 7(1):30–40, 2007.

[206] Mehdi Neek-Amal, Francois M. Peeters, Irina V. Grigorieva, and Andre K. Geim. Commensurability Effects in Viscosity of Nanoconfined Water. *ACS Nano*, 10(3):3685–3692, mar 2016.

[207] R. R. Nair, H. A. Wu, P. N. Jayaram, I. V. Grigorieva, and A. K. Geim. Unimpeded Permeation of Water Through Helium-Leak-Tight Graphene-Based Membranes. *Science*, 335(6067):442–444, jan 2012.

[208] Roman D. Bulushev, Lorenz J. Steinbock, Sergey Khlybov, Julian F. Steinbock, Ulrich F. Keyser, and Aleksandra Radenovic. Measurement of the Position-Dependent Electrophoretic Force on DNA in a Glass Nanocapillary. *Nano Letters*, 14(11):6606–6613, nov 2014.

[209] Carl W. Fuller, Shiv Kumar, Mintu Porel, Minchen Chien, Arek Bibillo, P. Benjamin Stranges, Michael Dorwart, Chuanjuan Tao, Zengmin Li, Wenjing Guo, Shundi Shi, Daniel Korenblum, Andrew Trans, Anne Aguirre, Edward Liu, Eric T. Harada, James Pollard, Ashwini Bhat, Cynthia Cech, Alexander Yang, Cleoma Arnold, Mirkó Palla, Jennifer Hovis, Roger Chen, Irina Morozova, Sergey Kalachikov, James J. Russo, John J. Kasianowicz, Randy Davis, Stefan Roever, George M. Church, and Jingyue Ju. Real-time single-molecule electronic DNA sequencing by synthesis using polymer-tagged nucleotides on a nanopore array. *Proceedings of the National Academy of Sciences*, 113(19):5233–5238, may 2016.

[210] Li-Chung Cheng, Chia-Yuan Chang, Chun-Yu Lin, Keng-Chi Cho, Wei-Chung Yen, Nan-Shan Chang, Chris Xu, Chen Yuan Dong, and Shean-Jen Chen. Spatiotemporal focusing-based widefield multiphoton microscopy for fast optical sectioning. *Optics Express*, 20(8):8939, apr 2012.

[211] M. A. A. Neil, R. Juškaitis, and T. Wilson. Method of obtaining optical sectioning by using structured light in a conventional microscope. *Optics Letters*, 22(24):1905, dec 1997.

[212] Alex G. F. de Beer, R. Kramer Campen, and Sylvie Roke. Separating surface structure and surface charge with second-harmonic and sum-frequency scattering. *Physical Review B*, 82(23):235431, dec 2010.

[213] Yixing Chen, Halil I. Okur, Nikolaos Gomopoulos, Carlos Macias-Romero, Paul S. Cremer, Poul B. Petersen, Gabriele Tocci, David M. Wilkins, Chungwen Liang, Michele Ceriotti, and Sylvie Roke. Electrolytes induce long-range orientational order and free energy changes in the H-bond network of bulk water. *Science Advances*, 2(4):1–9, 2016.

[214] Robert J. Hunter. *Foundations of Colloid Science*. Oxford University Press, 2nd edition, 2001.

[215] Mario Löbbus, Wolfram Vogelsberger, Jürgen Sonnefeld, and Andreas Seidel. Current Considerations for the Dissolution Kinetics of Solid Oxides with Silica. *Langmuir*, 14(16):4386–4396, aug 1998.

[216] Jessica N. Malin, Joseph G. Holland, and Franz M. Geiger. Free Energy Relationships in the Electric Double Layer and Alkali Earth Speciation at the Fused Silica/Water Interface. *The Journal of Physical Chemistry C*, 113(41):17795–17802, oct 2009.

[217] Zili Wu and Steven H. Overbury, editors. *Catalysis by Materials with Well-Defined Structures*. Elsevier, 1st edition, 2015.

[218] Gerhard Ertl. Reactions at Surfaces: From Atoms to Complexity (Nobel Lecture). *Angewandte Chemie International Edition*, 47(19):3524–3535, apr 2008.

[219] Gabor A. Somorjai. *Introduction to Surface Chemistry and Catalysis*. Wiley, 1994.

[220] Scott C. Warren, Kislon Voïtchovsky, Hen Dotan, Celine M. Leroy, Maurin Cornuz, Francesco Stellacci, Cécile Hébert, Avner Rothschild, and Michael Grätzel. Identifying champion nanostructures for solar water-splitting. *Nature Materials*, 12(9):842–849, sep 2013.

[221] Ruperto G. Mariano, Kim McKelvey, Henry S. White, and Matthew W. Kanan. Selective increase in CO_2 electroreduction activity at grain-boundary surface terminations. *Science*, 358(6367):1187–1192, dec 2017.

[222] Albert K. Engstfeld, Sylvain Brimaud, and R. Jürgen Behm. Potential-Induced Surface Restructuring-The Need for Structural Characterization in Electrocatalysis Research. *Angewandte Chemie International Edition*, 53(47):12936–12940, nov 2014.

[223] A.K. Engstfeld, J. Klein, S. Brimaud, and R.J. Behm. Electrochemical stability and restructuring and its impact on the electro-oxidation of CO: Pt modified Ru(0001) electrodes. *Surface Science*, 631:248–257, jan 2015.

[224] Martin Ruge, Jakub Drnec, Björn Rahn, Finn Reikowski, David A. Harrington, Francesco Carlà, Roberto Felici, Jochim Stettner, and Olaf M. Magnussen. Structural Reorganization of Pt(111) Electrodes by Electrochemical Oxidation and Reduction. *Journal of the American Chemical Society*, 139(12):4532–4539, mar 2017.

[225] David Polcari, Philippe Dauphin-Ducharme, and Janine Mauzeroll. Scanning Electrochemical Microscopy: A Comprehensive Review of Experimental Parameters from 1989 to 2015. *Chemical Reviews*, 116(22):13234–13278, nov 2016.

[226] A. J. Bard, F.-R. F. Fan, D. T. Pierce, P. R. Unwin, D. O. Wipf, and F. Zhou. Chemical Imaging of Surfaces with the Scanning Electrochemical Microscope. *Science*, 254(5028):68–74, oct 1991.

[227] Carlos Macias-Romero, Claire Teulon, Marie Didier, and Sylvie Roke. Endogenous SHG and 2PEF coherence imaging of substructures in neurons in 3D. *Optics Express*, 27(3):2235, feb 2019.

[228] Sarah L Horswell, Alexei L N Pinheiro, Elena R Savinova, Matthias Danckwerts, Bruno Pettinger, Mau-scheng Zei, and Gerhard Ertl. A Comparative Study of Hydroxide Adsorption on the (111), (110), and (100) Faces of Silver with Cyclic Voltammetry, Ex Situ Electron Diffraction, and In Situ Second Harmonic Generation. *Langmuir*, 20(25):10970–10981, dec 2004.

[229] A.A. Tamburello-Luca, P. Hébert, P.F. Brevet, and H.H. Girault. Surface second harmonic study of anion adsorption at the mercury | electrolyte interface. *Journal of Electroanalytical Chemistry*, 409(1-2):123–129, jun 1996.

[230] Shah M.A. Baten, Alan G Taylor, and C Paul Wilde. Second Harmonic Generation studies of the oxidation of metal electrodes: Compact and hydrous oxide growth at gold electrodes in acid solutions. *Electrochimica Acta*, 53(23):6829–6834, oct 2008.

[231] O.A. Aktsipetrov, A.V. Melnikov, T.V. Murzina, A.A. Nikulin, and A.N. Rubtsov. DC-electric-field-induced optical second harmonic generation at the smooth metal-electrolyte interface. *Surface Science*, 336(1-2):225–231, aug 1995.

[232] L Werner, F Marlow, W Hill, and U Retter. Optical second harmonic generation at Hg electrodes. The adsorption of aniline. *Chemical Physics Letters*, 194(1-2):39–44, jun 1992.

[233] G. Lüpke, G. Marowsky, R. Steinhoff, A Friedrich, B. Pettinger, and D. M. Kolb. Symmetry superposition studied by surface second-harmonic generation. *Physical Review B*, 41(10):6913–6919, apr 1990.

[234] G.L. Richmond, J.M. Robinson, and V.L. Shannon. Second harmonic generation studies of interfacial structure and dynamics. *Progress in Surface Science*, 28(1):1–70, jan 1988.

[235] G.L. Richmond. Surface second-harmonic generation from sulfate ions adsorbed on silver electrodes. *Chemical Physics Letters*, 106(1-2):26–29, apr 1984.

[236] R. Georgiadis, G. A. Neff, and G. L. Richmond. Effect of optical resonances on the second harmonic response from Ag(111) and Ag(110) in solution. *The Journal of Chemical Physics*, 92(7):4623–4625, apr 1990.

[237] P Guyot-Sionnest, A Tadjeddine, and A Liebsch. Electronic distribution and nonlinear optical response at the metal-electrolyte interface. *Physical Review Letters*, 64(14):1678–1681, apr 1990.

[238] B Pettinger, J Lipkowski, and S Mirwald. In situ SHG studies of adsorption induced surface reconstruction of Au(111)-electrodes. *Electrochimica Acta*, 40(1):133–142, jan 1995.

[239] B Pettinger, S Mirwald, and J Lipkowski. Microfacetting of Au(110) electrodes: An optical second-harmonic generation study. *Applied Physics A Materials Science and Processing*, 60(2):121–125, feb 1995.

[240] Christoph Bilger and Bruno Pettinger. The SHG anisotropy pattern of a reconstructed gold(110) electrode. *Chemical Physics Letters*, 294(4-5):425–433, sep 1998.

[241] Yujin Tong, François Lapointe, Martin Thämer, Martin Wolf, and R Kramer Campen. Hydrophobic Water Probed Experimentally at the Gold Electrode/Aqueous Interface. *Angewandte Chemie International Edition*, 56(15):4211–4214, apr 2017.

[242] N. Bloembergen, R. K. Chang, S. S. Jha, and C H Lee. Optical Second-Harmonic Generation in Reflection from Media with Inversion Symmetry. *Physical Review*, 174(3):813–822, oct 1968.

[243] Robert M. Corn, Marco Romagnoli, Marc D. Levenson, and Michael R. Philpott. Second harmonic generation at thin film silver electrodes via surface polaritons. *The Journal of Chemical Physics*, 81(9):4127–4132, nov 1984.

[244] Nikolaos Gomopoulos, Cornelis Lütgebaucks, Qinchao Sun, Carlos Macias-Romero, and Sylvie Roke. Label-free second harmonic and hyper Rayleigh scattering with high efficiency. *Optics Express*, 21(1):815, jan 2013.

[245] Oscar Diaz-Morales, Federico Calle-Vallejo, Casper de Munck, and Marc T. M. Koper. Electrochemical water splitting by gold: evidence for an oxide decomposition mechanism. *Chemical Science*, 4(6):2334, 2013.

[246] Gabor A. Somorjai. Modern Surface Science and Surface Technologies: An Introduction. *Chemical Reviews*, 96(4):1223–1236, jan 1996.

[247] Per-Odd Eggen. A Simple Hydrogen Electrode. *Journal of Chemical Education*, 86(3):352, mar 2009.

[248] Gregor Zwaschka, Martin Wolf, R. Kramer Campen, and Yujin Tong. A Microscopic Model of the Electrochemical Vibrational Stark Effect: Understanding VSF Spectroscopy of (bi)Sulfate on Pt(111). *Surface Science*, 678(March):78–85, dec 2018.

[249] Fu Xiang Wang, Francisco J. Rodríguez, Willem M. Albers, Risto Ahorinta, J. E. Sipe, and Martti Kauranen. Surface and bulk contributions to the second-order nonlinear optical response of a gold film. *Physical Review B*, 80(23):233402, dec 2009.

[250] Gediminas Niaura, Adolfas K. Gaigalas, and Vincent L. Vilker. Surface-Enhanced Raman Spectroscopy of Phosphate Anions: Adsorption on Silver, Gold, and Copper Electrodes. *The Journal of Physical Chemistry B*, 101(45):9250–9262, nov 1997.

[251] B.E. Conway, E. Ralph White, and J. O'M Bockris. *Book 1985_Conway - Modern aspects of electrochemistry.pdf*. Plenum Press, 1985.

[252] Motohiro Kasuya, Tsukasa Sogawa, Takuya Masuda, Toshio Kamijo, Kohei Uosaki, and Kazue Kurihara. Anion Adsorption on Gold Electrodes Studied by Electrochemical Surface Forces Measurement. *The Journal of Physical Chemistry C*, 120(29):15986–15992, jul 2016.

[253] M. Weber, I.R. de Moraes, A.J. Motheo, and F.C. Nart. In situ vibrational spectroscopy analysis of adsorbed phosphate species on gold single crystal electrodes. *Colloids and Surfaces A: Physicochemical and Engineering Aspects*, 134(1-2):103–111, mar 1998.

[254] Fernando Silva and Ana Martins. Surface structural effects on specific adsorption of oxoanions on gold single crystal electrodes. *Journal of Electroanalytical Chemistry*, 467(1-2):335–341, jun 1999.

[255] L. Declan Burke, John A. Collins, and Maria A. Murphy. Redox and electrocatalytic activity of copper in base at unusually low, premonolayer potentials. *Journal of Solid State Electrochemistry*, 4(1):34–41, nov 1999.

[256] Ulmas Zhumaev, Alexander V Rudnev, Jian-Feng Li, Akiyoshi Kuzume, Thu-Hien Vu, and Thomas Wandlowski. Electro-oxidation of Au(111) in contact with aqueous electrolytes: New insight from in situ vibration spectroscopy. *Electrochimica Acta*, 112:853–863, dec 2013.

[257] Koji Yoshida, Akiyoshi Kuzume, Peter Broekmann, Ilya V. Pobelov, and Thomas Wandlowski. Reconstruction and electrochemical oxidation of Au(110) surface in 0.1 M H2SO4. *Electrochimica Acta*, 139:281–288, sep 2014.

[258] H. Angerstein-Kozlowska, B.E. Conway, A. Hamelin, and L. Stoicoviciu. Elementary steps of electrochemical oxidation of single-crystal planes of Au—I. Chemical basis of processes involving geometry of anions and the electrode surfaces. *Electrochimica Acta*, 31(8):1051–1061, aug 1986.

[259] H. Angerstein-Kozlowska, B.E. Conway, A. Hamelin, and L. Stoicoviciu. Elementary steps of electrochemical oxidation of single-crystal planes of Au Part II. A chemical and structural basis of oxidation of the (111) plane. *Journal of Electroanalytical Chemistry and Interfacial Electrochemistry*, 228(1-2):429–453, aug 1987.

[260] Antoinette Hamelin, Zofia Borkowska, and Janusz Stafiej. A double layer study of the (210) and (111) faces of gold in aqueous $NaBF_4$ solutions. *Journal of Electroanalytical Chemistry and Interfacial Electrochemistry*, 189(1):85–97, jul 1985.

[261] Zofia Borkowska and Ulrich Slimming. Perchlorate adsorption on polycrystalline gold electrodes in aqueous perchloric acid. *Journal of Electroanalytical Chemistry and Interfacial Electrochemistry*, 312(1-2):237–244, aug 1991.

[262] V. Climent, N. García-Araez, E. Herrero, and J. Feliu. Potential of zero total charge of platinum single crystals: A local approach to stepped surfaces vicinal to Pt(111). *Russian Journal of Electrochemistry*, 42(11):1145–1160, 2006.

[263] Angel Cuesta, Markus Kleinert, and Dieter M. Kolb. The adsorption of sulfate and phosphate on Au(111) and Au(100) electrodes: an in situ STM study. *Physical Chemistry Chemical Physics*, 2(24):5684–5690, 2000.

[264] L. D. Burke, A. J. Ahern, and A P O'Mullane. High energy states of goldand their importance in electrocatalytic processes at surfaces and interfaces. *Gold Bulletin*, 35(1):3–10, mar 2002.

[265] Robert W. Boyd, Zhimin Shi, and Israel De Leon. The third-order nonlinear optical susceptibility of gold. *Optics Communications*, 326:74–79, sep 2014.

[266] Xingyou Lang, Lihua Qian, Pengfei Guan, Jian Zi, and Mingwei Chen. Localized surface plasmon resonance of nanoporous gold. *Applied Physics Letters*, 98(9):093701, feb 2011.

[267] Jessica Rodríguez-Fernández, Alison M Funston, Jorge Pérez-Juste, Ramón A. Álvarez-Puebla, Luis M. Liz-Marzán, and Paul Mulvaney. The effect of surface roughness on the plasmonic response of individual sub-micron gold spheres. *Physical Chemistry Chemical Physics*, 11(28):5909, 2009.

[268] Hugh Stott Taylor. A theory of the catalytic surface. *Proceedings of the Royal Society of London. Series A, Containing Papers of a Mathematical and Physical Character*, 108(745):105–111, may 1925.

[269] Marc T. M. Koper. Structure sensitivity and nanoscale effects in electrocatalysis. *Nanoscale*, 3(5):2054, 2011.

[270] Anthony P. O'Mullane. From single crystal surfaces to single atoms: investigating active sites in electrocatalysis. *Nanoscale*, 6(8):4012–4026, 2014.

[271] Manuel J. S. Farias and Juan M. Feliu. Determination of Specific Electrocatalytic Sites in the Oxidation of Small Molecules on Crystalline Metal Surfaces. *Topics in Current Chemistry*, 377(1):5, feb 2019.

[272] José Solla-Gullón, Paramaconi Rodríguez, Enrique Herrero, Antonio Aldaz, and Juan M. Feliu. Surface characterization of platinum electrodes. *Phys. Chem. Chem. Phys.*, 10(10):1359–1373, 2008.

[273] Toshihiro Kondo, Jun Morita, Kazuya Hanaoka, Satoru Takakusagi, Kazuhisa Tamura, Masamitu Takahasi, Ju N.Ichiro Mizuki, and Kohei Uosaki. Structure of Au(111) and Au(100) single-crystal electrode surfaces at various potentials in sulfuric acid solution determined by in situ surface X-ray scattering. *Journal of Physical Chemistry C*, 111(35):13197–13204, 2007.

[274] M. A. Schneeweiss and D. M. Kolb. Oxide formation on Au(111) an in situ STM study. *Solid State Ionics*, 94(1-4):171–179, 1997.

[275] Norbert Weiher. *Combined in situ and ex situ Studies of an Electrochemical Interface*. PhD thesis, Free University of Berlin, 2003.

[276] Tobias Binninger, Rhiyaad Mohamed, Kay Waltar, Emiliana Fabbri, Pieter Levecque, Rüdiger Kötz, and Thomas J. Schmidt. Thermodynamic explanation of the universal correlation between oxygen evolution activity and corrosion of oxide catalysts. *Scientific Reports*, 5(1):12167, dec 2015.

[277] S.J Xia and V.I Birss. A multi-technique study of compact and hydrous Au oxide growth in 0.1 M sulfuric acid solutions. *Journal of Electroanalytical Chemistry*, 500(1-2):562–573, mar 2001.

[278] L. D. Burke and P. F. Nugent. The electrochemistry of gold: II the electrocatalytic behaviour of the metal in aqueous media. *Gold Bulletin*, 31(2):39–50, jun 1998.

[279] M. Wohlfahrt-Mehrens and J. Heitbaum. Oxygen evolution on Ru and RuO_2 electrodes studied using isotope labelling and on-line mass spectrometry. *Journal of Electroanalytical Chemistry and Interfacial Electrochemistry*, 237(2):251–260, nov 1987.

[280] Stéphane Fierro, Tina Nagel, Helmut Baltruschat, and Christos Comninellis. Investigation of the oxygen evolution reaction on Ti/IrO_2 electrodes using isotope labelling and on-line mass spectrometry. *Electrochemistry Communications*, 9(8):1969–1974, aug 2007.

[281] Katerina Macounova, Marina Makarova, and Petr Krtil. Oxygen evolution on nanocrystalline RuO_2 and $Ru_{0.9}Ni_{0.1}O_{2-\delta}$ electrodes - DEMS approach to reaction mechanism determination. *Electrochemistry Communications*, 11(10):1865–1868, oct 2009.

[282] Charles C. L. McCrory, Suho Jung, Jonas C. Peters, and Thomas F. Jaramillo. Benchmarking Heterogeneous Electrocatalysts for the Oxygen Evolution Reaction. *Journal of the American Chemical Society*, 135(45):16977–16987, nov 2013.

[283] D. L. Burke and Anthony P. O'Mullane. Generation of active surface states of gold and the role of such states in electrocatalysis. *Journal of Solid State Electrochemistry*, 4(5):285–297, may 2000.

[284] Long Luo and Henry S. White. Electrogeneration of single nanobubbles at sub-50-nm-radius platinum nanodisk electrodes. *Langmuir*, 29(35):11169–11175, 2013.

[285] Qianjin Chen, Hilke S. Wiedenroth, Sean R. German, and Henry S. White. Electrochemical Nucleation of Stable N_2 Nanobubbles at Pt Nanoelectrodes. *Journal of the American Chemical Society*, 137(37):12064–12069, sep 2015.

[286] Qianjin Chen, Long Luo, and Henry S. White. Electrochemical generation of a hydrogen bubble at a recessed platinum nanopore electrode. *Langmuir*, 31(15):4573–4581, 2015.

[287] Hang Ren, Sean R. German, Martin A. Edwards, Qianjin Chen, and Henry S. White. Electrochemical Generation of Individual O_2 Nanobubbles via H_2O_2 Oxidation. *The Journal of Physical Chemistry Letters*, 8(11):2450–2454, jun 2017.

[288] Sean R. German, Martin A. Edwards, Hang Ren, and Henry S. White. Critical Nuclei Size, Rate, and Activation Energy of H_2 Gas Nucleation. *Journal of the American Chemical Society*, 140(11):4047–4053, mar 2018.

[289] Qianjin Chen, Long Luo, Hamaseh Faraji, Stephen W. Feldberg, and Henry S. White. Electrochemical Measurements of Single H_2 Nanobubble Nucleation and Stability at Pt Nanoelectrodes. *The Journal of Physical Chemistry Letters*, 5(20):3539–3544, oct 2014.

[290] D. E. Westerheide and J. W. Westwater. Isothermal growth of hydrogen bubbles during electrolysis. *AIChE Journal*, 7(3):357–362, sep 1961.

[291] J.P. Glas and J.W. Westwater. Measurements of the growth of electrolytic bubbles. *International Journal of Heat and Mass Transfer*, 7(12):1427–1443, dec 1964.

[292] James R. T. Seddon, E. Stefan Kooij, Bene Poelsema, Harold J. W. Zandvliet, and Detlef Lohse. Surface Bubble Nucleation Stability. *Physical Review Letters*, 106(5):056101, feb 2011.

[293] Min Guan, Wen Guo, Lianhua Gao, Yuzhao Tang, Jun Hu, and Yaming Dong. Investigation on the Temperature Difference Method for Producing Nanobubbles and Their Physical Properties. *ChemPhysChem*, 13(8):2115–2118, jun 2012.

[294] T. Zambelli, J. Wintterlin, J. Trost, and G. Ertl. Identification of the "Active Sites" of a Surface-Catalyzed Reaction. *Science*, 273(5282):1688–1690, sep 1996.

[295] S. Dahl, A. Logadottir, R. C. Egeberg, J. H. Larsen, I. Chorkendorff, E. Törnqvist, and J. K. NØrskov. Role of steps in N_2 activation on Ru(0001). *Physical Review Letters*, 83(9):1814–1817, 1999.

[296] Kazuhiko Amakawa, Sabine Wrabetz, Jutta Kröhnert, Genka Tzolova-Müller, Robert Schlögl, and Annette Trunschke. In Situ Generation of Active Sites in Olefin Metathesis. *Journal of the American Chemical Society*, 134(28):11462–11473, jul 2012.

[297] Blake J. Plowman, Anthony P. O'Mullane, and Suresh K. Bhargava. The active site behaviour of electrochemically synthesised gold nanomaterials. *Faraday Discussions*, 152:43–62, 2011.

[298] Serhiy Cherevko, Nadiia Kulyk, and Chan-Hwa Chung. Utilization of surface active sites on gold in preparation of highly reactive interfaces for alcohols electrooxidation in alkaline media. *Electrochimica Acta*, 69:190–196, may 2012.

[299] Blake J. Plowman, Matthew R. Field, Suresh K. Bhargava, and Anthony P. O'Mullane. Exploiting the Facile Oxidation of Evaporated Gold Films to Drive Electroless Silver Deposition for the Creation of Bimetallic Au/Ag Surfaces. *ChemElectroChem*, 1(1):76–82, jan 2014.

[300] Poul L. Hansen, Jakob B. Wagner, Stig Helveg, Jens R. Rostrup-Nielsen, Bjerne S. Clausen, and Henrik Topsøe. Atom-Resolved Imaging of Dynamic Shape Changes in Supported Copper Nanocrystals. *Science*, 295(5562):2053–2055, 2002.

[301] Thomas Lunkenbein, Julia Schumann, Malte Behrens, Robert Schlögl, and Marc G. Willinger. Formation of a ZnO Overlayer in Industrial Cu/ZnO/Al_2O_3 Catalysts Induced by Strong Metal-Support Interactions. *Angewandte Chemie International Edition*, 54(15):4544–4548, apr 2015.

[302] Andrzej Wieckowski. *Interfacial Electrochemistry: Theory: Experiment, and Applications*. CRC Press, nov 1999.

[303] Lee Sunggyu, editor. *Encyclopedia of Chemical Processing*. CRC Press, 1st edition, 2005.

[304] Serhiy Cherevko, Angel A. Topalov, Aleksandar R. Zeradjanin, Ioannis Katsounaros, and Karl J. J. Mayrhofer. Gold dissolution: towards understanding of noble metal corrosion. *RSC Advances*, 3(37):16516, 2013.

[305] L. D. Burke, V. J. Cunnane, and B. H. Lee. Unusual Postmonolayer Oxide Behavior of Gold Electrodes in Base. *Journal of The Electrochemical Society*, 139(2):399, 1992.

[306] Kai Zeng and Dongke Zhang. Recent progress in alkaline water electrolysis for hydrogen production and applications. *Progress in Energy and Combustion Science*, 36(3):307–326, jun 2010.

[307] R. W. Zurilla, R. K. Sen, and E. Yeager. The Kinetics of the Oxygen Reduction Reaction on Gold in Alkaline Solution. *Journal of The Electrochemical Society*, 125(7):1103, 1978.

[308] Antoinette Hamelin, M.J. Sottomayor, F. Silva, Si-Chung Chang, and Michael J. Weaver. Cyclic voltammetric characterization of oriented monocrystalline gold surfaces in aqueous alkaline solution. *Journal of Electroanalytical Chemistry and Interfacial Electrochemistry*, 295(1-2):291–300, nov 1990.

[309] A. Hamelin. Cyclic voltammetry at gold single-crystal surfaces. Part 1. Behaviour at low-index faces. *Journal of Electroanalytical Chemistry*, 407(1-2):1–11, may 1996.

[310] Xiaoping Gao, Gregory J. Edens, Antoinette Hamelin, and Michael J. Weaver. Charge-dependent atomic-scale structures of high-index and (110) gold electrode surfaces as revealed by scanning tunneling microscopy. *Surface Science*, 318(1-2):1–20, oct 1994.

[311] A. Hamelin. The surface state and the potential of zero charge of gold (100): a further assessment. *Journal of Electroanalytical Chemistry*, 386(1-2):1–10, apr 1995.

[312] Acacio Rincón, Daniele Desideri, and Enrico Bernardo. Functional glass-ceramic foams from 'inorganic gel casting' and sintering of glass/slag mixtures. *Journal of Cleaner Production*, 187:250–256, jun 2018.

[313] Claes G. Granqvist. Electrochromics for smart windows: Oxide-based thin films and devices. *Thin Solid Films*, 564:1–38, aug 2014.

[314] Adam Ellison and Iván A. Cornejo. Glass Substrates for Liquid Crystal Displays. *International Journal of Applied Glass Science*, 1(1):87–103, mar 2010.

Igor Nahalka

igornahalka@gmail.com, +41 76 652 05 92,
Les Rives de la Morges 3, 1110, Morges Switzerland

WORK EXPERIENCE

Jan. 2017 – Jan. 2020 **Ph. D. employee, Marie Curie Early State Researcher** (FBI network)
Multimodal imaging of surface chemistry dynamics at solid/liquid interfaces
Instrumentation, Microscopy, Nonlinear optics, Data processing, Electrochemistry
Supervisor: Sylvie Roke, Laboratory for fundamental BioPhotonics, EPFL, Switzerland
Co-supervisor: Arianna Marchioro, Laboratory for fundamental BioPhotonics, EPFL

Sep. 2015 – Jun. 2016 **Researcher, Institute of Photonics and Electronics ASCR**
Developing of micro-flow chamber for controlled fabrication of ZnO nanostructures
Clean room, Scanning electron microscopy, Atomic force microscopy, Focused ion beam, 3D designing, Prototyping, Instrumentation
Supervisor: Jan Grym, Laboratory of synthesis and characterization of nanomaterials, Prague, Czech Republic

EDUCATION

Sep. 2016 – Sep. 2020 **Ph. D. in Photonics**
Thesis: Heterogeneity of surface chemistry revealed by second harmonic imaging
École Polytechnique Fédérale de Lausanne (EPFL), Switzerland

Sep. 2014 – June 2016 **M. Sc. in Optics and Nanotechnology**
Thesis: Hydrothermal growth and characterization of semiconductor nanostructures
Czech Technical University in Prague, Czech Republic

Sep. 2015 – June 2016 **Exchange program in Optical Sciences**
Optical technologies and Chinese language
Zhejiang University China

Sep. 2010 – June 2013 **B. Sc. in Physics**
Thesis: Developing and optimizing a device for photolithography
Czech Technical University in Prague, Czech Republic

AWARDED PRIZES & GRANTS

June 2019 **Best Poster Award**, Biophotonics Summer School, Sweden

2017 – 2020 **Marie Curie Early State Researcher** (FBI: Functional multimodal BioImaging), EPFL, Switzerland

SKILLS AND QUALIFICATIONS

Languages Slovak (mother tongue), English (Fluent), German (basic), Hungarian (fluent), Czech (fluent), Spanish (basic), Chinese (basic)

Computer Skills Matlab, Python, LaTeX, ImageJ, Rhino 3D, LabVIEW, Zemax
Adobe Illustrator, Adobe Photoshop, MS Office

Industry Skills Cleanroom, Wet lab, Developing of optical setups,
Signal processing, Image and Video processing, Data acquisition,
Optical microscopy, Scanning electron microscopy, Atomic force microscopy,
3D printing, Prototyping, Data Processing, Instrumentation

Technology Lasers, Nonlinear optics, Spatial light modulators, Photolithography,
Fabrication of nanostructures

Soft Skills Low-level management, Collaboration, Persistence, Innovation, Conflict management

TRAINING

Aug. 2019	Workshop: **Optical design in Zemax** with Herbert Gross from Zeiss**,** Lausanne, Switzerland
Nov. 2019	Workshop: **Fiber lasers**, Marie Curie meeting in Copenhagen NKT, Denmark
Mar. 2019	**Organizer of Marie Curie** meeting in Lausanne (60 people), Switzerland
Mar. 2019	Workshop: **Entrepreneurship**, Marie Curie meeting in Lausanne, Switzerland
June 2018	Workshop: **European Patent Office**, Marie Curie meeting in Munich, Germany
June 2018	Workshop: **Bioethics**, Marie Curie meeting in Munich, Germany
Feb. 2018	Nature journal editors: **Writing Skills**, Marie Curie meeting in Eindhoven, Netherlands
Sep. 2017	Workshop: **Presentation Skills**, Marie Curie meeting in Vienna, Austria

PUBLICATIONS

2020	**I. Nahalka**[1], G. Zwaschka[1], R. K. Campen, A. Marchioro, and S. Roke, Mapping Electrochemical Heterogeneity at Gold Surfaces: A Second Harmonic Imaging Study, Submitted (**2020**).
2020	G. Zwaschka[1], **I. Nahalka**[1], A. Marchioro, Y. Tong, S. Roke, and R. K. Campen. Imaging the Heterogeneity of the Oxygen Evolution Reaction on Gold Electrodes Operando: Activity is Highly Local, *ACS Catalysis*, **2020**, *10*, 6084–6093.
2017	C. Macias-Romero, **I. Nahalka**, H. I. Okur, S. Roke, Optical Imaging of Surface Chemistry and Dynamics in Confinement, *Science*, **2017**, *357*, 784–788.

SCIENTIFIC CONFERENCES

Dec. 2019	**Photonics Day** conference, Neuchâtel, Switzerland
June 2019	**Recent Development in Bioimaging**: Biophotonics Summer School in Ven, Sweden
Sep. 2018	**Swiss Chemical Society** conference, Lausanne, Switzerland
July 2018	Gordon Research Conference: **Water and Aqueous Solutions**, Holderness, New Hampshire, USA

TEACHING EXPERIENCES

2017 - 2019	**Teaching Assistant**: Interfaces in Biology and Nanoscience (25 students), Bachelor course, EPFL
2017 – 2018	**Teaching Assistant**: Nonlinear Optics (20 students), Ph. D. course, EPFL

CHARACTER REFERENCES

Professor Sylvie Roke
Laboratory for fundamental BioPhotonics
EPFL

EPFL STI IBI-STI LBP
BM 4112, Station 17
CH-1015 Lausanne

Contact: sylvie.roke@epfl.ch
+41 21 693 11 91

Dr. Arianna Marchioro
Laboratory for fundamental BioPhotonics
EPFL

EPFL STI IBI-STI LBP
BM 4113, Station 17
CH-1015 Lausanne

Contact: arianna.marchioro@epfl.ch
+41 21 693 61 80

**Ce document a été imprimé au Centre d'impression EPFL,
imprimerie climatiquement neutre, certifiée myClimate.**